



Ingeniaritza Goi Eskola Teknikoa
Escuela Técnica Superior de Ingeniería
Bilbao

Ph.D. Thesis

**Design methodology for MAST-type parallel
manipulators based on kinematic, dynamic and
stiffness criteria: theoretical and experimental
application to the 2PRU-1PRS**

Presented by:
Saioa Herrero Villalibre

belonging to the
Mechanical Engineering Department
Faculty of Engineering in Bilbao
University of the Basque Country (UPV/EHU)
Spain

To obtain the degree of:
Doctor of Philosophy in Mechanical Engineering

Thesis Advisor:
Prof. Dr.- Eng. Charles Pinto

July 2016, Bilbao

Dedicated to my parents

*The noblest pleasure
is the joy of understanding.
Leonardo da Vinci*

Acknowledgements

Recuerdo la primera vez que tuve que escribir un documento técnico, el esfuerzo que me costó ceñirme a frases directas, claras y concisas, y no poder dar rienda suelta a mi expresión. Paradójicamente, hoy, cuando después de tanto tiempo de duro trabajo y esfuerzo por fin tengo la oportunidad de expresar de verdad lo que siento, apenas sé cómo hacerlo. Durante estos años de doctorado ha habido momentos muy duros, momentos divertidos, mucho trabajo y mucho aprendido, pero si tuviera que quedarme con algo de todo ello serían sin duda las personas que he tenido a mi lado.

Charles, no puedo sino darte las gracias por haber confiado en mí desde el principio. Gracias por tu apoyo continuo y por sacar siempre un hueco de tu apretada agenda para sentarte conmigo a repasar ecuaciones, a corregir papers, a buscar soluciones o ejercer, incluso, de psicólogo. Gracias por recibirme siempre con una sonrisa, por enseñarme a tomar perspectiva y a relativizar; por animarme a pensar, a buscar nuevas ideas y a no rendirme; por marcarme el camino pero dejarme caminarlo a mi ritmo. Gracias también al resto de fantásticos profesores de nuestro grupo: a Oscar por ayudarme a ver como sencilla hasta la ecuación más tortuosa; a Víctor por dirigirme el proyecto fin de carrera y ofrecerme después continuar en el grupo; a Alfonso por tener siempre una palabra de ánimo y apoyo. No todo el mundo tiene la suerte de trabajar en aquello que le gusta, y yo lo he conseguido gracias en gran parte a vosotros. Gracias de corazón a los cuatro.

En cuanto a mis compañeros, qué decir de ellos. Mikel, quién te iba a decir que la "chica del mecanismo del coche" te iba a dar tanta guerra. Me empezaste a ayudar entonces y no lo has dejado de hacer ni un instante. Gracias por haberte involucrado tanto en esta tesis y por hacerme ver que puedo contar contigo; por hacer divertidas todas esas horas de taller de pruebas y montaje; por todos esos cafés llenos de anécdotas y risas, y por animarme tanto en mis peores momentos. Eres un compañero increíble, pero aún mejor amigo. Moni, eres una súper compañera, una súper profe, una súper researcher, una súper amiga y ahora también una súper mami. Gracias por tener siempre una palabra bonita para dedicarme; es un inmenso honor trabajar contigo y tenerte como amiga. Asier, si no fuese por tí seguiría pasando veinte mil variables a una función de Matlab, y lo sabes. Gracias por tus ideas y por las reuniones improvisadas en los pasillos; por dejar de reunirse un ratito y bajar a comer, y por hacer de ello ratos inolvidables. Larrea, único con tus chistes, gracias por hacerme ver que no soy yo quien debe juzgar mi trabajo, pues me falta perspectiva y me sobra cansancio. Constantino, comenzamos juntos en el Máster y aquí seguimos, codo con codo, peleándonos con nuestras tesis hasta el último instante. Ha sido un placer tenerte como compañero de viaje. Gracias también a Javi por tu aportación en esta tesis; por los buenos y no tan buenos momentos, porque de todos ellos se aprende y nos hacen más fuertes. Erik, gracias por hacer mi primer año en la asignatura tan fácil; por tus ironías, que le dan chispa al día a día, y por compartir conmigo la forma de ver el trabajo. Y por supuesto, gracias también a mis compañeros de la sala de doctorandos: a Eneko, por las conversaciones y consejos que me ofreciste desde el sector trasero de la sala; a Abásolo, fuente inagotable de geniales anécdotas, por tu gran método de euskera técnico para euskaldunberris; y a Olatz y Nekane, por preocuparos tanto y darme ánimos.

En esta tesis hay mucho de mí, y en mí hay mucho de quienes comparten conmigo la vida. Ellos son mi familia y amigos, que se interesan siempre tanto por cuanto hago, y me apoyan en cada nueva aventura. Gracias a los padres de Mandar y a Sonali por el gran cariño y apoyo mostrado. Por supuesto, nada de esto habría sido lo mismo sin mi hermano Diego,

que siempre ha estado a mi lado, dándome ánimos, sirviéndome de guía y haciendo del mundo un lugar más divertido. También a Eva, por sus consejos, y por regalarnos siempre su sonrisa. Gracias a Unax y a Ane por llenar de tanta alegría nuestras vidas. Para mis abuelos, Ángel y Bárbara, no tengo palabras. Me habéis enseñado el valor de las pequeñas cosas y a sentirme siempre orgullosa de quiénes somos; me habéis dado vuestro cariño incondicional y me habéis hecho sentir como la persona más hermosa. Amoma, no me acostumbro a echarte de menos.

Mandar, dicen que las mejores cosas en la vida ocurren por casualidad, y tú eres el mejor ejemplo de ello; jamás podré agradecerle lo suficiente a esta tesis el haberme dado la oportunidad de conocerte. Gracias por tu inmensa paciencia conmigo y con mi trabajo. Incluso en la distancia, te siento siempre a mi lado, escuchando mis dudas y mis miedos, animándome a seguir y haciéndome reír incluso en los días más oscuros. Tú, que haces mis alegrías más grandes y las penas más pequeñas, te has convertido además en mi revisor y corrector de inglés personal, leyendo todas y cada una de las páginas de este trabajo, y haciéndonos a las dos, a esta tesis y a mí, mejores. Eres maravilloso. Te quiero.

Y por último, doy las gracias a mis padres, Ramiro y Julia, porque vosotros sois mi vida. Me habéis inculcado vuestra curiosidad por el mundo que nos rodea y vuestro amor por el arte en todas sus expresiones; nadie mejor que vosotros ha sabido ver y comprender mi mente científica, mi espíritu aventurero y mi alma de artista. Gracias por enseñarme a creer en mí misma, por hacerme ver que con esfuerzo e ilusión podemos llegar mucho más allá de los límites de nuestros sueños. Gracias por vuestro apoyo y amor infinitos. Esta tesis jamás habría sido posible sin vosotros.

Saioa

Abstract

This thesis presents research in the field of parallel manipulators. We can basically divide industrial robots in two groups – parallel and serial manipulators. Parallel manipulators are composed of a mobile and a fixed platform connected by several legs. They are of great interest for industrial application because they are more rigid and display better dynamic performance than serial manipulators. We focus on the design of parallel manipulators and, specifically, on the multi-axis shaking tables (MAST). These machines are linkage-based systems that generate a coupled motion in their end-effector by combining translations and rotations. Their main applications are the dynamic testing of structures or mechanical components - they are essential to experimentally verify the safety and reliability of pieces or structures under dynamic load conditions.

In this thesis we present two methodologies. The first one analyses the performance of a MAST-type parallel manipulator with known geometric parameters. The second one optimizes the geometric parameters taking into account two performances – the size and regularity of the workspace and the power consumption. Even though we particularize them for the 2PRU-1PRS parallel manipulator, both methodologies are valid for any MAST-type parallel manipulator. Moreover, we present the development of a prototype of the 2PRU-1PRS parallel manipulator, which we use to validate the methodologies proposed.

The thesis is organized as follows:

In **Part I** we give an overview of the literature existing in the field of parallel manipulators. We start with a little history of the origin of parallel manipulators. We present two possible classifications – the first one considers their application and the second one, their number of degrees of freedom. We also present the general consideration that we have to take into account when designing a parallel manipulator.

Part II presents the methodologies we propose in this work. We first work out the requirements and constraints that a MAST for automobile pieces testing purposes has to fulfil. In order to simulate realistic environment conditions of the car, we need three movements – a translation along the vertical Z-axis and two rotations about X- and Y-axes for roll and pitch. We compare different kinematic structures and choose our MAST to be a 2PRU-1PRS parallel manipulator with specific dimensional relations. This structure ideally ensures the required excitation motions. Then, we develop two general methodologies – analysis and optimization of the manipulator.

In **Part III** we present the analysis methodology. We first introduce and describe the 2PRU-1PRS parallel manipulator. We then develop the kinematic, stiffness and dynamic equations. Besides, we describe the procedure to obtain the useful workspace free of singularities by taking different restrictions into account.

In **Part IV** we develop the second methodology – the optimization of the parallel manipulator. We propose two optimization methods. The first one optimizes the geometric parameters in order to get the biggest and more regular useful workspace as possible. The latter obtains the geometric parameters that lead to the lowest power consumption along a given trajectory. We apply both methods to the 2PRU-1PRS parallel manipulator and show their efficient performance.

Part V goes deeply into the design of a prototype that we have built in

the laboratory of COMPMECH Research Group in the department of Mechanical Engineering in the University of the Basque Country. We describe all the components of the prototype – linear guides, motors, gearheads, revolte joints, spherical joint, universal joints, mobile and fixed platform and limbs – some of which being commercial and others being specially designed and built for the prototype. We compare numerical results with analyses done by using finite element methods and experimental methods on the prototype. We see minor differences in the results due to clearances between joints that appear in the prototype.

In **Part VI** we give the conclusions and possible future work.

Claim of originality

- In the initial stage of the thesis, we study the constraints and requirements that a MAST-type parallel manipulator has to fulfil in order to be used as testing machine for automobile pieces. In order to simulate realistic environment conditions of the car, we need a translation along the vertical Z-axis and two rotations about X- and Y-axes for roll and pitch. We compare different MAST-type parallel manipulators that perform these movements and conclude that the best one for application is the 2PRU-1PRS parallel manipulator.
- Then, we present two methodologies. The first one analyses the performance of the manipulator by taking kinematic, stiffness and dynamic considerations into account. The latter presents two optimization methods that take the size and regularity of the useful workspace and the power consumption along a given trajectory.
- Finally, we design and build a prototype that we use to validate the previous methodologies by comparing numerical results with results obtained by applying finite element and experimental methods.

General Index

Acknowledgements	III
Abstract	VII
General Index	XI

I	State of the Art	1
1	Parallel Manipulators. Literature Review	3
1.1.	Robotics. General terms	3
1.1.1.	Types of robots	4
1.1.2.	Serial manipulators	8
1.2.	Parallel manipulators. Research and classification	12
1.2.1.	Parallel manipulators vs serial manipulators	12
1.2.2.	Background	15
1.2.3.	Classification of parallel manipulators	19
1.2.3.1.	Classification by application	19
1.2.3.2.	Classification by DOF	29
1.2.4.	Designing process	35
2	MAST	37
2.1.	Multi-axis machines	37

2.2.	Multi-axis shaking tables	39
2.2.1.	Applications	39
2.2.2.	Requirements	40
2.2.3.	History	41

II	Methodology of Design	49
3	Requirements and Constraints	51
4	Methodology proposed	59

III	2PRU-1PRS. Manipulator Analysis	65
5	2PRU-1PRS Description	67
6	Kinematics	69
6.1.	Kinematics	69
6.1.1.	Position problem	69
6.1.1.1.	Inverse position problem	69
6.1.1.2.	Direct position problem	71
6.1.2.	Velocity and acceleration problems	73
6.2.	Developing the kinematic problem of the 2PRU-1PRS PM	74
6.2.1.	Position Problem of the 2PRU-1PRS PM	75
6.2.2.	Velocity Problem	82
6.2.3.	Acceleration Problem	84
7	Singularities	87
7.1.	Singularities	87
7.2.	Obtaining the singularities of the 2PRU-1PRS parallel ma- nipulator	93
7.2.1.	IKP Singularities	93

7.2.2. DKP Singularities	94
7.2.3. Manipulability	94
8 Workspaces and Joint Space	95
8.1. Workspaces	95
8.2. Obtaining the workspace of the 2PRU-1PRS parallel ma- nipulator	100
8.2.1. IKP Singularities	101
8.2.2. DKP Singularities	102
8.2.3. Spherical Joint Restrictions	103
8.2.4. Linear Guides Restrictions	104
8.2.5. Useful Workspace	104
8.2.6. Biggest Geometric Object in the Useful Workspace	104
8.3. Joint Space	104
9 Stiffness	105
9.1. Stiffness	105
9.2. Matrix structural analysis method	113
10 Dynamics	121
10.1. Dynamics	121
10.2. Developing the dynamics of the 2PRU-1PRS parallel ma- nipulator	126
10.2.1. Dynamic analysis of the platform	129
10.2.2. Dynamic analysis of limb 1	133
10.2.3. Dynamic analysis of limb 2	138
10.2.4. Dynamic analysis of limb 3	143

IV Manipulator Optimization	151
11 Optimization Criteria	153
11.1. Optimization methods in parallel manipulators	153

11.2. Optimization criteria proposed	157
11.2.1. Maximise geometry object in the useful WS	157
11.2.2. Minimise the power consumption	160
12 Particular case: 2PRU-1PRS manipulator	163
12.1. Maximise the sphere in the useful WS of the 2PRU-1PRS	164
12.2. Minimise the power consumption	170
12.2.1. Trajectory I	173
12.2.2. Trajectory II	176
12.2.3. Trajectory III	180
12.3. Interpreting results	183

V Prototype	185
13 Solution Chosen	187
14 Design of the Prototype	189
14.1. Component design	189
14.1.1. Linear guides, motors and gearheads	189
14.1.2. Revolute, universal and spherical joints	191
14.1.3. Fixed platform, mobile platform and limbs	199
14.2. Validation of the design	202
15 Analysis	207
15.1. Kinematic Problem	207
15.1.1. Trajectory I	208
15.1.2. Trajectory II	211
15.1.3. Trajectory III	213
15.1.4. Interpreting results	215
15.2. Singularities	216
15.2.1. Interpreting results	218
15.3. Workspace	219

15.3.1. Interpreting results	224
15.4. Stiffness	224
15.4.1. Analytical method	225
15.4.2. Finite element method	227
15.4.3. Experimental analysis	232
15.4.4. Interpreting results	233
15.5. Dynamics	234
15.5.1. Trajectory I	235
15.5.2. Trajectory II	236
15.5.3. Trajectory III	238
15.5.4. Interpreting results	239
15.6. Natural Frequencies	241
15.6.1. Finite element method	241
15.6.2. Experimental results	246
15.6.3. Interpreting results	252

VI Conclusions and Future Work	255
16 Conclusions	257
17 Future Work	261
References	263
Figure Index	287
Table Index	293

Part I

State of the Art

1

Parallel Manipulators. Literature Review

1.1. Robotics. General terms

In 1920, the Czech writer Karel Čapek wrote his first play: R.U.R. The play starts in the factory Rossumovi Univerzální Roboti (R.U.R. or Rossum's Universal Robot in English) that makes artificial people. The name of these artificial creatures is robota (robot), which in Czech means forced labor. Besides, the name Rossum is an allusion to the Czech word rozum, meaning reason. As their name suggest, the role of the robots is to do the tedious work while humans relax. But they suddenly rebel against humans and wipe out the human race. The play was performed for the first time in 1921 and it became quite popular all around the world, being translated into thirty languages. Since then, many authors have based their science fiction novels on robots.

Some years later, in 1942, Isaac Asimov introduced the Three Laws of Robotics in his short story Runaround. These laws state what every robot should follow:

1. A robot may not injure a human being or, through inaction, allow a human being to come to harm.
2. A robot must obey the orders given it by human beings except where such orders would conflict with the First Law.
3. A robot must protect its own existence as long as such protection does not conflict with the First or Second Laws.

Nowadays, after many years of technological progress, we still use the term robot to describe any mechanical device that is capable of performing a variety of human tasks on command or by being programmed in advance. Besides, the Three Laws of Robotics describe what, still today, our common sense tells us to take into account when creating a new robot. As Isaac Asimov himself said:

I have my answer ready whenever someone asks me if I think that my Three Laws of Robotics will actually be used to govern the behaviour of robots, once they become versatile and flexible enough to be able to choose among different courses of behaviour.

My answer is, "Yes, the Three Laws are the only way in which rational human beings can deal with robots – or with anything else."

But when I say that, I always remember (sadly) that human beings are not always rational.

1.1.1. Types of robots

The concept of robot is defined by different institutions, and we mention here two of them. The Robotic Industries Association (RIA) [1] defines robot as *“a reprogrammable, multifunctional manipulator, designed to move materials, parts, tools or devices, by means of variable programmed movements, with the purpose of accomplishing different tasks. The robot is an automatically operating equipment, adaptable to complex conditions of the environment in which it operates, by means of reprogramming, managing to prolong, amplify and replace one or more human functions in its*

interactions with the environment“. The British Automation and Robot Association (BARA) [2] defines robot as “*a reprogrammable device, designed to manipulate parts, tools and other production means, through variable programmed motions, to accomplish specific fabrication tasks.*“

Types of robots by application

- **Industrial robots:** used in an industrial environment. They have many and different applications such as welding, material handling, painting or milling. The most widely used ones are the robotic manipulators. The robotic manipulators can manipulate objects with their end-effector. The end-effector can move with a maximum of six degrees of freedom. They have two possible architectures: serial and parallel. Figure 1.1a shows a ABB parallel manipulator from the ABB Group [3].
- **Household robots:** we use them at home to help us with domestic work. There are many type of devices, such as robotic vacuum cleaners, gutter cleaners, lawnmowers or even robots that clean the litter box of the cat. In Fig. 1.1b we see the Roomba vacuum cleaner from the iRobot Corporation [4].
- **Medical robots:** these robots help in surgical operations, rehabilitation therapy, prosthetics, and so on. A very common example is the *da Vinci* Surgical System from Intuitive Surgical Company [5]. As we see in Fig. 1.1c, it enables surgeons to perform operations through a few small incisions and includes several key features. It translates the movements of the hands of the surgeon into smaller, precise movements of tiny instruments inside the body of the patient.
- **Exploration robots:** autonomous mobile platforms that can carry out many different tasks as, for example, sensing, exploring or environmental monitoring. The exploration robots used in space missions belong to this kind of robots. Figure 1.1d shows the Mars Curiosity

Rover. The NASA [6] sent this robot to Mars to collect samples of materials found in that planet.

- **Aerial robots:** we also know them as *Unmanned Aerial Vehicles* (UAV). They are very useful for aerial surveillance, search and rescue, border patrol, inspections, management of natural risks, intervention in hostile environments and agriculture. One example is The Saviour Aerial Robot (PARS) shown in Fig. 1.1e and developed by the RTS Lab [7].
- **Aquatic robots:** they explore oceans, lakes and deep waters in the reefs. They are also called *Autonomous Underwater Vehicles* (AUV) and they carry high resolution cameras to assist scientists in mapping the seabed. They can gather complex data in ocean environments and create 3D models of the seafloor. One of these AUV is the Crabster CR200, shown in Fig. 1.1f, designed by the Korean Institute of Ocean Science and Technology (KIOST) [8].
- **Military robots:** they are used in military operations and can be bomb disposal robots, transportation robots or reconnaissance drones, among others. The robot shown in Fig. 1.1g is the BigDog, built by Boston Dynamics [9], and which is called to be "The Most Advanced Rough – Terrain Robot on Earth". It often happens that robots that were initially created for military purposes become useful in civil purposes.
- **Entertainment robots:** as their name suggests, they are used for entertainment. This category is very broad, since it includes everything from toy robots such as the Aibo dog seen in Fig. 1.1h from Sony [10] to heavy articulated robot arms used as motion simulators.

In this thesis we work with an industrial parallel manipulator. Thus, we will focus now on robotic manipulators. We will describe both serial and parallel manipulators, compare them and describe when we should use one kind of manipulator or the other.

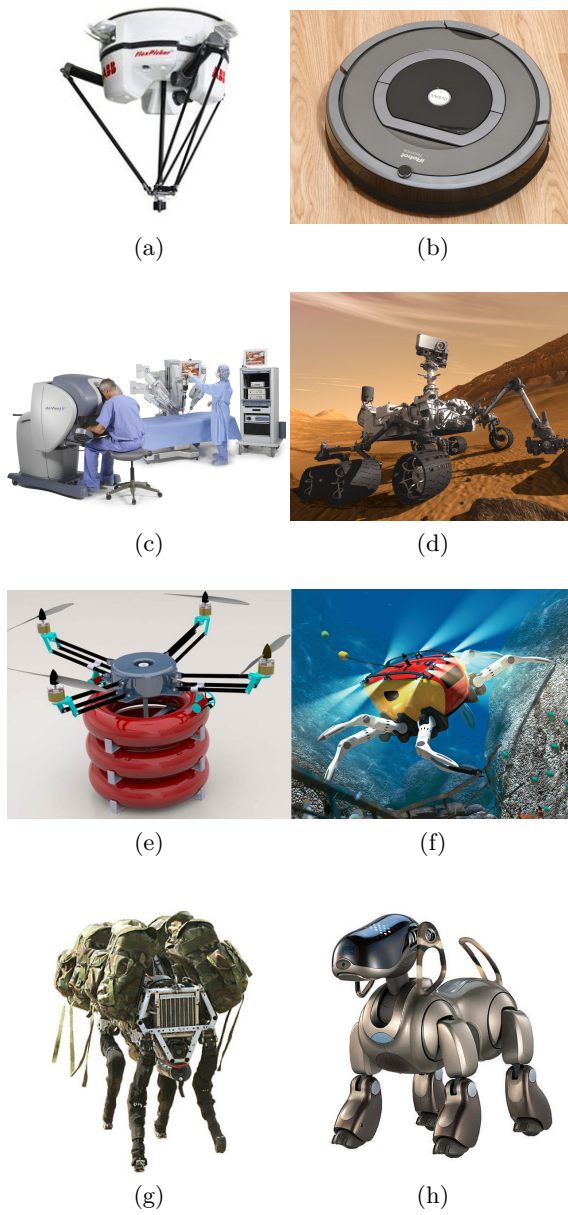


Figure 1.1: Types of robots by applications

1.1.2. Serial manipulators

A manipulator is a mechanical system whose purpose is to manipulate objects. There are mainly two kinds of manipulators: serial and parallel manipulators. The serial manipulators were the first ones to be used in industry. They are basically a succession of rigid bodies that connect a fixed platform with an end-effector. The part responsible for manipulating the desired object is the end-effector. The movement of the end-effector depends on the geometry of every part of the manipulator and on the way they are connected. The maximum number of degrees of freedom that the end-effector can have in space is six.

In 1956, Joseph Engelberger, an engineer, physicist and entrepreneur met the inventor George Devol to talk about Devol's latest invention. A fan of Asimov's stories, Engelberger got excited about this invention, which sounded "like a robot" to him. After almost two years of collaborative development, they created their first prototype, the Unimate 001, shown in Fig. 1.2.

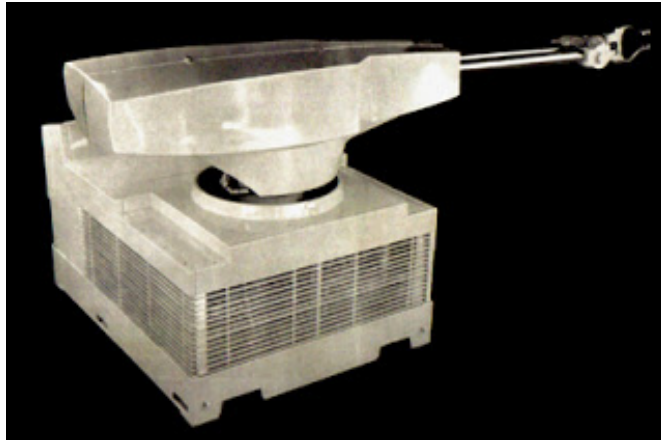


Figure 1.2: Unimate robot. Courtesy of Unimation

They installed it on an assembly line for the first time at a General Motors die casting plant in Trenton, New Jersey. In 1961 Engelberger established Unimation (Universal Automation Inc.) to develop the business in robotics industry he had created. The Unimate robot became really popular and many companies installed it in their manufacturing plants. It had two main benefits – they performed jobs that were unpleasant and dangerous for humans and, additionally, increased the production speed. However, and as Engelberger himself explained [11], they had to invest lots of money and time to convince people that these robots were not dangerous and were not going to rebel against humanity as in the science fiction novels. Joseph Engelberger is nowadays considered as the father of robotics.

During the 1960s and 1970s, serial robots underwent further development and more models appeared in the market. Victor Scheinman developed the PUMA robot (*Programmable Universal Machine for Assembly* or *Programmable Universal Manipulation Arm*) for Unimation. The PUMA robot, still used nowadays, is a six degrees of freedom serial robot. We see it in Fig. 1.3.



Figure 1.3: PUMA robot. Courtesy of Unimation

Its design is presented in three different categories: 200, 500, and 700 series. While the 200 Series is a small desktop unit, the 500 Series can reach almost 2 meters up and the 700 Series is even larger. The 700 Series was intended for assembly line, paint, and welding work. During the seventies, different companies installed thousands of Unimates and PUMAs in their workplaces. The first prototype of a PUMA robot was built for General Motors, that donated it in 2002 to the Smithsonian Institution's National Museum of American History, recognizing its great importance in the history of development of robots.

Currently, we can find different serial robots in the market. One of the most used architectures is the SCARA robot (*Selective Compliance Assembly Robot Arm* or *Selective Compliance Articulated Robot Arm*). Its end-effector has four degrees of freedom and its main characteristics are high speed and acceleration, large workspace and good adaptability and flexibility. Additionally, it has a single pedestal mount, so it requires a small footprint and provides an easy way of mounting. Its applications include pick and place, assembling, painting, food processing and packaging. Figure 1.4 shows a SCARA robot developed by Adept [12].



Figure 1.4: SCARA robot. Courtesy of Adept

There are other serial architectures, such as the *Cartesian robot*, the *Cylindrical robot* or the *Polar robot*. The Cartesian robot has three prismatic joints whose axes coincide with the three Cartesian axes. The Cylindrical robot is very similar to the Cartesian robot, but its axes are arranged in a cylindrical coordinate system. In the same way, the axes of the Polar robot are arranged in a polar coordinate system.

Finally, we have to highlight the impact the 6-axis serial robot has had in the industry. The end-effector of these robots can move with six degrees of freedom, offering a high flexibility to accomplish any kind of motion. One of the best known 6-axis robots is the KUKA robot, developed by KUKA Robot Group [13]. We can see it in Fig. 1.5.



Figure 1.5: 6-axis serial robot. Courtesy of KUKA Robotics

The 6-axis serial robots are widely used in industry mainly due to the big workspace of their end-effector, their high speed and their flexibility to adapt to different applications. They have many and different applications, as for example: machine tool operations, automotive industry, handling, welding processes, packing, picking, testing or inspection. Nevertheless, they also have some drawbacks, such as low ratio of load capacity to robot mass, low stiffness and repeatability and poor accuracy.

1.2. Parallel manipulators. Research and classification

We define parallel manipulators (PM) as given by Merlet [14]: *"A parallel robot is made up of an end-effector with 'n' degrees of freedom, and of a fixed base, linked by at least two independent kinematic chains. Actuation takes place through 'n' simple actuators."*

1.2.1. Parallel manipulators vs serial manipulators

First of all, we have to note that serial and parallel manipulators are not competitors in the market: both have their own market niche. To decide which type of manipulator is best for a specific application, we first have to know the requirements that the manipulator should fulfil for that particular application.

If we compare both types of manipulators, we see that parallel manipulators have some advantages, which we will presently discuss. One of them is an excellent load/weight ratio. The reason is that the closed-loop kinematic chains distribute the payload between the different limbs that connect the fixed platform with the end-effector.

Additionally, parallel manipulators have a higher stiffness all over the workspace. Unlike the serial manipulators, the kinematic chains of parallel manipulators share the loads and make the stiffness higher. This high stiff-

ness ensures a minimal deformation of the limbs, allowing a high positioning accuracy of the end-effector.

Besides, parallel manipulators have lower inertia than serial manipulators. The joints of the serial manipulators are actuated joints. This is to say, there is a motor in each joint between the different elements. In parallel manipulators, however, only some kinematic pairs are actuated, whose number is usually equal to the number of degrees of freedom (dofs) of the mobile platform. If the number of legs is equal to the number of dofs, as is usually the case, it is possible to actuate only one kinematic pair per leg allowing all motors to be mounted close to the base. In this way, parallel manipulators have to move less heavy mass than the serial manipulators, making the inertia lower.

Nevertheless, parallel manipulators have also some drawbacks compared to serial manipulators. The most important one is that their workspace is smaller and more complex than the workspace of serial manipulators. For both types of manipulators the workspace depends on the geometrical and mechanical limits of the design. These limits are more restrictive in parallel manipulators: legs can collide and there are many passive joints that introduce joint limit constraints, as Uchiyama et al. [15] explained. In addition, the workspace of parallel manipulators is also limited by the singularities, which are positions where we lose control of the motion of the manipulator. This implies that the workspace of parallel manipulators is usually restricted to a small region.

Table 1.1 summarizes the comparison between serial and parallel manipulators.

Table 1.1: Parallel manipulators vs serial manipulators

Feature	Serial manipulator	Parallel manipulator
Workspace	Large	Small and complex
Forward kinematics	Easy	Very difficult
Inverse kinematics	Difficult	Easy
Position error	Accumulates	Averages
Force error	Averages	Accumulates
Maximum force	Limited by min. actuator force	Summation of all actuator forces
Stiffness	Low	High
Dynamic characteristics	Poor	Good
Modelling and solving dynamics	Relatively simple	Very complex
Inertia	Large	Small
Payload/weight ratio	Low	High
Speed and acceleration	Low	High
Accuracy	Low	High
Calibration	Relatively simple	Complicated
Workspace/robot ratio	High	Low

1.2.2. Background

There is a general belief that parallel manipulators appeared after serial robots in order to overcome the drawbacks of serial architectures. However, as Bonev [16] clarifies, theoretical works related to parallel mechanisms date back to many centuries.

In 1928, the inventor James E. Gwinnett [17] patented a motion platform for the entertainment industry. The device, shown in Fig. 1.6, was based on a spherical parallel mechanism. We know it as one of the first such amusement devices. However, it is not clear if it was the first design of a multi-degree-of-freedom parallel mechanism nor if it was ever built.

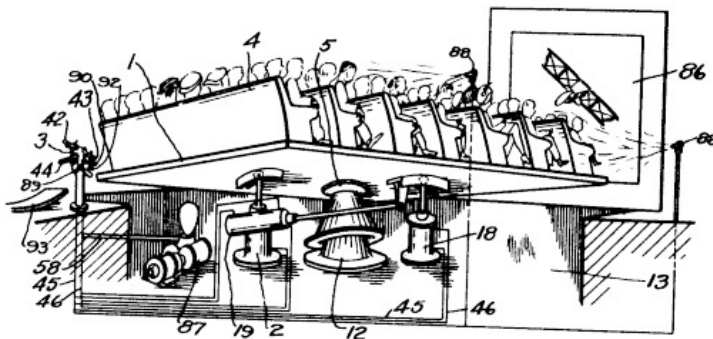


Figure 1.6: Possibly the first spatial parallel mechanism, by Gwinnett

According to Bonev [16], only a decade later, Willard L.V. Pollard invented a parallel manipulator for automated spray painting. It was a 5 degrees of freedom parallel robot with rotary motors fixed to the base. Three motors controlled the position of the tool head and the two other motors controlled the orientation by transmitting the motion to the tool via cables. Even though this robot is known as the first industrial parallel robot design, it was never built. In fact, the son of Willard L.V. Pollard, Willard L.G. Pollard Jr., was the co-designer of the first industrial parallel robot to be

built. Williard Pollard Jr. [18] patented a spray painting robot consisting of two parts – an electrical control system and a mechanical manipulator based on a pantograph, shown in Fig. 1.7.

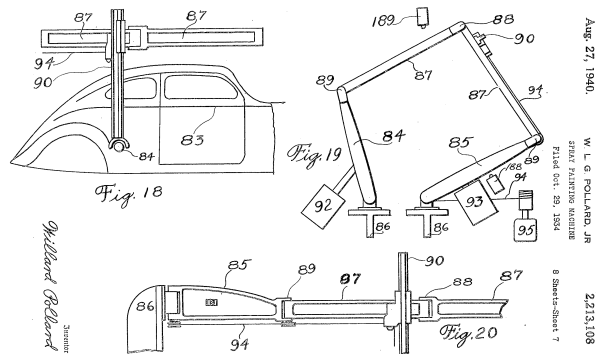


Figure 1.7: Spray painting machine patented by Pollard Jr.

Few years later, in 1947, Gough invented a new parallel manipulator: an octahedral hexapod with variable length strut. Gough was a distinguished engineer at Dunlop Rubber Co., in England. He invented this new manipulator called *universal tire-testing machine* or the *universal rig* in order to solve problems of aero-landing loads: they needed an universal machine to define the properties of tires under combined loads. As Gough [19] explained, the hexapods with three vertical jacks and three horizontal ones were already very common at that time. However, the new thing about Gough platform was how the struts were arranged. Gough needed large ranges of motion, so he arranged the struts symmetrically, forming an octahedron. The first Gough platform, shown in Fig. 1.8a was fully operational in 1954. At the very beginning, the extensible struts were manually adjustable screw jacks, but years later they updated the machine with digitally controlled motor drives and electronics. The universal rig was operational in the Dunlop factory until the factory closed. Since then, the first Gough platform

is in the Science Museum Wroughton. Figure 1.8b shows the universal rig before its retirement in 2000.

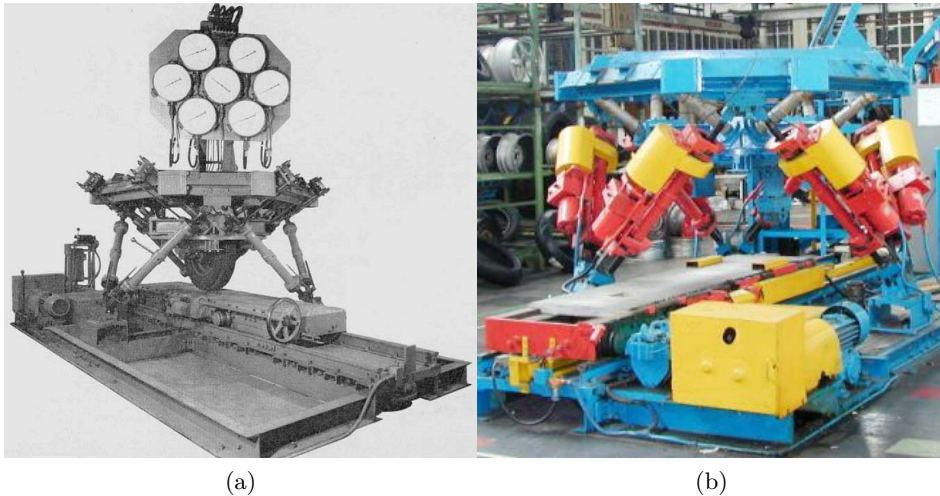


Figure 1.8: Gough's platform at Dunlop factory: (a) in 1950; (b) in 2000

In 1965, Stewart [20] described the 6 degrees of freedom flight simulator shown in Fig. 1.9. There exists certain confusion between this design and the tire-testing machine designed by Gough. In fact, the octahedral hexapod is usually referred as *Gough-Stewart platform*. We have to remark, thus, that the design that Stewart presented had some differences from the Gough platform regarding the arrangement of the kinematic chains. Therefore, we can not consider them as the same platform.

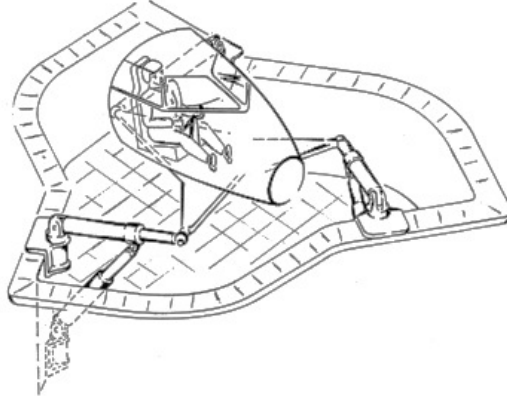


Figure 1.9: Flight simulator proposed by Stewart

Almost at the same time, but in the US, Cappel was requested to improve an existing conventional 6 degrees of freedom vibration system based on a hexapod. The system had four horizontal actuators instead of three. This configuration was so complex to control that the forces fractured the table. By observing this, Cappel came up with the same solution as Gough had already proposed. Surprisingly, Cappel did not know about the platforms designed by Gough or Stewart and he patented his platform in 1964 [21] to be a motion simulator. In this way, Cappel became the developer of the first ever flight simulator based on the octahedral hexapod. Figure 1.10a shows the design he patented and Fig. 1.10b shows the first flight simulator based on that patent.

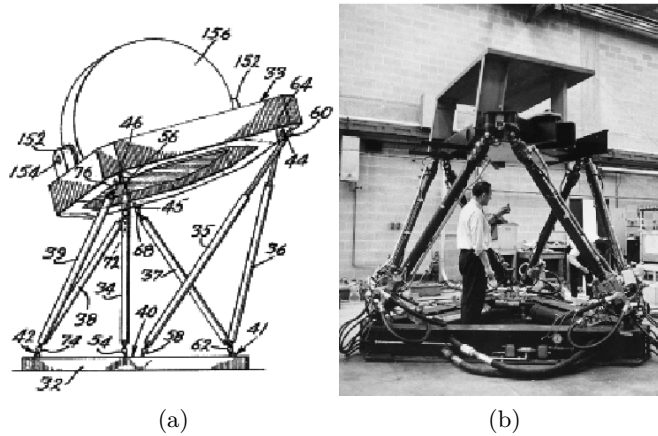


Figure 1.10: Platform proposed by Cappel: (a) patent; (b) flight simulator

We can say that Gough, Stewart and Cappel were the pioneers of parallel robots by proposing designs that are still used nowadays, inspiring many other researches all over the world.

1.2.3. Classification of parallel manipulators

We can classify parallel manipulators taking very different characteristics into account. We now give examples of robots according to two interesting and common classifications of parallel manipulators – by the application and by the number of degrees of freedom.

1.2.3.1. Classification by application

Pick & place and handling

Pick and place systems are manipulators that lift, move and place objects in a desired location. These kinds of manipulators require high speed, high stiffness and very good accuracy. Based on these requirements, parallel manipulators are a very good solution. There are, mainly, two suitable

architectures. Parallel manipulators with three spatial translation dof comprise the first type of architecture. The second architecture is comprised of parallel manipulators with 3 independent translations and one rotation, also called Schönflies-Motion parallel manipulators.

In the early 80's, Clavel [22] designed a parallel manipulator with three translational and one rotational degrees of freedom: the *Delta* parallel robot. The Delta robot has three parallelogram-based legs. These three parallelograms make the mobile platform move with purely translational degrees of freedom, maintaining its orientation. A fourth leg allows the end-effector to rotate with respect to the mobile platform. Thirty-six patents cover the design of the Delta robot. Among them we can consider the WIPO patent [23], the US patent [24] and the European patent [25] as the most important ones. Figure 1.11 shows a schematic representation of the Delta robot. Since Clavel patented it, the Delta robot has been one of the most successful parallel manipulators in industry. In 1999, Clavel got the Golden Robot Award for his innovative work.

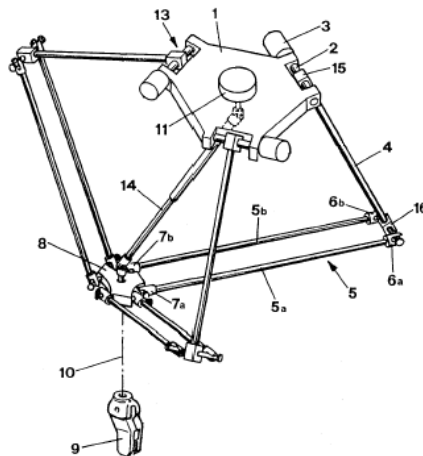


Figure 1.11: Schematic representation of the Delta robot

The impact of the Delta robot in industry has been such that almost thirty years later, it is still one of the most used architectures. One example is the *Flexpicker* robot developed by ABB Group [3]. This robot is used for light assembly, material handling and pick & place applications. The vacuum gripper allows it to pick and place products at a very high speed. The latest model is the IRB 360-6, shown in Fig. 1.12, which has a handling capacity of 6 kg and a working diameter of 1600 mm.



Figure 1.12: Flexpicker model IRB 360-6. Courtesy of ABB

Bosch Packaging Technology Company [26] offers a wide offer of packaging systems based on the Delta robot. In Fig. 1.13 we see the system *Paloma*. This system is able to pick and place products into flow wappers, cartoners or thermoformers with vision-guided high speed Delta Robots. It can be used for a wide variety of applications handling food and non-food items. Each robot in the system can manage products at a speed of 120 products per minute. The vision control is useful for load/line balancing and it ensures that only good quality products are packed.



Figure 1.13: Packaging system Paloma. Courtesy of Bosch

Another example of commercial manipulator based on the Delta robot are the Genkotsu series robots of FANUC [27]. This series covers several high speed picking and assembly robots. One of them is the FANUC M-2*i*A. It presents six different models, in order to get the desired number of degrees of freedom at the end-effector and the required workspace. Figure 1.14a shows the M-2*i*A/3S model in a fast process of arranging food, while Fig. 1.14b shows the M-2*i*A/3A model in a fast packaging of gift box application. They can also include vision or force sensors for additional intelligent functions.

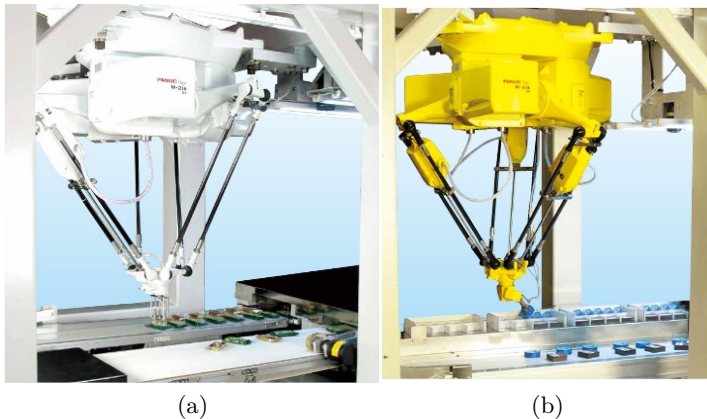


Figure 1.14: M-2*i*A robot in: (a) food application; (b) packaging application

Simulators

In aircraft industry it is very important to have suitable flight simulators in order to test the new aircrafts' handling qualities, cockpit systems and displays, operational procedures and other procedures that involve human factors in the cockpit. The *Generic Research Aircraft Cockpit Environment* or GRACE [28], shown in Fig. 1.15, is the flight simulator of the National Aerospace Laboratory (NLR) in Netherlands. It is very well suited for the evaluation of new aircraft technologies from their concept phase up to deployment in real aircraft.



Figure 1.15: GRACE flight simulator. Courtesy of NLR

Apart from aircraft, there are also other interesting situations that we can simulate using parallel manipulators like, for example, earthquakes. Earthquakes are characterized by a combined horizontal and vertical ground motion. Thus, we can simulate them using a suitable 2-DOF PM. The simulation of a seismic motion helps to understand the earthquake effects and to predict the behaviour of buildings and, in general, any civil engineering structures. Carvalho et al. [29] presented a study of feasibility for

an earthquake simulator by using the CaPaMan structure. They simulated the frequency, amplitude and acceleration magnitude of seismic motion by exciting the mobile platform with a suitable input motion.

Medical applications

Medical parallel manipulators are the ones used for surgery, medical training, rehabilitation therapy, prosthetics and assistance to people with disabilities.

Shoham et al. [30] presented, in 2003, a new approach to robot-assisted spine and trauma surgery. They proposed a miniature surgical robot with parallel architecture that can be directly mounted on the bone. Mazor Robotics [31] commercialized the device with the name of *Spine Assist* robot. The goal of the SpineAssist device is to increase the precision during surgery while reducing radiation exposure and time of the surgery. According to them, the device should bring higher success rates for surgery and less risk for complications. The device is being used for surgeries where implants are attached to the spine (e.g. spinal fusion, correcting scoliosis). Sukovich et al. [32] described the early clinical experience with the Spine Assist. Based on this concept, Plaskos et al. [33], Song et al. [34] and Wolf et al. [35] have developed bone-attached parallel robots for knee arthroplasty. In the field of neurosurgery, the *SurgiScope* robot stands out. The robot, developed by the Intelligent Surgical Instruments & systems, is a Delta robot tool-holder device dedicated to microscopic applications. The surgeon and operating team always have control of the robot during operations. It is designed for microscope-assisted neurosurgical applications, supporting all types of operations and the most common positioning.

Li et al. [36] introduced the concept of medical parallel robot for chest compression in the process of cardiopulmonary resuscitation. They proposed a three degrees of freedom translational parallel manipulator for this purpose. In Fig. 1.16a we see the operation that the robot has to do and in Fig. 1.16b we see the CAD design of the robot.

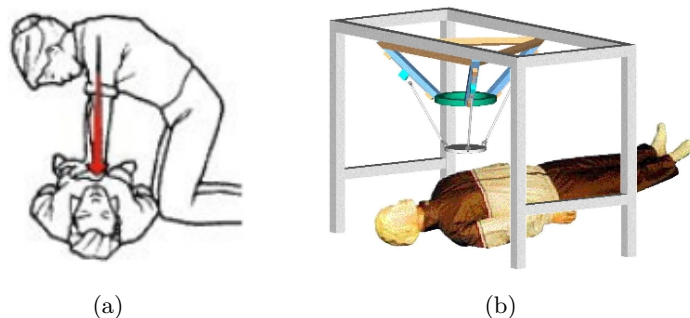


Figure 1.16: Medical PM for resuscitation: (a) force to be done; (b) CAD

Another very interesting application of parallel robots in medical field is the rehabilitation processes. Takanabu et al. [37], for example, suggested the use of a parallel manipulator for the training for mouth opening and closing for the rehabilitation of patients with jaw problems.

Merlet [38] proposed a family of modular wire-driven parallel robots: *MARIONET*. The use of wires instead of rigid legs is a natural solution to the workspace problem of parallel manipulators. This family of robots is developed at INRIA Sophia Antipolis research center [39]. The *MARIONET* family includes five wire-driven parallel manipulators. The *MARIONET-REHAB*, that can reach a maximal speed of 100m/s, is mostly used for rehabilitation. Harshe [40] proposed a potential application of the *MARIONET-REHAB* for lower limb rehabilitation. He combined the wire-driven parallel manipulator with force sensors, accelerometers and motion capture in order to get detailed information of the motion. Figure 1.17a shows the CAD of *MARIONET-REHAB* for this application and Fig. 1.17b shows the prototype during tests in the laboratory at INRIA Sophia Antipolis. *MARIONET-VR* is able to lift a human and was also designed for rehabilitation. The large *MARIONET-CRANE*, that has a workspace volume larger than 2000 cubic meters, is aimed to be used as a rescue device during natural catastrophes. In Fig. 1.17c we see how it manipulates a possible

victim and in Fig. 1.17d we see how it can be used to free a victim from rumbles. The MARIONET-ASSIST is a robot for transfer operation in assistance robotics, like lifting elderly and improving their mobility. Finally, the MARIONET-SCHOOL robots are used for demonstration and teaching scientific concepts.

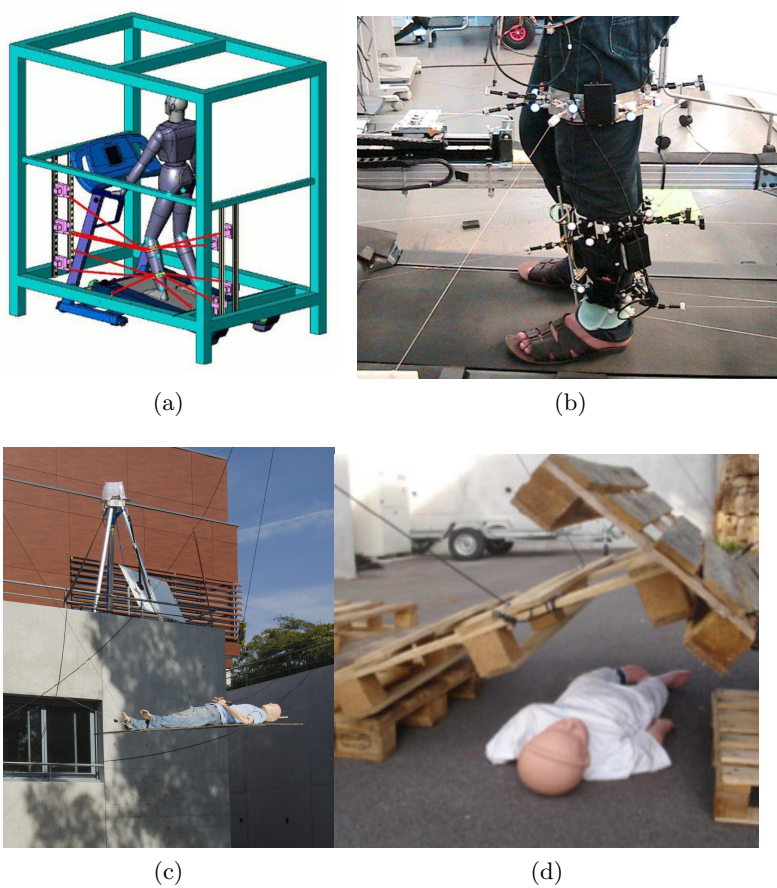


Figure 1.17: MARIONET: (a) REHAB CAD; (b) REHAB prototype; (c) CRANE taking a victim; (D) CRANE freeing a victim. Courtesy of INRIA

The research of parallel manipulators keeps moving forward. In 2015 Ibrahim et al. [41] presented a new 4 degrees of freedom endoscopic parallel manipulator for laparoscopic surgery. They manufactured an annealed stainless steel prototype and tested it successfully.

Machine tools

Machine tools are devices that change the shape, surface or properties of an object. Their most common operations are turning, milling, cutting, grinding, edging, abrading, drilling, nibbling or shaping. Traditional machine tools have serial architecture. However, many authors, as for example Fassi et al. [42], Zhang [43] or Pandilov et al. [44], have outlined that machining trends towards high-speed solutions nowadays and, thus, there is an increasing demand of high dynamic performance machine tools with high stiffness and reduced moving mass. Therefore, parallel-robot based machine tools, also called *Parallel Kinematic Machines* (PKM), seem to be a good solution.

The first commercial PKM was the *Variax Hexacenter* or only *Variax*, developed by Fives Giddings & Lewis [45] in 1994. The Variax is a six degrees of freedom parallel manipulator with a crossed leg and hydraulic isolation system. The crossed leg provides a higher stiffness compared to other PKMs. The isolation system absorbs the energy of the machine movement, making it more accurate. Geldart et al. [46] compared the Variax with other two serial machine centres and concluded that the higher stiffness of the Variax indicated that the PKMs had potential advantages in machining operations.

Wahl [47] developed for the DS Technologie Company in Germany the 3 degree of freedom *Sprint Z3 parallel kinematic tool head*, one of the most successful parallel kinematic machines. As Carretero et al. [48] and Pond et al. [49] showed, this PKM presents many advantages like high speed, high stiffness, good dexterity and large orientation capability. Inspired by the Sprint Z3 head, Huang et al. [50] patented a new tool head named A3. The

two tool heads, shown in Fig. 1.18, have the same degrees of freedom: two rotations and one translation, but they present some variations from an architectural point of view. Chen et al. [51] compared both tool heads in terms of motion/force transmission. They concluded that the A3 head parameters outperforms the Sprint Z3 head in terms of motion/force transmission, so the A3 can be a good alternative for industrial applications.

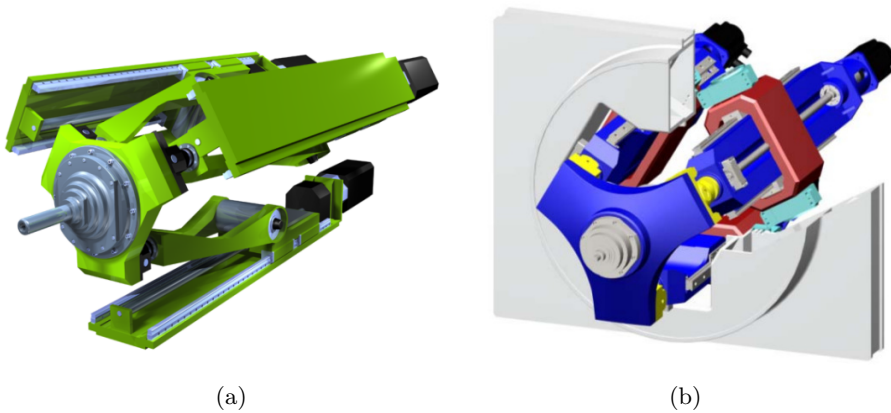


Figure 1.18: Typical tool heads: (a) the Sprint Z3; (b) A3 tool head

Many machine centres integrate PKMs, as Pandilov et al. [44] described. One example is the Cosmo Center PM-600 developed by Okuma and shown in Fig. 1.19a, a fully parallel mechanism machine tool developed for high efficiency production of aluminium parts. Another example is the Vertical Turning Machine Index V100 [52], shown in Fig. 1.19b.

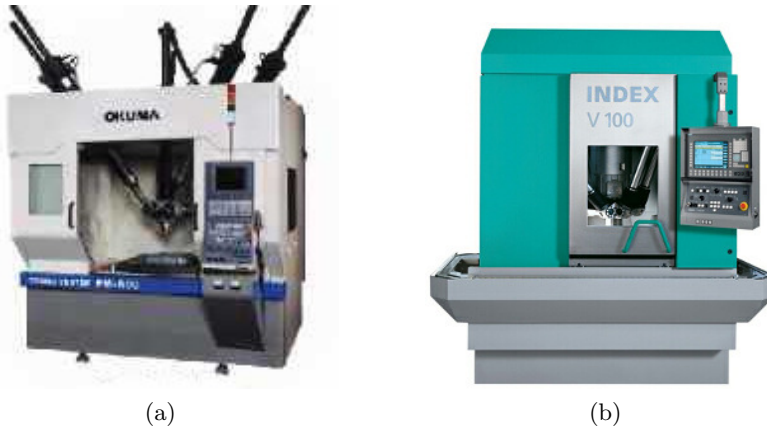


Figure 1.19: Two PKMs: (a) Cosmo Center. Courtesy of Okuma; (b) V100. Courtesy of Index

1.2.3.2. Classification by DOF

When classifying parallel manipulators according to their number of degrees of freedom, we first have to consider if they are planar or spatial manipulators. Planar manipulators can only have maximum three degrees of freedom – two translations and one rotation. As explained by Boudreau et al. [53] and Duffy [54], these are the planar parallel manipulators with the most interesting applications.

Spatial parallel manipulators can have a maximum number of degrees of freedom of six – three translations and three rotations in space. 6-DOF parallel manipulators have six actuated leg and each leg has six degrees of freedom. That is why they are usually called *hexapods*. The most emblematic representation is the Gough platform, previously described. Another example of parallel robot with six degrees of freedom is the *Hexa* robot, presented by Pierrot et al. [55] in 1991 and shown in Fig. 1.20.

Spatial parallel manipulators with less than six degrees of freedom are called *lower mobility* parallel manipulators. They are useful in tasks that



Figure 1.20: Hexa 6-DOF parallel manipulator

do not require full rigid motions of the end-effector, where the use of the lower-mobility parallel manipulators may save much cost. Unlike the 6-DOF parallel manipulators, the legs of a fully parallel lower mobility parallel manipulator may have more degrees of freedom than the mobile platform. However, the combination of the legs constraints generates the desired reduced mobility of the mobile platform. The structure of all the limbs is usually the same. If so, we can name the mechanism type by specifying the number of legs and the sequence of joints distributed along any of them, starting from the fixed platform to the mobile platform. Besides, if the actuators are adjacent to the base we can use simplified design procedures and manufacturing processes. The most typical lower mobility parallel manipulators are those with three pure translations, three pure rotations and Schönflies motion.

Lower mobility decoupled parallel manipulators are parallel mechanisms with less than six dofs and with decoupled geometry. Until now, it is difficult to design a decoupled parallel manipulator with translational and rotational movement simultaneously. However, under some rules, it is relatively easy to design a decoupled parallel manipulator with pure translational or rotational movements.

The first translational parallel manipulator was the Delta robot, already described. There are also other interesting translational manipulators, such as the 3-UPU presented by Tsai et al. [56] or the 3-RRPRR PM introduced by Di Gregorio et al. [57]. Carriato et al. [58] presented a new family of translational parallel manipulators – the 3-PRRRR. They determined the design and assembly conditions that guarantee the pure translation of the mobile platform. Among commercial robots, the Triglide hybrid robot, shown in Fig. 1.21a, ensures a constant end-effector orientation by using well-known parallelogram-linkages. Figure 1.21b shows another example of hybrid robot with a translational parallel manipulator: the Verne machining centre, from Fatronik Tecnalía [59]. The VERNE machine consists of a parallel module and a tilting table. The vertices of the moving platform of the parallel module are connected to a fixed-base plate through three legs. Each leg uses a pair of rods linking a prismatic joint to the moving platform through two pairs of spherical joints. Two legs are identical parallelograms, while the third one differs from the other two legs. Due to the arrangement of the links and joints, the two identical legs prevent the platform from rotating about Y- and Z-axes, while the third one prevents it from rotation about X-axis.



Figure 1.21: Two machine centres with PKMs: (a) Cosmo Center PM-600. Courtesy of Okuma; (b) Vertical Turning Machine V100. Courtesy of Index

Pure rotational parallel manipulators, also known as *spherical manipulators*, allow three rotations about one point. Gosselin et al. [60], [61] studied the 3-DOF 3-3R spherical parallel manipulator and applied it to build a fast camera-orienting device, the *Agile Eye*. The structure of the manipulator is shown in Fig. 1.22a. The axes of all the revolute joints intersect at one common point which is the center of rotation of the device. The three motors of the manipulator are fixed to the base. The main application of the Agile Eye is the tracking of objects moving at high speed using a camera, but it could also be used to control the orientation of mirrors, lasers or any device to be oriented precisely at high speed. Di Gregorio [62] presented the 3-URC wrist, a new spherical parallel manipulator with three equal legs. The passive joints are only cylindrical and revolute joints, and the actuators are adjacent to the base. They defined the mounting and manufacturing conditions that make the platform motion to be spherical. Recently, Enferadi et al. [63] proposed a new fully spherical parallel manipulator: the 3(RSS)-S PM, shown in Fig. 1.22b, thought for celestial orientation and rehabilitation applications. In addition to orient a body like with any spherical manipulator, if we rotate all motors simultaneously we can rotate the rigid body around a vertical axis interminably.

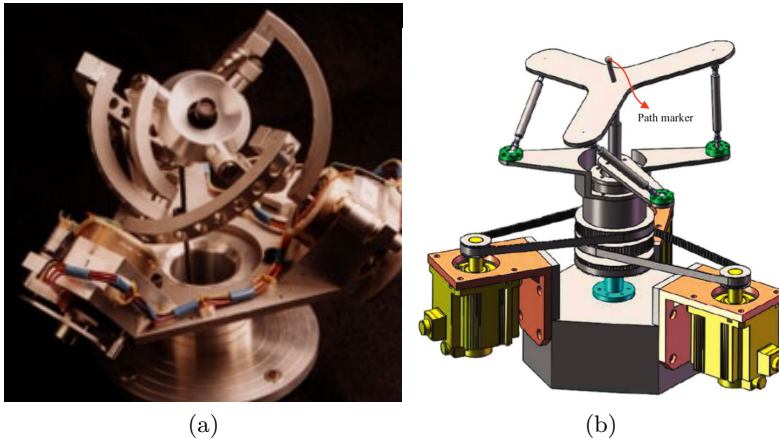


Figure 1.22: Spherical manipulators: (a) Agile Eye; (b) 3(RSS)-S PM

The 3-DOF parallel manipulators with one translational and two rotational degrees of freedom (1T2R) is a very important category of lower-mobility parallel manipulators. The 3-RPS, 3-PRS, 3-RRS and 3-PPS are typical parallel manipulators of this category. Hunt [64] introduced the 3-RPS PM in 1983 and, since then, it has been widely studied and used for different purposes. Carretero et al. [65] applied it for telescope applications, while Hernández et al. [66] proposed it as tool head of machine tools. The 3-PRS parallel manipulator, presented by Carretero et al. [48] in 2000 and shown in Fig. 1.23a, has also focused the attention of many researches and has been used in the Sprint Z3 tool head (previously described), as motion simulator or as coordinate measuring machine. The 3-RRS and the 3-PPS PMs also have several applications. For example, Itul et al. [67] studied the potential use of the 3-RRS PM for the orientation of a TV satellite dish or sun tracker and Teo et al. [68] proposed the 3-PPS for UV nanoimprint lithography applications. Despite these architectures being the most common ones, there are also novel 1T2R PM. Hao et al. [69] presented the 3-PSP PM as tool head for high speed machining of structural aircraft components, while Hosseini [70], [71] proposed the 3-CRS/PS PM, shown in Fig. 1.23b.

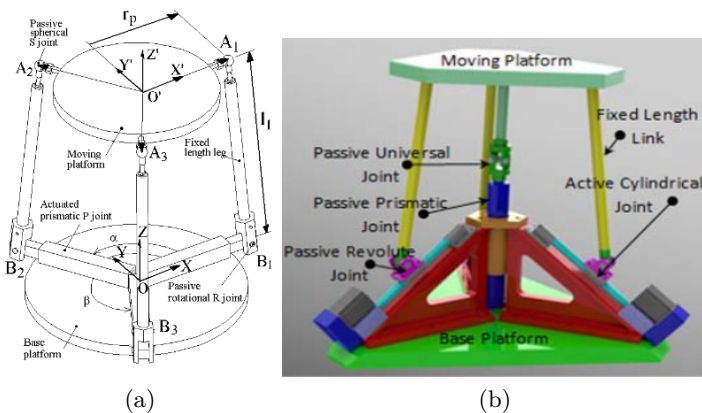


Figure 1.23: 1T2R PMs: (a) 3-PRS PM; (b) 3-CRS/PS PM

Even if the most typical lower mobility parallel manipulators are 3-DOF mechanisms, there are also some 4-DOF and 5-DOF parallel manipulators with interesting applications. In 2002, Zlatanov et al. [72] found out that there were few parallel manipulators with less than six but more than three degrees of freedom. Thus, they introduced a new family of parallel architectures with four degrees of freedom and highlighted their potential application as flight and motion simulators. Also in 2002, Huang et al. [73] developed a general methodology for type synthesis of symmetrical parallel manipulators with lower mobility. Based on this methodology, they presented three novel lower mobility parallel manipulators – a 3-DOF PM (the translational 3-RRRRR) and two 5-DOF PMs (the 3-RR(RRR) PM and the 5-UPU PM). Few years later, in 2007, Zhu et al. [74] described eighteen fully symmetrical 5-DOF-R2T parallel manipulators with better actuating modes. Eleven of them were existing ones and the another seven were novel ones. Figure 1.24a shows the 5-(RRR)(RR) PM, one of the manipulators proposed. Ibrahim et al. [41] have recently designed, manufactured and tested successfully a 4-DOF endoscopic parallel manipulator for minimally invasive surgery. The endoscopic manipulator is shown in Fig. 1.24b.

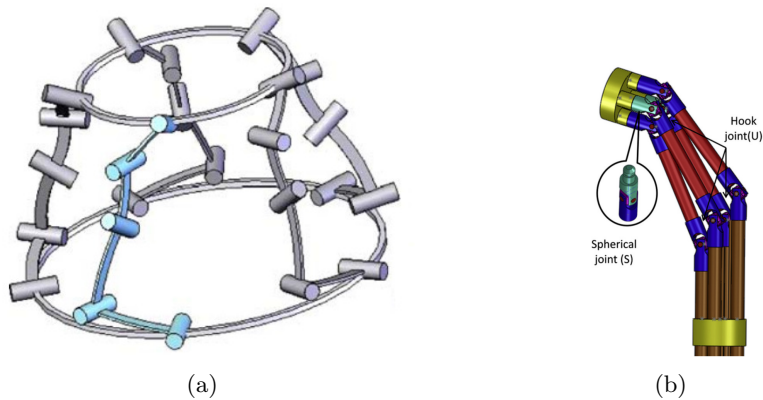


Figure 1.24: Novel lower mobility PMs: (a) 5-(RRR)(RR) proposed by Zhu PM; (b) endoscopic PM proposed by Ibrahim

1.2.4. Designing process

In order to design a new parallel manipulator, we have to consider all the requirements needed for the application we want to design it for. These requirements include aspects like geometry and structural characteristics, kinematic and dynamic behaviour, stiffness performance or size and/or shape of the workspace. A complete methodology to design parallel manipulators should follow the steps we describe below:

1. First of all, we have to define the performance requirements that the manipulator has to fulfil in a certain application or the specifications that a potential client determines.
2. Then, we have to take those performance requirements into account to define the geometry, kinematic, stiffness and dynamic characteristics of the manipulator. These characteristics can be given by, for example, the volume of the manipulator, the useful workspace, the kind of movements that the manipulator can follow, its maximum velocities and accelerations, the stiffness and the payload capacities, the accuracy or the dynamic forces and natural frequencies.
3. Once we know all the requirements that the manipulator has to fulfil, we define the morphological synthesis. The morphological synthesis determines the kinematic structure of the manipulator. This is to say, the number and type of elements, kinematic joints and kinematic chains that compose the manipulator.
4. After defining the type of architecture of the manipulator, we proceed with the dimensional synthesis. The dimensional synthesis consists of defining the basic dimensions of the manipulator. These dimensions are the main design variables that we have to determine by applying optimization methods in order to get the best possible values.
5. We have to check the possible collisions between elements in order to define more precisely the area where the manipulator can reach.

6. Then, we have to do static, dynamic and vibration analyses so we can get the secondary dimensions of the manipulator, such as the thickness of the elements, the wideness and, in general, small dimensions of the manipulator. The development of these theoretical and experimental analyses is divided in the following steps:
 - Initial dimensioning.
 - Obtaining the stiffness maps for the different configurations of the manipulator in its workspace.
 - Adjustment of the dimensions of the secondary elements taking the stiffness maps into account.
 - Solving the inverse dynamic problem to dimension the actuators.
 - Obtaining the lowest natural frequencies and the corresponding vibration modes inside the workspace to get possible resonances of the platform.
 - Making some parts of the manipulator more rigid, if necessary.
7. Experimental check of the correct performance of the manipulator.

This can be an iterative process in which the different modifications and verifications lead to the complete definition of the manipulator.

2

MAST

2.1. Multi-axis machines

Multi-axis machines are linkage-based systems able to generate a coupled motion in their end-effector by combining translations and rotations. They have many applications in industry, such as the multi-axis testing tables, flight simulators or vehicle simulators.

We give a brief description of the different multi-axis machines according to their application field.

- **Multi-axis shaking tables (MAST).** They are used for dynamic testing of structures or mechanical components, like the one commercialized by Moog [75] and shown in Fig. 2.1a.
- **Multi-axis simulation tables.** Used as vehicles and flights simulators. They are mostly Gough-platform-based systems. They integrate very complex real time control algorithms to reproduce displacements and accelerations with exactitude. In Fig. 2.1b we see a hexapod used for flight simulations by Lufthansa.

- **Multi-axis positioning systems (MAPS).** These systems allow the precise positioning of antennas, lenses, surgical elements and so on. The solar trackers used to guide the solar panels, like the one shown in Fig. 2.1c, are a typical example.



(a)



(b)



(c)

Figure 2.1: Multi-axis machines: (a) multi-axis shaking table. Courtesy of Moog; (b) multi-axis simulation table. Courtesy of Lufthansa; (c) multi-axis positioning system

In this work we focus on the multi-axis shaking tables and describe them with more detail below.

2.2. Multi-axis shaking tables

The functional capability of components and systems under seismic and other dynamic conditions, like random shocks or vibrations, has to be ensured in many engineering sectors. This is done by verifying experimentally the safety and reliability of large components or structures under dynamic load conditions. The multi-axis shaking tables are principally designed for experimental verification of the safe functioning of large components and subsystems under seismic conditions, such as vibration tests on structural models, simulation of dynamic loading of systems in the aerospace industry or automotive component validation and durability testing.

2.2.1. Applications

Shaking tables are of great value in civil engineering because they are the only experimental device that can replicate the true nature of an earthquake input. Shaking tables apply motion to the base of the structure that we want to analyse. Thus, they introduce realistic inertia forces in every element of the structure, generating response displacements and stresses.

Besides being used for seismic testing, another common application of the MAST is the experimental validation of various different components such as seat, heaters, combustible deposits, motor supports or suspension systems. In these cases the movements to be simulated are more complex than the movements needed in a seismic simulation. They can be a periodic excitation, random forces or a fatigue testing with displacements and rotations. Unlike for the seismic testing, in these kind of shaking tables the rotation of the component to be analysed is usually more important than the translations.

Knowing the modal parameters of a structure is essential to validate

the analytical dynamic models. Besides, it can improve the design of the structures analysed. Füllekrug [76] proposes using of the same set-up used for earthquake simulation and dynamic qualification of structures to obtain a modal identification of the tested structure. In this way, we can obtain very valuable data without much additional experimental effort. However, this process requires suitable modal identification methods. Füllekrug described both the theory and the basic principles of modal identification by using multi-axial excitation. Additionally, he illustrated the application of frequency and time-domain identification by testing a laboratory structure.

2.2.2. Requirements

Earthquakes can produce a ground motion in all six degrees of freedom, but the earthquake sites can only measure the acceleration in three of them – two horizontal and one vertical. The first usable record of an actual earthquake is the one that took place in Long Beach, in the U.S.A. in 1933, that Ruge [77]-[78] used as inputs of his shaking table.

It often happens that we get the acceleration in only one degree of freedom as specification for testing purposes. In those cases, we can consider that a uniaxial table is satisfactory. The drawback is that we have to know how to remove the motion in the remaining five degrees of freedom. Early tables were 6-DOF mechanisms with physical restraints to fix some of the degrees of freedoms. This introduced unknown forces that modified the desired motion. Real earthquakes do not repeat themselves in a precise way, so these types of shaking tables can be suitable to simulate earthquakes. However, if we want to test a piece for precisely defined inputs we need a more accurate control system.

2.2.3. History

The beginning of the development of shaking tables dates back to the 19th century. In his work, Severn [79] went over one century of history of the shaking tables. We resume it below.

Shaking tables with simple oscillatory motion

As Muir-Wood [80] explained, the first attempt at testing the effects of an earthquake took place at the end of the 19th century in Japan. Milne and Omori used a railway truck as testing device. They excited the test piece with an oscillatory motion by attaching a bar eccentrically to a hand-driven wheel, as shown in Fig. 2.2.

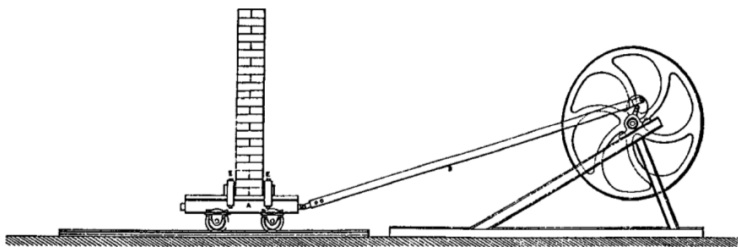


Figure 2.2: The Milne-Omori railway truck shaking table

Some years later, in 1906, Rogers [81] built a more sophisticated shaking table. As we see in Fig. 2.3, the table had a box attached and both were separated from a fixed platform by rollers that constrained the movement of the box to a single horizontal direction. A motor drove a balancing wheel. Additionally, there was a crank connecting the wheel and the box eccentrically. In this way, the motion of the box was basically sinusoidal with a frequency between 0.5 and 4.6 Hz. The response measurements were recorded on a hand-operated paper-covered drum labelled as G in Fig. 2.3. The pencils (H) recorded the motion of the box and of a block (F) embedded in the sand in the box.

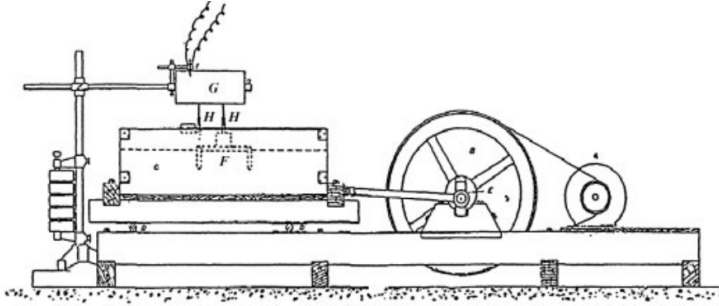


Figure 2.3: Shaking table proposed by Rogers

Excitation using springs and pendulums

After the big earthquake that destroyed a great part of Tokyo city in 1923 and the earthquake in Santa Barbara (U.S.A.) in 1925, the research in seismic simulation was accelerated. The Stanford University in the U.S.A. created a committee of engineers to analyse which was the best way to carry out vibration experiments with models of engineering structures. This committee decided to create a laboratory to work with shaking tables and it was Dr. Jacobsen and his team ([82], [83], [84], [85]) who took this task up. The two main topics they had to decide about were the type of input that was necessary and the way to get it. They used the word 'savage' to describe the characteristics of real earthquakes and the word 'civilised' to refer to continuous and oscillatory disturbances that had already been achieved in laboratories. They concluded that it was not possible to repeat any particular experiment using savage inputs and, thus, the civilised inputs were the only satisfactory option. However, they considered that the horizontal input that Rogers had used was not an appropriate solution and they implemented two civilised inputs. As we see in Fig. 2.4, a pendulum impacted through a spring attached to one end of the table. A group of springs supported the table on the other end. In that way, there was an initial shock that produced a decaying motion of the table. Over a period of 25 years Jacobsen kept working on his shaking table and making im-

provements. He introduced force and moment dynamometers, but he still could not measure either velocity or acceleration.

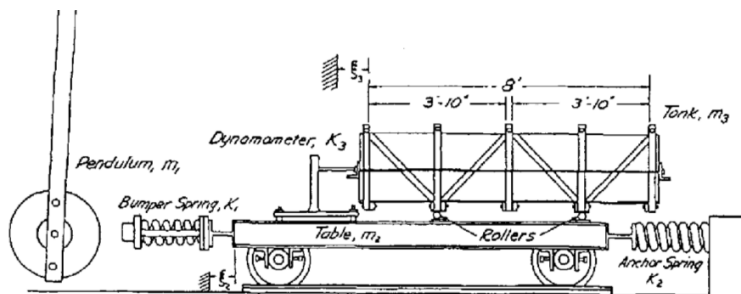


Figure 2.4: Shaking table designed by Jacobsen

Many researchers from all over the world based their shaking tables on the design of Jacobsen. In 1936, Mononobe et al. [86] described 1:100 scale models of earth dams tested using shaking tables. They used optical methods – including motion pictures – to measure the displacements.

In 1956, Oberti [87] presented a Jacobsen-type table that could be excited in three ways – by a pendulum-spring combination, by an eccentric mass device or by electromagnetic vibrators. Also in the 50s, Clough and Pirtz [88] built another Jacobsen type table to study the behaviour of rock-fill dams. Thanks to the developments during the Second World War, by this time there were already accelerometers and linear variable differential transformer (LVDT) available for measuring the accelerations and displacements. They used them to record the measurements of the rockfill dams.

Excitation using liquid-filled actuators – First modern shaking tables

In 1933 raised water tanks collapsed in Long Beach, California (U.S.), due to an earthquake. This gave an idea to Ruge [77], [78], a seismology researched at MIT, to build a new shaking table. He constructed a table

suspended from above using piano wires. He also used an array of wires that attached the table to the floor so there was no rotation. Ruge realized that the mechanical systems used until then did not give adequate representation of the motion of real earthquakes. Ruge introduced an oil-driven piston and controlled its position by using a device that gave the motions of a real earthquake as inputs. We see the sketch of this configuration in Fig. 2.5. This concept is the one that, after more than eight decades of developments, has given us our current shaking tables.

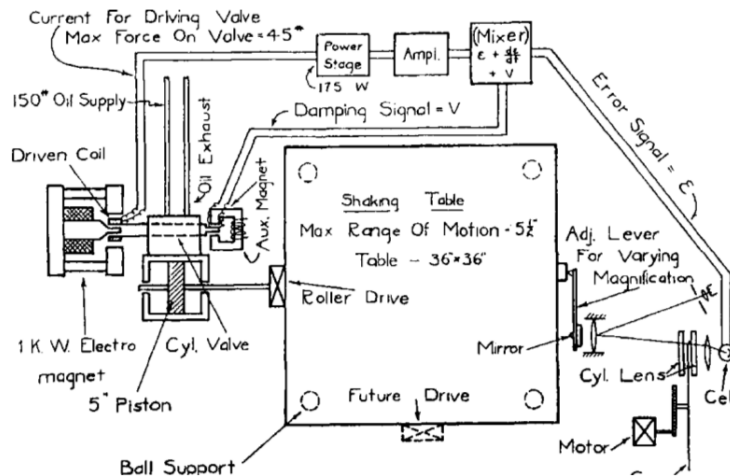


Figure 2.5: Sketch of Ruge's shaking table

The second world war brought a wide development of hydraulic power systems with military purposes. The first to apply these innovations to shaking tables was, probably, the Building Research Institute at Jassy in Romania [89]. They moved a 10x10 m table by using two electro-hydraulic actuators. The accelerations up to 0.4 g

The University of Illinois earthquake simulator [90], [91] had a similar architecture to the one developed by Clough and Pirtz. The main difference

was that the University of Illinois earthquake simulator used a controlled electro-hydraulic actuator to drive it instead of a pendulum. Besides, the MTS Systems Corporation, that had been newly created, was the advisor to Illinois in control system related topics. Three different kind of inputs were possible – displacement, velocity or acceleration time-histories. Nevertheless, they chose to control the displacement in order to avoid physical damages to the table. Additionally, they attached a LVDT to compare input and output displacements. They studied different combinations of the three type of input, time-compression ratios and viscous damping. They concluded that the acceleration input gave better results for low time-compression ratios, whereas when the ratio was bigger than 5 the displacement input was better.

In 1965 a research group at University of California studied the possibility of building a big table of 30.5x30.5 m [92] with several hydraulic actuators. They first tried to introduce an active control system, but the technology had not developed enough to be successful. Thus, they had to abandon the project. Instead, Rea and Penzien [93] built a 6x6 m table. They signed a contract with MTS to design the hydraulic actuators, servos-valves and the electronic control system. The table had 3 horizontal actuators and four vertical. They were supposed to produce a horizontal and a vertical motion, respectively. However, some unexpected pitch and roll motions also occurred. In order to keep them to a minimum, they added passive hydraulic devices to act in parallel. The input was an acceleration time-history, so they used a small computer to obtain the velocity and displacement time-histories by integrating the inputs. They used these time-histories to check that they did not exceed the performance limits of the table. The control of this shaking table at the University of California had a high importance in the development of shaking tables. It controlled five DOF, the sixth one being controlled by a sliding mechanism. Additionally, transducers measured displacements and forces. The aim of the control was to reduce the unexpected rotations of the platform as much as possible and ensure that the velocity and displacement limits were not exceeded.

By 1970 the electronics and computing had already developed in such a way that the servo-hydraulic-electronic control of actuators was a real possibility. Moreover, tables with such actuators were available in many universities, private companies and research labs. The largest one belonged to the National Centre for Disaster Prevention in Tsukuba Science City. As Sawada et al. [94] described, it was capable of horizontal motion of a test piece of 500 t or a vertical motion of a piece of 200 t. However, this table did not have a control as the table of University of California had. The table at Tsukuba used mechanical systems to remove the unwanted displacements.

Development of 6-DOF control

In the 50s the construction of nuclear power stations began in Europe, which brought along the interest in building shaking tables. This interest led to the construction of the SAMSON 5x5 m shaking table in the mid-70s in Jülich, Germany. This table had 9 actuators – one of them took the dead weight of the table and the test piece while the role of the rest was to control all the six DOF of the shaking table. Figure 2.6 shows the SAMSON shaking table. Out of the eight actuators used for the control, four were horizontal and four vertical. The horizontal actuators applied their force at the mid-side of the table. Thanks to that, together they could provide forces in two horizontal axes as well as control the yaw. Each of the vertical actuators was attached to a corner of the table, providing the vertical forces required in the tests and controlling the pitch and roll. According to this design, the minimum number of actuators needed to control the 6-DOF of a shaking table is eight. But this fact introduced two significant steps in the control system – the inverse and the direct kinematic problems. In the inverse kinematic problem, the values of the translations and rotations are converted into instructions for the actuators (one for each). The direct kinematic problem converts the recorded values of the actuators into the displacement and rotation components. The Jülich table incorporated these two innovations, but the computational time needed in the 70s was so high that the control was "out of real time". Besides, it was also necessary that the properties of the testpiece did not change during the test.

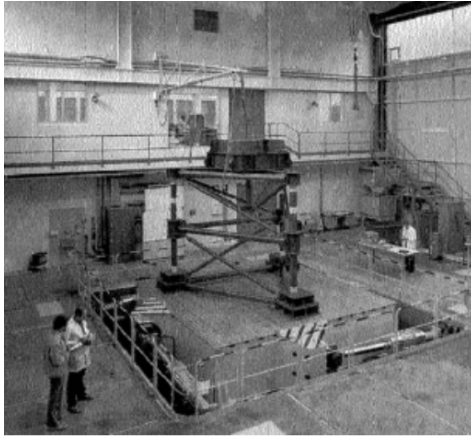


Figure 2.6: 6-DOF SAMSON shaking table

Germany abandoned nuclear power generation, so the Jülich project was abandoned after few years. However, in the early 80s, the Bristol University based its shaking table on it. The main differences were that this new shaking table was smaller than the one in Jülich and that the vertical actuators themselves supported the dead weight of the table and the test piece.

Although Germany had abandoned its nuclear power program, other countries in Europe continued with their nuclear programs and, thus, with their interest on shaking tables. Thanks to this, laboratories around Europe developed their own shaking tables. The most important European shaking table installation is at the French Alternative Energies and Atomic Energy Commission (Commissariat à l'énergie atomique et aux énergies alternatives, CEA) [95].

We have to note that in addition to the European researches, other countries, specially U.S. and Japan, made big developments. The continuation of all these researches lead to the real-time active control systems that we use nowadays.

Part II

Methodology of Design

3

Requirements and Constraints

In this work we present and analyse a MAST for automobile pieces testing purposes. If we define a reference system with the X- and Y-axes in the plane of a road – perpendicular to each other and one of them along the road – and the Z-axis perpendicular to that plane, we can simulate the movements of a car by using one translation along Z-axis and several rotations about X- and Y-axes.

As we have already seen, 3-DOF parallel mechanisms with one translation and two rotations are known as 1T2R. One of the most common used ones is the 3PRS parallel manipulator. Carretero et al. [48] introduced it in 2000. They studied its kinematics for a configuration with the limbs at 120° from each other and leaning linear guides. Figure 3.1 shows the manipulator in that configuration with the nomenclature they used. As we see, the 3PRS manipulator consists of a fixed and a mobile platform connected by three identical limbs. The limbs are composed of a prismatic joint (P), a revolute joint (R) and a spherical joint (S).

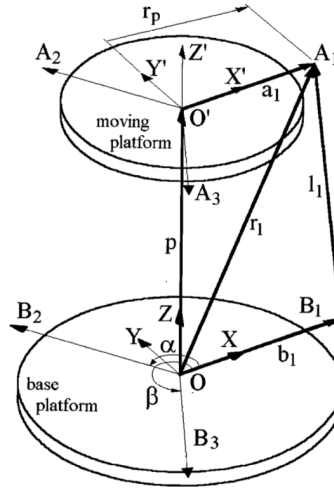


Figure 3.1: 3PRS PM proposed by Carretero

Equation (3.1) presents the mobility criterion that Hunt [96] presented to get the number of degrees of freedom of a mechanism.

$$M = 6 \cdot (n - g - 1) + \sum_{i=1}^g f_i \quad (3.1)$$

where M is the number of degrees of freedom of the manipulator, n is the number of bodies that compose the mechanism, g is the number of joints and f_i is the number of degrees of freedom of the i -th joint. In the 3PRS PM, $n = 8$, $g = 9$, $f_i = 1$ for each of the prismatic and revolute joints and $f_i = 3$ for the spherical joint. By replacing these values in Eq. (3.1), we get that the manipulator has 3 degrees of freedom, as Eq. (3.2) shows. The 3-DOF of the manipulator are a translation along Z -axis and two rotations about X - and Y -axes.

$$M = 6 \cdot (8 - 9 - 1) + 3 \cdot (1 + 1 + 3) = 3 \quad (3.2)$$

Carretero et al. [48] studied the kinematics of the manipulator and saw that small movements appeared also in the DOF where there was supposed

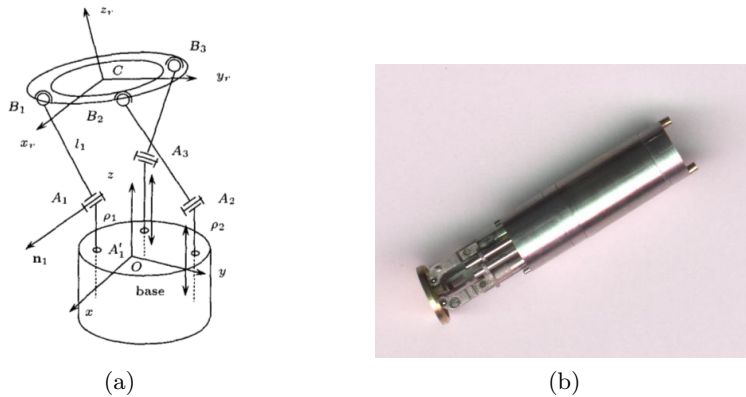


Figure 3.3: 3PRS PM proposed by Merlet: (a) sketch; (b) prototype

Pond and Carretero [49] compared these three 3PRS configurations – shown in Fig. 3.4 – in terms of dexterity. They obtained the dexterous WS of the three configurations and saw that the one with biggest WS was the one that Tsai et al. presented – with linear actuators in vertical position and the legs pointing inwards.

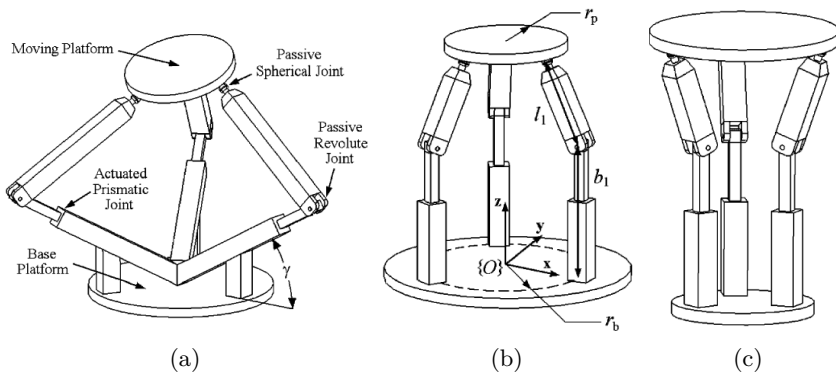


Figure 3.4: Different 3PRS PMs compared: (a) Carretero et al.; (b) Tsai et al.; (c) Merlet

Li et al. [99] compared the 3PRS parallel mechanism with different limb arrangements. They classified the 3PRS PMs into four categories and seven subcategories, that we show in Table 3.1 and Fig. 3.5. They studied the kinematic problem and obtained the parasitic motions for each of the subcategories. According to their results, the number of parasitic motions depends on the limb arrangements – category 1 and subcategory 2.1 have three parasitic motions, subcategories 2.2, 3.1 and 4.1 have only one parasitic motion and subcategories 3.2 and 4.2 have no parasitic motion. As we see in Fig. 3.5, the spherical centres in subcategories 3.1 and 4.1 are collinear, so the mobile platform is a line and we would not have space to fix a test piece. The same thing happens with subcategory 3.1.

Table 3.1: Categories of the 3PRS PM

	Geometrical condition of LPs
1	Three LPs do not intersect at a line
2	Three LPs intersect at a line with noncollinear spherical centres 2.1: three LPs are arranged simmetrically 2.2: two LPs are coincident and perpendicular to the other LP
3	Three LPs intersect at a line with collinear spherical centres 3.1: three LPs are arranged symmetrically 3.2: two LPs are coincident and perpendicular to the other LP
4	Three LPs are parallel to one another 4.1: with noncollinear spherical centres 4.2: with collinear spherical centres

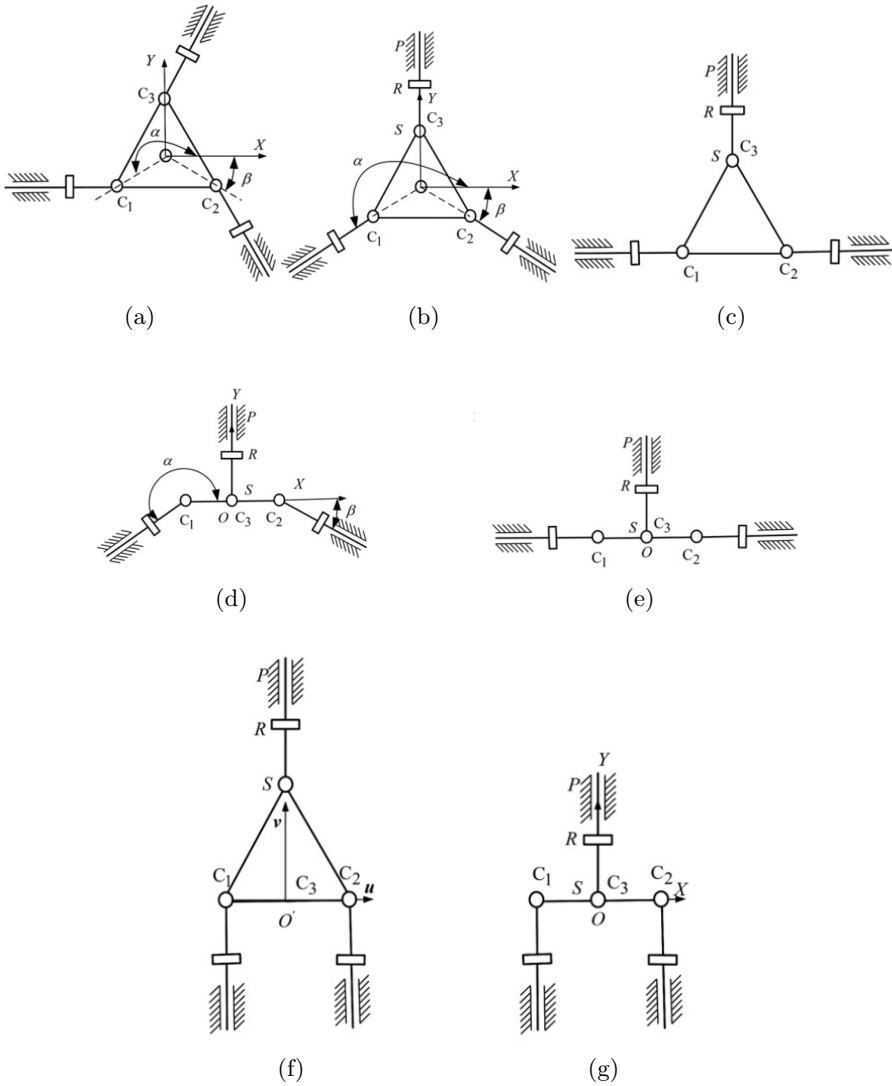


Figure 3.5: Categories of the 3PRS PM: (a) category 1; (b) subcategory 2.1; (c) subcategory 2.2; (d) subcategory 3.1; (e) subcategory 3.2; (f) subcategory 4.1; (g) subcategory 4.2

Since in subcategory 2.2 there is no parasitic motion about Z-axis, we could replace the spherical joints of the first and third limbs by several universal joints that allow rotations about X- and Y-axes, making it a 2PRU-1PRS parallel manipulator.

Xie et al. [100] compared the orientation capability and the parasitic motions of this novel 2PRU-1PRS PM with another one – the 2PRU-1PUR parallel manipulator. Figure 3.6 shows the two novel architectures.

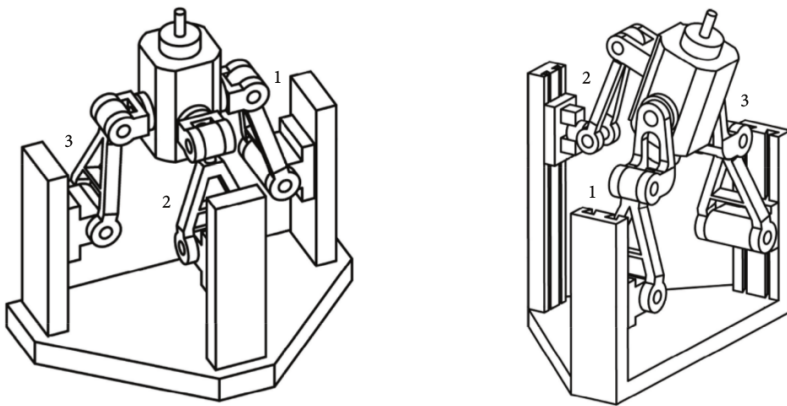


Figure 3.6: Novel architectures compared by Xie et al.: (a) 2PRU-1PRS PM; (b) 2PRU-1PUR

They studied the motion/force transmission performance of both mechanisms. In order to do it, they defined the *local transmission index* (LTI), which evaluates the motion/force transmissibility. By using that concept, they defined a *good transmission workspace* (GTW). In the GTW there is a maximal circular region, where they defined the index of *good transmission orientation capability* (GTOC). The *global transmission index* (GTI) gives information about the motion/force transmission performance of the mechanisms over that circular region. They also introduced the concept of the

global average parasitic motion (GAPM), that studies the parasitic motion distribution over the circular region. They compared the GTOC, GTI and GAPM of the two mechanisms and saw that the performance of the 2PRU-1PRS parallel manipulator was better.

Taking all these studies into account, we chose our MAST to be a 2PRU-1PRS parallel manipulator as shown in Fig. 3.7.

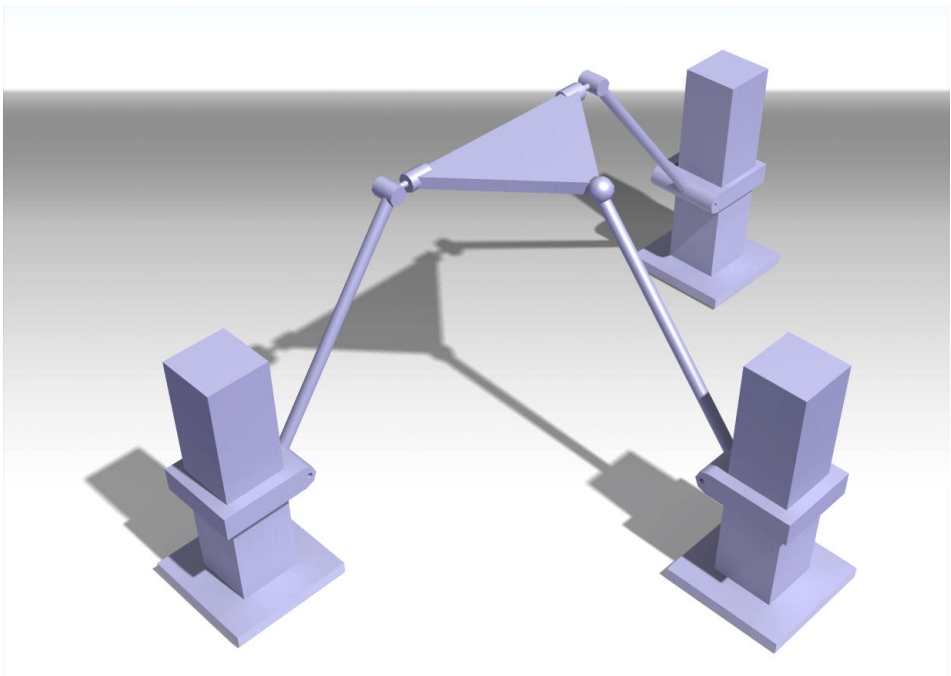


Figure 3.7: Manipulator analysed in this work

Methodology proposed

In this work we present two methodologies. The first one analyses the performance of a MAST-type parallel manipulator with known geometric parameters. The second one optimizes the geometric parameters of a MAST parallel manipulator taking into account two performances – the size and regularity of its workspace and the power consumption along a given trajectory.

We note that even if we present the methodologies for the case of the 2PRU-1PRS parallel manipulator they are valid for any other MAST configuration.

Methodology for the performance analysis

As we already know, parallel manipulators have many advantages over serial ones. One of them is their great accuracy. Thus, when designing a parallel manipulator, it is elementary to study exhaustively the position problem. The position problem consists of obtaining the exact position of each element of the manipulator. We solve the position problem by relating the inputs and the outputs of the manipulator by using as many equations as limbs the manipulator has – three in our case. Since parasitic motions affect the accuracy of parallel manipulators, it is also very important to

check if the manipulator has parasitic motions or not. If yes, we calculate them in order to know the real position of the end-effector at each single position.

Another advantage of parallel manipulators is their high stiffness. Even if there are different methods to calculate the stiffness of a parallel manipulator, in this methodology we propose to obtain it by applying the structural matrix method. In this way, we see if the stiffness of our manipulator is good enough for the chosen application and identify the areas of the workspace where there is a higher stiffness.

Parallel manipulators are usually used for applications where not only high stiffness is required but high velocity and acceleration too. By differentiating the position problem once and twice we get, respectively, the velocity and acceleration equations and, thus, we can calculate the velocity and acceleration of any point of the parallel manipulator at any trajectory position. This analysis lets us know if the end-effector reaches the velocity and acceleration required for the specific application and if the actuation system is in its allowed working range. Besides, the Jacobian matrices obtained in the velocity problem allow us to detect singular positions of the manipulator, and solving the acceleration problem is necessary for the dynamic analysis.

High dynamic capacity is characteristic of parallel manipulators. Once the acceleration is solved, we analyse the dynamics of the manipulator by using the Newton-Euler approach. We get all the reaction forces in the joints and the actuators. To do this, we first need to either determine the material of the elements or get their masses as data.

Great accuracy, high velocity, acceleration and good dynamic performance are very interesting advantages of parallel manipulators. Nevertheless, they also have some drawbacks that we have to consider when designing a new parallel manipulator. The two main ones are small workspace and the possibility of having singular positions in it. The workspace is the set of

positions that the end-effector can reach, and for parallel manipulators it is much smaller than for serial manipulators. Thus, when designing a new parallel manipulator, we usually do it in such a way that we try to get the biggest workspace possible. What happens is that singularities often appear inside the workspace. Singularities are specific positions of the manipulator where we lose control of it. Because of this, we avoid the areas where the manipulator crosses a singular position or even reach a position near it, making the useful workspace even smaller. According to this, we obtain the useful workspace of the manipulator by taking the restrictions of the joints and actuators, as well as the possible singularities into account.

Figure 4.1 represents the analysis methodology we propose for a MAST-type parallel manipulator.

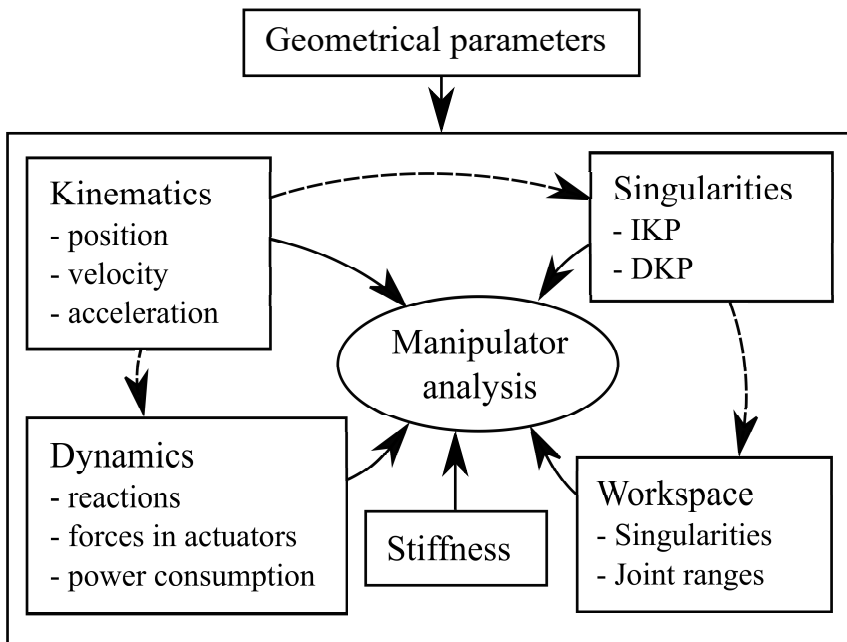


Figure 4.1: Analysis methodology

We validate this analysis methodology by applying it for a certain 2PRU-1PRS parallel manipulator. We compare the numeric results with analysis done by using finite element methods and experimental methods on a prototype built in the laboratory of COMPMECH research group.

Methodology for optimization

In the second methodology we propose an optimization of the geometric parameters of a parallel manipulator. An optimization process can take very different objective functions into account or even consider more than one function at the same time. Due to the reduced workspace of parallel manipulators, a common optimization objective is to get the biggest workspace as possible. We present two optimization methods – the first one finds the geometric parameters for the biggest useful workspace and the second one finds the geometric parameters combination that leads to the lowest power consumption for a given trajectory. Thus, we have to define the ranges of the geometric parameters we want to optimize and a step size to discretize them. Then, we get the finite number of geometric parameters combinations to be checked.

The first optimization method calculates the useful workspace for each of the geometric parameters combinations. The useful workspace is the one that we get after we consider all the joints and actuators restrictions. Besides, the useful workspace has to be free of singularities so we ensure that the manipulator can follow a trajectory inside that workspace without crossing any singular position. The size of the useful workspace is very important, but also its regularity – a big useful workspace but very irregular is not practical. Thus, we propose to consider the best geometric parameters combination as the one that leads to a useful workspace containing the biggest desired geometry object. Moreover, we obtain the set of geometric parameters combinations for which the geometry object is not the biggest but is big enough. This set of combinations is the one we optimize for in the second optimization method.

The second optimization criteria optimizes the set of geometric parameters that we obtain in the first method in order to get the lowest power consumption during a desired trajectory. In this way, we ensure that the result has also a big and regular enough workspace. In this optimization process we first have to define the trajectory for which we want to optimize the manipulator. Note that different trajectories may lead to different results. We solve the kinematic and dynamic problems for each geometric parameters combinations we want to study. We only consider the combinations for which the requirements of the joints and specifications of the actuators and motors are fulfilled. We then obtain the power consumption along the desired trajectory. The best parameters combination is the one that leads to the lowest power consumption. Figure 4.2 shows the basic steps to follow in the optimization process.

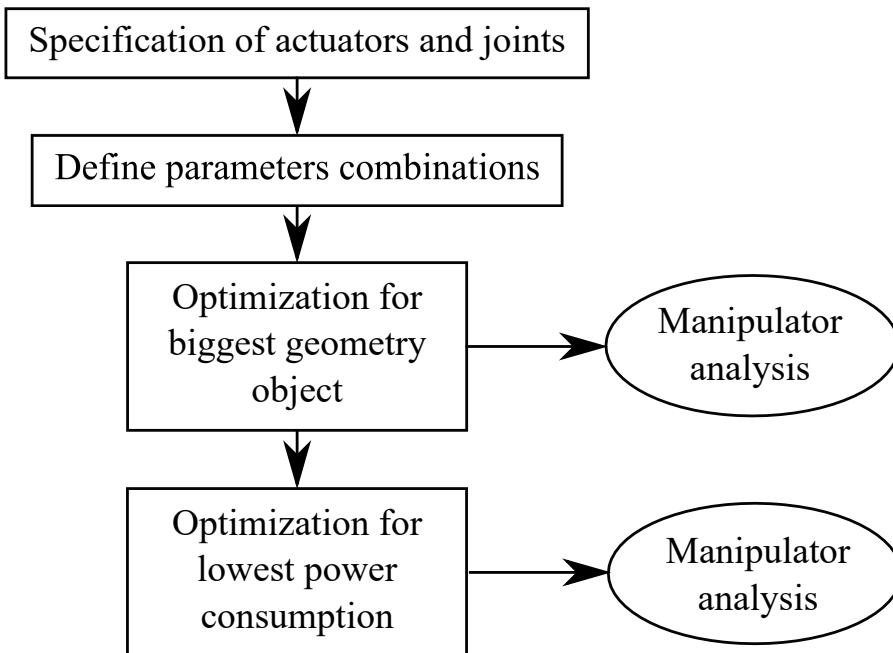


Figure 4.2: Optimization methodology

Part III

2PRU-1PRS. Manipulator Analysis

5

2PRU-1PRS Description

Figure 5.1 shows the mechanism we analyse in this work. It consists of a mobile and a fixed platform connected by three limbs. The mobile platform is an isosceles triangle with a base of $2R$ and a height of R , while the fixed platform – also isosceles-triangle-shaped – has a base of $2H$ and a height of H . The first and the third limbs are identical chains that consist of, starting from the base, a prismatic joint, a revolute joint and a universal joint (PRU). However, the second limb is composed of a prismatic joint, a revolute joint and a spherical joint (PRS). Additionally, the limb planes of the first and third limbs are coincident and perpendicular to the second one.

As we saw in Chapter 3, the 2PRU-1PRS parallel manipulator in this configuration has the same three degrees of freedom as the 3PRS PM – a vertical translation and two rotations about two perpendicular axes intersecting at the fixed platform center. As shown in Fig. 5.1, we fix a base coordinate frame, $(O_{X,Y,Z})$, at the center of the base platform with the Z -axis vertical and the X -axis pointing towards the C_1 point. Similarly, we define the moving coordinate frame, (P_{x_p,y_p,z_p}) , with the z_p -axis normal to the mobile platform plane and the x_p -axis pointing towards the A_1 point. According to this, the 3-DOF are a translation along the Z -axis and two

rotations about the X- and Y-axes (ψ and θ , respectively). The parasitic motion is the one we obtained in Chapter 3 – a translation along the X-axis whose expression is given by Eq. (5.1).

$$x = R \cdot (s\theta \cdot s\psi) \quad (5.1)$$

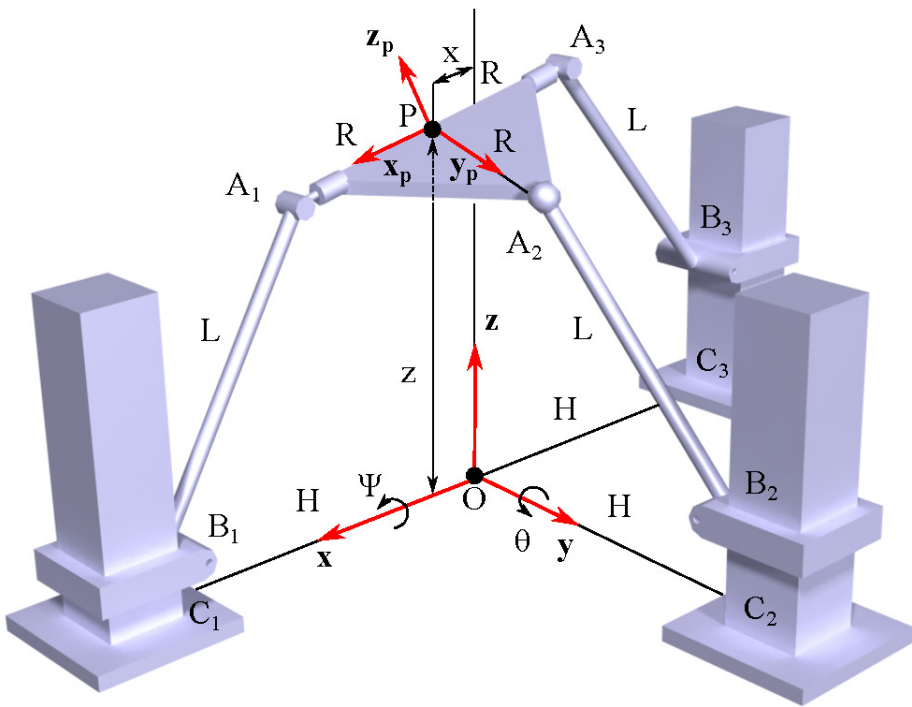


Figure 5.1: Sketch of the manipulator

6

Kinematics

6.1. Kinematics

Solving the kinematics of a parallel manipulator consists of obtaining the position, velocity and acceleration of all the elements of the manipulator.

6.1.1. Position problem

The position problems analyse the position and orientation of all the elements that constitute the robot. There are two different kinds of position problems – the inverse position problem and the direct position problem.

6.1.1.1. Inverse position problem

In the inverse position problem the position and orientation of the end-effector are known and we obtain the position of the actuators and the rest of elements of the manipulator. This is to say, the inverse position problem consists of mapping from the Cartesian space to the joint space. The inverse position problem can have several solutions. We label those different solutions as *working modes*.

We usually get the inverse position problem by solving a system of quadratic equations. We obtain the equations of that system by analysing each kinematic loop chain that relates the output parameters (position and orientation) with the corresponding inputs.

In [48], Carretero et al. analysed the inverse kinematics of the 3-PRS parallel manipulator. They obtained the loop equation of each limb of the manipulator, solved the system and saw that there were two possible working modes – one corresponding to the manipulator with its limbs pointing inwards and the other, outwards.

Gosselin et al. [101]-[61] solved the inverse kinematic problem of the Agile Eye. They obtained three quadratic equations by considering the loop equation of each of the three limbs of the manipulator. The equation system lead to 8 possible solution.

Rezaei et al. [102] presented the kinematic analysis of the 3-PSP parallel manipulator. The special characteristic of this manipulator is that the user can choose how to run it – in non-pure translational mode or in coupled mixed-type modes. In their work, Rezaei et al. solved the inverse kinematic problem for both modes. For the coupled mixed-type mode they obtained a numerical solution, while for the non-pure translational mode the solution was analytical. Other authors of novel manipulators, like Hosseini [71], Zhao et al. [103] or Ibrahim et al. [41], also analysed the kinematics of their manipulators by using the corresponding close loop equation.

Another way of solving the inverse position problem is to apply Screw Theory like Altuzarra et al. [104] did. Chen et al. [51] used this theory to analyse the 3-PRS and the 3-RPS parallel manipulators. Li and Xu [105] also studied the kinematics of the 3-PRS parallel manipulator by using screw theory. Finally, Cheng et al. [106] introduced a finite element method for kinematic analysis of a parallel hip joint manipulator. In this method there is no need to define the loop equation of the manipulator or reference systems. Additionally, we do not have to solve nonlinear equations. Cheng

et al. [106] saw that the finite element method is an universal method to solve the kinematics of parallel manipulators with any DOF.

As we have already seen, the workspace is an essential characteristic of parallel manipulators that we have to take into account when designing them. The workspace is the set of points that the end-effector of a particular parallel manipulator can reach. Thus, we have to solve the inverse position problem of the manipulator to get its workspace. This makes the obtaining of the workspace of the manipulator the greatest application of solving its inverse position problem.

6.1.1.2. Direct position problem

The direct position problem consists of obtaining the position and orientation of each single element of the robot, including the end-effector, for given input values of the actuators. In other words: the direct position problem – also known as forward position problem – consists of mapping from the joint space to the Cartesian space. In a general case, this is a very complex problem.

If we want to control the position of a manipulator along a certain trajectory, we have to solve the inverse position problem. Once we know the inputs that we need, we send the command to the actuators so they reach their corresponding position. The problem is that there are usually some errors in the movement of the actuators. Thus, the real position of the end-effector is not the desired one and it is, in principle, unknown. If we solve the direct position problem, we get the real position of the end-effector and we can make the necessary corrections in the actuators so the trajectory is the desired one. According to this, besides solving the inverse position problem, we need to solve the direct position problem in order to have a good control of the manipulator.

As Merlet [107] explained, the equations in the direct position problem of parallel manipulators are non-linear and the unknown variables – position and orientation – appear in all of them. Therefore, the equation system is

highly coupled and, thus, it is very complex to solve. We have two main ways to solve the system – analytically and numerically.

Solving the system analytically is quite difficult and it is not always possible. The general solving method, as Tancredi et al. [108] explained, consists of getting the expression of one equation with only one variable. This is useful to solve the direct position problem only if we can get an univariate polynomial of degree four or less. Since this is very difficult to get, there are other options like the polynomial continuation methods proposed by Sommese et al. [109] or the use of Gröbner bases as explained by Dhingra et al. [110].

Another possibility could be solving the system numerically by using, for example, the Newton-Raphson method. However, this method is iterative, so it does not ensure that we get the solution in the required loop control time. Besides, the Newton-Raphson method has local convergence, so, in order to get a correct result, we have to know if we are close to the solution we want to find.

With the goal of overcoming these drawbacks and getting all the solutions of the direct position problem, called *assemble modes*, we can use the Newton-Raphson method and interval analysis, presented by Jaulin et al. [111], at the same time. This method is known as the Hansen method, proposed by Didrit et al. [112]. Merlet [113] applied the Hansen method to solve the direct position problem of the Gough platform.

The biggest drawbacks of numeric methods are high computational cost and that we have to evaluate Jacobian matrices. If the Jacobian matrices are singular we get no convergence to the solution. Some authors have presented alternatives to deal with those drawbacks. As an example, Petuya et al. [114], [115] presented the generic iterative method and applied it satisfactorily to parallel manipulators.

In case we have redundant information, like the position of some ele-

ments, the direct problem becomes simpler. Baron and Angeles [116], [117], [118], [119], [120], Bonev et al. [121], Chiu and Perng [122] and Venanzi and Parenti-Castelli [123] used redundant sensors to get that extra information, while Baron and Angeles [118] used also cameras.

6.1.2. Velocity and acceleration problems

Parallel manipulators have high speed and accelerations. This, along with small masses, gives them very good dynamic characteristics. Thus, in order to analyse the dynamics of a manipulator, we first have to study their velocity equation. Besides, as we will see in Chapter 7, the study of singularities is based on Jacobian matrices, which we get by solving the velocity problem of the manipulator. All this makes the study of the velocity a very important issue when analysing parallel manipulators.

The expression for the velocity is usually given by Eq. (6.1)

$$\mathbf{A} \cdot \dot{\mathbf{x}} = \mathbf{B} \cdot \dot{\mathbf{q}} \quad (6.1)$$

where $\dot{\mathbf{q}}$ and $\dot{\mathbf{x}}$ are the input and output velocities of the manipulator and \mathbf{A} and \mathbf{B} are the corresponding Jacobian matrices.

Similarly, the expression for the acceleration is the derivative of the velocity expression. As we have said, solving the acceleration problem is essential for the study of the dynamics of parallel manipulators.

Many authors, as for example Rezaei et al. [102], Zhao et al. [103], Zhang et al. [124], studied the velocity and acceleration problems of parallel manipulators by applying the expression written above. However, there are other ways of studying the velocity problem. García de Jalón et al. [125] or Eischen et al. [126] proposed two different alternatives based on the Finite Elements Method. Those methods are related with the adimensional Jacobian formulation presented by Hernández et al. [127] and Altuzarra et al. [128] and developed by Salgado [129].

6.2. Developing the kinematic problem of the 2PRU-1PRS PM

We analyse the kinematic problem of the 2PRU-1PRS parallel manipulator. Figure 6.1 shows the parameters and vectors we need for the development of the position, velocity and acceleration problems.

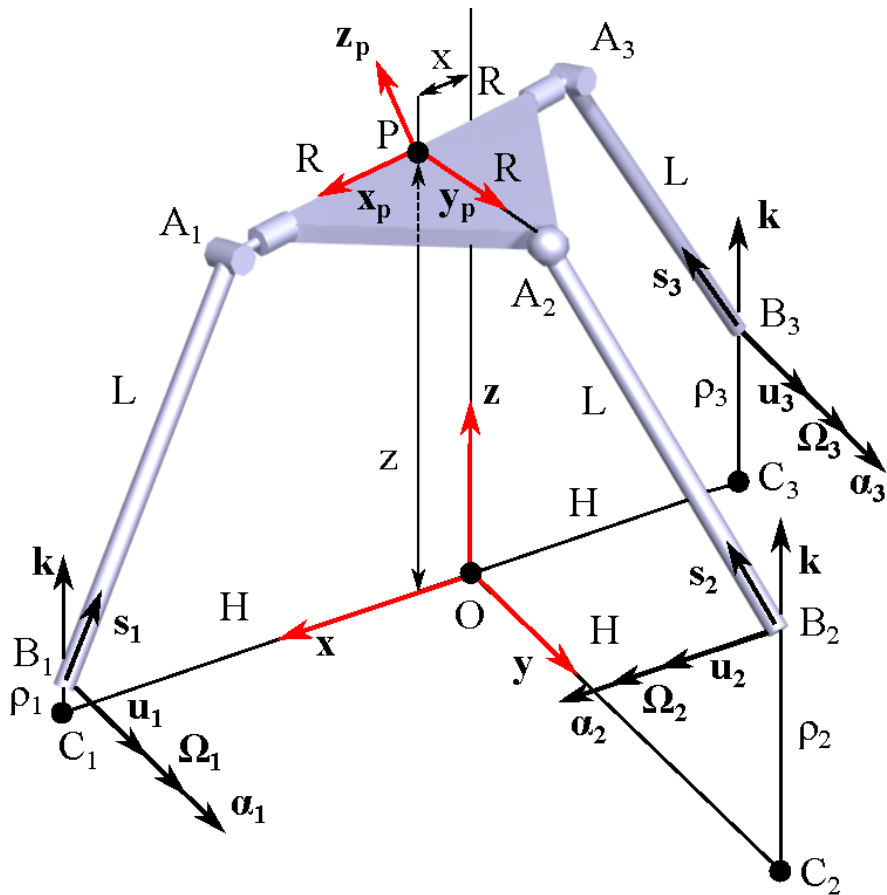


Figure 6.1: Sketch of the manipulator

6.2.1. Position Problem of the 2PRU-1PRS PM

In the inverse position problem the rotations about X- and Y-axes, ψ and θ respectively, and the translation along Z-axis are known and we have to calculate the position of all points of the manipulator that depend on them.

Vectors \mathbf{a}_i , given by Eq. (6.2), define the position of the A_i points in the mobile frame P_{x_p, y_p, z_p} .

$$\begin{aligned}\mathbf{a}_1 &= [R, 0, 0] \\ \mathbf{a}_2 &= [0, R, 0] \\ \mathbf{a}_3 &= [-R, 0, 0]\end{aligned}\tag{6.2}$$

We express the A_i points in the fixed frame as \mathbf{A}_i , given by Eq. (6.3) and Eq. (6.4), in vectorial and matrix notations, respectively. \mathbf{Rot} is the transformation matrix that relates the mobile reference system with the fixed system and \mathbf{P} is the vector that defines the position of the point P in the fixed reference system.

$$\mathbf{A}_i = \mathbf{P} + \mathbf{Rot} \cdot \mathbf{a}_i^T\tag{6.3}$$

$$\mathbf{A}_i = \begin{bmatrix} x \\ y \\ z \end{bmatrix} + \begin{bmatrix} Rot_{11} \cdot a_{ix} + Rot_{12} \cdot a_{iy} + Rot_{13} \cdot a_{iz} \\ Rot_{21} \cdot a_{ix} + Rot_{22} \cdot a_{iy} + Rot_{23} \cdot a_{iz} \\ Rot_{31} \cdot a_{ix} + Rot_{32} \cdot a_{iy} + Rot_{33} \cdot a_{iz} \end{bmatrix}\tag{6.4}$$

According to this, Eq. (6.5) expresses the components of each point A_i .

$$\begin{aligned}A_{ix} &= x + Rot_{11} \cdot a_{ix} + Rot_{12} \cdot a_{iy} + Rot_{13} \cdot a_{iz} \\ A_{iy} &= y + Rot_{21} \cdot a_{ix} + Rot_{22} \cdot a_{iy} + Rot_{23} \cdot a_{iz} \\ A_{iz} &= z + Rot_{31} \cdot a_{ix} + Rot_{32} \cdot a_{iy} + Rot_{33} \cdot a_{iz}\end{aligned}\tag{6.5}$$

We obtain the rotation matrix by applying rotations of ϕ , θ and ψ , about z_p -, y_p - and x_p -axes, respectively, as seen in Eq. (6.6).

$$\mathbf{Rot}_{\phi,\theta,\psi} = \begin{bmatrix} c\phi & -s\phi & 0 \\ s\phi & c\phi & 0 \\ 0 & 0 & 1 \end{bmatrix} \cdot \begin{bmatrix} c\theta & 0 & s\theta \\ 0 & 1 & 0 \\ -s\theta & 0 & c\theta \end{bmatrix} \cdot \begin{bmatrix} 1 & 0 & 0 \\ 0 & c\psi & -s\psi \\ 0 & s\psi & c\psi \end{bmatrix} \quad (6.6)$$

By simplifying Eq. (6.6) we get the expression of the rotation matrix, given by Eq. (6.7).

$$\mathbf{Rot}_{\phi,\theta,\psi} = \begin{bmatrix} c\phi \cdot c\theta & -s\phi \cdot c\psi + c\phi \cdot s\theta \cdot s\psi & s\phi \cdot s\psi + c\phi \cdot s\theta \cdot c\psi \\ s\phi \cdot c\theta & c\phi \cdot c\psi + s\phi \cdot s\theta \cdot s\psi & -c\phi \cdot s\psi + s\phi \cdot s\theta \cdot c\psi \\ -s\theta & c\theta \cdot s\psi & c\theta \cdot c\psi \end{bmatrix} \quad (6.7)$$

The geometry of the manipulator implies that the limbs have to remain always in the limb plane. We define vector \mathbf{u}_i perpendicular to the respective limb planes. Thus, \mathbf{u}_i are given by Eq. (6.8).

$$\begin{aligned} \mathbf{u}_1 &= \begin{bmatrix} 0 & 1 & 0 \end{bmatrix}^T \\ \mathbf{u}_2 &= \begin{bmatrix} 1 & 0 & 0 \end{bmatrix}^T \\ \mathbf{u}_3 &= \mathbf{u}_1 \end{aligned} \quad (6.8)$$

The perpendicularity condition allows us to formulate Eq. (6.9).

$$\mathbf{A}_i \cdot \mathbf{u}_i = 0 \quad (6.9)$$

We apply that condition for the first limb and we get Eq. (6.10).

$$\mathbf{A}_1 \cdot \mathbf{u}_1 = \begin{bmatrix} A_{1x} & A_{1y} & A_{1z} \end{bmatrix} \cdot \begin{bmatrix} 0 \\ 1 \\ 0 \end{bmatrix} \quad (6.10)$$

According to Eq. (6.10), the perpendicularity condition for the first limb is given by Eq. (6.11).

$$A_{1y} = 0 \quad (6.11)$$

By combining Eq. (6.5) and Eq. (6.11) we get Eq. (6.12).

$$y + Rot_{21} \cdot a_{1x} + Rot_{22} \cdot a_{1y} + Rot_{23} \cdot a_{1z} = 0 \quad (6.12)$$

We substitute Eq. (6.6) and Eq. (6.2) in Eq. (6.12) and get Eq. (6.13).

$$y + R \cdot (c\psi \cdot s\phi) = 0 \quad (6.13)$$

For the second limb, the restriction of remaining in the limb plane is given by Eq. (6.14). By simplifying it we get Eq. (6.15).

$$\mathbf{A}_2 \cdot \mathbf{u}_2 = \begin{bmatrix} A_{2x} & A_{2y} & A_{2z} \end{bmatrix} \cdot \begin{bmatrix} 1 \\ 0 \\ 0 \end{bmatrix} \quad (6.14)$$

$$A_{2x} = 0 \quad (6.15)$$

We take Eq. (6.5) and Eq. (6.15) into account and get Eq. 6.16.

$$x + Rot_{11} \cdot a_{2x} + Rot_{12} \cdot a_{2y} + Rot_{13} \cdot a_{2z} = 0 \quad (6.16)$$

By substituting Eq. (6.2) and Eq. (6.6) in Eq. (6.16) we obtain Eq. (6.17).

$$x + R \cdot (-c\theta \cdot s\phi + c\phi \cdot s\theta \cdot s\psi) = 0 \quad (6.17)$$

Since the third limb is analogous to the first one, the restriction condition is given by Eq. (6.18) and we simplify it as Eq. (6.19).

$$\mathbf{A}_3 \cdot \mathbf{u}_3 = \begin{bmatrix} A_{3x} & A_{3y} & A_{3z} \end{bmatrix} \cdot \begin{bmatrix} 0 \\ 1 \\ 0 \end{bmatrix} \quad (6.18)$$

$$A_{3y} = 0 \quad (6.19)$$

We substitute Eq. (6.19) in Eq. (6.5) and get the restriction condition as given in Eq. (6.20).

$$y + Rot_{21} \cdot a_{3x} + Rot_{22} \cdot a_{3y} + Rot_{23} \cdot a_{3z} = 0 \quad (6.20)$$

Finally, we substitute Eq. (6.6) and Eq. (6.2) in Eq. (6.20) and get Eq. (6.21).

$$y - R \cdot (c\psi \cdot s\phi) = 0 \quad (6.21)$$

Equations (6.13), (6.17) and (6.21) define the system of equations that we have to solve to get the values of the parasitic motions. From Eq. (6.13) and Eq. (6.21) we get the value of the the rotation about the Z-axis (ϕ) and the translation along the Y-axis (y), given by Eq. (6.22) and Eq. (6.23), respectively. We substitute the value of ϕ and y in Eq. (6.17) and get the translation along X-axis, given by Eq. (6.24). According to this, there is only one parasitic motion – the translation along X-axis, which corresponds with the classification that Li et al. [99] proposed.

$$\phi = 0 \quad (6.22)$$

$$y = 0 \quad (6.23)$$

$$x = R \cdot (s\theta \cdot s\psi) \quad (6.24)$$

As we see in Fig. 6.1, the loop equation of each limb is given by Eq. (6.25). We use this loop equation to calculate the value of the three actua-

tors, but first we have to obtain the value of each vector in the equation.

$$\mathbf{A}_i = \mathbf{C}_i + \mathbf{C}_i \mathbf{B}_i + \mathbf{A}_i \mathbf{B}_i \quad (6.25)$$

\mathbf{C}_i points are fixed points, and they are defined by Eq. (6.26)

$$\begin{aligned} \mathbf{C}_1 &= [H \ 0 \ 0]^T \\ \mathbf{C}_2 &= [0 \ H \ 0]^T \\ \mathbf{C}_3 &= [-H \ 0 \ 0]^T \end{aligned} \quad (6.26)$$

where, as we have already see, H is the value of the radius of the fixed platform.

The \mathbf{B}_i points remain always in the limb planes and, additionally, the actuators $\mathbf{B}_i \mathbf{C}_i$ are always perpendicular to the XY plane. Hence, the \mathbf{B}_{ix} and \mathbf{B}_{iy} components are constant, while the \mathbf{B}_{iz} component depends on the value of the actuators in each position, ρ_i , as shown in Eq. (6.27).

$$\begin{aligned} \mathbf{B}_1 &= [H \ 0 \ \rho_1]^T \\ \mathbf{B}_2 &= [0 \ H \ \rho_2]^T \\ \mathbf{B}_3 &= [-H \ 0 \ \rho_3]^T \end{aligned} \quad (6.27)$$

Since the rotation about the Z -axis (ϕ) is a parasitic motion and is null, Eq. (6.28) is fulfilled. Thus, we express the rotation matrix $\mathbf{Rot}_{\phi,\theta,\psi}$ as Eq. (6.29).

$$\begin{aligned} c\phi &= 1 \\ s\phi &= 0 \end{aligned} \quad (6.28)$$

$$\mathbf{Rot}_{\phi,\theta,\psi} = \begin{bmatrix} c\theta & s\theta \cdot s\psi & s\theta \cdot c\psi \\ 0 & c\psi & -s\psi \\ -s\theta & c\theta \cdot s\psi & c\theta \cdot c\psi \end{bmatrix} \quad (6.29)$$

According to this, Eq. (6.30) gives the A_i points in the fixed reference system (x,y,z) .

$$\mathbf{A}_i = \begin{bmatrix} x \\ 0 \\ z \end{bmatrix} + \begin{bmatrix} c\theta \cdot a_{ix} + s\theta \cdot s\psi \cdot a_{iy} + s\theta \cdot c\psi \cdot a_{iz} \\ c\psi \cdot a_{iy} - s\psi a_{iz} \\ -s\theta \cdot a_{ix} + c\theta \cdot s\psi \cdot a_{iy} + c\theta \cdot c\psi \cdot a_{iz} \end{bmatrix} \quad (6.30)$$

By substituting the value of a_i for each limb in Eq. (6.30), we get the value of the A_i points in the fixed reference system.

- **First limb:** the expression to obtain the value of A_1 is given by Eq. (6.31).

$$\mathbf{A}_1 = \begin{bmatrix} x \\ 0 \\ z \end{bmatrix} + \begin{bmatrix} c\theta \cdot R \\ 0 \\ -s\theta \cdot R \end{bmatrix} \quad (6.31)$$

By substituting the value of the parasitic motion, we get Eq. (6.32).

$$A_1 = \left[R \cdot (c\theta - s\psi \cdot s\theta) \quad 0 \quad z - R \cdot s\theta \right]^T \quad (6.32)$$

- **Second limb:** the expression of A_2 is given by Eq. (6.33). We replace the value of the parasitic motion and get Eq. (6.34).

$$\mathbf{A}_2 = \begin{bmatrix} x \\ 0 \\ z \end{bmatrix} + \begin{bmatrix} s\theta \cdot s\psi \cdot R \\ c\psi \cdot R \\ c\theta \cdot s\psi \cdot R \end{bmatrix} \quad (6.33)$$

$$A_2 = \left[0 \quad R \cdot c\psi \quad z + R \cdot c\theta \cdot s\psi \right]^T \quad (6.34)$$

- **Third limb:** similarly, we write the expression for A_3 as given by Eq. (6.35). We get Eq. (6.36) by replacing the values of the parasitic

motion in Eq. (6.35).

$$\mathbf{A}_i = \begin{bmatrix} x \\ 0 \\ z \end{bmatrix} + \begin{bmatrix} -c\theta \cdot R \\ 0 \\ s\theta \cdot R \end{bmatrix} \quad (6.35)$$

$$A_3 = \begin{bmatrix} -R \cdot (c\theta + s\psi \cdot s\theta) & 0 & z + R \cdot s\theta \end{bmatrix}^T \quad (6.36)$$

We rewrite the loop equation Eq. (6.25) as Eq. (6.37). We can now obtain the value of the actuator displacements by substituting the values of the vectors obtained above into the loop equation.

$$\mathbf{A}_i \mathbf{B}_i = \mathbf{A}_i - \mathbf{C}_i - \mathbf{C}_i \mathbf{B}_i \quad (6.37)$$

As we see in Fig 6.1, the norm of $\mathbf{A}_i \mathbf{B}_i$ is the length of the limbs. Equation (6.38) gives its expression.

$$\begin{aligned} |\mathbf{A}_i \mathbf{B}_i|^2 = L = & (\mathbf{A}_{ix} - \mathbf{C}_{ix} - \mathbf{C} \mathbf{B}_{ix})^2 + (\mathbf{A}_{iy} - \mathbf{C}_{iy} - \mathbf{C} \mathbf{B}_{iy})^2 + \\ & + (\mathbf{A}_{iz} - \mathbf{C}_{iz} - \mathbf{C} \mathbf{B}_{iz})^2 \end{aligned} \quad (6.38)$$

The first limb is always in the XZ plane, so the coordinates in the Y-axis are null. Taking this condition into account, we apply Eq. (6.38) to the first limb, getting Eq. (6.39).

$$L = (\mathbf{A}_{1x} - \mathbf{C}_{1x} - \mathbf{C} \mathbf{B}_{1x})^2 + (\mathbf{A}_{1z} - \mathbf{C}_{1z} - \mathbf{C} \mathbf{B}_{1z})^2 \quad (6.39)$$

By substituting the value of the coordinates of the vectors previously obtained, we get the value of the displacement of the first actuator, ρ_1 , given by Eq. (6.40).

$$\begin{aligned} L^2 = & (R \cdot (c\theta - s\theta \cdot s\psi) - H)^2 + (z - R \cdot s\theta - \rho_1)^2 \\ \sqrt{L^2 - (R \cdot (c\theta - s\theta \cdot s\psi) - H)^2} = & (z - R \cdot s\theta - \rho_1)^2 \\ \rho_1 = & z - R \cdot s\theta - \sqrt{L^2 - (R \cdot (c\theta - s\theta \cdot s\psi) - H)^2} \end{aligned} \quad (6.40)$$

In the case of the second limb, it always remains in the YZ plane, so the components in the X-axis are null. We get Eq. (6.41) by replacing that condition in Eq. (6.38) for the second limb.

$$L = (\mathbf{A}_{2y} - \mathbf{C}_{2y} - \mathbf{CB}_{2y})^2 + (\mathbf{A}_{2z} - \mathbf{C}_{2z} - \mathbf{CB}_{2z})^2 \quad (6.41)$$

We substitute the value of the components of the corresponding vectors and get the expression for the displacement of the second actuator, ρ_2 , given by Eq. (6.42).

$$\begin{aligned} L^2 &= (R \cdot c\psi - H)^2 + (z + R \cdot c\theta \cdot s\psi - \rho_2)^2 \\ \sqrt{L^2 - (R \cdot c\psi - H)^2} &= z + R \cdot c\theta \cdot s\psi - \rho_2 \\ \rho_2 &= z + R \cdot c\theta \cdot s\psi - \sqrt{L^2 - (R \cdot c\psi - H)^2} \end{aligned} \quad (6.42)$$

In the same way as for the first limb, all the component in the Y-axis of the third limb are null. If we apply Eq. (6.38) to the third limb, we get Eq. (6.43).

$$L = (\mathbf{A}_{3x} - \mathbf{C}_{3x} - \mathbf{CB}_{3x})^2 + (\mathbf{A}_{3z} - \mathbf{C}_{3z} - \mathbf{CB}_{3z})^2 \quad (6.43)$$

By substituting the value of the components of the vectors in Eq. (6.43), we get the expression for the displacement of the third actuator, ρ_3 , given by Eq. (6.44).

$$\begin{aligned} L^2 &= (-R \cdot (c\theta + s\theta \cdot s\psi) + H)^2 + (z + R \cdot s\theta - \rho_3)^2 \\ \sqrt{L^2 - (-R \cdot (c\theta + s\theta \cdot s\psi) + H)^2} &= z + R \cdot s\theta - \rho_3 \\ \rho_3 &= z + R \cdot s\theta - \sqrt{L^2 - (-R \cdot (c\theta + s\theta \cdot s\psi) + H)^2} \end{aligned} \quad (6.44)$$

6.2.2. Velocity Problem

We can also express the loop equation of the manipulator as Eq. (6.45). By differentiating it, we obtain the expression for the velocity of the mobile

platform in vectorial notation, given by Eq. (6.46)

$$\mathbf{OP} = \mathbf{OC}_i + \mathbf{CB}_i + \mathbf{BA}_i + \mathbf{A}_i\mathbf{P} \quad (6.45)$$

$$\mathbf{v}_p = \dot{\rho}_i\mathbf{k} + \boldsymbol{\Omega}_i \times (\mathbf{B}_i\mathbf{A}_i) + \boldsymbol{\Omega}_p \times (\mathbf{A}_i\mathbf{P}) \quad (6.46)$$

where $\boldsymbol{\Omega}_p$ is the angular velocity of the mobile platform, \mathbf{k} is a vertical unit vector, \mathbf{v}_p is the linear velocity of the platform and $\boldsymbol{\Omega}_i$ is the angular velocity of each leg, as seen in Fig. 6.1.

We multiply Eq. (6.46) by unit vector \mathbf{s}_i as given by Eq. (6.47) and rewrite Eq. (6.47) into Eq. (6.48).

$$\mathbf{s}_i \cdot \mathbf{v}_p = \mathbf{s}_i \cdot (\dot{\rho}_i\mathbf{k}) + \mathbf{s}_i \cdot (\boldsymbol{\Omega}_i \times (\mathbf{B}_i\mathbf{A}_i)) + \mathbf{s}_i \cdot (\boldsymbol{\Omega}_p \times \mathbf{A}_i\mathbf{P}) \quad (6.47)$$

$$\mathbf{s}_i \cdot \mathbf{v}_p = \dot{\rho}_i \cdot (\mathbf{s}_i\mathbf{k}) + \boldsymbol{\Omega}_i \cdot (\mathbf{B}_i\mathbf{A}_i \times \mathbf{s}_i) + \boldsymbol{\Omega}_p \cdot (\mathbf{A}_i\mathbf{P} \times \mathbf{s}_i) \quad (6.48)$$

Since \mathbf{s}_i and $\mathbf{B}_i\mathbf{A}_i$ are collinear, $\mathbf{B}_i\mathbf{A}_i \times \mathbf{s}_i = 0$, so we get Eq. (6.49).

$$\mathbf{s}_i \cdot \mathbf{v}_p + \boldsymbol{\Omega}_i \cdot (\mathbf{PA}_i \times \mathbf{s}_i) = \dot{\rho}_i \cdot (\mathbf{s}_i\mathbf{k}) \quad (6.49)$$

If we multiply Eq. (6.46) by a unit vector perpendicular to the limb plane, \mathbf{u}_i we have Eq. (6.50), which we rewrite as Eq. (6.51).

$$\mathbf{u}_i \cdot \mathbf{v}_p = \mathbf{u}_i \cdot (\dot{\rho}_i\mathbf{k}) + \mathbf{u}_i \cdot (\boldsymbol{\Omega}_i \times (\mathbf{B}_i\mathbf{A}_i)) + \mathbf{u}_i \cdot (\boldsymbol{\Omega}_p \times \mathbf{A}_i\mathbf{P}) \quad (6.50)$$

$$\mathbf{u}_i \cdot \mathbf{v}_p = \dot{\rho}_i \cdot (\mathbf{u}_i\mathbf{k}) + \boldsymbol{\Omega}_i \cdot (\mathbf{B}_i\mathbf{A}_i \times \mathbf{u}_i) + \boldsymbol{\Omega}_p \cdot (\mathbf{A}_i\mathbf{P} \times \mathbf{u}_i) \quad (6.51)$$

Since \mathbf{u}_i and $\boldsymbol{\Omega}_i$ are collinear, $\mathbf{u}_i \times \boldsymbol{\Omega}_i = 0$. Besides, \mathbf{u}_i and \mathbf{k} are perpendicular, $\mathbf{u}_i\mathbf{k} = 0$, so we get Eq. (6.52).

$$\mathbf{u}_i \cdot \mathbf{v}_p + \boldsymbol{\Omega}_p \cdot (\mathbf{PA}_i \times \mathbf{u}_i) = 0 \quad (6.52)$$

If we express Eq. (6.49) and Eq. (6.52) in matrix notation, we get Eq. (6.53) and if we write it in a compact way we have Eq. (6.54)

$$\begin{bmatrix} \mathbf{s}_1^T & (\mathbf{PA}_1 \times \mathbf{s}_1)^T \\ \mathbf{s}_2^T & (\mathbf{PA}_2 \times \mathbf{s}_2)^T \\ \mathbf{s}_3^T & (\mathbf{PA}_3 \times \mathbf{s}_3)^T \\ \mathbf{u}_1^T & (\mathbf{PA}_1 \times \mathbf{u}_1)^T \\ \mathbf{u}_2^T & (\mathbf{PA}_2 \times \mathbf{u}_2)^T \\ \mathbf{u}_3^T & (\mathbf{PA}_3 \times \mathbf{u}_3)^T \end{bmatrix} \cdot \begin{bmatrix} \mathbf{v}_p \\ \boldsymbol{\Omega}_p \end{bmatrix} = \begin{bmatrix} \mathbf{s}_1 \mathbf{k} & 0 & 0 \\ 0 & \mathbf{s}_2 \mathbf{k} & 0 \\ 0 & 0 & \mathbf{s}_3 \mathbf{k} \\ 0 & 0 & 0 \\ 0 & 0 & 0 \\ 0 & 0 & 0 \end{bmatrix} \cdot \begin{bmatrix} \dot{\rho}_1 \\ \dot{\rho}_2 \\ \dot{\rho}_3 \end{bmatrix} \quad (6.53)$$

$$\mathbf{J}_x \cdot \begin{bmatrix} \mathbf{v}_p \\ \boldsymbol{\Omega}_p \end{bmatrix} = \mathbf{J}_q \cdot \dot{\rho}_i \quad (6.54)$$

where \mathbf{J}_x is Jacobian matrix of the direct problem and \mathbf{J}_q is the Jacobian matrix of the inverse problem.

6.2.3. Acceleration Problem

We differentiate Eq. (6.46) again and get the vectorial expression for the acceleration, given by Eq. (6.55)

$$\begin{aligned} \mathbf{a}_p = & \ddot{\rho}_i \mathbf{k} + \boldsymbol{\alpha}_i \times \mathbf{A}_i \mathbf{B}_i + \boldsymbol{\Omega}_i \times (\boldsymbol{\Omega}_i \times \mathbf{A}_i \mathbf{B}_i) + \\ & + \boldsymbol{\alpha}_p \times \mathbf{A}_i \mathbf{P} + \boldsymbol{\Omega}_p \times (\boldsymbol{\Omega}_p \times \mathbf{A}_i \mathbf{P}) \end{aligned} \quad (6.55)$$

where \mathbf{a}_p and $\boldsymbol{\alpha}_p$ are the linear and angular accelerations of the mobile platform, and $\boldsymbol{\alpha}_i$ is the angular velocity of the i -limb, as seen in Fig. 6.1.

If we multiply Eq. (6.55) by the unit vector \mathbf{u}_i we get Eq. (10.7).

$$\begin{aligned} \mathbf{u}_i \cdot \mathbf{a}_p = & \mathbf{u}_i \cdot \ddot{\rho}_i \mathbf{k} + \mathbf{u}_i \cdot (\boldsymbol{\alpha}_i \times \mathbf{A}_i \mathbf{B}_i) + \mathbf{u}_i \cdot (\boldsymbol{\Omega}_i \times (\boldsymbol{\Omega}_i \times \mathbf{A}_i \mathbf{B}_i)) + \\ & + \mathbf{u}_i \cdot (\boldsymbol{\alpha}_p \times \mathbf{A}_i \mathbf{P}) + \mathbf{u}_i \cdot (\boldsymbol{\Omega}_p \times (\boldsymbol{\Omega}_p \times \mathbf{A}_i \mathbf{P})) \end{aligned} \quad (6.56)$$

We rewrite Eq. (6.56) and we get Eq. (6.57).

$$\begin{aligned} \mathbf{u}_i \cdot \mathbf{a}_p = & \mathbf{u}_i \cdot \ddot{\rho}_i \mathbf{k} + \mathbf{B}_i \mathbf{A}_i \times (\mathbf{u}_i \cdot \boldsymbol{\alpha}_i) + \mathbf{u}_i \cdot (\boldsymbol{\Omega}_i \cdot (\boldsymbol{\Omega}_i \cdot \mathbf{A}_i \mathbf{B}_i)) - \\ & - \mathbf{A}_i \mathbf{B}_i \cdot (\boldsymbol{\Omega}_i \cdot \boldsymbol{\Omega}_i) + \boldsymbol{\alpha}_p \cdot (\mathbf{A}_i \mathbf{P} \times \mathbf{u}_i) + \mathbf{u}_i \cdot (\boldsymbol{\Omega}_p \times (\boldsymbol{\Omega}_p \times \mathbf{A}_i \mathbf{P})) \end{aligned} \quad (6.57)$$

Since \mathbf{u}_i and \mathbf{k} are perpendicular, $\mathbf{u}_i \cdot \mathbf{k} = 0$. Also, since $\boldsymbol{\Omega}_i$ and $\mathbf{A}_i \mathbf{B}_i$ are perpendicular, $\boldsymbol{\Omega}_i \cdot \mathbf{A}_i \mathbf{B}_i = 0$. \mathbf{u}_i and $\boldsymbol{\alpha}_i$ are collinear, $\mathbf{u}_i \times \boldsymbol{\alpha}_i = 0$. Besides, \mathbf{u}_i and $\mathbf{A}_i \mathbf{B}_i$ are perpendicular, so $\mathbf{u}_i \cdot \mathbf{A}_i \mathbf{B}_i = 0$. We get Eq. (6.58), also expressed as Eq. (6.59).

$$\mathbf{u}_i \cdot \mathbf{a}_p = \boldsymbol{\alpha}_p \cdot (\mathbf{A}_i \mathbf{P} \times \mathbf{u}_i) + \mathbf{u}_i \cdot (\boldsymbol{\Omega}_p \times (\boldsymbol{\Omega}_p \times \mathbf{A}_i \mathbf{P})) \quad (6.58)$$

$$\mathbf{u}_i \cdot \mathbf{a}_p + \boldsymbol{\alpha}_p \cdot (\mathbf{P} \mathbf{A}_i \times \mathbf{u}_i) = \mathbf{u}_i \cdot (\boldsymbol{\Omega}_p \times (\boldsymbol{\Omega}_p \times \mathbf{A}_i \mathbf{P})) \quad (6.59)$$

We multiply Eq. (6.55) by the unit vector \mathbf{s}_i and get Eq. (6.60).

$$\begin{aligned} \mathbf{s}_i \cdot \mathbf{a}_p = & \mathbf{s}_i \cdot \ddot{\rho}_i \mathbf{k} + \mathbf{s}_i \cdot (\boldsymbol{\alpha}_i \times \mathbf{A}_i \mathbf{B}_i) + \mathbf{s}_i \cdot (\boldsymbol{\Omega}_i \times (\boldsymbol{\Omega}_i \times \mathbf{A}_i \mathbf{B}_i)) + \\ & + \mathbf{s}_i \cdot (\boldsymbol{\alpha}_p \times \mathbf{A}_i \mathbf{P}) + \mathbf{s}_i \cdot (\boldsymbol{\Omega}_p \times (\boldsymbol{\Omega}_p \times (\mathbf{A}_i \mathbf{P}))) \end{aligned} \quad (6.60)$$

By rewriting Eq. (6.60) we obtain Eq. (6.61).

$$\begin{aligned} \mathbf{s}_i \cdot \mathbf{a}_p = & \mathbf{s}_i \cdot \ddot{\rho}_i \mathbf{k} + \boldsymbol{\alpha}_i \cdot (\mathbf{B}_i \mathbf{A}_i \times \mathbf{s}_i) + \mathbf{s}_i \cdot (\boldsymbol{\Omega}_i \cdot (\boldsymbol{\Omega}_i \cdot \mathbf{A}_i \mathbf{B}_i)) - \\ & - (\mathbf{A}_i \mathbf{B}_i \cdot (\boldsymbol{\Omega}_i \cdot \boldsymbol{\Omega}_i)) + \boldsymbol{\alpha}_p \cdot (\mathbf{A}_i \mathbf{P} \times \mathbf{s}_i) + \mathbf{s}_i \cdot (\boldsymbol{\Omega}_p \times (\boldsymbol{\Omega}_p \times \mathbf{A}_i \mathbf{P})) \end{aligned} \quad (6.61)$$

Since $\mathbf{B}_i \mathbf{A}_i$ and \mathbf{s}_i are collinear, $\mathbf{B}_i \mathbf{A}_i \times \mathbf{s}_i = 0$, and $\boldsymbol{\Omega}_i$ and $\mathbf{A}_i \mathbf{B}_i$ are perpendicular, $\boldsymbol{\Omega}_i \cdot \mathbf{A}_i \mathbf{B}_i = 0$, we can write Eq. (6.61) as Eq. (6.62).

$$\begin{aligned} \mathbf{s}_i \cdot \mathbf{a}_p + \boldsymbol{\alpha}_p \cdot (\mathbf{P} \mathbf{A}_i \times \mathbf{s}_i) = & \ddot{\rho}_i \cdot \mathbf{s}_i \mathbf{k} + \mathbf{s}_i \cdot (\boldsymbol{\Omega}_p \times (\boldsymbol{\Omega}_p \times \mathbf{A}_i \mathbf{P})) - \\ & - \mathbf{A}_i \mathbf{B}_i \cdot |\boldsymbol{\Omega}_i|^2 \end{aligned} \quad (6.62)$$

Finally, we simplify Eq. (6.62) and get Eq. (6.63).

$$\begin{aligned} \mathbf{s}_i \cdot \mathbf{a}_p + \boldsymbol{\alpha}_p \cdot (\mathbf{P} \mathbf{A}_i \times \mathbf{s}_i) = & \ddot{\rho}_i \cdot \mathbf{s}_i \mathbf{k} + \mathbf{s}_i \cdot (\boldsymbol{\Omega}_p \times (\mathbf{P} \mathbf{A}_i \times \boldsymbol{\Omega}_p)) - \\ & - \mathbf{A}_i \mathbf{B}_i \cdot |\boldsymbol{\Omega}_i|^2 \end{aligned} \quad (6.63)$$

We express Eq. (6.59) and Eq. (6.62) in matrix notation and get Eq. (6.64). We can also write it in compact way, as shown in Eq. (6.65).

$$\begin{aligned}
& \begin{bmatrix} (\mathbf{s}_1^T & (\mathbf{PA}_1 \times \mathbf{s}_1))^T \\ (\mathbf{s}_2^T & (\mathbf{PA}_2 \times \mathbf{s}_2))^T \\ (\mathbf{s}_3^T & (\mathbf{PA}_3 \times \mathbf{s}_3))^T \\ (\mathbf{u}_1^T & (\mathbf{PA}_1 \times \mathbf{u}_1))^T \\ (\mathbf{u}_2^T & (\mathbf{PA}_2 \times \mathbf{u}_2))^T \\ (\mathbf{u}_3^T & (\mathbf{PA}_3 \times \mathbf{u}_3))^T \end{bmatrix} \cdot \begin{bmatrix} \mathbf{a}_p \\ \boldsymbol{\alpha}_p \end{bmatrix} = \begin{bmatrix} \mathbf{s}_1 \mathbf{k} & 0 & 0 \\ 0 & \mathbf{s}_2 \mathbf{k} & 0 \\ 0 & 0 & \mathbf{s}_3 \mathbf{k} \\ 0 & 0 & 0 \\ 0 & 0 & 0 \\ 0 & 0 & 0 \end{bmatrix} \cdot \begin{bmatrix} \ddot{\rho}_1 \\ \ddot{\rho}_2 \\ \ddot{\rho}_3 \end{bmatrix} + \\
& + \begin{bmatrix} \mathbf{s}_1 \cdot (\boldsymbol{\Omega}_p \times (\mathbf{PA}_1 \times \boldsymbol{\Omega}_p) - \mathbf{A}_1 \mathbf{B}_1 \cdot |\boldsymbol{\Omega}_1|^2) \\ \mathbf{s}_2 \cdot (\boldsymbol{\Omega}_p \times (\mathbf{PA}_2 \times \boldsymbol{\Omega}_p) - \mathbf{A}_2 \mathbf{B}_2 \cdot |\boldsymbol{\Omega}_2|^2) \\ \mathbf{s}_3 \cdot (\boldsymbol{\Omega}_p \times (\mathbf{PA}_3 \times \boldsymbol{\Omega}_p) - \mathbf{A}_3 \mathbf{B}_3 \cdot |\boldsymbol{\Omega}_3|^2) \\ \mathbf{u}_1 \cdot (\boldsymbol{\Omega}_p \times (\boldsymbol{\Omega}_p \times \mathbf{A}_1 \mathbf{P})) \\ \mathbf{u}_2 \cdot (\boldsymbol{\Omega}_p \times (\boldsymbol{\Omega}_p \times \mathbf{A}_2 \mathbf{P})) \\ \mathbf{u}_3 \cdot (\boldsymbol{\Omega}_p \times (\boldsymbol{\Omega}_p \times \mathbf{A}_3 \mathbf{P})) \end{bmatrix} \quad (6.64)
\end{aligned}$$

$$\mathbf{H}_x \cdot \begin{bmatrix} \mathbf{a}_p \\ \boldsymbol{\alpha}_p \end{bmatrix} = \mathbf{H}_q \cdot \ddot{\boldsymbol{\rho}} + \text{Ind} \quad (6.65)$$

Singularities

7.1. Singularities

Singular configurations are those for which the rank of the Jacobian matrices involved become deficient. These configurations are undesirable because the degrees of freedom of the system change instantaneously and makes the system uncontrollable.

Gosselin and Angeles [130] analysed the singularities of closed-loop kinematic chains and classified them in three main groups – type I, type II and type III – by taking the properties of the Jacobian matrices of the chain into account. We describe the three groups below. In order to do it, we write the general expression of the velocity of a parallel manipulator as Eq. (7.1), where \mathbf{A} is the Jacobian matrix of the direct problem, $\dot{\mathbf{x}}$ is the vector with the outputs of the system, \mathbf{B} is the Jacobian matrix of the inverse problem and $\dot{\boldsymbol{\theta}}$ is the vector that contains the corresponding inputs.

$$\mathbf{A} \cdot \dot{\mathbf{x}} + \mathbf{B} \cdot \dot{\boldsymbol{\theta}} = 0 \quad (7.1)$$

- **Singularities type I**

The first kind of singularity appears when Eq. (7.2) is verified.

$$|\mathbf{B}| = 0 \quad (7.2)$$

This type of singularity corresponds to a configuration where the end-effector reaches a boundary of the workspace. The boundary can be either the external boundary of the workspace or an internal boundary limiting different subregions of the workspace where the number of branches of the inverse kinematic problem is not the same. Another way of defining these types of singularities is to say that they are a set of points where different branches of the inverse kinematic problem meet. Typically, the velocities in these configurations are orthogonal to the boundary and towards the outside of the workspace. We say that the output link loses at least one degree of freedom, which means that the output link can resist forces and moments without exerting any torque or force at the powered joints. In mechanisms, in these configurations the output link is in a deadpoint.

- **Singularities type II**

The second kind of singularity occurs when Eq. (7.3) is fulfilled.

$$|\mathbf{A}| = 0 \quad (7.3)$$

This condition leads to a configuration where the end-effector is movable even when all the actuated joints are locked. This kind of singularity corresponds to a point or set of points where different branches of the direct kinematic problem meet. In this case, the output link gains one or more degrees of freedom – the output can not resist one or more forces or moments even when the actuators are locked. In mechanisms we say that the input link is in a deadpoint.

■ Singularities type III

The third kind of singularity requires that both first and second conditions are fulfilled at the same time, as Eq. (7.4) shows.

$$|\mathbf{B}| = 0 \quad \& \quad |\mathbf{A}| = 0 \quad (7.4)$$

If a mechanism reaches a position with this kind of singularity, the end-effector can suffer finite motions when the actuators are locked or there can be a finite movement in the inputs for no motion in the outputs.

As Chablat and Wenger [131] described, the set of points of workspace for which the sign of the determinant of the Jacobian matrix \mathbf{B} does not change defines a *working mode*. Similarly, the set of postures for which the determinant of the Jacobian matrix \mathbf{A} does not change define a *assembling mode*.

Even if this classification is the most used one, it only studies the input and output terms, without taking into account the passive velocity terms. Because of that, there are some other kind of singularities that are not considered in this classification. Taking this into account, some other authors have presented more general classifications for singular positions of parallel mechanisms. Zlatanov et al. [132], for example, divided the singularities in the six types that we describe below:

- (i)-(ii) **Redundant input (RI)/output (RO)**: when a non-zero input/output is possible with zero input/output.
- (iii-iv) **Impossible input (II)/output (IO)**: a certain input/output is not feasible for any output/input.
- (v) **Redundant passive motion (RPM)**: a non-zero instantaneous motion is possible with both the input and the output being equal to zero.

- (vi) **Increased instantaneous mobility (IIM)**: the transitory or instantaneous mobility is higher than the full cycle mobility of the kinematic chain.

They explained how there is an interdependence of singularity types. Table 7.1 shows the singularity type combinations that are possible. They labelled each possible combination as a *singularities class*. According to that, the singularity set of any mechanism can be divided into up to 21 classes. They analysed the singularities of a general mechanism exhaustively in order to obtain not only the singularity set as a whole, but also its partition into classes. The class of a singularity is important because it tells us how the instantaneous-kinematics properties of the mechanism degenerate at the singularity.

Table 7.1: Singularity classes presented by Zlatanov et al.

	IO	II	IIM	IO <i>and</i> II	IO <i>and</i> IIM	II <i>and</i> IIM	IO <i>and</i> II <i>and</i> IIM
RI	x						
RO		x					
RPM			x				
RI <i>and</i> RO			x	x	x	x	x
RI <i>and</i> RPM				x	x		x
RO <i>and</i> RPM				x		x	x
RI <i>and</i> RO <i>and</i> RPM			x	x	x	x	x

Notash [133] classified special configurations of parallel manipulators in degeneracies related to the branches and uncertainty configurations of the parallel architecture. In a branch degeneracy, the parallel manipulator can not provide a required end-effector motion, while in a uncertainty configuration the parallel manipulator can not resist/apply a required end-effector force or torque. Close to degenerate configurations the manipulator has very poor motion performance. Similarly, near uncertainty configurations the force transmission performance of the manipulator is very poor. Notash studied the uncertainty configurations of three-branch parallel manipulators with spherical branch-end joints by using screw theory. He analysed the possible uncertainty cases and presented the characteristics of the unconstrained instantaneous DOFs that correspond to each uncertainty case. Finally, he proposed joint actuation layouts to eliminate the uncertainty and gave examples of application.

López et al. [134] applied the classification presented by Gosselin and Angeles [130] in order to identify the singularities of the Delta robot. They set the determinant of the inverse and direct Jacobian matrices to zero and obtained several undesirable postures of the manipulator. They show that the singularities related to the inverse Jacobian matrix appear when the limbs belonging to the same kinematic chain lie in a plane. Two of those configurations are when the robot is completely extended or contracted – they indicate the boundaries of the workspace. Apart from obtaining the singularities of the inverse and direct Jacobian matrices, they introduced the idea of intermediate Jacobian matrices. Intermediate Jacobian matrices are simpler to evaluate but still contain the information of traditional Jacobian matrices. Moreover, we can also use the information they give to find structural singularities.

In order to detect and analyse the singular positions, symbolic computation is practical for some specific parallel manipulators and algebraic methods are quite limited, as Altuzarra et al. [135] noted. Some authors, for example Kumar [136], proposed methods based on the degeneracy of the screws. These methods are similar to the lie geometry, that Merlet [14] used

in his study of parallel manipulators. Park and Kim [137] presented another alternative by using Riemannian geometric formulation to characterize a singularity as a dimensional change in manipulability.

Altuzarra et al. [135] presented a general procedure to get an automated analysis of the singularities of any mechanism for a given configuration. It uses a base of the motion space, which they obtained from a velocity equation characterized by a geometric matrix. By using this procedure, we can obtain the degree of freedom that corresponds to each singularity, uncontrolled motion and kinematic dependencies. This procedure is a help to design singularity-free path planning and also to choose the actuators and the necessary redundant devices. The approach used is independent of the choice of inputs and outputs, so the procedure is valid for open, closed or hybrid kinematic chains and redundant or non-redundant manipulators. Altuzarra et al. [135] analysed the different types of singularities for the manipulator in a given configuration by using a method based in vectors that form a basis of the null-subspace of the geometric matrix. However, they used a numerical method to detect the singular positions.

Rezaei et al. [102] obtained the non-pure rotational and non-pure translational Jacobian matrices of the 3-PSP parallel manipulator to relate the angular and translational velocities of the moving platform with the actuated joints. They analysed the three conventional singularities and saw that the 3-PSP robot is free of conventional singularities. nevertheless, they found constraint singularities by analysing the Jacobian of constraint. The constraint singularities appear when the lengths of all three linear rods are equal.

Nigatu et al. [138] proposed a new methodology of formulating Jacobian matrix for limited degrees of freedom parallel mechanisms. They formulated the Jacobian matrix in a simple and integrated form by using screw mathematics. The resulting 6x6 Jacobian matrix provides clear information about the architecture and singularities of the manipulator. As example, they applied the method to the 3PRS parallel manipulator.

7.2. Obtaining the singularities of the 2PRU-1PRS parallel manipulator

In this Section, we present the general analysis of conventional singularities for a given position of the 2PRU-1PRS parallel manipulator. As we saw in Chapter 6, for the 2PRU-1PRS parallel manipulator, the expression that Gosselin and Angeles [130] used to analyse the three types of conventional singularities – $\mathbf{A} \cdot \dot{\mathbf{x}} + \mathbf{B} \cdot \dot{\boldsymbol{\theta}} = 0$ – is given by Eq. (7.5)

$$\mathbf{J}_x \cdot \begin{bmatrix} \mathbf{v}_p \\ \dot{\boldsymbol{\Omega}}_p \end{bmatrix} = \mathbf{J}_q \cdot \dot{\boldsymbol{\rho}}_i \quad (7.5)$$

where \mathbf{J}_x is Jacobian matrix of the direct problem, \mathbf{J}_q is the Jacobian matrix of the inverse problem, $[\mathbf{v}_p \ \dot{\boldsymbol{\Omega}}_p]^T$ is the vector containing the output velocities and $\dot{\boldsymbol{\rho}}_i$ is the vector of the input velocities.

7.2.1. IKP Singularities

When the determinant of \mathbf{J}_q is zero, the manipulator is in a singularity of the inverse kinematic problem, or a singularity of type I, as Eq. (7.6) shows.

$$|\mathbf{J}_q| = 0 \longrightarrow \text{Singularity of the IKP (type I)} \quad (7.6)$$

The expression of \mathbf{J}_q for the 2PRU-1PRS PM is given by Eq. (7.7).

$$\mathbf{J}_q = \begin{bmatrix} \mathbf{s}_1 \mathbf{k} & 0 & 0 \\ 0 & \mathbf{s}_2 \mathbf{k} & 0 \\ 0 & 0 & \mathbf{s}_3 \mathbf{k} \\ 0 & 0 & 0 \\ 0 & 0 & 0 \\ 0 & 0 & 0 \end{bmatrix} \quad (7.7)$$

The singularities of the IKP correspond to the boundaries of the workspace. This is to say, the IKP singularities appear when the limbs of the

manipulator reach their limits. In these positions, the end-effector of the manipulator is stuck and can not achieve the desired DOF.

7.2.2. DKP Singularities

Singularities of the DKP – or type II – appear when the determinant of the Jacobian matrix \mathbf{J}_x is zero, as Eq. (7.8) shows.

$$|\mathbf{J}_x| = 0 \longrightarrow \text{Singularity of the DKP} \quad (\text{type II}) \quad (7.8)$$

Equation (7.9) gives the expression of \mathbf{J}_x for the 2PRU-1PRS parallel manipulator.

$$\mathbf{J}_x = \begin{bmatrix} \mathbf{s}_1^T & (\mathbf{PA}_1 \times \mathbf{s}_1)^T \\ \mathbf{s}_2^T & (\mathbf{PA}_2 \times \mathbf{s}_2)^T \\ \mathbf{s}_3^T & (\mathbf{PA}_3 \times \mathbf{s}_3)^T \\ \mathbf{u}_1^T & (\mathbf{PA}_1 \times \mathbf{u}_1)^T \\ \mathbf{u}_2^T & (\mathbf{PA}_2 \times \mathbf{u}_2)^T \\ \mathbf{u}_3^T & (\mathbf{PA}_3 \times \mathbf{u}_3)^T \end{bmatrix} \quad (7.9)$$

In the singular positions of the DKP the end-effector of the manipulator is able to move infinitesimally without changing the value of the inputs. This is to say: some degrees of freedom become uncontrollable.

7.2.3. Manipulability

Articular forces can become very large near singular configurations. Thus, it is interesting to know how far from a singular position the manipulator is. In order to have an index that measures the nearness to a singularity, Yoshikawa [139] introduced the concept of *manipulability*.

The manipulability is the absolute value of the determinant of the inverse Jacobian. A small manipulability means that the articular forces may become very large for some applied external forces or torques.

Workspaces and Joint Space

8.1. Workspaces

The workspace (WS) represents the poses that the end-effector of the manipulator can reach. The representation of the possible translations of the end-effector of a parallel manipulator is easy. However, a complete representation of the workspace is not possible when the manipulator has 6-DOF. In that case the only possibility is to represent subsets of the workspace. Taking this into account, Merlet [14] defined different types of workspace. In order to do it, he labelled a specific point C of the end-effector as *reference point*. The coordinates and orientation of that reference point define the pose of the robot. We describe the different types of workspaces below:

- **Constant orientation workspace** or **translation workspace**: set of locations that the reference point can reach for given orientation.
- **Orientation workspace**: set of possible rotations around the reference point.
- **Maximal workspace** or **reachable workspace**: locations that the reference point can reach for at least one orientation of the mobile platform.

- **Inclusive orientation workspace:** locations that the reference point can reach for at least one orientation among a set defined by ranges on orientation parameters.
- **Total orientation workspace:** set of locations that the reference point can reach for all the orientations of a set defined by ranges on the orientation parameters.
- **Dextrous workspace:** set of locations of the reference point for which all orientations are possible.

Parallel manipulators have, compared to serial manipulators, higher stiffness and accuracy but smaller workspace. Thus, the workspace is considered one of the most important design factors of parallel manipulators. It is thus essential to have an efficient calculation method to determine it, as Corral et al. [140] and Altuzarra et al. [141] highlighted. There are three factors that can restrict the motion of a parallel manipulator – the mechanical limits on the passive joints, the interferences between links and the limits of the actuators. The method chosen to get the WS has to take all these factors into account. There are different methods to obtain the WS of a parallel manipulator – analytical methods, discretization methods or geometric methods.

Analytical methods.

Analytical methods are based on the fact that when a point is on the border of the workspace the velocity of the manipulator along the normal to the border is equal to zero. This method needs to calculate the Jacobian matrix of the manipulator, whose closed-form is not known. Besides, this method is not convenient to take into account either the constraint of link interfaces or the mechanical limits on the passive joints. Thus, most of these methods are very dependent on the architecture of the manipulator, so they are only useful for specific manipulators.

Agrawal [142] determined the configurations of pin-parallel systems for which the component of the velocity of the reference point along the outward normal to the boundary is null. He analysed parallel systems by basing on the properties of serial chains as derived from the theory of screw systems. He gave the condition of boundary existence in terms of conditions on a special screw system associated with the end-effector.

Di Gregorio and Zanforlin [143] analysed the workspace boundaries in two different translational parallel manipulators – the DELTA robot and the 3-RUU. They obtained a fourth degree polynomial equation that expressed analytically the surfaces bounding their workspace. They showed the use of the analytic expression of the boundaries – that had an explicit form – by applying it to a particular example.

Bonev at Gosselin [144] presented a methodology to obtain analytically and represent the workspace boundaries of symmetrical spherical parallel manipulators. They derived compact expressions for the workspace boundaries of a 3-DOF symmetrical spherical parallel manipulator. They proposed and implemented a fast numerical method for representing the constant-torsion workspace. Besides, they gave many examples of the constant-torsion workspace and the whole orientation workspace for the 3-RRR parallel manipulator.

Geometrical methods.

Geometrical methods compute the WS of each limb separately and then calculate the intersection of all single-limb-workspaces to get the workspace of the manipulator. The main disadvantages are that these methods are only useful for 3-DOF robots. Besides they usually need another geometric tool, such as CAD.

Merlet [145] presented an exact and fast geometrical method to calculate the workspace of parallel manipulators with constant orientation. This method took all the constraints of the manipulator into account and could

obtain the area and volume of the workspace easily.

Merlet [146] also presented an algorithm to compute and represent two of the three possible rotations of the end-effector around a fixed point. Since the method was purely geometrical, it implied few calculations and, thus, lead to a very fast and efficient algorithm.

Liu et al. [147] determined the workspace of the DELTA robot geometrically. They demonstrated the results by using AutoCAD. They also related the workspace volume with the link lengths and obtained atlases of the workspace. They presented the workspace shape for robots with different dimensions. This method represented an interesting tool for the computer aided design of robotic mechanisms.

Liu et al. kept working on the workspace of the DELTA robot and in [148] they proposed a new geometrical approach to obtain the workspace of the Delta robot. They introduced the concept of *maximum inscribed workspace* and defined it as the set of all maximum inscribed circles in the workspace section of a DELTA robot. Their design could detect voids inside the workspace by checking some simple relations between geometric parameters. They applied the method to obtain the workspace of a DELTA robot and to design a DELTA robot with a desired workspace. However, this method, which is simple and effective, is also valid for other parallel manipulators with linear actuators whose reachable workspace can be obtained geometrically.

Discretization methods.

Discretization methods create a mesh of possible poses of the end-effector. Each pose has to be checked to see if they belong to the useful WS, usually solving the inverse kinematic problem (IKP). This method has different advantages, such as the simple computational implementation and the ability to implement all kinds of constraints. But it also has the disadvantages of high computational cost and accuracy dependence on step

size of the mesh. In order to deal with the high computational cost, many authors have proposed different methods that combine discretization and geometrical methods. They first apply the geometrical restrictions in order to obtain a preliminary boundary of the workspace. Then, they study each point of the preliminary workspace in order to check that all constraints are fulfilled.

Merlet [149] determined the constant orientation workspace, the total orientation workspace and the inclusive orientation workspace of a 6-DOF Gough-type parallel manipulator. He compared the workspace volumes of four different robot geometries and saw that for robots with similar dimensions the joints layout has a big influence on the workspace volume. The method is applicable to other kinds of parallel manipulators.

Andrioaia et al. [150] analysed the workspace of a DELTA robot by applying a combined geometrical and discretization method. They first defined the limits of the workspace in X-, Y- and Z-axes. These limits gave a cube which they discretized in finite number of points. Then they checked, one by one, if those points fulfilled the requirements of the geometrical parameters. They applied the method for a case study and obtained the results by programming the method in MATLAB.

Herrero et al. [151] obtained the workspace of the reconfigurable parallel manipulator PARAGRIP by combining geometrical and discretization methods. They obtained the useful workspace of the manipulator – the workspace free of singularities and limb collisions, and where the limits of the joints were fulfilled – for different configurations of the manipulator. They also obtained the biggest sphere in the useful workspace in order to study its regularity.

8.2. Obtaining the workspace of the 2PRU-1PRS parallel manipulator

In this work, we present a discretization method to obtain the useful WS of the 2PRU-1PRS parallel manipulator for given geometry parameters (GP) and input ranges. In our case, since the outputs are two rotations and one translation, we define the workspace by giving the combinations of rotations about X- and Y-axes and translation along Z-axis that the end-effector can achieve. This method is also useful for any kind of parallel manipulator whose constraints are known.

We define the set *StudyPoints* as the candidate-poses for the workspace. There are, mainly, two ways to provide the candidate-poses for the workspace. The first one is based on the propagation of a wave front, as Macho et al. [152] explained, while the second one requires setting the range for the outputs and their discretization step. This study uses the latter.

We construct the set the *StudyPoints* by dividing the axes into equal number of parts. Thus, in this case, *StudyPoints* is the set of points which lie in the 3 dimensional space bounded by the ranges previously defined. We also define the geometry parameters and the physical restrictions given by the ranges of the linear guides and the spherical joint.

We solve the Inverse Kinematic Problem for all the candidate-poses for the WS and obtain the value of displacements for the linear guides. The candidate-poses for the WS whose linear guide values are real define the WS_0 , as see in Eq. (8.1). If any of the actuators' value is imaginary, it means that the manipulator cannot reach that position and, thus, the candidate-pose studied can not be in the WS.

$$\text{if } \rho_i \in \Re \longrightarrow \text{candidate - pose}_i \in WS_0 \quad (8.1)$$

Additionally, we have to check which points of the WS_0 fulfil the restrictions of the direct kinematic problem, the spherical joint and the linear

guides. The set of candidate-poses that fulfil all those restrictions defines the useful workspace. The flowchart given in Fig. 8.1 summarizes the steps we will follow to get the useful WS of the manipulator.

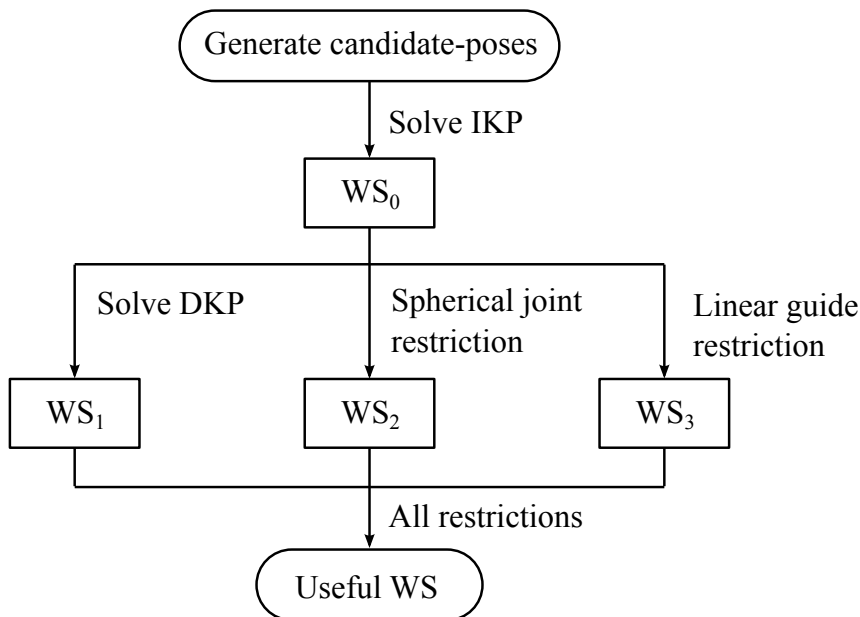


Figure 8.1: Flowchart for obtaining the useful WS

8.2.1. IKP Singularities

When a manipulator is in a singularity of the inverse kinematic problem, the end-effector is stuck and it can not move in the direction of the 3DOF. Thus, in order to have a correct manipulator functioning, we have to avoid those positions. In practice, these singularities appear on the boundary of the WS_0 .

8.2.2. DKP Singularities

When the manipulator reaches a singularity of the direct kinematics problem, it is able to move in an infinitesimally without changing the value of the inputs. This is to say: some degrees of freedom become uncontrollable. As we have already seen in Chapter 7, mathematically, this happens when the determinant of the Jacobian matrix, $|\mathbf{J}_x|$, is null. According to that, the $|\mathbf{J}_x|$ of all the points of a free-singularity region have the same sign, as Gosselin and Angeles [130] and Altuzarra et al. [135] explained. Thus, to get the singularity free WS, we calculate the $|\mathbf{J}_x|$ for the points in the WS_0 . We divide the WS into two parts depending on the sign of $|\mathbf{J}_x|$, as seen in Fig. 8.2. That division is expressed by Eq. (8.2).

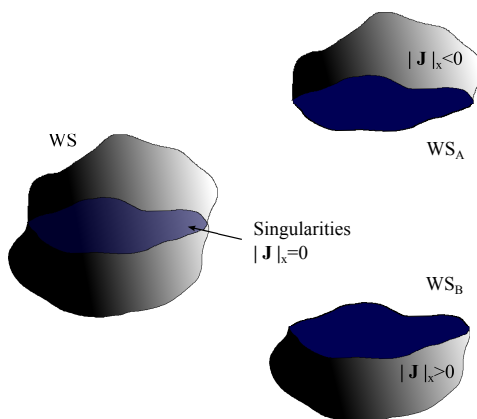


Figure 8.2: Division of the WS based on polarity of $|\mathbf{J}_x|$

$$\begin{aligned}
 0 < |\mathbf{J}_x| &\longrightarrow WS_A \\
 |\mathbf{J}_x| = 0 &\longrightarrow \text{singularity}
 \end{aligned}
 \tag{8.2}$$

$$|\mathbf{J}_x| < 0 \longrightarrow WS_B
 \tag{8.3}$$

WS_A is the part of the WS with positive $|\mathbf{J}_x|$ while WS_B is the part of the WS with negative $|\mathbf{J}_x|$. For a given trajectory of the manipulator,

we define the initial position of the MP as MPP_0 with its corresponding value of $|\mathbf{J}_x|$, $|\mathbf{J}_x|_0$. For a singularity-free WS, $|\mathbf{J}_x|$ of all points of the WS must have the same sign, as Macho et al. [152] and Haidong et al. [153] highlighted. According to this criterion, Eq. (8.4) defines the WS free of singularities, denoted by WS_1 .

$$\begin{aligned} \text{if } \quad & \text{sign } |\mathbf{J}_x|_{WS_A} = \text{sign } |\mathbf{J}_x|_0 \longrightarrow WS_A \equiv WS_1 \\ \text{if } \quad & \text{sign } |\mathbf{J}_x|_{WS_B} = \text{sign } |\mathbf{J}_x|_0 \longrightarrow WS_B \equiv WS_1 \end{aligned} \quad (8.4)$$

8.2.3. Spherical Joint Restrictions

The range of the spherical joint is a very restricted variable. Ideally it can rotate freely, but in practice it has limits that we have to take into account. Figure 8.3 shows the angle between the i limb and the neutral position of the spherical joint, defined as μ_i .

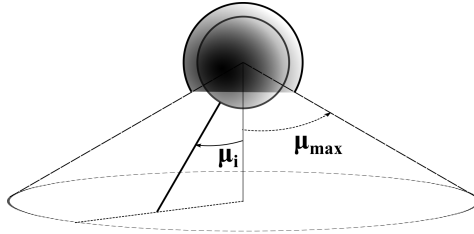


Figure 8.3: Sphere Joint

Equation (8.5) gives the condition that μ_i has to fulfil – it has to be always in the range of the spherical joint rotation. The set of *StudyPoints* of the WS_0 that fulfil the restriction of the spherical joint define the WS_2 workspace.

$$|\mu_i| < \mu_{max} \quad (8.5)$$

8.2.4. Linear Guides Restrictions

We obtain the values of the linear guides for all the points in the WS_0 by solving the IKP . We have already checked that they are real solutions, but we also have to check if those values fulfil the limits of the real linear guides, as seen in Eq. (8.6). The set of *StudyPoints* of the WS_0 that fulfil this restriction define the WS_3 workspace.

$$\rho_{i_{min}} < \rho_i < \rho_{i_{max}} \quad (8.6)$$

8.2.5. Useful Workspace

We define the useful workspace, WS_{use} , as the set of points that fulfil all the previous conditions. Thus, the WS_{use} is expressed by Eq. (8.7).

$$WS_{use} = WS_1 \cap WS_2 \cap WS_3 \quad (8.7)$$

8.2.6. Biggest Geometric Object in the Useful Workspace

Since WS of one PM configuration can be bigger than of another but also be more irregular, an interesting criterion to know if a WS is good enough or not is to compare both the size and the regularity of the WS_{use} . An easy way to know the regularity of a WS is to obtain the biggest geometric object in it, GO.

8.3. Joint Space

When we solve the inverse kinematic problem we obtain the set of inputs, (ρ_1, ρ_2, ρ_3) associated with the useful workspace. This set of inputs is the Joint Space and it gives us information about the value of the linear guides for each pose of the WS_{use}

9

Stiffness

9.1. Stiffness

Stiffness, k , is the resistance of an elastic body to deflection or deformation by an applied force. Equation (9.1) gives the expression of the stiffness

$$k = F/\delta \quad [N/m] \quad (9.1)$$

where F is the applied force in one direction and δ the deformation in the same direction. According to this, the higher the stiffness of a body is, the smaller is the deformation for a given force.

As we have already seen, one advantage of parallel manipulators over serial manipulators is their higher stiffness. In Fig. 9.1 we see a schematic representation of the comparison between the stiffness in serial manipulators and parallel manipulators. In both Fig. 9.1a and Fig. 9.1b we have represented two kinematic chains by drawing several springs. The rigidity of the springs are K_1 and K_2 , respectively. In the first figure, the springs are linked serially. The equivalent stiffness of the system is given by Eq. (9.2). In the second figure the springs are parallel to each other, and both of them are connected to the fixed element. In this case, the equivalent stiffness is given by Eq. (9.3). As we see, the equivalent stiffness when the chains are

parallel is higher than the equivalent stiffness for the serial chains.

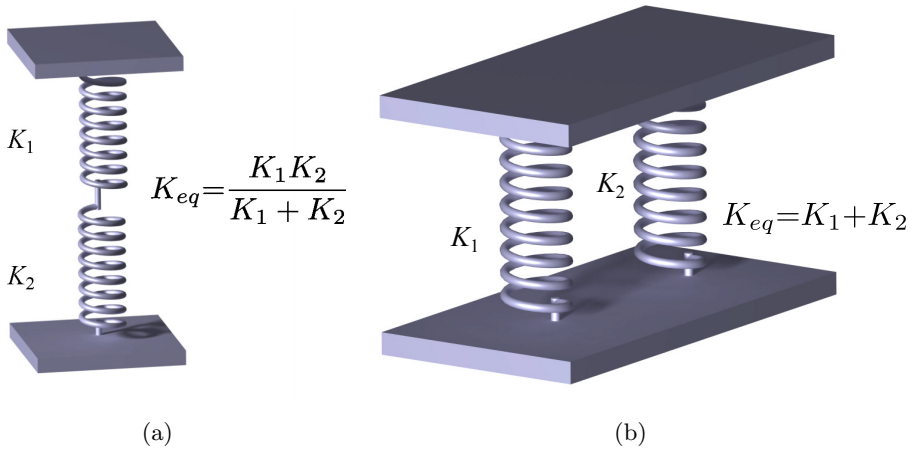


Figure 9.1: Equivalent stiffness for: (a) two serial chains; (b) two parallel chains

$$K_{eq} = K_1 \cdot K_2 / (K_1 + K_2) \quad (9.2)$$

$$K_{eq} = K_1 + K_2 \quad (9.3)$$

However, the architecture of the parallel manipulators is very complex, which makes obtaining their stiffness very complicated. Many researchers have worked to develop different methods to calculate the stiffness easily.

Finite Element analysis method (FEM)

The idea of the finite element method is to decompose the physical model of the manipulator in a finite number of elements. The elements are jointed to each other in common points called nodes. The stiffness matrices of the elements give the compliant relations between adjacent nodes. The finite elements have standard shape for which the stiffness matrix is known, as described by Avilés [154].

The global matrix of the model contains the static equilibrium equation for each node. This global matrix defines the relation between the applied forces and the node deflections. The stiffness in the desired direction is obtained by using the inverse of the stiffness matrix calculated.

This process is automated in the CAD-environment softwares. The meshing process is the one that decomposes the model into a finite number of elements. In commercial programs the meshing only needs the definition of the discretization step and the mesh type. The mesh type can be linear or parabolic. The results are both numerical and graphical, and they give the deformation and the stress in each node of the model. In this way, the user can immediately identify the areas where the stress is high and thus, identify the potential dangerous areas.

The biggest advantage of the FEM is its high accuracy, that only depends on the discretization step. Besides, the joints can be modelled with the real dimensions and shape, so it is a very useful method for manipulators. The disadvantages are, on one hand, the limit of computer memory. When the discretization step becomes smaller, the accuracy increases, but the problem of limited computer memory appears. On the other hand, the meshing is valid only for one position. Thus, if we want to obtain the stiffness for different points of the workspace, we have to repeat the meshing of the model in each position. Due to this need for remeshing, authors usually use FEM to validate the results obtained with other methods or have an estimation of the stiffness for certain positions and applied loads.

Bouzgarrou et al. [155] studied the stiffness of a new 3T1R parallel manipulator. The manipulator has four identical legs, that can fold an angle. They first analysed the influence of that folding angle in the stiffness of one leg and they saw that the stiffness was smaller for angles of 90° . Then, they used the FEM to design an experimental technique to calculate the stiffness of the whole manipulator all over the workspace.

Kozyrev et al. [156] analysed the stiffness of the Isoglide parallel manipulator. They chose the best shape for the section of the elements by comparing the stiffness results for two different shapes. They also calculated the stiffness of the whole manipulator in different positions for different types of loading. They saw that the stiffness for axial forces applied directly along the main axes was really mediocre. Based on these results, they proposed two solutions to improve the stiffness of the manipulator.

Matrix structural analysis method

Also known as *the displacement method* or *direct stiffness method*, this method is based on the ideas of the finite element method. It breaks up a complicated system into discrete structural elements. Those elements have simple elastic and dynamic properties that can be expressed in a matrix form. The elements connect to each other in the nodes. When there are applied loads on the mechanism each node suffers a translation and/or a rotation. Those displacements – translations and rotations – depend on the configuration of the mechanism and the boundary conditions. We can calculate all the nodal displacements from a complete analysis of the mechanism. We will describe the whole method with more details when applying it to the 2PRU-1PRS parallel manipulator in Section 9.2.

If we compare the elements that the matrix structural analysis method uses with the ones in FEM, the elements in the matrix structural method are larger, such as beams or arcs, as Martin [157] described. Thus, the computational cost is less than in FEM. The matrix structural method has a reasonable trade-off between accuracy and computational cost.

Traditionally, the matrix structural analysis method has been used to analyse structures, but in the last years different authors have applied it to calculate the stiffness of parallel manipulators. The great advantage of this method is that it is very systematic and that we can also apply it to hyper-static parallel manipulators.

Clinton et al. [158] developed a mathematical model to obtain the stiffness of a Stewart-platform-based milling machine. They estimated the system parameters by applying experimental stiffness measurements. Then, they applied the matrix structural analysis method to get the stiffness of the manipulator for different positions in the workspace. They made two assumptions for the application of the method. According to the first one, the elements were pin jointed at each end and unable to transmit moments from one element to the other. And according to the second, the deflection under load took place mainly on the legs of the machine, so they implemented a very high stiffness to the mobile platform. The results obtained by this method were found to be satisfactorily close to those obtained by the experimental method.

Deblaise et al. [159] proposed a different approach to calculate the stiffness matrix of parallel manipulators by using the same method. They applied the matrix structural analysis to a DELTA parallel structure. They assumed that the mobile platform was perfectly rigid. They developed two models – in the first one they took the joints as perfect, while in the second they also considered the stiffness of the joints. They validated the method by using experimental measurements and they saw that the second model is more realistic than the first one.

Gonçalves et al. [160] analysed the stiffness of the 6-RSS parallel manipulator. They simplified the problem by assuming the stiffness of joints and actuators to be negligible. In this way, they took the blocked actuators as boundary conditions and the rotational joints as fixed. They compared the results with the results obtained with FEM.

In the same line of work, Corral [161] studied the stiffness of two different parallel manipulators – the DAEDALUS I and the ARABA I, two prototypes developed in the University of the Basque Country. He applied the matrix structural analysis method to get the stiffness for different points in the workspace. He checked the results with FEM analysis, as well as with experimentation.

Virtual Joint modeling method

The methods based on virtual joint modeling treat the links of parallel manipulators as rigid and assume the joints to be compliant, all the existing flexibilities being accumulated only in the joints. This approximation is equivalent to adding virtual springs to the joints. In this way, these methods simplify the model by taking the stiffness matrix as lumped, which in reality is distributed.

Salisbury [162] presented the conventional formulations for the mapping of stiffness matrices between the cartesian and joint spaces. Gosselin [163] developed a tool based on this formulation to analyse the stiffness of parallel manipulators. A big limitation of this method is that he assumed that the only sources of flexibility were the actuator joints, the rest of the components being rigid. In order to take the flexibility of the links into account, Zhang [164] proposed a lumped model. In this model, the links are replaced by rigid beams mounted on revolute joints plus a torsional spring placed at the existing joints.

Later, Chen et al. [165] demonstrated that the conventional formulation is only valid when the manipulator is in unloaded equilibrium configuration. To overcome this problem, they proposed the Conservative Congruence Transformation (CCT), which is valid also when the manipulator is not in its unloaded equilibrium configuration. Chen et al. [166] and Alici et al. [167] developed the results to consider the external loads.

A key issue of these methods is how to define the virtual spring param-

ters. At the very beginning, Gosselin [168] or Pigoski et al. [169] presented each actuated joint as a single one-dimensional virtual spring. Afterwards, Majou et al. [170] took the flexibility of the links into account by increasing the number of virtual joints, including several translational and rotational virtual springs in each joint. In the latest works, Pashkevich et al. [171] and Klimchik et al. [172] have used 6-dimensional virtual joints. To identify them, they have applied a method based on FEM. This increases the accuracy of the Virtual Joint Modeling method, which is now comparable to the accuracy of the FEM, but with lower computational cost.

Razei et al. [173] presented two analytical methods to calculate the stiffness of a 3PSP parallel manipulator. The 3PSP manipulator analysed has two fixed platforms and one mobile platform joined by three identical limbs. The first method they presented applies the principle of virtual work to a lumped model of the manipulator. The biggest limitation of this method is that it considers the mobile platform as rigid. The second method considers the model as a distributed system. This method obtains the stiffness of the manipulator by taking the strain energy of the main components of the manipulator into account, as well as using Castigliano's theorem. This method considers the mobile platform to be flexible and takes the bending of all compliant modules into account. They compared the results obtained with the two methods with results obtained by using the FEM and checked that the second model was more realistic than the first one.

Klimchik et al. [174] presented a non-linear stiffness modeling technique that calculates the stiffness of parallel manipulators composed by perfect or non-perfect serial chains. When the manipulator has non-perfect chains, there is an inaccuracy in the geometry that produces internal forces. The authors took those internal forces into account. Besides the internal forces produced by the geometric inaccuracy, they considered another two kind of loads at the same time – an external force applied to the end-effector and external loadings applied to the intermediate points. This method is valid for both over-constrained and under-constrained parallel manipulators, with small or large deflections.

Experimental methods

Experimental measurements in the real model are really useful when validating the mathematical models of the stiffness of parallel manipulators. It happens often that it is not possible to work with the real model. In those cases, a common option is to work with experimental prototypes, which are usually scale or simplified models.

The experimental measurements must be as precise as possible. Otherwise, they will not be a correct reference to validate the mathematical models with. The basic equipment to measure the stiffness in parallel manipulators is a load application system and a displacement measurement system. The load application system can be a punctual load or a load cell, but in both cases the value of the applied load must be known. The displacement measurement system has to be any kind of system that gets the linear and angular displacement, such as calipers, inclinometers or laser measurement systems.

Clinton et al. [158] validated the system stiffness model by comparing the results of the model with the experimental measurements made on the NIST Ingersoll Octahedral-Hexapod. They used the procedure outlined in the ASME standard B5.54 [175]. They applied the load by using a force gauge and recorded the displacements thanks to digital dial indicators. They selected the measurement positions taking the machine symmetry into account. The authors saw that they could improve the experimental techniques to get further refinement in the results. However, they concluded that they were good enough to validate the stiffness model.

Aginaga et al [176] analysed the stiffness of the 6-RUS parallel manipulator by using inverse singularities and compared the results with experimental measurements on the prototype. Since it was not possible to measure the stiffness in the whole workspace, they chose specific configurations based on the analytical results. In analytical results they had seen that total inverse singularities were the positions with highest stiffness.

Thus, they chose to make the measurements on inverse singular and non-singular configurations to compare the stiffness difference between them. They applied the loads and measured the displacements as Company et al. [177] had already done – they applied the loads using a dynamometer and measured the displacements with dial indicators. Since a dynamometer can only apply forces and not torques, they could not apply a torque on the gravity center. To overcome this problem, they applied external loads on the vertices of the mobile platform. Similarly, dial indicators measure only linear displacements and not angular ones, so they measured the displacements of the vertices of the mobile platform. In order to prevent possible errors, they repeated each experimental measurement twice, as proposed by Ceccarelli et al. [178]. Another option could have been to preload the mechanism at the equilibrium position, as Pinto et al. [179] did.

We have seen the common methods in use to calculate stiffness. In the following Section will present the method we chose to use, along with the reasons for choosing that method.

9.2. Matrix structural analysis method

We use the matrix structural analysis method to obtain the stiffness of the manipulator in any pose in the workspace. This method involves discretizing the manipulator into a finite number of beam elements. These elements are connected to each other and to the fixed element by using different kinds of joints. The connection points are called nodes. The method estimates the components of the stiffness relations to solve the force or displacement problem expressed by Eq. (9.4),

$$\mathbf{F} = \mathbf{K} \cdot \mathbf{\Delta} \tag{9.4}$$

where \mathbf{F} is the force vector, \mathbf{K} is the stiffness matrix and $\mathbf{\Delta}$ is the displacement vector. The force vector contains the external forces and moments in each node, while the displacement vector contains the displacements and rotations that take place in the same node. Thus, the stiffness matrix expresses a relation between the displacement of the nodes and the external

forces applied. The most important characteristics of the stiffness matrix are that it is a square, symmetric and strictly positive definite matrix.

We get the stiffness matrix of the whole model by assembling the stiffness matrices of all elements, taking into account the nodes that different elements share, and also the kinematic restrictions among the elements. Once we have obtained the stiffness matrix, we calculate the stiffness of the manipulator in one direction for given force. The flow chart seen in Fig. 9.2 shows the basic steps of the stiffness matrix method.

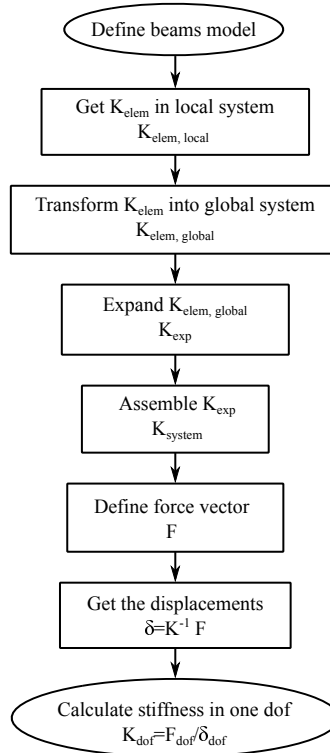


Figure 9.2: Basic steps of the stiffness matrix method

We define the beams model for our manipulator by using one beam element for each leg and four beam elements for the mobile platform. In this way, the model has seven beams and 8 nodes in total. Figure 9.3 gives the numeration used to refer each element and node.

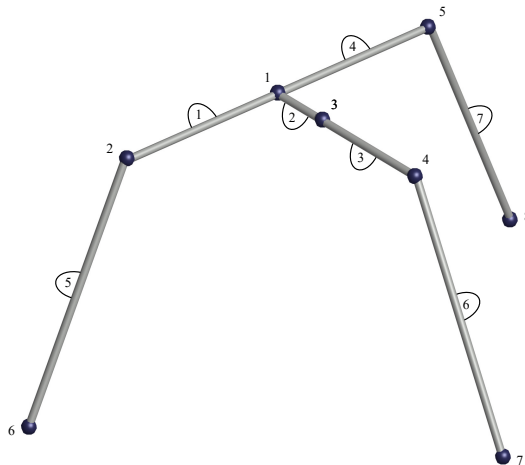


Figure 9.3: Elements and nodes numeration

Figure 9.4 represents the local reference system defined in a beam element. It also shows the 6 dof in each node – 3 of translation and 3 of rotation. These dof are the displacement possibilities of the node. We label the nodes of the element as i and j and, without loss of generality, assume that the number j is greater than i . We define a cartesian right-handed local reference system with the u -axis along the beam, with origin at i and pointing towards j . The v - and w -axes define a plane perpendicular to the u -axis.



Figure 9.4: Beams axes

We define the stiffness matrix of each element in local reference system as \mathbf{K}_{elem} , given by Eq. (9.5), where the submatrices \mathbf{A}_1 , \mathbf{A}_2 and \mathbf{B} are given by the expressions Eq. (9.6), Eq. (9.7) and Eq. (9.8), respectively. We notice that to obtain the elemental stiffness matrices we need to know the geometry parameters of each element and the material properties. The geometry parameters of an element are its length (L), its transversal section (A), and the inertia moments (I_y , I_z and J). The material properties that appear in the stiffness matrices are the modulus of elasticity (E), and the shear modulus (G).

$$\mathbf{K}_{elem,L} = \begin{bmatrix} \mathbf{A}_1 & \mathbf{B}^T \\ \mathbf{B} & \mathbf{A}_2 \end{bmatrix} \quad (9.5)$$

$$\mathbf{A}_1 = \begin{bmatrix} EA/L & 0 & 0 & 0 & 0 & 0 \\ 0 & 12EI_z/L^3 & 0 & 0 & 0 & 6EI_z/L^2 \\ 0 & 0 & 12EI_y/L^3 & 0 & -6EI_y/L^2 & 0 \\ 0 & 0 & 0 & GJ/L & 0 & 0 \\ 0 & 0 & -6EI_y/L^2 & 0 & 4EI_y/L & 0 \\ 0 & 6EI_z/L^2 & 0 & 0 & 0 & 4EI_z/L \end{bmatrix} \quad (9.6)$$

$$\mathbf{A}_2 = \begin{bmatrix} EA/L & 0 & 0 & 0 & 0 & 0 \\ 0 & 12EI_z/L^3 & 0 & 0 & 0 & -6EI_z/L^2 \\ 0 & 0 & 12EI_y/L^3 & 0 & 6EI_y/L^2 & 0 \\ 0 & 0 & 0 & GJ/L & 0 & 0 \\ 0 & 0 & 6EI_y/L^2 & 0 & 4EI_y/L & 0 \\ 0 & -6EI_z/L^2 & 0 & 0 & 0 & 4EI_z/L \end{bmatrix} \quad (9.7)$$

$$\mathbf{B} = \begin{bmatrix} -EA/L & 0 & 0 & 0 & 0 & 0 \\ 0 & -12EI_z/L^3 & 0 & 0 & 0 & -6EI_z/L^2 \\ 0 & 0 & -12EI_y/L^3 & 0 & 6EI_y/L^2 & 0 \\ 0 & 0 & 0 & -GJ/L & 0 & 0 \\ 0 & 0 & -6EI_y/L^2 & 0 & 2EI_y/L & 0 \\ 0 & 6EI_z/L^2 & 0 & 0 & 0 & 2EI_z/L \end{bmatrix} \quad (9.8)$$

We now have to assemble the stiffness matrices of all the elements to obtain the stiffness matrix of the whole system. In order to do this, we have to take into account the orientation of the elements and the nodes each one affects. We have defined the elementary stiffness matrices in the local reference systems, but each element has a different orientation in the space. Thus, we have to express all the elementary matrices in the global reference system by applying Eq. (9.9), where \mathbf{T} is the transformation matrix.

$$\mathbf{K}_{elem,G} = \mathbf{T}^T \cdot \mathbf{K}_{elem,L} \cdot \mathbf{T} \quad (9.9)$$

The size of both \mathbf{K}_L and \mathbf{K}_G is 12x12, so in order to transform one into the other we need a 12x12 transformation matrix, as seen in Eq. (9.10). We define the \mathbf{T}_{3x3} transformation matrix as the matrix whose columns are the direction cosines of the mobile reference system in the global reference

system, as Eq. (9.11) shows. Notice that, since every element has a different orientation in the space, the transformation matrix is different for each element.

$$\mathbf{T} = \begin{bmatrix} \mathbf{T}_{3x3} & [0]_{3x3} & [0]_{3x3} & [0]_{3x3} \\ [0]_{3x3} & \mathbf{T}_{3x3} & [0]_{3x3} & [0]_{3x3} \\ [0]_{3x3} & [0]_{3x3} & \mathbf{T}_{3x3} & [0]_{3x3} \\ [0]_{3x3} & [0]_{3x3} & [0]_{3x3} & \mathbf{T}_{3x3} \end{bmatrix}_{12x12} \quad (9.10)$$

$$\mathbf{T}_{3x3} = \begin{bmatrix} u_x & v_x & w_x \\ u_y & v_y & w_y \\ u_z & v_z & w_z \end{bmatrix} \quad (9.11)$$

If two elements share a dof it means that the displacement or rotation – depending on the kind of DOF it is – in that dof is the same for the two elements. When two elements are connected at a node by a rigid joint, the two elements share all the dof in the node. However, if two elements are connected by a kinematic joint, the elements only share the dof of the node that the kinematic joint constrains, but not the ones that the joint allows. In our model there are three different types of kinematic joints – revolution joints between the fixed element and the elements 5, 6 and 7, universal joints connecting the element 1 with the element 5 and the element 4 with the element 7 and a spherical joint between the element 3 and the element 6. Figure 9.5 shows the degrees of freedoms allowed in each kind of kinematic joint.

As the beam model of our manipulator has 8 nodes and each node has 6 DOF, the total number of degrees of freedom is 48. We label these degrees of freedom in Fig. 9.6 with numbers 1 to 48. The DOF drawn in black represent the DOF that the elements meeting in that node share, while the DOF drawn in red are the ones that the kinematic joints allow.

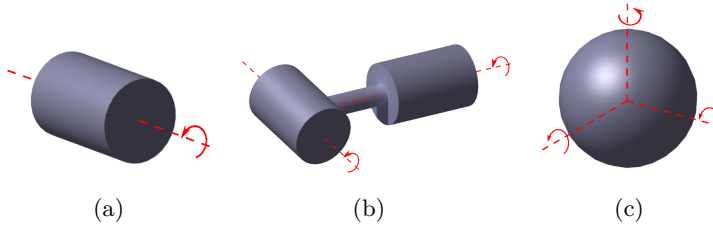


Figure 9.5: Degrees of freedom allowed in: (a) revolution joint; (b) universal joint; (c) spherical joint

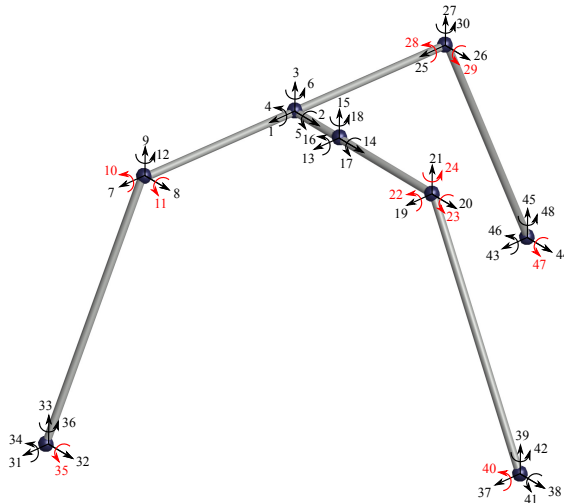


Figure 9.6: Degrees of freedom numeration

According to this, the size of the stiffness matrix of the system is 48x48. We get it by assembling the expanded matrices of all the elements, as given in Eq. (9.12). The expanded matrix of an element is a 48x48 sized matrix with non-zero stiffness terms in the DOF that the element affects and zeros in the rest.

$$\mathbf{K} = \mathbf{K}_{sys} = \sum \mathbf{K}_{G_i,exp} \quad (9.12)$$

We want to calculate the stiffness of the manipulator in vertical direction in the gravity center of the mobile platform. The gravity center of the mobile platform is placed on the node 3. Thus, we calculate the stiffness by applying a force in the direction given by DOF labelled 15, and by measuring the subsequent deformation in this direction.

We define a force vector as given in Eq. (9.13), \mathbf{F} being a vector of size 48x1 with all terms null except the one corresponding to the dof 15.

$$\mathbf{F}_{48x1} = [0 \ 0 \ \dots \ F_{15} \ 0 \ \dots \ 0]^T \quad (9.13)$$

We now obtain the deformation that the applied force generates in the manipulator. The equilibrium equation of the system is given by Eq. (9.14), so we get the deformation by applying Eq. (9.15).

$$\mathbf{F}_{48x1} = \mathbf{K}_{48x48} \cdot \mathbf{\Delta}_{48x1} \quad (9.14)$$

$$\mathbf{\Delta}_{48x1} = \mathbf{K}_{48x48}^{-1} \cdot \mathbf{F}_{48x1} \quad (9.15)$$

Finally, we get the stiffness in a certain direction by dividing the external force applied in the corresponding DOF by the displacement in that DOF, as Eq. (9.16) shows.

$$k_i = F_i/\delta_i \quad (9.16)$$

10

Dynamics

10.1. Dynamics

The dynamics of parallel manipulators is very complicated due to the multiple closed-loop chains. However, it is essential for the simulation and control. Besides, we can also use it for the dynamic optimum design of the manipulator.

There are many approaches to solve the dynamics of a parallel manipulators - the most used ones are the Newton-Euler approach, the Lagrangian method, Kane's method and the virtual work principle.

The Newton-Euler method

This method uses Newtonian mechanics to formulate the dynamic equations of motion of the manipulator. The steps of the method are mainly two. In the first one we note the force and moment balance equations. In the second one we use kinematic relations and constraint forces to reduce the number of equations. The Newton-Euler method calculates all the internal reactions exactly so the computational cost is very high. The computation of the internal reactions of the system is useful for the design of the ma-

nipulator, but not for its control law. Thus, the interest of this method depends on the application of the dynamic problem.

Many authors have used the Newton-Euler approach to solve the dynamics of parallel manipulators. Dasgupta and Mruthyunjaya [180], [181], for example, used the Newton-Euler approach to analyse the dynamics of the Stewart platform, while Gugliemetti and Longchamp [182] used it to solve the dynamics of the DELTA robot. Khalil and Guegan [183] obtained both the inverse and direct dynamic problem solutions of the Gough platform. Carvalho and Ceccarelli [184] solved the inverse dynamic problem of the Cassino parallel manipulator by using the Newton-Euler approach.

Wang et al. [185] presented a simplified strategy for a real-time control of the dynamic model of a 6-UPS parallel manipulator. They decomposed the dynamic model into 18 terms independently by separating the inertial forces and moments of inertia of legs and platform. They simulated different movements and investigated the contribution of each term in the dynamic model. Besides, they proposed simplified strategies and simulated the previous movements again by using them. They saw that the simplification error was small enough and that the computational efficiency improved greatly.

Khalil and Ibrahim [186] presented a general method to calculate the inverse and direct dynamic models of parallel manipulators. They expressed the models by using a single equation with all the elements needed. They applied the method on two different parallel robots - the 3-UPS parallel manipulator and the C5 robot - but the method is valid for most PM.

Hao et al. [69] modelled the dynamic problem of the 3-PSP 3-DOF parallel manipulator by applying the Newton-Euler approach. They analysed its dynamics with and without considering the parasitic motions. They compared both cases with numerical simulation results. They saw that the error of the actuating force between the two cases affected very little the dynamics, so parasitic motions were ignored.

The Lagrangian method

The Lagrangian method uses the Lagrangian functions to formulate dynamic equations of motion. It first considers the constraints and kinematics of the problem and then writes the equations of motion. There is one equation per degree of freedom. The hardest work in Lagrangian mechanics is to find a proper set of generalized coordinates and to express the kinematics. Once it is done, the rest is uncomplicated.

Lee and Geng [187] analysed the dynamics of a general Stewart platform by considering the limbs connecting the mobile and fixed platform as flexible actuators. They derived a set of 12 Lagrange equations by using tensor representation. The 12 Lagrange equations were reduced to six equations for the Stewart platform whose actuators are rigid. They also discussed the model-based control approach for the end-effector of the Stewart platform.

Abdellatif and Heiman [188] used the Lagrangian method to get the dynamic equations of a 6-DOF fully parallel manipulator. They considered open-loop sub-chains and derived their dynamics with respect to known generalized coordinates and velocities. The choice of the sub-chains's generalized coordinates was crucial to get an efficient derivation of the dynamics. The computational cost was better than other works that were known in the literature. They used different simulations and experimental results to validate their method.

Liu et al. [189] developed the dynamic problem of the PSS 6-DOF parallel manipulator by applying the Lagrange method. Then, they simplified the model to get an easier case of analysis and controller design. They simulated the simplified model, which showed that the model was effective. Additionally, they designed a bionic horse as experimental application. The bionic horse simulated the motion of a real horse and could be used, for example, for entertainment purposes. The experimental results allowed them to evaluate and optimize the performance of the system.

Kane's method

Professor T. R. Kane, from the Stanford University presented this method [190] in order to overcome the disadvantages of Newton-Euler and Lagrangian methods. It is based on a modification of Newton's equations. As Kane and Levinson [191] explained, the method produces motion equations that need fewer multiplications and additions than other techniques, so its computational cost is lower. Its main application in parallel manipulators is the obtaining of direct dynamics. The process of modelling using Kane's method is clear and normative, so it is a good option to automate the dynamic modelling.

Wang et al. [192] used Kane's method to get the dynamic modelling of a spatial 6-DOF parallel manipulator. They described the parallel manipulator as a rigid body and got the direct dynamic equations. Then, they compared the results with Simulink and SimMechanics simulations. They concluded that Kane's method was effective to model the manipulator.

In [193], Liu et al. presented the dynamic analysis of the Gough platform based on Kane's equation. They first treated the mobile platform and the legs as independent substructures. They obtained their dynamic equations by applying Kane's equation and then used the constraints among substructures that Lagrange multipliers introduce to put all equations together. They applied the method to the Gough platform, but they concluded that the method is also valid for any type of parallel manipulators.

Wu et al. [194] solved the inverse dynamic problem of the 6-SPS parallel manipulator by using the principle of Kane. They considered inertial forces of all links and mobile platform and took the orientation parameters and Euler angles as generalized coordinates. They verified the approach with simulation results. They used MATLAB to program the dynamic calculation and ADAMS to verify the analysis.

Virtual work principle

The virtual work principle develops the dynamic equations by applying D'Alembert's principle to obtain the equilibrium equations. This principle says that when a rigid body in equilibrium suffers virtual compatible displacements, the total virtual work of all external forces is zero. The constraint forces and moments of the robot system do not appear in this formulation, which makes it useful for obtaining the inverse dynamics for real-time control applications.

Geike and McPhee [195] presented an approach to solve the inverse dynamics for planar parallel manipulators with 3-DOF and spatial parallel manipulators with 6-DOF. They formulated the kinematic and dynamic equations by combining linear graph theory, the principle of virtual work and symbolic programming. They demonstrated the features of the formulation by analysing two parallel manipulators - the planar RRR manipulator and the Gough platform.

Zhao and Gao [196] applied the principle of virtual work and the concept of link Jacobian matrices to solve the inverse dynamics of a 6-DOF parallel manipulator used as seismic simulator. The constraint forces and moments did not appear in the motion equations and there were no differential equations, so the method lead to efficient algorithms. This method could also be useful for other kind of mechanisms.

In [197], Zhao evaluated the dynamic performance of the DELTA robot. He developed the inverse dynamics by applying the principle of virtual work and the link Jacobian matrices. He proposed the maximum torque index and the maximum power index to evaluate the dynamic performance of the robot.

García-Murillo et al. [198] obtained the generalized forces of a 2(3-RRPS) parallel manipulators by combining the Klein form of the Lie algebra with the principle of virtual work. They compared numerical results with

simulations done with ADAMS software. The instantaneous values of the internal reactions of the mechanism and the calculation of the energy of the entire system were not necessary. This method is useful to size the motors of the manipulator for a given application.

Zhao et al. [103] proposed a rigid-body dynamic model to solve the dynamics of a 3 rotational parallel manipulator. Their method was also based on the principle of virtual work and the concept of link Jacobian matrices. They obtained the inverse dynamics in an exhaustive decoupled way and concluded that the development energy consumption computation can be very useful for the dynamic optimum design and motion planning while considering the energy conservation.

Other methods

Even if the previous four methods are the most used ones, there are also other methods to solve the dynamics of parallel manipulators. By using the finite element method, for example, we can consider the elements of a parallel manipulator as flexible and get more precision in the results. This is what Piras et al. [199] and Du et al. [200] did.

Inverse dynamics of parallel manipulators involve many mechanics principles, but also many mathematical methods, such as the Lie algebra used by Müller and Maiber [201] or the symbolic programming applied by Geike and McPhee [202] and McPhee et al. [203].

10.2. Developing the dynamics of the 2PRU-1PRS parallel manipulator

In this Section we solve the dynamic problem by applying the Newton-Euler approach – we obtain the reactions in all the joints of the manipulator. To do it, we solve the equation system given by Eq. (10.1), with \mathbf{A} being a matrix with the coefficients that multiply the vector of forces \mathbf{F} and \mathbf{c} being the independent terms of the system. We get the different equations of the

system by analysing the mobile platform and the three limbs independently.

$$\mathbf{A} \cdot \mathbf{f} = \mathbf{c} \tag{10.1}$$

Figure 10.1 shows the reaction forces and moments as well as the weights in the 2PRU-1PRS parallel manipulator. We note that we analyse the manipulator without the linear guides, so there are no applied forces. According to the action-reaction principle, the value of the forces in the linear guides are equal to the reaction forces in the rotation joint.

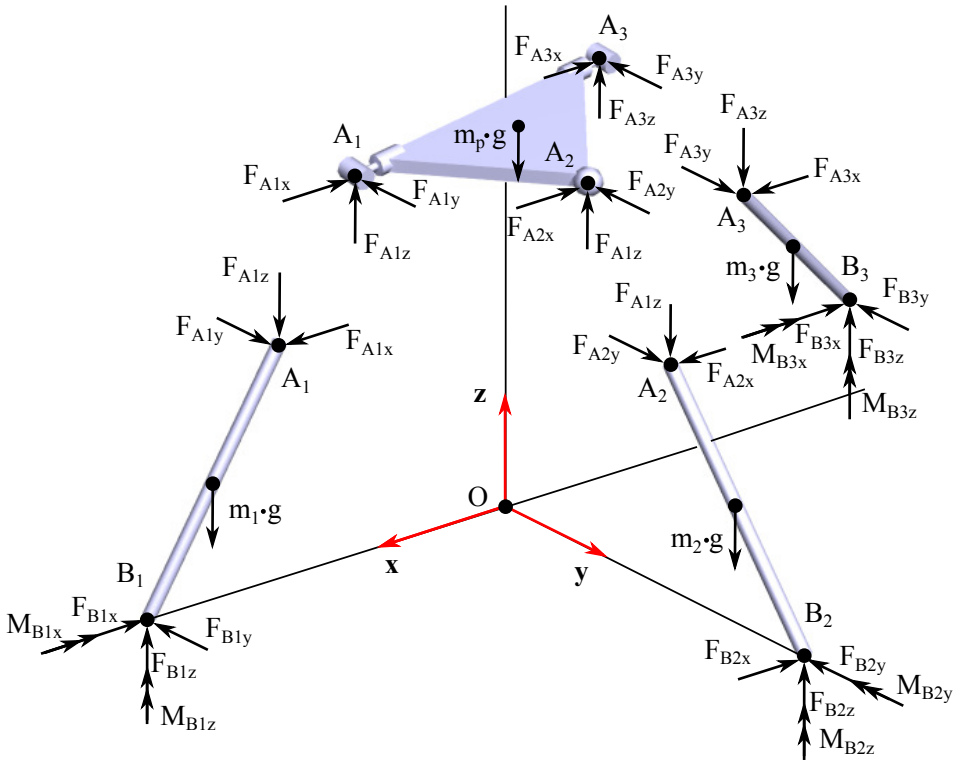


Figure 10.1: Reaction forces, moments and weights in the manipulator

Figure 10.2 presents the vectors and parameters we need to solve the dynamics of the manipulator.

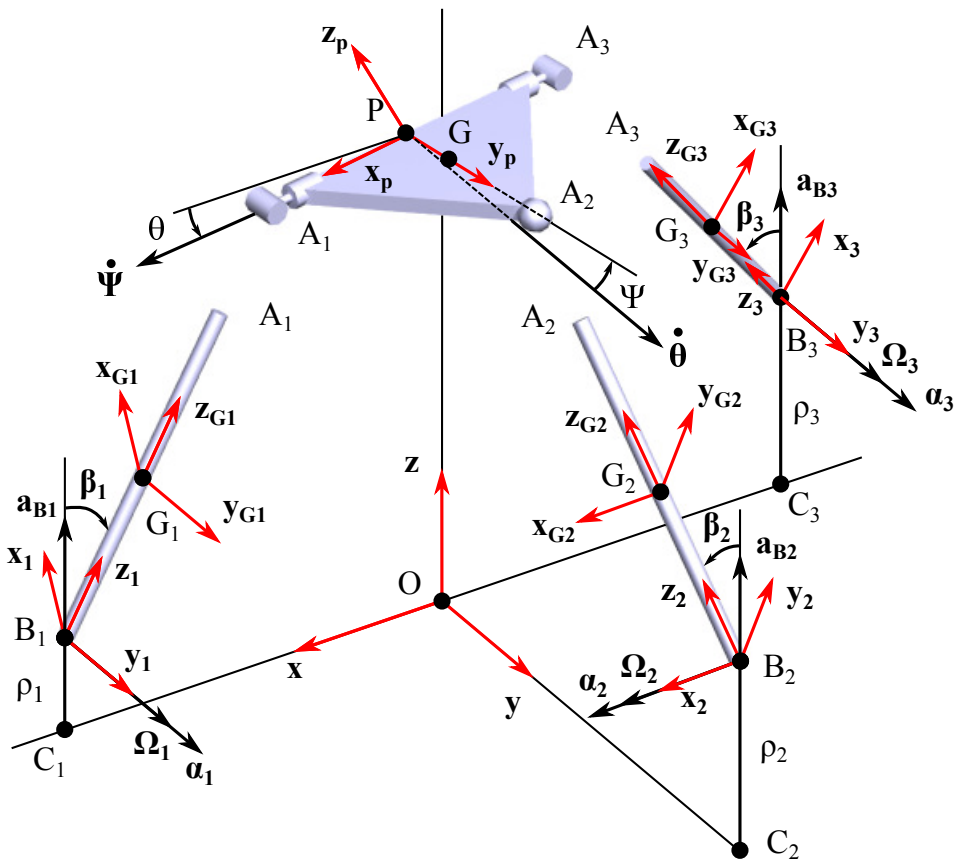


Figure 10.2: Parameters of the dynamic problem

10.2.1. Dynamic analysis of the platform

The sum of reaction forces in the platform has to be equal to the inertia forces. We obtain the inertia forces by multiplying the mass of the platform (m) by the linear acceleration of the gravity centre (\mathbf{a}_G), as we see in Eq. (10.2).

$$\sum \mathbf{F} = m \cdot \mathbf{a}_G \quad (10.2)$$

We write Eq. (10.2) as the equation system given by Eq. (10.3), Eq. (10.4) and Eq. (10.5),

$$F_{A1x} + F_{A2x} + F_{A3x} = m \cdot a_{Gx} \quad (10.3)$$

$$F_{A1y} + F_{A2y} + F_{A3y} = m \cdot a_{Gy} \quad (10.4)$$

$$F_{A1z} + F_{A2z} + F_{A3z} = m \cdot a_{Gz} + m \cdot g \quad (10.5)$$

We now calculate the value of the linear acceleration of the gravity centre of the mobile platform, given by Eq. (10.6)

$$\mathbf{a}_G = \mathbf{a}_p + \boldsymbol{\alpha}_p \times \mathbf{PG} + \boldsymbol{\Omega}_p \times (\boldsymbol{\Omega}_p \times \mathbf{PG}) \quad (10.6)$$

where \mathbf{a}_p is the linear acceleration of the point P, $\boldsymbol{\alpha}_p$ is the angular acceleration of the platform, \mathbf{PG} is the vector that goes from the point P to the gravity centre of the mobile platform (G) and $\boldsymbol{\Omega}_p$ is the angular velocity of the platform. All vectors are referred to in the fixed reference system, (X,Y,Z), as shown in Fig. 10.2. We obtain the value of all these vectors, necessary to get the components of the \mathbf{a}_G .

Equation (10.7) gives the acceleration of the point P.

$$\mathbf{a}_p = \begin{bmatrix} \ddot{x}_p & \ddot{y}_p & \ddot{z}_p \end{bmatrix}^t \quad (10.7)$$

Since the parasitic motion along the Y-axis is null, we get Eq. (10.8).

$$\mathbf{a}_p = \begin{bmatrix} \ddot{x}_p & 0 & \ddot{z}_p \end{bmatrix}^T \quad (10.8)$$

Vector \mathbf{PG} in the mobile reference system is known and given by Eq. (10.9). We express it in the fixed reference system by multiplying it by the rotation matrix \mathbf{Rot} as shown by Eq. (10.10).

$$[\mathbf{PG}]^{x_p y_p z_p} = \begin{bmatrix} 0 & G_y & 0 \end{bmatrix}^T \quad (10.9)$$

$$\mathbf{PG} = \mathbf{Rot} \cdot [\mathbf{PG}]^{x_p y_p z_p} \quad (10.10)$$

We expand Eq. (10.10) and get Eq. (10.11).

$$\mathbf{PG} = \begin{bmatrix} G_y \cdot s\theta \cdot s\psi & G_y \cdot c\psi & G_y \cdot c\theta \cdot s\psi \end{bmatrix}^T \quad (10.11)$$

Equation (10.12) gives the angular velocity of the platform in the fixed reference.

$$\boldsymbol{\Omega}_p = \begin{bmatrix} \dot{\psi} \cdot c\theta & \dot{\theta} & -\dot{\psi} \cdot s\theta \end{bmatrix}^T \quad (10.12)$$

We differentiate it and get the angular acceleration of the platform, given by Eq. (10.13).

$$\boldsymbol{\alpha}_p = \begin{bmatrix} \ddot{\psi} \cdot c\theta - \dot{\psi} \cdot s\theta \cdot \dot{\theta} & \ddot{\theta} & -\ddot{\psi} \cdot s\theta + \dot{\psi} \cdot c\theta \cdot \dot{\theta} \end{bmatrix}^T \quad (10.13)$$

We already have all the vectors that appear in Eq. (10.6), so we rewrite it as Eq. (10.14). According to this, we get the components of the acceleration of the gravity centre of the mobile platform, which we need for Eq. (10.4) and Eq. (10.5), the three first equations of the equation system we have to solve.

$$\begin{aligned} \mathbf{a}_G = & \begin{bmatrix} \ddot{x}_p \\ 0 \\ \ddot{z}_p \end{bmatrix} + \begin{bmatrix} \ddot{\psi} \cdot c\theta - \dot{\psi} \cdot s\theta \cdot \dot{\theta} \\ \ddot{\theta} \\ -\ddot{\psi} \cdot s\theta + \dot{\psi} \cdot c\theta \cdot \dot{\theta} \end{bmatrix} \times \begin{bmatrix} G_y \cdot s\theta \cdot s\psi \\ G_y \cdot c\psi \\ G_y \cdot c\theta \cdot s\psi \end{bmatrix} + \\ & + \begin{bmatrix} \dot{\psi} \cdot c\theta \\ \dot{\theta} \\ -\dot{\psi} \cdot s\theta \end{bmatrix} \times \left(\begin{bmatrix} \dot{\psi} \cdot c\theta \\ \dot{\theta} \\ -\dot{\psi} \cdot s\theta \end{bmatrix} \times \begin{bmatrix} G_y \cdot s\theta \cdot s\psi \\ G_y \cdot c\psi \\ G_y \cdot c\theta \cdot s\psi \end{bmatrix} \right) \end{aligned} \quad (10.14)$$

We obtain the next three equations of the equation system by applying the angular momentum theorem, Eq. (10.15)

$$\mathbf{N}_G = \sum [\mathbf{G}\mathbf{A}_i \times \mathbf{F}_{Ai}]^{xyz} = \left[\frac{d\mathbf{H}_G}{dt} \right]^{xyz} \quad (10.15)$$

where \mathbf{N}_G is the sum of the momentum created by the reaction forces and $\left[\frac{d\mathbf{H}_G}{dt} \right]^{xyz}$ is the derivative of the angular momentum in the fixed reference system. We first calculate the derivative of the angular momentum and then obtain the sum of force momentums.

The expression of the angular momentum in the mobile reference system is given by Eq. (10.16)

$$\left[\mathbf{H}_G \right]^{x_p y_p z_p} = \mathbf{I}_G \cdot \boldsymbol{\omega}_p \quad (10.16)$$

where \mathbf{I}_G is the inertia matrix in G and $\boldsymbol{\omega}_p$ is the angular velocity of the platform, expressed by Eq. (10.17), both in the mobile reference system.

$$\boldsymbol{\omega}_p = \left[\dot{\psi} \quad \dot{\theta} \cdot c\psi \quad -\dot{\theta} \cdot s\psi \right]^T \quad (10.17)$$

The expression of the derivative of the angular momentum in the mobile frame is given by Eq. (10.18)

$$\left[\frac{d\mathbf{H}_G}{dt} \right]^{x_p y_p z_p} = \mathbf{I}_G \cdot \dot{\boldsymbol{\omega}}_p + \boldsymbol{\omega}_p \times \left[\mathbf{H}_G \right]^{x_p y_p z_p} \quad (10.18)$$

where $\dot{\boldsymbol{\omega}}_p$ is the angular acceleration of the platform in the mobile reference system, given by Eq. (10.19).

$$\dot{\boldsymbol{\omega}}_p = \left[\ddot{\psi} \quad \ddot{\theta} \cdot c\psi - \dot{\psi} \cdot \dot{\theta} \cdot s\psi \quad -\ddot{\theta} \cdot s\psi - \dot{\theta} \cdot \dot{\psi} \cdot c\psi \right]^T \quad (10.19)$$

We refer the derivative of the angular momentum in the fixed frame by multiplying Eq. (10.18) by the rotation matrix, as seen in Eq. (10.20).

$$\left[\frac{d\mathbf{H}_G}{dt} \right]^{xyz} = \mathbf{Rot} \cdot \left[\frac{d\mathbf{H}_G}{dt} \right]^{x_p y_p z_p} \quad (10.20)$$

Equation 10.21 gives the value of the sum of force momentums

$$\mathbf{N}_G = \mathbf{GA}_1 \times \mathbf{F}_{A1} + \mathbf{GA}_2 \times \mathbf{F}_{A2} + \mathbf{GA}_3 \times \mathbf{F}_{A3} \quad (10.21)$$

with \mathbf{GA}_i being the vector that goes from the gravity centre of the mobile platform to the A_i points in the fixed reference system.

Equation (10.22) shows the value of \mathbf{GA}_1 , \mathbf{GA}_2 and \mathbf{GA}_3 in the mobile frame.

$$\begin{aligned} [\mathbf{GA}_1]^{x_p y_p z_p} &= [R \quad -G_y \quad 0]^T \\ [\mathbf{GA}_2]^{x_p y_p z_p} &= [0 \quad R - G_y \quad 0]^T \\ [\mathbf{GA}_3]^{x_p y_p z_p} &= [-R \quad -G_y \quad 0]^T \end{aligned} \quad (10.22)$$

We express the \mathbf{GA}_i vectors in the fixed frame by multiplying Eq. (10.22) by the rotation matrix, as we see in Eq. (10.23).

$$\mathbf{GA}_i = \mathbf{Rot} \cdot [\mathbf{GA}_i]^{x_p y_p z_p} \quad (10.23)$$

By applying Eq. (10.23) for the three limbs, we get the value of \mathbf{GA}_1 , \mathbf{GA}_2 and \mathbf{GA}_3 in the fixed frame, as shown in Eq. (10.24).

$$\begin{aligned} \mathbf{GA}_1 &= [R \cdot c\theta - G_y \cdot s\theta \cdot s\psi \quad -G_y \cdot c\psi \quad -R \cdot s\theta - G_y \cdot c\theta \cdot s\psi]^T \\ \mathbf{GA}_2 &= [(R - G_y) \cdot s\theta \cdot s\psi \quad (R - G_y) \cdot c\psi \quad (R - G_y) \cdot c\theta \cdot s\psi]^T \\ \mathbf{GA}_3 &= [-R \cdot c\theta - G_y \cdot s\theta \cdot s\psi \quad -G_y \cdot c\psi \quad R \cdot s\theta - G_y \cdot c\theta \cdot s\psi]^T \end{aligned} \quad (10.24)$$

We now apply the values obtained in Eq. (10.20) and Eq. (10.24) in Eq.

(10.15), so we get Eq. (10.25), Eq. (10.26) and Eq. (10.27).

$$\begin{aligned}
& -G_y \cdot c\psi \cdot F_{A1z} - (-R \cdot s\theta - G_y \cdot c\theta \cdot s\psi) \cdot F_{A1y} + \\
& +(R - G_y) \cdot c\psi \cdot F_{A2z} - (R - G_y) \cdot c\theta \cdot s\psi \cdot F_{A2y} - G_y \cdot c\psi \cdot F_{A3z} - \\
& -(R \cdot c\theta - G_y \cdot c\theta \cdot s\psi) \cdot F_{A3y} = dH_x
\end{aligned} \tag{10.25}$$

$$\begin{aligned}
& (-R \cdot s\theta - G_y \cdot c\theta \cdot s\psi) \cdot F_{A1x} - (R \cdot c\theta - G_y \cdot s\theta \cdot s\psi) \cdot F_{A1z} + \\
& +(R - G_y) \cdot c\theta \cdot s\psi \cdot F_{A2x} - (R - G_y) \cdot s\theta \cdot s\psi \cdot F_{A2z} + \\
& +(R \cdot s\theta - G_y \cdot c\theta \cdot s\psi) \cdot F_{A3x} - -(-R \cdot c\theta - G_y \cdot s\theta \cdot s\psi) \cdot F_{A3z} = dH_y
\end{aligned} \tag{10.26}$$

$$\begin{aligned}
& (R \cdot c\theta - G_y \cdot s\theta \cdot s\psi) \cdot F_{A1y} + G_y \cdot c\psi \cdot F_{A1x} + \\
& +(R - G_y) \cdot s\theta \cdot s\psi \cdot F_{A2y} - (R - G_y) \cdot c\psi \cdot F_{A2x} + \\
& +(-R \cdot c\theta - G_y \cdot s\theta \cdot s\psi) \cdot F_{A3y} - (-G_y \cdot c\psi) \cdot F_{A3x} = dH_z
\end{aligned} \tag{10.27}$$

10.2.2. Dynamic analysis of limb 1

The sum of forces in the first limb has to be equal to the mass of the limb multiplied by the acceleration of its gravity centre, G_1 , as we see in Eq. (10.28)

$$\sum \mathbf{F}_1 = m_1 \cdot \mathbf{a}_{G1} \tag{10.28}$$

where $\sum \mathbf{F}_1$ is the sum of forces in the first limb, M_1 is the mass of the limb and \mathbf{a}_{G1} is the acceleration of its gravity centre. Figure 10.1 shows all the forces in the first limb. Taking them into account, we get Eq. (10.29), Eq. (10.30) and Eq. (10.31).

$$F_{B1x} - F_{A1x} = m_1 \cdot a_{G1x} \tag{10.29}$$

$$F_{B1y} - F_{A1y} = m_1 \cdot a_{G1y} \tag{10.30}$$

$$F_{B1z} - F_{A1z} = m_1 \cdot a_{G1z} + m_1 \cdot g \tag{10.31}$$

We express the acceleration of the gravity centre of the first limb as Eq. (10.32)

$$\mathbf{a}_{G_1} = \mathbf{a}_{B_1} + \boldsymbol{\alpha}_1 \times \mathbf{B}_1 \mathbf{G}_1 + \boldsymbol{\Omega}_1 \times (\boldsymbol{\Omega}_1 \times \mathbf{B}_1 \mathbf{G}_1) \quad (10.32)$$

with \mathbf{a}_{B_1} being the acceleration of the B_1 point, $\boldsymbol{\alpha}_1$ being the angular acceleration of the limb, $\mathbf{B}_1 \mathbf{G}_1$ being the vector that refers to G_1 with respect to B_1 and $\boldsymbol{\Omega}_1$ being the angular velocity of the limb.

The acceleration of the point B_1 is given by Eq. (10.33).

$$\mathbf{a}_{B_1} = \begin{bmatrix} 0 & 0 & \ddot{\rho}_1 \end{bmatrix}^T \quad (10.33)$$

Equation (10.34) gives the value of $\mathbf{B}_1 \mathbf{G}_1$ in the mobile reference system.

$$[\mathbf{B}_1 \mathbf{G}_1]^{x_1 y_1 z_1} = \begin{bmatrix} 0 & 0 & G_{1z} \end{bmatrix}^T \quad (10.34)$$

We write $\mathbf{B}_1 \mathbf{G}_1$ in the fixed frame by multiplying Eq. (10.34) by the rotation matrix that expresses the mobile reference systems in the fixed reference system for the first limb.

$$\mathbf{B}_1 \mathbf{G}_1 = \mathbf{Rot}_1 \cdot [\mathbf{B}_1 \mathbf{G}_1]^{x_1 y_1 z_1} \quad (10.35)$$

Equation (10.36) gives the rotation matrix and Eq. (10.37) shows the resulting value of $\mathbf{B}_1 \mathbf{G}_1$ in the fixed frame.

$$\mathbf{Rot}_1 = \begin{bmatrix} c\beta_1 & 0 & -s\beta_1 \\ 0 & 1 & 0 \\ s\beta_1 & 0 & c\beta_1 \end{bmatrix} \quad (10.36)$$

$$\mathbf{B}_1 \mathbf{G}_1 = \begin{bmatrix} -s\beta_1 G_{1z} & 0 & c\beta_1 G_{1z} \end{bmatrix}^T \quad (10.37)$$

The angular velocity and acceleration in the fixed frame are given by Eq. (10.38) and Eq. (10.39), respectively.

$$\boldsymbol{\Omega}_1 = \begin{bmatrix} 0 & -\dot{\beta}_1 & 0 \end{bmatrix}^T \quad (10.38)$$

$$\boldsymbol{\alpha}_1 = \begin{bmatrix} 0 & -\ddot{\beta}_1 & 0 \end{bmatrix}^T \quad (10.39)$$

We get Eq. (10.40) by substituting the obtained values in Eq. (10.32).

$$\mathbf{a}_{G1} = \begin{bmatrix} 0 \\ 0 \\ \ddot{\rho}_1 \end{bmatrix} - \begin{bmatrix} 0 \\ \ddot{\beta}_1 \\ 0 \end{bmatrix} \times \begin{bmatrix} -G_{1z} \cdot s\beta_1 \\ 0 \\ G_{1z} \cdot c\beta_1 \end{bmatrix} + \begin{bmatrix} 0 \\ -\dot{\beta}_1 \\ 0 \end{bmatrix} \times \left(\begin{bmatrix} 0 \\ -\dot{\beta}_1 \\ 0 \end{bmatrix} \times \begin{bmatrix} G_{1z} \cdot s\beta_1 \\ 0 \\ G_{1z} \cdot c\beta_1 \end{bmatrix} \right) \quad (10.40)$$

Thus, the components of \mathbf{a}_{G1} are given as Eq. (10.41).

$$\begin{aligned} a_{G1x} &= (-\ddot{\beta}_1 \cdot c\beta_1 \cdot G_{1z} + \dot{\beta}_1^2 \cdot s\beta_1 \cdot G_{1z}) \\ a_{G1y} &= 0 \\ a_{G1z} &= (\ddot{\rho}_1 - \ddot{\beta}_1 \cdot s\beta_1 \cdot G_{1z} - \dot{\beta}_1^2 \cdot c\beta_1 \cdot G_{1z}) \end{aligned} \quad (10.41)$$

We replace Eq. (10.41) in Eq. (10.29), Eq. (10.30) and Eq. (10.31) and get three more equations of the system we have to solve.

We apply the angular momentum theorem to the first limb, given by Eq. (10.42)

$$\mathbf{N}_{G1} = \sum \left[\mathbf{d}_1 \times \mathbf{F}_i + \mathbf{M}_i \right]^{xyz} = \left[\frac{d\mathbf{H}_{G1}}{dt} \right]^{xyz} \quad (10.42)$$

where $\sum \left[\mathbf{d}_1 \times \mathbf{F}_i + \mathbf{M}_i \right]^{xyz}$ is the sum of momentums and $\left[\frac{d\mathbf{H}_{G1}}{dt} \right]^{xyz}$ is the derivative of the angular momentum for the first limb and referred with respect to the fixed reference system. We first calculate the derivative of the angular momentum and then the sum of momentums.

The expression of the angular momentum for the first limb in the mobile reference system (x_{G1}, y_{G1}, z_{G1}) is given by Eq. (10.43)

$$\left[\mathbf{H}_{G1} \right]^{x_{G1}y_{G1}z_{G1}} = \mathbf{I}_{G1} \cdot \boldsymbol{\omega}_1 \quad (10.43)$$

\mathbf{I}_{G1} being the inertia matrix in G_1 and $\boldsymbol{\omega}_1$ the angular velocity of the first limb in the (x_{G1}, y_{G1}, z_{G1}) mobile reference system.

Thus, we get the expression of the derivative of the angular momentum in the mobile reference system (x_{G1}, y_{G1}, z_{G1}) as Eq. (10.44).

$$\left[\frac{d\mathbf{H}_{G1}}{dt} \right]^{x_{G1}y_{G1}z_{G1}} = \mathbf{I}_G \cdot \alpha_1 + \Omega_1 \times \mathbf{H}_{G1} \quad (10.44)$$

By substituting the corresponding vectors we get Eq. (10.45) Its result is given in Eq. (10.46).

$$\left[\frac{d\mathbf{H}_{G1}}{dt} \right]^{x_{G1}y_{G1}z_{G1}} = \begin{bmatrix} I_{u1} & 0 & 0 \\ 0 & I_{v1} & 0 \\ 0 & 0 & I_{w1} \end{bmatrix} \cdot \begin{bmatrix} 0 \\ -\ddot{\beta}_1 \\ 0 \end{bmatrix} + \begin{bmatrix} 0 \\ -\dot{\beta}_1 \\ 0 \end{bmatrix} \times \begin{bmatrix} 0 \\ -I_{v1} \cdot \ddot{\beta}_1 \\ 0 \end{bmatrix} \quad (10.45)$$

$$\left[\frac{d\mathbf{H}_{G1}}{dt} \right]^{x_{G1}y_{G1}z_{G1}} = \begin{bmatrix} 0 & -\ddot{\beta}_1 \cdot I_{v1} & 0 \end{bmatrix}^T \quad (10.46)$$

We get the derivative of the angular momentum in the fixed frame by multiplying Eq. (10.46) by the rotation matrix \mathbf{Rot}_1 , as seen in Eq. (10.47).

$$\left[\frac{d\mathbf{H}_{G1}}{dt} \right]^{xyz} = \mathbf{Rot}_1 \cdot \left[\frac{d\mathbf{H}_{G1}}{dt} \right]^{x_{G1}y_{G1}z_{G1}} \quad (10.47)$$

Equation (10.48) gives the resulting components of the derivative of the angular momentum.

$$\begin{aligned} dH_{1x} &= 0 \\ dH_{1y} &= -\ddot{\beta}_1 \cdot I_{v1} \\ dH_{1z} &= 0 \end{aligned} \quad (10.48)$$

We now calculate the sum of momentum in the first limb by applying Eq. (10.49).

$$\mathbf{N}_{G_1} = \mathbf{G}_1 \mathbf{A}_1 \times \mathbf{F}_{A_1} + \mathbf{G}_1 \mathbf{B}_1 \times \mathbf{F}_{B_1} + \mathbf{M}_{B_1} \quad (10.49)$$

Equation (10.50) shows the value of $\mathbf{G}_1 \mathbf{A}_1$ in the mobile reference system (x_1, y_1, z_1) .

$$\left[\mathbf{G}_1 \mathbf{A}_1 \right]^{x_1 y_1 z_1} = \begin{bmatrix} 0 & 0 & L - G_{1z} \end{bmatrix}^T \quad (10.50)$$

By multiplying Eq. (10.50) by the rotation matrix \mathbf{Rot}_1 we get the value of $\mathbf{G}_1 \mathbf{A}_1$ in the fixed frame, as shown in Eq. (10.51). The result is given by Eq. (10.52).

$$\mathbf{G}_1 \mathbf{A}_1 = \mathbf{Rot}_1 \cdot \left[\mathbf{G}_1 \mathbf{A}_1 \right]^{x_1 y_1 z_1} \quad (10.51)$$

$$\mathbf{G}_1 \mathbf{A}_1 = \begin{bmatrix} -(L - G_{1z}) \cdot s\beta_1 & 0 & (L - G_{1z}) \cdot c\beta_1 \end{bmatrix}^T \quad (10.52)$$

We expand Eq. (10.49) and substitute the value of the corresponding vectors, obtaining Eq. (10.53).

$$N_{G_1} = \begin{bmatrix} -(L_1 - G_{1z}) \cdot s\beta_1 \\ 0 \\ (L_1 - G_{1z}) \cdot c\beta_1 \end{bmatrix} \times \begin{bmatrix} F_{A1x} \\ F_{A1y} \\ F_{A1z} \end{bmatrix} + \begin{bmatrix} G_{1z} s \cdot \beta_1 \\ 0 \\ -G_{1z} \cdot c\beta_1 \end{bmatrix} \times \begin{bmatrix} F_{B1x} \\ F_{B1y} \\ F_{B1z} \end{bmatrix} + \begin{bmatrix} M_{B1x} \\ 0 \\ M_{B1z} \end{bmatrix} \quad (10.53)$$

We split Eq. (10.53) up and get the components of \mathbf{N}_{G_1} , as Eq. (10.54) shows.

$$\begin{aligned} N_{G1x} &= -(L_1 - G_{1z}) \cdot c\beta_1 \cdot F_{A1y} + G_{1z} \cdot c\beta_1 \cdot F_{B1y} + M_{B1x} \\ N_{G1y} &= (L_1 - G_{1z}) \cdot (c\beta_1 \cdot F_{A1x} + s\beta_1 \cdot F_{A1z}) - G_{1z} \cdot (c\beta_1 \cdot F_{B1x} + s\beta_1 \cdot F_{B1z}) \\ N_{G1z} &= -(L_1 - G_{1z}) \cdot s\beta_1 \cdot F_{A1y} + G_{1z} \cdot s\beta_1 \cdot F_{B1y} + M_{B1z} \end{aligned} \quad (10.54)$$

We already have all the vectors that appear in Eq. (10.42), which now we rewrite as the next three equations of the equation system – by Eq. (10.55), Eq. (10.56) and Eq. (10.57).

$$-(L_1 - G_{1z}) \cdot c\beta_1 \cdot F_{A1y} + G_{1z} \cdot c\beta_1 \cdot F_{B1y} + M_{B1x} = 0 \quad (10.55)$$

$$(L_1 - G_{1z}) \cdot (c\beta_1 \cdot F_{A1x} + s\beta_1 \cdot F_{A1z}) - \\ -G_{1z} \cdot (c\beta_1 \cdot F_{B1x} + s\beta_1 \cdot F_{B1z}) = -\ddot{\beta}_1 \cdot I_{v1} \quad (10.56)$$

$$-(L_1 - G_{1z}) \cdot s\beta_1 \cdot F_{A1y} + G_{1z} \cdot s\beta_1 \cdot F_{B1y} + M_{B1z} = 0 \quad (10.57)$$

10.2.3. Dynamic analysis of limb 2

The sum of forces in the second limb has to be equal to the mass of the limb multiplied by the acceleration of its gravity centre, as Eq. (10.58) shows

$$\sum \mathbf{F}_2 = m_2 \cdot \mathbf{a}_{G2} \quad (10.58)$$

where $\sum \mathbf{F}_2$ is the sum of all the forces in the second limb, m_2 is the mass of the second limb and \mathbf{a}_{G2} is the acceleration of its gravity centre (G_2) in the fixed reference system. In Fig. 10.1 we see the forces in the second limb. Taking them into account we rewrite Eq. (10.58) as Eq. (10.59), Eq. (10.60) and Eq. (10.61), three new equations of the equation system to solve.

$$F_{B2x} - F_{A2x} = m_2 \cdot a_{G2x} \quad (10.59)$$

$$F_{B2y} - F_{A2y} = m_2 \cdot a_{G2y} \quad (10.60)$$

$$F_{B2z} - F_{A2z} = m_2 \cdot a_{G2z} + m_2 \cdot g \quad (10.61)$$

We calculate the acceleration of the gravity centre of the second limb by applying Eq. (10.62)

$$\mathbf{a}_{G2} = \mathbf{a}_{B2} + \boldsymbol{\alpha}_2 \times \mathbf{B}_2\mathbf{G}_2 + \boldsymbol{\Omega}_2 \times (\boldsymbol{\Omega}_2 \times \mathbf{B}_2\mathbf{G}_2) \quad (10.62)$$

where \mathbf{a}_{B2} is the acceleration of the B_2 point, $\boldsymbol{\alpha}_2$ is the angular acceleration of the second limb, $\mathbf{B}_2\mathbf{G}_2$ is the vector that goes from the point B_2 to the gravity centre of the limb and $\boldsymbol{\Omega}_2$ is the angular velocity of the second limb.

We obtain all the vectors we need to calculate \mathbf{a}_{G_2} . Equation (10.63) gives the acceleration of the B_2 point.

$$\mathbf{a}_{B_2} = \begin{bmatrix} 0 & 0 & \ddot{\rho}_2 \end{bmatrix}^T \quad (10.63)$$

We express $\mathbf{B}_2\mathbf{G}_2$ in the mobile reference system (x_2, y_2, z_2) as Eq. (10.64) and in the fixed reference system as Eq. (10.65)

$$\left[\mathbf{B}_2\mathbf{G}_2\right]^{x_2y_2z_2} = \begin{bmatrix} 0 & 0 & G_{2z} \end{bmatrix}^T \quad (10.64)$$

$$\mathbf{B}_2\mathbf{G}_2 = \mathbf{Rot}_2 \cdot \left[\mathbf{B}_2\mathbf{G}_2\right]^{x_2y_2z_2} \quad (10.65)$$

with \mathbf{Rot}_2 being the rotation matrix that represents the mobile reference systems in the fixed reference system. It is written as Eq. (10.66), where β_2 is the angle between the limb and the vertical, and the resulting value of $\mathbf{B}_2\mathbf{G}_2$ in the fixed frame is given by Eq. (10.67).

$$\mathbf{Rot}_2 = \begin{bmatrix} 1 & 0 & 0 \\ 0 & c\beta_2 & -s\beta_2 \\ 0 & s\beta_2 & c\beta_2 \end{bmatrix} \quad (10.66)$$

$$\mathbf{B}_2\mathbf{G}_2 = \begin{bmatrix} -s\beta_2 \cdot G_{2z} & 0 & c\beta_2 \cdot G_{2z} \end{bmatrix}^T \quad (10.67)$$

The angular velocity and the angular acceleration of the second limb in the fixed frame are given by Eq. (10.68) and Eq. (10.69), respectively.

$$\boldsymbol{\Omega}_2 = \begin{bmatrix} \dot{\beta}_2 & 0 & 0 \end{bmatrix}^T \quad (10.68)$$

$$\boldsymbol{\alpha}_2 = \begin{bmatrix} \ddot{\beta}_2 & 0 & 0 \end{bmatrix}^T \quad (10.69)$$

We now write the expression of \mathbf{a}_{G_2} as Eq. (10.70).

$$\mathbf{a}_{G_2} = \begin{bmatrix} 0 \\ 0 \\ \ddot{\rho}_2 \end{bmatrix} + \begin{bmatrix} \ddot{\beta}_2 \\ 0 \\ 0 \end{bmatrix} \times \begin{bmatrix} 0 \\ -G_{2z} \cdot s\beta_2 \\ G_{2z} \cdot c\beta_2 \end{bmatrix} + \begin{bmatrix} \dot{\beta}_2 \\ 0 \\ 0 \end{bmatrix} \times \left(\begin{bmatrix} \dot{\beta}_2 \\ 0 \\ 0 \end{bmatrix} \times \begin{bmatrix} 0 \\ -G_{2z} \cdot s\beta_2 \\ G_{2z} \cdot c\beta_2 \end{bmatrix} \right) \quad (10.70)$$

We split Eq. (10.70) up and get the components of \mathbf{a}_{G_2} , given by Eq. (10.71).

$$\begin{aligned} a_{2x} &= 0 \\ a_{2y} &= -(\dot{\beta}_2^2 \cdot G_{2z} \cdot c\beta_2 + \ddot{\beta}_2 \cdot G_{2z} \cdot c\beta_2) \\ a_{2z} &= \ddot{\rho}_2 + \ddot{\beta}_2 \cdot G_{2z} \cdot c\beta_2 - \dot{\beta}_2^2 \cdot G_{2z} \cdot c\beta_2 \end{aligned} \quad (10.71)$$

With the value of the components of \mathbf{a}_{G_2} , we write Eq. (10.59), Eq. (10.60) and Eq. (10.61).

We obtain three more equations of the system by applying the angular momentum theorem to the second limb, as expressed in Eq. (10.72)

$$\mathbf{N}_{G_2} = \sum [\mathbf{d}_2 \times \mathbf{F}_2 + \mathbf{M}_2]^{xyz} = \left[\frac{d\mathbf{H}_{G_2}}{dt} \right]^{xyz} \quad (10.72)$$

with $\sum [\mathbf{d}_2 \times \mathbf{F}_2 + \mathbf{M}_2]^{xyz}$ being the sum of momentum in the second limb in the fixed reference system and $\left[\frac{d\mathbf{H}_{G_2}}{dt} \right]^{xyz}$ being the derivative of the angular momentum in the fixed frame. We first calculate the derivative of the angular momentum and then the sum of momentum.

Equation (10.73) gives the angular momentum for the second limb in the mobile reference system ($x_{G_2}, y_{G_2}, z_{G_2}$)

$$[\mathbf{H}_{G_2}]^{x_{G_2}y_{G_2}z_{G_2}} = \mathbf{I}_{G_2} \cdot \boldsymbol{\Omega}_2 \quad (10.73)$$

\mathbf{I}_{G_2} being the inertia matrix in G_2 and $\boldsymbol{\omega}_2$ being the angular velocity of the second limb in the ($x_{G_2}, y_{G_2}, z_{G_2}$) mobile reference system.

According to this, the derivative of the angular momentum in the mobile reference system is given by Eq. (10.74).

$$\left[\frac{d\mathbf{H}_{G_2}}{dt} \right]^{x_{G_2}y_{G_2}z_{G_2}} = \mathbf{I}_G \cdot \alpha_2 + \boldsymbol{\Omega}_2 \times \mathbf{H}_{G_2} \quad (10.74)$$

We substitute the corresponding vectors in Eq. (10.74) and get Eq. (10.75). Its result is given by Eq. (10.76).

$$\left[\frac{d\mathbf{H}_{G2}}{dt} \right]^{x_{G2}y_{G2}z_{G2}} = \begin{bmatrix} I_{u2} & 0 & 0 \\ 0 & I_{v2} & 0 \\ 0 & 0 & I_{w2} \end{bmatrix} \cdot \begin{bmatrix} \ddot{\beta}_2 \\ 0 \\ 0 \end{bmatrix} + \begin{bmatrix} \dot{\beta}_2 \\ 0 \\ 0 \end{bmatrix} \times \begin{bmatrix} I_{u2} \cdot \ddot{\beta}_2 \\ 0 \\ 0 \end{bmatrix} \quad (10.75)$$

$$\left[\frac{d\mathbf{H}_{G2}}{dt} \right]^{x_{G2}y_{G2}z_{G2}} = \left[\ddot{\beta}_2 \cdot I_{u2} \quad 0 \quad 0 \right]^T \quad (10.76)$$

We get the derivative for the angular momentum in the fixed frame by multiplying Eq. (10.76) by the rotation matrix \mathbf{Rot}_2 , as shown in Eq. (10.77).

$$\left[\frac{d\mathbf{H}_{G2}}{dt} \right]^{xyz} = \mathbf{Rot}_2 \cdot \left[\frac{d\mathbf{H}_{G2}}{dt} \right]^{x_{G2}y_{G2}z_{G2}} \quad (10.77)$$

The resulting components of the derivative angular momentum are given by Eq. (10.78).

$$\begin{aligned} dH_{2x} &= \ddot{\beta}_2 \cdot I_{u2} \\ dH_{2y} &= 0 \\ dH_{2z} &= 0 \end{aligned} \quad (10.78)$$

We calculate the sum of momentum in the second limb by solving Eq. (10.79).

$$\mathbf{N}_{G2} = \mathbf{G}_2 \mathbf{A}_2 \times \mathbf{F}_{A2} + \mathbf{G}_2 \mathbf{B}_2 \times \mathbf{F}_{B2} + \mathbf{M}_{B2} \quad (10.79)$$

Equation (10.80) gives the value of $\mathbf{G}_2 \mathbf{A}_2$ in the mobile reference system (x_2, y_2, z_2) .

$$\left[\mathbf{G}_2 \mathbf{A}_2 \right]^{x_2 y_2 z_2} = \left[0 \quad 0 \quad L_2 - G_{2z} \right]^T \quad (10.80)$$

We get the value of $\mathbf{G}_2\mathbf{A}_2$ in the fixed reference system by multiplying Eq. (10.80) by the rotation matrix \mathbf{Rot}_2 , as see in Eq. (10.81). The result is given by Eq. (10.82).

$$\mathbf{G}_2\mathbf{A}_2 = \mathbf{Rot}_2 \cdot [\mathbf{G}_2\mathbf{A}_2]^{x_2y_2z_2} \quad (10.81)$$

$$\mathbf{G}_2\mathbf{A}_2 = \begin{bmatrix} 0 & -(L_2 - G_{2z}) \cdot s\beta_2 & (L_2 - G_{2z}) \cdot c\beta_2 \end{bmatrix}^T \quad (10.82)$$

By taking Eq. (10.82) and the forces and momentums in the second limb – shown in Fig. 10.1 – into account we write Eq. (10.79) as Eq. (10.83).

$$\mathbf{N}_{G_2} = \begin{bmatrix} 0 \\ -(L_2 - G_{2z}) \cdot s\beta_2 \\ (L_2 - G_{2z}) \cdot c\beta_2 \end{bmatrix} \times \begin{bmatrix} F_{A2x} \\ F_{A2y} \\ F_{A2z} \end{bmatrix} + \begin{bmatrix} 0 \\ G_{2z} \cdot s\beta_2 \\ -G_{2z} \cdot c\beta_2 \end{bmatrix} \times \begin{bmatrix} F_{B2x} \\ F_{B2y} \\ F_{B2z} \end{bmatrix} + \begin{bmatrix} 0 \\ M_{B2y} \\ M_{B2z} \end{bmatrix} \quad (10.83)$$

We split Eq. (10.83) up and get the components of \mathbf{N}_{G_2} , given by Eq. (10.84).

$$\begin{aligned} \mathbf{N}_{G_{2x}} &= -(L_2 - G_{2z}) \cdot (s\beta_2 \cdot F_{A2z} + c\beta_2 \cdot F_{A2y}) + \\ &\quad + G_{2z} \cdot (s\beta_2 \cdot F_{B2z} + c\beta_2 \cdot F_{B2y}) \\ \mathbf{N}_{G_{2y}} &= (L_2 - G_{2z}) \cdot c\beta_2 \cdot F_{A2x} - G_{2z} \cdot c\beta_2 \cdot F_{B2x} \\ \mathbf{N}_{G_{2z}} &= (L_2 - G_{2z}) \cdot s\beta_2 \cdot F_{A2x} - G_{2z} \cdot s\beta_2 \cdot F_{B2x} + M_{B2z} \end{aligned} \quad (10.84)$$

We make Eq. (10.78) and Eq. (10.84) equal and get the three next equations of the system we have to solve – Eq. (10.85), Eq. (10.86) and Eq. (10.87).

$$\begin{aligned} &-(L_2 - G_{2z}) \cdot (s\beta_2 \cdot F_{A2z} + c\beta_2 \cdot F_{A2y}) + \\ &\quad + G_{2z} \cdot (s\beta_2 \cdot F_{B2z} + c\beta_2 \cdot F_{B2y}) = \ddot{\beta}_2 \cdot I_{u2} \end{aligned} \quad (10.85)$$

$$(L_2 - G_{2z}) \cdot c\beta_2 \cdot F_{A2x} - G_{2z} \cdot c\beta_2 \cdot F_{B2x} = 0 \quad (10.86)$$

$$(L_2 - G_{2z}) \cdot s\beta_2 \cdot F_{A2x} - G_{2z} \cdot s\beta_2 \cdot F_{B2x} + M_{B2z} = 0 \quad (10.87)$$

10.2.4. Dynamic analysis of limb 3

The sum of forces in the third limb must be equal to the mass of the limb multiplied by the acceleration of its gravity centre. Equation (10.88) shows this condition

$$\sum \mathbf{F}_3 = m_3 \cdot \mathbf{a}_{G3} \quad (10.88)$$

where $\sum \mathbf{F}_3$ is the sum of forces in the third limb, m_3 is the mass of the limb and \mathbf{a}_{G3} is the linear acceleration of the gravity centre of the limb. We see the forces in the third limb in Fig. 10.1. Taking them into account, we write the next three equations of the system to be solved – Eq. (10.89), Eq. (10.90) and Eq. (10.91).

$$F_{B3x} - F_{A3x} = m_3 \cdot a_{G3x} \quad (10.89)$$

$$F_{B3y} - F_{A3y} = m_3 \cdot a_{G3y} \quad (10.90)$$

$$F_{B3z} - F_{A3z} = m_3 \cdot a_{G3z} + m_3 \cdot g \quad (10.91)$$

Equation (10.92) gives the acceleration of the gravity centre of the third limb

$$\mathbf{a}_{G3} = \mathbf{a}_{B3} + \boldsymbol{\alpha}_3 \times \mathbf{B}_3\mathbf{G}_3 + \boldsymbol{\Omega}_3 \times (\boldsymbol{\Omega}_3 \times \mathbf{B}_3\mathbf{G}_3) \quad (10.92)$$

where \mathbf{a}_{B3} is the acceleration of the B_3 point, $\boldsymbol{\alpha}_3$ is the angular acceleration of the third limb, $\mathbf{B}_3\mathbf{G}_3$ is the vector that goes from B_3 to G_3 and $\boldsymbol{\Omega}_3$ is the angular velocity of the limb.

The acceleration of the B_3 point is given by Eq. (10.93).

$$\mathbf{a}_{B3} = \begin{bmatrix} 0 & 0 & \ddot{\rho}_3 \end{bmatrix}^T \quad (10.93)$$

The value of $\mathbf{B}_3\mathbf{G}_3$ in the mobile reference system (x_3, y_3, z_3) is given by Eq. (10.94).

$$\left[\mathbf{B}_3\mathbf{G}_3 \right]^{x_3y_3z_3} = \begin{bmatrix} 0 & 0 & G_{3z} \end{bmatrix}^T \quad (10.94)$$

We get $\mathbf{B}_3\mathbf{G}_3$ in the fixed reference system by applying Eq. (10.95)

$$\mathbf{B}_3\mathbf{G}_3 = \mathbf{Rot}_3 \cdot \left[\mathbf{B}_3\mathbf{G}_3 \right]^{x_3y_3z_3} \quad (10.95)$$

with \mathbf{Rot}_3 being the rotation matrix that expresses the mobile reference systems in the fixed reference, which is given by Eq. (10.96). The resulting value of $\mathbf{B}_3\mathbf{G}_3$ in the fixed reference system is given by Eq. (10.97).

$$\mathbf{Rot}_3 = \begin{bmatrix} c\beta_3 & 0 & s\beta_3 \\ 0 & 1 & 0 \\ -s\beta_3 & 0 & c\beta_3 \end{bmatrix} \quad (10.96)$$

$$\mathbf{B}_3\mathbf{G}_3 = \begin{bmatrix} s\beta_3 \cdot G_{3z} & 0 & c\beta_3 \cdot G_{3z} \end{bmatrix}^T \quad (10.97)$$

The angular velocity and acceleration of the third limb in the fixed reference system are given by Eq. (10.98) and Eq. (10.99), respectively.

$$\boldsymbol{\Omega}_3 = \begin{bmatrix} 0 & \dot{\beta}_3 & 0 \end{bmatrix}^T \quad (10.98)$$

$$\boldsymbol{\alpha}_3 = \begin{bmatrix} 0 & \ddot{\beta}_3 & 0 \end{bmatrix}^T \quad (10.99)$$

We substitute the value of the obtained vectors in Eq. (10.92) and get the value of \mathbf{a}_{G3} , as seen in Eq. (10.100).

$$\mathbf{a}_{G3} = \begin{bmatrix} 0 \\ 0 \\ \ddot{\rho}_3 \end{bmatrix} + \begin{bmatrix} 0 \\ \ddot{\beta}_3 \\ 0 \end{bmatrix} \times \begin{bmatrix} (G_{3z} \cdot s\beta_3) \\ 0 \\ G_{3z} \cdot c\beta_3 \end{bmatrix} + \begin{bmatrix} 0 \\ \dot{\beta}_3 \\ 0 \end{bmatrix} \times \left(\begin{bmatrix} 0 \\ \dot{\beta}_3 \\ 0 \end{bmatrix} \times \begin{bmatrix} G_{3z} \cdot s\beta_3 \\ 0 \\ G_{3z} \cdot c\beta_3 \end{bmatrix} \right) \quad (10.100)$$

We split Eq. (10.100) up and get the components of \mathbf{a}_{G3} , given by Eq. (10.101).

$$\begin{aligned} a_{G3x} &= G_{3z} \cdot c\beta_3 \cdot \ddot{\beta}_3 - G_{3z} \cdot s\beta_3 \cdot \dot{\beta}_3^2 \\ a_{G3y} &= 0 \\ a_{G3z} &= \ddot{\rho}_3 - G_{3z} \cdot s\beta_3 \cdot \ddot{\beta}_3 - G_{3z} \cdot c\beta_3 \cdot \dot{\beta}_3^2 \end{aligned} \quad (10.101)$$

We obtain the last three equations of the system we have to solve by applying the angular momentum theorem for the third limb, expressed by Eq. (10.109)

$$\mathbf{N}_{G3} = \sum [\mathbf{d}_3 \times \mathbf{F}_3 + \mathbf{M}_i]^{xyz} = \left[\frac{d\mathbf{H}_{G3}}{dt} \right]^{xyz} \quad (10.102)$$

where $\sum [\mathbf{d}_3 \times \mathbf{F}_3 + \mathbf{M}_3]^{xyz}$ is the sum of momentum for the third limb and $\left[\frac{d\mathbf{H}_{G3}}{dt} \right]^{xyz}$ is the derivative of the angular momentum, both in the fixed frame. We first obtain the derivative of the angular momentum and then the sum of momentums.

The angular momentum for the third limb in the mobile reference system (x_{G3}, y_{G3}, z_{G3}) is given by Eq. (10.103)

$$[\mathbf{H}_{G3}]^{x_{G3}y_{G3}z_{G3}} = \mathbf{I}_{G3} \cdot \boldsymbol{\Omega}_3 \quad (10.103)$$

where \mathbf{I}_{G3} is the inertia matrix in G_3 and $\boldsymbol{\omega}_3$ is the angular velocity of the third limb in the (x_{G3}, y_{G3}, z_{G3}) mobile reference system.

We express the derivative of the angular momentum in the reference system (x_{G3}, y_{G3}, z_{G3}) as Eq. (10.104).

$$\left[\frac{d\mathbf{H}_{G3}}{dt} \right]^{x_{G3}y_{G3}z_{G3}} = \mathbf{I}_G \cdot \boldsymbol{\alpha}_3 + \boldsymbol{\Omega}_3 \times \mathbf{H}_{G3} \quad (10.104)$$

By substituting the corresponding values we get Eq. (10.105), the result being Eq. (10.106).

$$\left[\frac{d\mathbf{H}_{G3}}{dt} \right]^{x_{G3}y_{G3}z_{G3}} = \begin{bmatrix} I_{u3} & 0 & 0 \\ 0 & I_{v3} & 0 \\ 0 & 0 & I_{w3} \end{bmatrix} \cdot \begin{bmatrix} 0 \\ \ddot{\beta}_3 \\ 0 \end{bmatrix} + \begin{bmatrix} 0 \\ \dot{\beta}_3 \\ 0 \end{bmatrix} \times \begin{bmatrix} 0 \\ I_{v3} \cdot \ddot{\beta}_3 \\ 0 \end{bmatrix} \quad (10.105)$$

$$\left[\frac{d\mathbf{H}_{G3}}{dt} \right]^{x_{G3}y_{G3}z_{G3}} = \begin{bmatrix} 0 & \dot{\beta}_3 \cdot I_{v3} & 0 \end{bmatrix}^T \quad (10.106)$$

We multiply Eq. (10.106) by the rotation matrix \mathbf{Rot}_3 and get the derivative of the angular momentum in the fixed reference system, as shown in Eq. (10.107).

$$\left[\frac{d\mathbf{H}_{G3}}{dt} \right]^{xyz} = \mathbf{Rot}_3 \cdot \left[\frac{d\mathbf{H}_{G3}}{dt} \right]^{x_{G3}y_{G3}z_{G3}} \quad (10.107)$$

The resulting components of the derivative of the angular momentum in the fixed reference system is given by Eq. (10.108).

$$\begin{aligned} dH_{3x} &= 0 \\ dH_{3y} &= \ddot{\beta}_3 \cdot I_{v3} \\ dH_{3z} &= 0 \end{aligned} \quad (10.108)$$

We obtain now the sum of momentum in the third limb by applying Eq. (10.109).

$$\mathbf{N}_{G3} = \mathbf{G}_3\mathbf{A}_3 \times \mathbf{F}_{A3} + \mathbf{G}_3\mathbf{B}_3 \times \mathbf{F}_{B3} + \mathbf{M}_{B3} \quad (10.109)$$

The value of $\mathbf{G}_3\mathbf{A}_3$ in the mobile reference system (x_3, y_3, z_3) is shown in Eq. (10.110).

$$\left[\mathbf{G}_3\mathbf{A}_3 \right]^{x_3y_3z_3} = \begin{bmatrix} 0 & 0 & L_3 - G_{3z} \end{bmatrix}^T \quad (10.110)$$

We get the value of $\mathbf{G}_3\mathbf{A}_3$ in the fixed reference system by multiplying Eq. (10.110) by the rotation matrix \mathbf{Rot} as shown in Eq. (10.111). The result is given by Eq. (10.112).

$$\mathbf{G}_3\mathbf{A}_3 = \mathbf{Rot}_3 \cdot \left[\mathbf{G}_3\mathbf{A}_3 \right]^{x_3y_3z_3} \quad (10.111)$$

$$\mathbf{G}_3\mathbf{A}_3 = \begin{bmatrix} (L_3 - G_{3z}) \cdot s\beta_3 & 0 & (L_3 - G_{3z}) \cdot c\beta_3 \end{bmatrix}^T \quad (10.112)$$

We replace the corresponding vectors in Eq. (10.109) and obtain Eq. (10.113).

$$N_{G3} = \begin{bmatrix} (L_3 - G_{3z}) \cdot s\beta_3 \\ 0 \\ (L_3 - G_{3z}) \cdot c\beta_3 \end{bmatrix} \times \begin{bmatrix} F_{A3x} \\ F_{A3y} \\ F_{A3z} \end{bmatrix} + \begin{bmatrix} -G_{3z} \cdot s\beta_3 \\ 0 \\ -G_{3z} \cdot c\beta_3 \end{bmatrix} \times \begin{bmatrix} F_{B3x} \\ F_{B3y} \\ F_{B3z} \end{bmatrix} + \begin{bmatrix} M_{B3x} \\ 0 \\ M_{B3z} \end{bmatrix} \quad (10.113)$$

We get the components of \mathbf{N}_{G3} by making the component of Eq. (10.113) equal, as shown in Eq. (10.114).

$$\begin{aligned} N_{G3x} &= -(L_3 - G_{3z}) \cdot c\beta_3 \cdot F_{A3y} + G_{3z} \cdot c\beta_3 \cdot F_{B3y} + M_{B3x} \\ N_{G3y} &= (L_3 - G_{3z}) \cdot c\beta_3 \cdot F_{A3x} - (L_3 - G_{3z}) \cdot s\beta_3 \cdot F_{A3z} - \\ &\quad - G_{3z} \cdot c\beta_3 \cdot F_{B3x} + G_{3z} \cdot s\beta_3 \cdot F_{B3z} \\ N_{G3z} &= (L_3 - G_{3z}) \cdot s\beta_3 \cdot F_{A3y} - G_{3z} \cdot s\beta_3 \cdot F_{B3y} + M_{B3z} \end{aligned} \quad (10.114)$$

We substitute the obtained values in Eq. (10.109) and get the last three equations of the system – Eq. (10.115), Eq. (10.116) and Eq. (10.117).

$$-(L_3 - G_{3z}) \cdot c\beta_3 \cdot F_{A3y} + G_{3z} \cdot c\beta_3 \cdot F_{B3y} + M_{B3x} = 0 \quad (10.115)$$

$$\begin{aligned} (L_3 - G_{3z}) \cdot c\beta_3 \cdot F_{A3x} - (L_3 - G_{3z}) \cdot s\beta_3 \cdot F_{A3z} - \\ - G_{3z} \cdot c\beta_3 \cdot F_{B3x} + G_{3z} \cdot s\beta_3 \cdot F_{B3z} = \ddot{\beta}_3 \cdot I_{v3} \end{aligned} \quad (10.116)$$

$$(L_3 - G_{3z}) \cdot s\beta_3 \cdot F_{A3y} - G_{3z} \cdot s\beta_3 \cdot F_{B3y} + M_{B3z} = 0 \quad (10.117)$$

Thanks to this development, we have a 24 equation system and 24 unknown variables. The equations of the system are Eq. (10.3)-(10.5), Eq. (10.25)-(10.27), Eq. (10.29)-(10.31), Eq. (10.55)-(10.57), Eq. (10.59)-(10.61), Eq. (10.85)-(10.87), Eq. (10.89)-(10.91) and Eq. (10.115)-(10.117). We express the system by using the expression $\mathbf{A} \cdot \mathbf{f} = \mathbf{C}$, where \mathbf{f} is the vector with all the reactions, \mathbf{A} is the matrix with the coefficients that

multiply the forces and \mathbf{c} is the independent term. Equation (10.118), Eq. (10.119) and Eq. (10.120) give the expressions of \mathbf{f} , \mathbf{A} and \mathbf{C} , respectively.

$$\mathbf{f} = \left[F_{A1x} \quad F_{A1y} \quad F_{A1z} \quad F_{A2x} \quad \dots \quad F_{B3z} \quad M_{B3x} \quad M_{B3z} \right]^T \quad (10.118)$$

$$\mathbf{A} = \begin{bmatrix} a_{1,1} & a_{1,2} & \dots & a_{1,24} \\ a_{2,1} & a_{2,2} & \dots & a_{2,24} \\ \dots & \dots & \dots & \dots \\ a_{24,1} & a_{24,2} & \dots & a_{24,24} \end{bmatrix} \quad (10.119)$$

$$\mathbf{c} = \left[m \cdot a_{Gx} \quad m \cdot a_{Gy} \quad m \cdot a_{Gz} + m \cdot g \quad \dots \quad 0 \quad \ddot{\beta}_3 \cdot I_{v3} \quad 0 \right]^T \quad (10.120)$$

The non-null components of \mathbf{A} are given by Eq. (10.121).

$$\begin{aligned}
& a_{1,1} = 1 & a_{1,4} = 1 & a_{1,7} = 1 \\
& a_{2,2} = 1 & a_{2,5} = 1 & a_{2,8} = 1 \\
& a_{3,3} = 1 & a_{3,6} = 1 & a_{3,9} = 1 \\
& a_{4,2} = R \cdot s\theta + G_y c\theta s\psi & a_{4,3} = -G_y c\psi & a_{4,5} = -(R - G_y) c\theta s\psi \\
& a_{4,6} = (R - G_y c\psi) & a_{4,8} = -Rs\theta + G_y c\theta s\psi & a_{4,9} = -G_y c\psi \\
& a_{5,1} = -Rs\theta - G_y c\theta s\psi & a_{5,3} = -Rc\theta + G_y s\theta s\psi & a_{5,4} = (R - G_y) c\theta s\psi \\
& a_{5,6} = -(R - G_y) s\theta s\psi & a_{5,7} = Rs\theta - G_y c\theta s\psi & a_{5,9} = Rc\theta + G_y s\theta s\psi \\
& a_{6,1} = G_y c\psi & a_{6,2} = Rc\theta - G_y s\theta s\psi & a_{6,4} = -(R - G_y) c\psi \\
& a_{6,5} = (R - G_y) s\theta s\psi & a_{6,7} = G_y c\psi & a_{6,8} = -Rc\theta - G_y s\theta s\psi \\
& a_{7,1} = -1 & a_{7,10} = 1 & a_{8,2} = -1 \\
& a_{8,11} = 1 & a_{9,3} = -1 & a_{9,12} = 1 \\
& a_{10,2} = (L - G_{1z}) c\beta_1 & a_{10,11} = G_{1z} c\beta_1 & a_{10,13} = 1 \\
& a_{11,1} = -(L - G_{1z}) c\beta_1 & a_{11,3} = -(L - G_{1z}) s\beta_1 & a_{11,10} = -G_{1z} c\beta_1 \\
& a_{11,12} = -G_{1z} s\beta_1 & a_{12,2} = (L - G_{1z}) s\beta_1 & a_{12,11} = G_{1z} s\beta_1 \\
& a_{12,14} = 1 & a_{13,4} = -1 & a_{13,15} = 1 \\
& a_{14,5} = -1 & a_{14,16} = 1 & a_{15,6} = -1 \\
& a_{15,17} = 1 & a_{16,5} = (L - G_{2z}) c\beta_2 & a_{16,6} = (L - G_{2z}) s\beta_2 \\
& a_{16,16} = G_{2z} c\beta_2 & a_{16,17} = G_{2z} s\beta_2 & a_{17,4} = -(L - G_{2z}) c\beta_2 \\
& a_{17,15} = -G_{2z} c\beta_2 & a_{17,18} = 1 & a_{18,4} = -(L - G_{2z}) s\beta_2 \\
& a_{18,15} = -G_{2z} s\beta_2 & a_{18,19} = 1 & a_{19,7} = -1 \\
& a_{19,20} = 1 & a_{20,8} = -1 & a_{20,21} = 1 \\
& a_{21,9} = -1 & a_{21,22} = 1 & a_{22,8} = (L - G_{3z}) c\beta_3 \\
& a_{22,21} = G_{3z} c\beta_3 & a_{22,23} = 1 & a_{23,7} = -(L - G_{3z}) c\beta_3 \\
& a_{23,9} = (L - G_{3z}) s\beta_3 & a_{23,20} = -G_{3z} c\beta_3 & a_{23,22} = G_{3z} s\beta_3 \\
& a_{24,8} = -(L - G_{3z}) s\beta_3 & a_{24,21} = -G_{3z} s\beta_3 & a_{24,24} = 1
\end{aligned} \tag{10.121}$$

Part IV

Manipulator Optimization

Optimization Criteria

11.1. Optimization methods in parallel manipulators

The performance of a parallel manipulator is very sensitive to the geometric parameters – a well dimensioned manipulator of any structural type generally improves the performance of a poorly designed manipulator with a structure that may seem more appropriate for the desired task.

Thus, optimization in parallel manipulators is extremely important. The optimization solution depends on the performance or performances we need to optimize. Thus, first of all, we need to define the application of the parallel manipulator we want to design and identify the most influential performances for the specific application.

Depending on the application, certain manipulator performance criteria may be more important than others, as Hüsing et al. [204] remarked. Those performance criteria include design for best position accuracy, design so that the workspace is the biggest possible one or a prescribed one, design for optimum velocity, force, stiffness, dynamic behaviour, manipulability or dexterity throughout the workspace. As Modungwa et al. [205]

highlighted, performance requirements of parallel manipulators may be antagonistic like, for example, the workspace and the accuracy. If so, we can not optimize both performances at the same time, but we can define an *appropriate design*. The objective of the appropriate design is not the optimization of a particular function but to ensure that the manipulator satisfies all the desired requirements.

As we have already seen, the small workspace is one of the biggest drawbacks of parallel manipulators. Thus, many authors have optimized different parallel manipulators in order to obtain a desired workspace. Merlet [14], [206] introduced a numerical procedure to determine all the possible geometries of a 6-DOF Gough-type parallel manipulator whose workspace included a desired one. Laribi et al. [207] proposed a method that combined genetic algorithm and fuzzy logic that obtained the parameters of a DELTA robot for a prescribed cuboid workspace. Kosinska et al. [208] determined the parameters of the DELTA robot for both prescribed cuboid workspace and wee-conditioned workspace. Huang et al. [209] presented an analytical approach to get the actuated joint stroke of a 6-PSS parallel manipulator for a prescribed cylindrical workspace with given orientation capability. Zhao et al. [210] minimized the leg length of parallel manipulators for a desired cylindrical dexterous workspace. Liu et al. [148] presented a performance charts method to determine the parameters of a DELTA robot for desired workspace with prescribed performance indices. Tsai and Joshi [211] proposed an optimization of the 3-PUP parallel manipulator by taking the quality of the workspace into account – they considered the dexterity for each position of the workspace. Zhang and Fang [212] optimized the geometrical parameters of the 3-PRS parallel manipulator to get a specific workspace. Hou and Zhao [213] optimized the 3-PUU parallel manipulator with medicine applications. In this case, optimizing the workspace of the robot was indispensable to improve the requirements of the patients.

Another performance index commonly used to optimize parallel manipulators is the dexterity. Pittens and Podhorodeski [214] maximized the local dexterity of a family of 6-DOF Stewart platform parallel manipula-

tors. Gosselin and Angeles [215] introduced the *global conditioning index* and used it to optimize the global dexterity of parallel 3-DOF planar and spatial manipulators. Barbosa et al. [216] and Lopes et al. [217] used the condition number of the inverse kinematic Jacobian matrix to measure the dexterity and optimize a 6-DOF parallel manipulator by using evolutionary algorithms. Nefzi et al [218] proposed direction-dependent Jacobian indices. They optimized these indices over a demanded workspace and used them in the design process of several parallel manipulators.

Another possibility is to optimize the manipulator for a desired stiffness. This is what Chakarov [219] did – he proposed a topological and dimensional optimization method of manipulators with desired stiffness. Babu et al. [220] presented a multi-objective optimization method for the 3-RPS parallel manipulator that considered the global conditioning index, the global stiffness index and the workspace volume.

The static/dynamic performance has received less attention in the literature, but since one of the main characteristics of parallel manipulators is their high kinematic and dynamic capacities, it is also interesting to take them into account when optimizing a parallel manipulator. The dynamic performance of a parallel manipulator is, generally, better when the mass is the minimum possible. The problem is that a smaller mass can lead to a lower stiffness value or to a smaller size of the elements and, thus, to a smaller workspace. According to that, we usually consider the dynamic performance together with the stiffness and/or the workspace size. Wu et al. [221] developed a dynamic model for spherical parallel manipulators based on the Lagrange multipliers that allows us to calculate the power consumption effectively. Based on this dynamic model, along with the kinematics and the stiffness of the manipulator, they designed a multi-objective optimization method for spherical parallel manipulators. They applied it to a 3-DOF unlimited-roll spherical parallel manipulator and obtained the Pareto-optimal solutions by using a genetic algorithm.

The most common techniques used to solve the optimization problem

are the objective-function based optimal design and the performance chart (atlas). In the objective-function technique we first have to define an objective function with specified constraints and then find the optimal result by applying an optimization algorithm. This technique is time-consuming and, due to the antagonism of performances, it is very difficult to find an optimum solution for multiple criteria. Besides, it is necessary to define an initial value, which is usually complicated.

A performance chart shows the relationship between a performance index and related design parameters in a small space, globally and very visually. In this way, a performance chart can show how antagonistic the chosen criteria are. If we compare the results obtained with this technique with the ones obtained by applying the objective-function technique, we see that the optimum result is more fuzzy when we apply the performance chart. However, the performance chart is more flexible – it provides more than one solution to a design problem. Therefore, the designer can adjust the optimum result by taking the design conditions into account. The most important fact in this technique is the presentation of the performance charts. The biggest drawback is that the value of each parameter of the manipulator can be between zero and infinity. Liu and Wang [222] presented the *parameter-finiteness normalization method* (PFNM) in order to find a solution to the parameter infinity problem. By using this method, they presented a new design methodology for mechanisms with fewer than five linear parameters. The main advantages of their method are that one performance criterion corresponds to a chart, that the optimal solution can consider multi-objective functions and that it guarantees the optimal solution and provides all the possible optimal solutions.

11.2. Optimization criteria proposed

We present two optimization methods to find the best combination of geometry parameters (GP) according to two different criteria.

The first method analyses the useful WS and its regularity for different GP combinations. The best GP combination is the one that leads to the useful WS with the highest regularity. The second method focusses on the power consumption along a given trajectory. In this case, the best GP combination is the one that consumes the lowest power.

We design both methods for any parallel manipulator and, in this work, we show how they perform for the particular case of the 2PRU-1PRS 3 DOF parallel manipulator.

11.2.1. Maximise geometry object in the useful WS

This method studies the useful WS for different GP combinations as well as its regularity. To obtain the WS for different GP combinations, we provide discrete candidate-values for the geometry parameters and create a set with all combinations. We call that set of combinations *StudyVariables*. Checking all *StudyVariables* would lead to high computational cost, but by applying some known particular conditions that the geometry of the manipulator has to fulfil we can reject many of them. We define the set of combinations that fulfil those particular conditions as suitable geometry parameters.

In a same way as explained in Section 8.1, we define discrete candidate-poses for the workspace, the *StudyPoints*, and obtain the useful WS and the largest geometry object (GO) contained in it for each GP combination. Generally, the biggest GO can be placed in more than one position in the useful WS. If that is so, we obtain all the positions where the biggest GO can be placed and label the number of positions where the GO can be as GOP. The best GP combination for the WS is the combination that leads to the useful WS containing the largest GO, GO_{max} . It can also happen

that more than one GP leads to the GO_{max} . In that case, we define the best GP for the WS to be the GP combination that leads to the GO_{max} with highest GOP. Whatever the case may be, we get the set of suitable GP for which the GO in the useful WS is at least $0.5 \cdot GO_{max}$. These suitable GP are the *StudyVariables* for the optimization of the power consumption of the next Section.

The flowchart given in Fig. 11.1 shows the steps to follow in this method:

1. Define the GP combinations.
2. Get the suitable GP combinations.
3. Get the useful WS for each suitable GP combination.
4. Obtain the GO for each GP and the number of positions where it can be placed.
5. Define the GO_{max} as the biggest GO.
6. Define the best GP combination as the one that leads to the GO_{max} .
7. If several GP lead to the GO_{max} , define the best GP combination as the one for which the GO_{max} can be placed in the highest number of positions.

In this work we choose the geometric object to be a sphere. Changing the object to be another geometric entity would yield a different best GP combination.

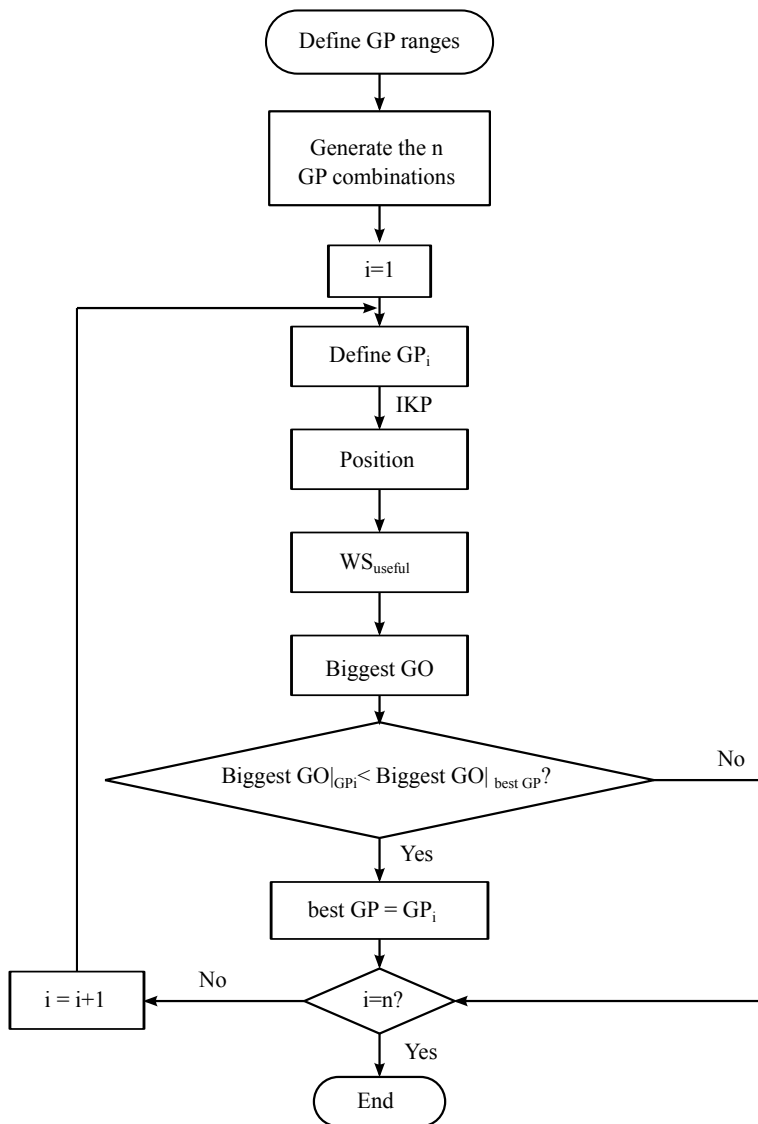


Figure 11.1: Optimization of GP to maximise the GO in the WS

11.2.2. Minimise the power consumption

The second method consists in finding, out of the *StudyVariables*, the GP combination that leads to the lowest power consumption of the motors. It is important to remark that the power consumption depends on the trajectory of the end-effector. Thus, before solving the dynamic problem, we have to define the trajectory of the end-effector for which we want to optimise the GP. Then, we have to solve the inverse dynamic problem and check that all the requirements of the linear guides, gear-heads and motors are fulfilled. This is to say, we have to check that the manipulator can really follow the trajectory we have defined. The GP combinations that fulfil the requirements are suitable GP combinations.

We obtain the power consumption for the suitable GP combinations along the trajectory. We calculate the power consumption as the mean value of the sum of the power required in all actuators. The best GP combination is the one that consumes the lowest power.

According to this, the steps to follow in this second are the ones shown in Fig. 11.2:

1. Get the *StudyVariables*.
2. Define the trajectory of the end-effector.
3. For each *StudyVariables* combination, solve the dynamics problem for the defined trajectory.
4. Check that the requirements of the motors and the linear guides are fulfilled – get the suitable GP combinations.
5. For the suitable GP combinations, obtain the power consumption.
6. Define the best GP combination as the one that leads to the lowest power consumption.

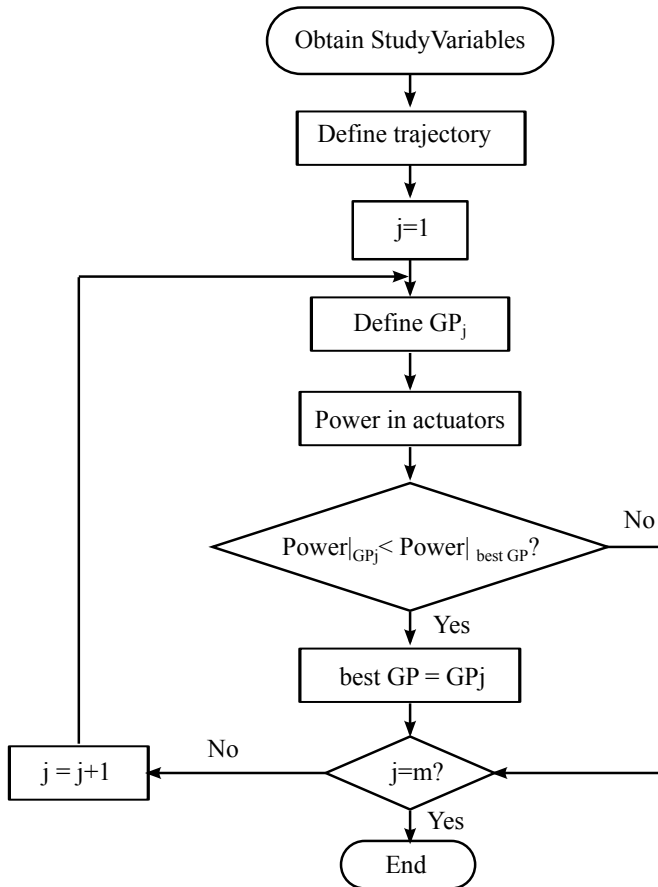


Figure 11.2: Optimization of GP to maximise the GO in the WS

Particular case: 2PRU-1PRS manipulator

In this Chapter we apply the method presented in Chapter 11 to the particular case of our manipulator – the 2PRU-1PRS 3 DOF parallel manipulator. We work with specific motors, planetary gear heads and linear guides. Additionally, we choose the geometric object to be a sphere and the trajectories of the end-effector to be harmonic trajectories.

As we have already seen in previous chapters, the geometry parameters of the 2PRU-1PRS manipulator are:

- H: radius of the fixed platform
- L: length of the limbs
- R: radius of the mobile platform
- t: thickness of the mobile platform
- s: radius of the cross-section of the limbs

We know that the geometry parameters that affect the WS are the radius of the mobile platform, the radius of the fixed platform and the length of the limbs, while the radius of the limbs and the thickness of the

mobile platform do not affect the WS.

12.1. Maximise the sphere in the useful WS of the 2PRU-1PRS

In this Section we get the optimum H, L and R combination to get the useful WS with the biggest sphere in it. The first step is to define set of GP combinations to be studied, the *StudyVariables*. We define the ranges of the geometry parameters as shown in Table 12.1.

Table 12.1: GP ranges for the optimization process

	Description	Value
H (m)	Fixed platform radius	(0.3,0.75)
L (m)	Limbs length	(0.2,0.65)
R (m)	Mobile platform radius	(0.2,0.65)

We define the number of discretizations for each GP to be 10, so we obtain the 1000 GP possible combinations. Optimizing all of them would lead to a very high computational cost, so we apply the restrictions that the geometry of the manipulator has to satisfy.

As we see in Fig. 12.1, the 2PRU-1PRS manipulator can have two configurations depending on the relation between the value of the radius of the mobile platform and the radius of the fixed platform. Figure 12.1a shows the configuration with the radius of the fixed platform bigger than the radius of the mobile platform, while Fig. 12.1b shows the configuration with the radius of the mobile platform bigger than the fixed one. In this work, we study the first configuration, so the *StudyVariables* have to fulfil the condition $H > R$.

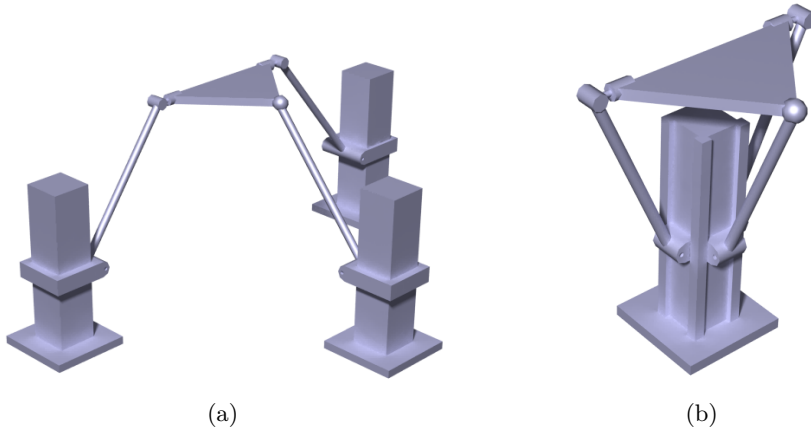


Figure 12.1: Possible configurations (a) $H > R$; (b) $H < R$

We also know that the sum of values of the radius of the mobile platform and the length of the limbs has to be greater than the radius of the fixed platform, $H < L + R$. Accordingly, there are two conditions that we have to apply when defining the suitable GP combinations:

1. The radius of the fixed platform is larger than the radius of the mobile platform, $H > R$
2. The radius of the fixed platform is smaller than the sum of the radius of the mobile platform and the length of the limbs, $H < R + L$

By applying those restrictions, we get only 529 suitable GP combinations. This is to say, the number of GP combinations to check has been reduced by 47.1 %, from the 1000 initial GP combinations to the 529 suitable GP combinations.

Similarly, we obtain the candidate-poses for the workspace, the *StudyPoints*. We define the limits of the space to be checked as shown in Table 12.2. We discretize each axis in 60 points, obtaining a cubic grid of size 60 x 60 x 60.

Thus, the total number of *StudyPoints* is 216000.

Table 12.2: Output limits

	Description	Value
ψ ($^\circ$)	rotation about X-axis	(-90,90)
θ ($^\circ$)	rotation about Y-axis	(-90,90)
z (m)	translation along Z-axis	(0.3,0.8)

We also define the ranges of the linear guides and the spherical joint as seen in the Table 12.3. These values correspond to the real values of the linear guides and spherical joint that we will use to build the prototype, as we will see in Chapter 14.

Table 12.3: Physical restrictions

	Description	Value
LG (m)	linear guide range	(0,0.3)
SJ ($^\circ$)	spherical joint range	(-25,25)

To have an idea of the regularity of the useful WS and be able to determine which solution is the best one, we obtain the useful WS and the biggest sphere in it for each suitable GP combination, S_{jmax} . A WS contains a sphere if the entire sphere is part of the WS. We denote the largest sphere from the set of all S_{jmax} by S_{max} . To know which sphere is the biggest one, we compare the radii of all the spheres. The best GP combination is the one that leads to the useful WS containing the S_{max} . Note that we can have multiple WS_j such that the radius of $S_{jmax} = \text{radius}$

of S_{max} . In that case, the best GP combination is the one that leads to the biggest sphere that can be placed in more number of positions.

For these set ranges, we get the useful WS and the biggest sphere in it for each GP combination. This biggest sphere has a radius of 7 discretization points. Table 12.4 shows the GP combinations that lead to the useful WS containing the biggest sphere and the number of positions where the biggest sphere can be placed.

Table 12.4: GP combinations for biggest sphere in WS

	H (m)	L (m)	R (m)	Sphere Positions
1	0.35	0.25	0.2	4
2	0.4	0.3	0.2	4
3	0.45	0.35	0.2	4
4	0.45	0.4	0.2	2
5	0.5	0.4	0.2	2
6	0.5	0.45	0.2	4
7	0.55	0.45	0.2	2
8	0.55	0.5	0.2	4
9	0.55	0.55	0.2	4
10	0.6	0.55	0.2	4
11	0.6	0.6	0.2	4
12	0.6	0.65	0.2	2
13	0.65	0.55	0.35	2
14	0.65	0.6	0.35	4
15	0.7	0.6	0.25	2

As we see, there are 15 GP combinations that lead to a useful WS

containing the biggest sphere. For 6 of those combinations the center of the biggest sphere can be placed in 2 different positions, while for the other 9 it can be placed in 4 different positions. Thus, there are 9 best GP combinations, given by Table 12.5.

Table 12.5: Best GP combinations for biggest sphere in maximum number of positions in WS

	H (m)	L (m)	R (m)
1	0.35	0.25	0.2
2	0.4	0.3	0.2
3	0.45	0.35	0.2
4	0.5	0.45	0.2
5	0.55	0.5	0.2
6	0.55	0.55	0.2
7	0.6	0.55	0.2
8	0.6	0.6	0.2
9	0.65	0.6	0.35

Figure 12.2 shows two of the best solutions and their WS containing the biggest sphere placed in the first possible position. In Fig. 12.2a we see the manipulator with $H=0.35$ m, $L=0.25$ m and $R=0.2$ m in horizontal position for a $z=0.5$ m. Fig. 12.2b presents the useful WS corresponding to that GP combination and the biggest sphere in it. We see another optimal solution in Fig. 12.2c. In this case the GP is $H=0.6$ m, $L=0.6$ m and $R=0.2$ m. Figure 12.2d shows its useful WS and the biggest sphere. As we can see, even if the biggest sphere is of the same size and it can be placed in the same number of places, the solution for the manipulator as well as the shape and position of the useful WS can be very different.

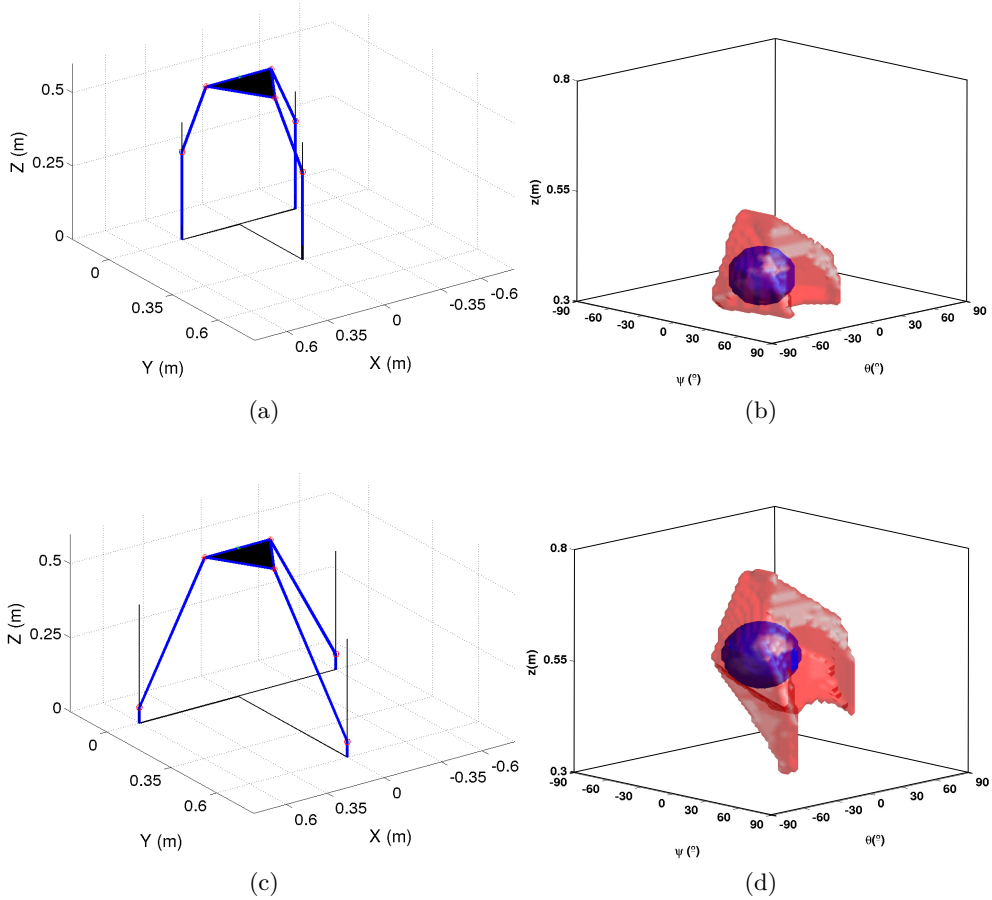


Figure 12.2: Two optimal GP: (a) sketch of $(H, L, R) = (0.35, 0.25, 0.2)$ m; (b) WS_{use} & S_{max} for $(H, L, R) = (0.35, 0.25, 0.2)$ m; (c) sketch of $(H, L, R) = (0.6, 0.6, 0.2)$ m; (d) useful WS & S_{max} for $(H, L, R) = (0.6, 0.6, 0.2)$ m

We get the GP combinations that lead to an useful WS containing a sphere at least $0.5 \cdot S_{max}$ and we label them as the *StudyVariables* for the next optimization method. There are 325 *StudyVariables* combinations in total.

12.2. Minimise the power consumption

In this Section we analyse the suitable GP combinations in order to determine which one is the best GP combination in terms of power consumption. We first define the *StudyVariables* to be the suitable GP combinations. We also define the radius of the limbs and the thickness of the mobile platform as the necessary parameters to solve the dynamic problem. Besides, we have to define the density of each element, and the gravity constant. We consider the material of the mobile platform to be aluminium and the material of the limbs, steel. Table 12.6 gives the value of all these parameters described.

Table 12.6: Parameters

	Definition	Value
ρ_{al} (kg/m ³)	Aluminium density	2710
ρ_{st} (kg/m ³)	Steel density	7850
s (m)	Radius of the limbs	0.005
e (m)	Thickness of the mobile platform	0.004
g (m/ s ²)	Gravity constant	9.81

We work for the motors, gear heads and linear guides that we will use when bulding the prototype. We present their data in Table 12.7 and in Chapter 14 we will justify the choice. We define a GP combination to be suitable in the optimization of the power consumption for a given trajectory when it fulfils all the restrictions of the linear guides, motors and the gear head.

Table 12.7: Motor, gearhead and linear guide data

		Value
Motor-Gear	Nominal current	24 A
	Max. power	150 W
	Max. speed	12000 rpm
	Nominal torque	0.177 Nm
	Reduction Ratio	15
LG	Displacement range	(0, 0.3) m
	Max, velocity	5 m/s
	Radial Load	300 N
	Belt Tension	200 N
	Displacement Ratio	0.07 m/rev

According to this, in order to be a suitable GP combinations for the optimization of the power consumption for a given trajectory, a GP combination has to fulfil the following conditions:

- The displacement of the linear guides has to be in their displacement range: $0 < \rho_i < 0.3$ m
- The velocity of the linear guides has to be lower than their velocity limit: $d\rho_i < 5$ m/s
- The radial load in the linear guides has to be lower than the maximum radial load: $F_{radial_i} < 300$ N
- The axial load in the linear guides has to be lower than the maximum belt tension: $F_{axial} < 200$ N

- The speed of the motors have to be lower than the maximum speed allowed: $Speed_{max} < 12000$ rpm. The expression that gives the speed of the motors is Eq. (12.1),

$$Speed_i = \frac{d\rho_i}{R_{gearhead}} \cdot \frac{60}{2\pi} \cdot Reduction\ Ratio \quad (r.p.m) \quad (12.1)$$

where $R_{gearhead}$ is the radius of the gearhead and we obtain by applying Eq. (12.2).

$$R_{gearhead} = \frac{Displacement\ Ratio}{2\pi} \quad (m) \quad (12.2)$$

- The power required by the motors has to be lower than the maximum power: $Pow_i < 150$ W. We calculate the power that the motors consume by applying Eq. (12.3).

$$Pow_i = d\rho_i \cdot F_{axial_i} \quad (W) \quad (12.3)$$

- The torque supported by the motors can not exceed the maximal possible torque: $T_i < 0.177$ Nm. We get the torque in the motors by solving Eq. (12.4).

$$T_i = \frac{mean(F_{axial_i}) \cdot R_{gearhead}}{Reduction\ Ratio} \quad (N \cdot m) \quad (12.4)$$

We repeat this checking process for each *Study Variables* and get the *suitable* GP combinations for the power optimization proces. We calculate the total power consumption during the studied trajectory for each *suitable* GP combination. The power consumption of one motor over the trajectory is obtained by integrating the power required by that motor over time, as shown in Eq. (12.5). Equation (12.6) gives the expression of the total power consumption, which is the sum of the power consumption of the three actuators.

$$Power\ consumption_i = \int Pot_i(t)dt \quad (W) \quad (12.5)$$

$$Power\ consumption_T = \sum Power\ consumption_i \quad (W) \quad (12.6)$$

We define the best GP combination in terms of power consumption as the *suitable* GP combination that requires the lowest power consumption for the trajectory analysed.

As we see, the power consumption depends on the trajectory of the mobile platform, so we have different solutions of best GP combination for different trajectories. In this work we optimize the manipulator for the three harmonic trajectories given in Table 12.8 – one rotation about X-axis, one rotation about Y-axis and one translation along Z-axis. We set the total time of the trajectory to be 4 seconds and discretize the trajectory in 500 parts, with the time step being 0.008 sec. We choose the frequency and the amplitude values to be the most common used for vehicle control vibration tests in Spain – frequency of 2.7 Hz and amplitude of 3° for the rotation trajectories and 3 m for the translation.

Table 12.8: Harmonic trajectories definition

	$traject(t) = C + A \cdot \sin(\omega t)$			
	C	A	$f = \omega / (2 \cdot \pi)$	t
X- and Y axes	0	3°	2,7 Hz	4 s
Z-axis	0,5 m	0,003 m	2,7 Hz	4 s

12.2.1. Trajectory I

The first trajectory is a rotation about X-axis. We solve the inverse kinematic and dynamic problems for the *Study Variables*. We see that the 325 *Study Variables* fulfil the requirements of the motors and the linear guides and they are, thus, suitable GP combinations. Figure 12.3 shows the total power consumption for all the suitable GP combinations for trajectory I. The GP combination (H, L, R)=(0.75, 0.3 0.6) m is the combination that consumes the most for this trajectory – 7.5687 W. The lowest power

consumption is 0.683 W and it corresponds to the GP combination $(H, L, R)=(0.35, 0.2, 0.2)$ m. Thus, $(H, L, R)=(0.35, 0.2, 0.2)$ m is the best GP combination for trajectory I.

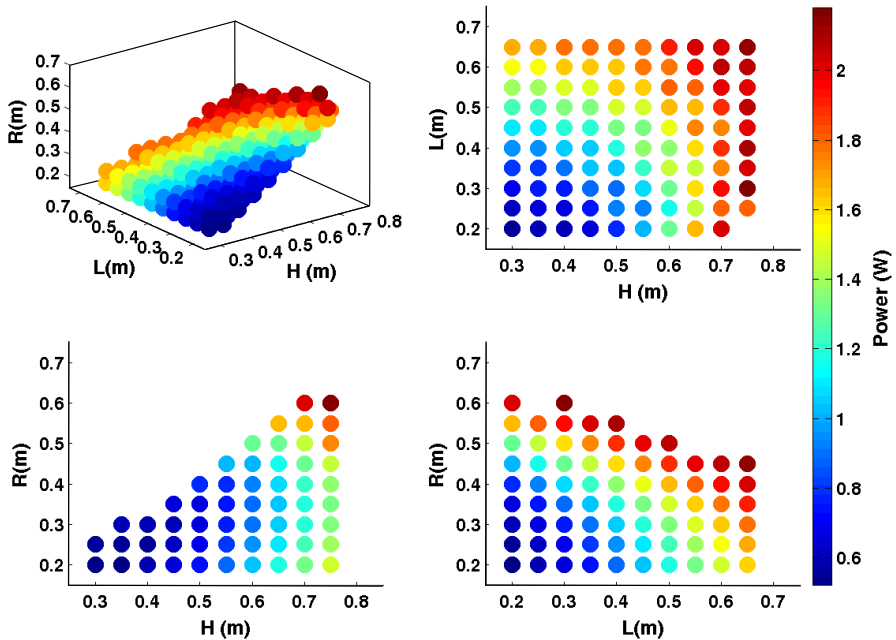


Figure 12.3: Power consumption for all the suitable GP for trajectory I

We now present the results for the best GP. Figure 12.4a and Fig. 12.4b show the displacement and the velocity of the linear guides, respectively. As we see, the displacement of the linear guides is always in their displacement range permitted, $[0, 0.3]$ m, and the velocity is lower than the maximum velocity allowed, 5 m/s. As we see, the first and third actuators do not move, so the speed of the first motor and the third one are null. The mean

value of the speed of the second motor is 1449 r.p.m., much lower than the speed limit of the motors.

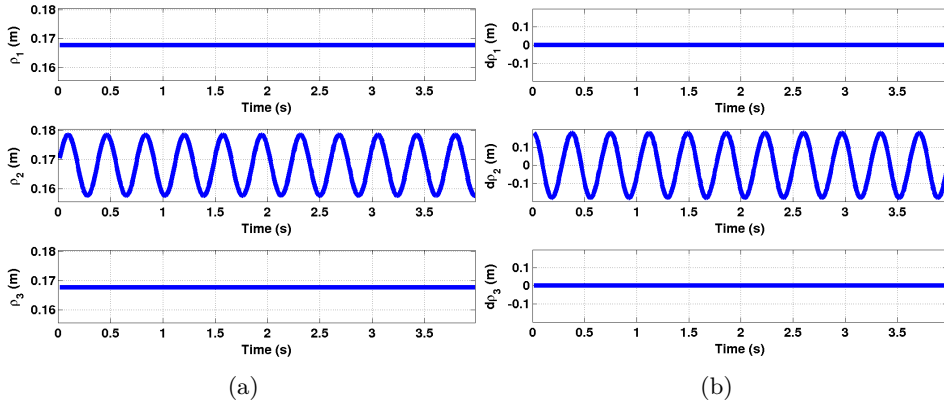


Figure 12.4: Trajectory I: (a) displacement of the linear guides ; (b) velocity of the linear guides

We present the axial force in the linear guides in Fig. 12.5a and the radial force in Fig. 12.5b. As we see, the axial force in the first and third linear is almost constant – it only varies from -1.3725 N to -1.3324 N – while for the second linear guide the variation range is $[-1.7918, -0.9174]$ N. On the contrary, radial force is null and constant for the second linear guide and for the first and third linear guides it varies from -0.5542 N to -0.3107 N. In both cases the forces are under the maximum limits at every moment in the trajectory. The power required by the motors along the trajectory is shown in Fig. 12.5c. It is null for the first and third linear guides and harmonic for the third one. The maximum value it takes is 0.2452 W, so it fulfils the power limitation of the motors. For this trajectory, the mean torque in the motors is 0.001 N · m, lower than T_{max} , so it also fulfils the torque requirement.

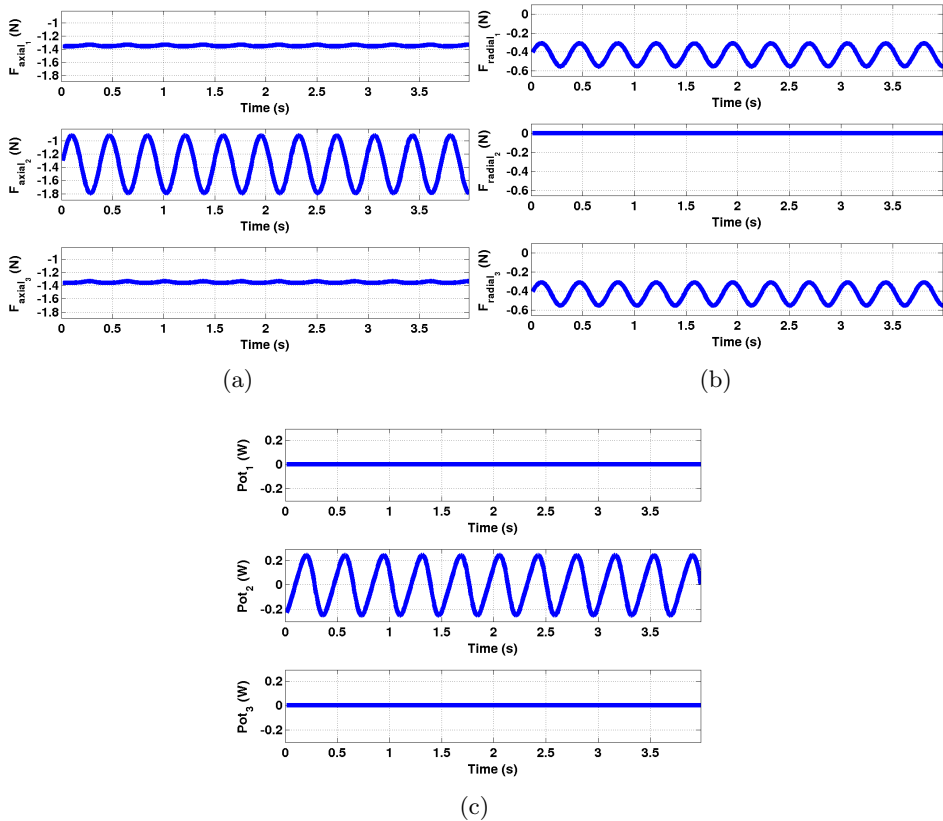


Figure 12.5: Trajectory I: (a) axial force in the linear guides ; (b) radial force in the linear guides; (c) power required by the motors

12.2.2. Trajectory II

The second trajectory is a rotation about Y-axis. We check if the *Study Variables* fulfil the restrictions of the linear guides and motors and see that all of them are suitable GP combinations. We get the total power consumption for all the suitable GP combinations during the harmonic trajectory about Y-axis and we put it in Fig. 12.6. In this case, the highest total power

consumption is 15.0413 W, corresponding again to the GP combination $(H, L, R) = (0.75, 0.3, 0.3)$ m. The lowest total power consumption is 1.2133 W, the best GP combination being, as for trajectory I, $(H, L, R) = (0.35, 0.2, 0.2)$ m.

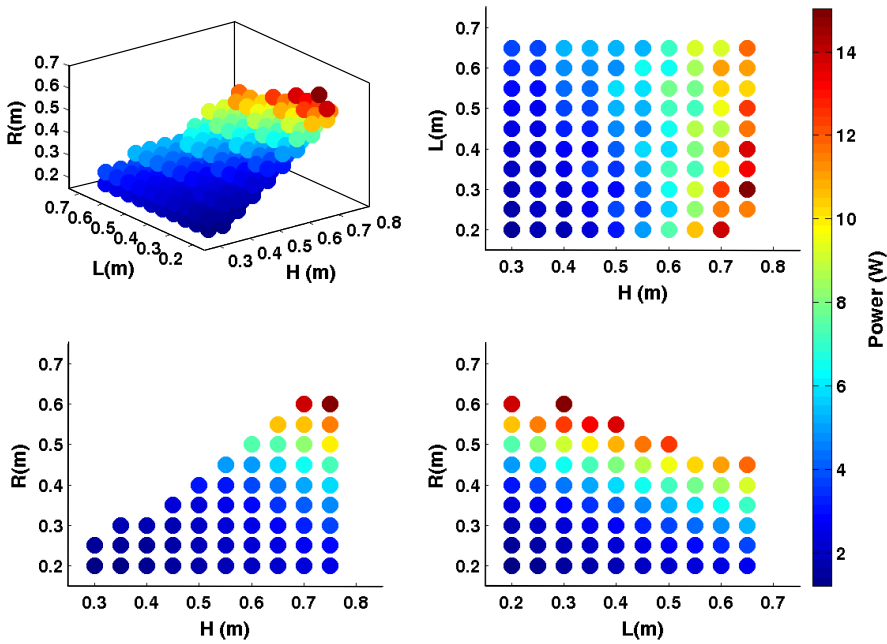


Figure 12.6: Power consumption for all the suitable GP for trajectory II

In Fig. 12.7a we see the displacement of the linear guides during trajectory II and in Fig. 12.7b, their velocity. Along this trajectory the second linear guide is motionless, placed at a distance of 0.1677 m from the reference plane. The first and third linear guides describe a harmonic trajectory with same amplitude and frequency but opposite direction. The maximum displacement value is 0.1785 m and the minimum, 0.1576 m. The velocity of

the second linear guide is null and the velocity of the first and third linear guides is another harmonic trajectory with maximum and minimum values equal to -0.1778 m/s and 0.1778 m/s, respectively. In this way, we see that the displacement range restriction, $(0, 0.3)$ m, as well as the velocity limit restriction, 5 m/s, are fulfilled.

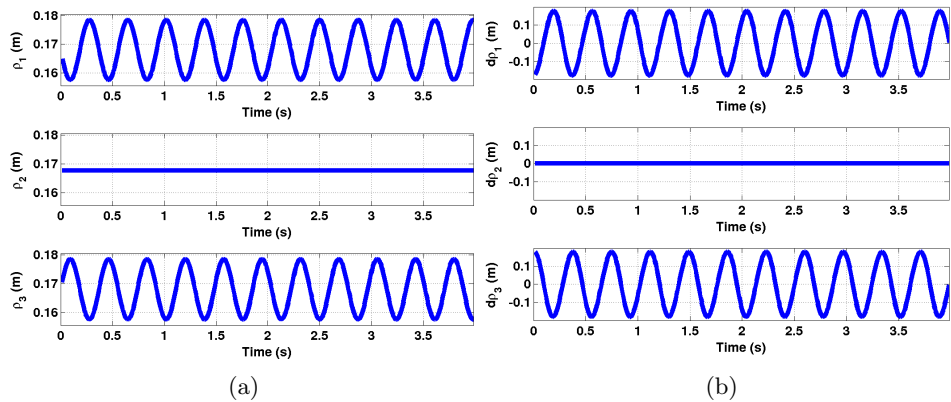


Figure 12.7: Trajectory II: (a) displacement of the linear guides ; (b) velocity of the linear guides

Figure 12.8a shows the axial force in the linear guides. It almost stays constant for the second linear guide, with a minimum value of -1.3508 N and a maximum value of -1.6226 N. However, for the first and third linear guides it varies from -1.7921 N to -0.9172 N following a harmonic function. In Fig. 12.8b we see the radial force in the linear guides. It varies harmonically in the three limbs, but its amplitude is higher for the second one – it varies from -0.6838 N to -0.1304 N for the first and third linear guides and from -0.5379 N to 0.523 N for the second one. For all limbs, both axial and radial forces are lower than the maximum forces that the linear guides can support. In Fig. 12.8c we present the power that the motors require. Since the second linear guide remains motionless, the second motor does not consume power, unlike the first and third ones, that require a maximum

power of 0.2452 W. This value is lower than the maximum power that the motors can provide. Accordingly, the mean torque in the first and third motors is 0.001 N · m and in the second motor, $9.929 \cdot 10^{-4}$ N · m. Finally, we calculate the mean speed of the motors – it is 1450 r.p.m. for the first and third motors and 0 r.p.m. for the second one.

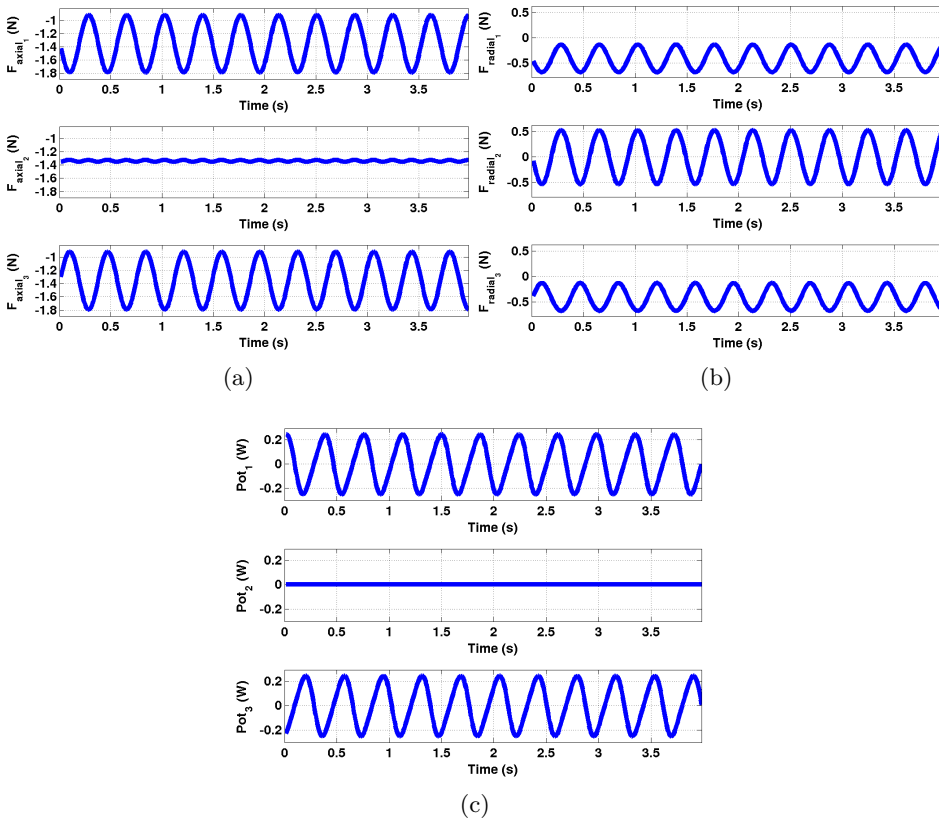


Figure 12.8: Trajectory II: (a) axial force in the linear guides ; (b) radial force in the linear guides

12.2.3. Trajectory III

Trajectory III is a translation along Z-axis. We solve the inverse kinematic and dynamic problems and check that in this case also all the *Study Variables* are suitable GP combinations. We get the total power consumption for each suitable GP combination and see that the GP combination that consumes the highest power is once more $(H, L, R) = (0.75, 0.3, 0.6)$ m – it consumes a total power of 2.1812 W. For this trajectory, we have two best GP combinations – $(H, L, R) = (0.35, 0.2, 0.2)$ m and $(H, L, R) = (0.3, 0.2, 0.2)$ m. Both combinations consume a total power of 0.5224 W. Figure 12.9 shows the power consumption for each suitable GP combination.

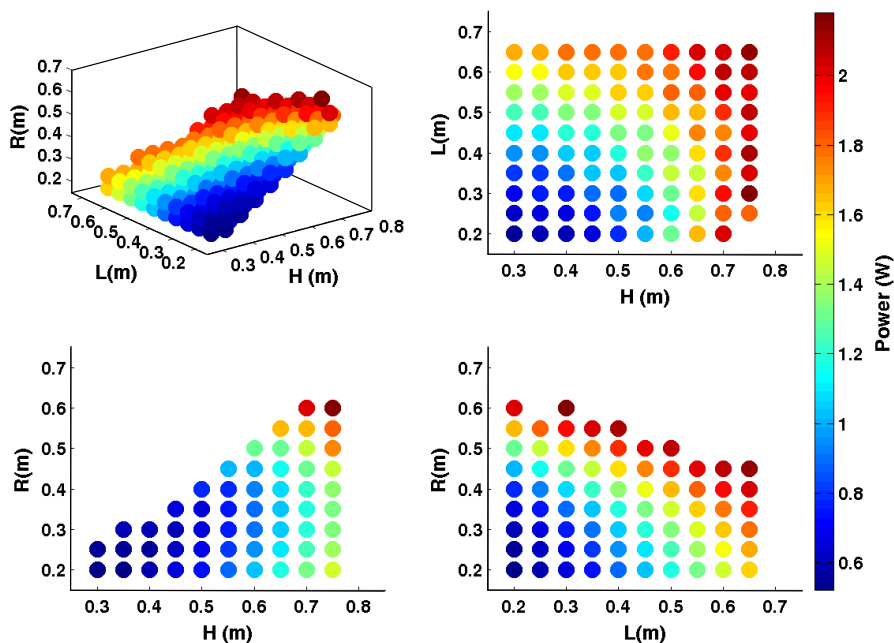


Figure 12.9: Power in the actuators for all the suitable the best GP for translation about Z-axis

We solve the inverse kinematic and dynamic problems for the best GP combination. Because of the symmetry of the manipulator, the values obtained in the linear guides and the motors have to be the same for the three limbs. Figure 12.10a presents the displacement of the linear guides, while Fig. 12.10b shows their velocity. They both follow a harmonic function, the minimum and maximum values being $[0.1647, 0.1707]$ m for the displacement and $[-0.0509, 0.0509]$ m/s for the velocity.

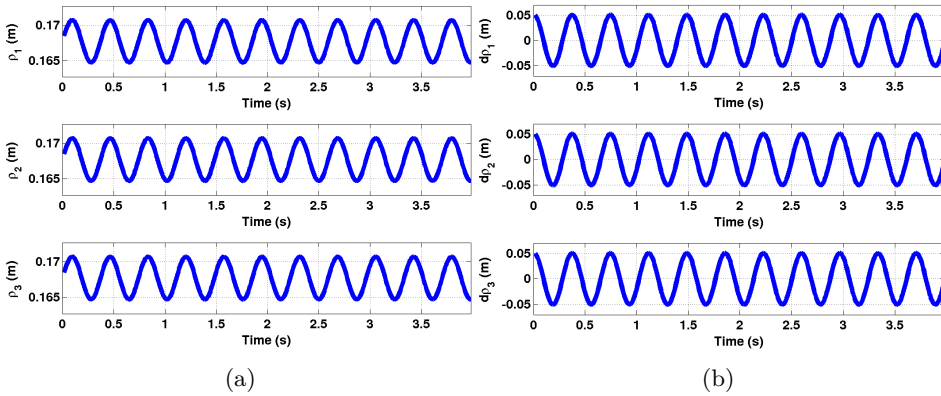


Figure 12.10: Trajectory III: (a) displacement of the linear guides ; (b) velocity of the linear guides

In Fig. 12.11a we see the axial forces in the linear guides, the minimum value being -1.4702 N and the maximum, -1.2327 N. Figure 12.11b shows the radial forces. The radial force in the second linear guide is null, while for the first and third linear guides is harmonic, with a minimum value of -0.4605 N and a maximum value of -0.3861 N. The axial forces, as well as the radial forces, are lower than the force limits of the linear guides. In Fig. 12.11c we see the power required by the motors. It is the same for the three of them, with a maximum of 0.0694 W in absolute value. The speed and the torque of the motors is also the same for the three limbs – the mean

speed is 415.58 r.p.m. and the torque 0.001 N ·m, so they both fulfil the requirements.

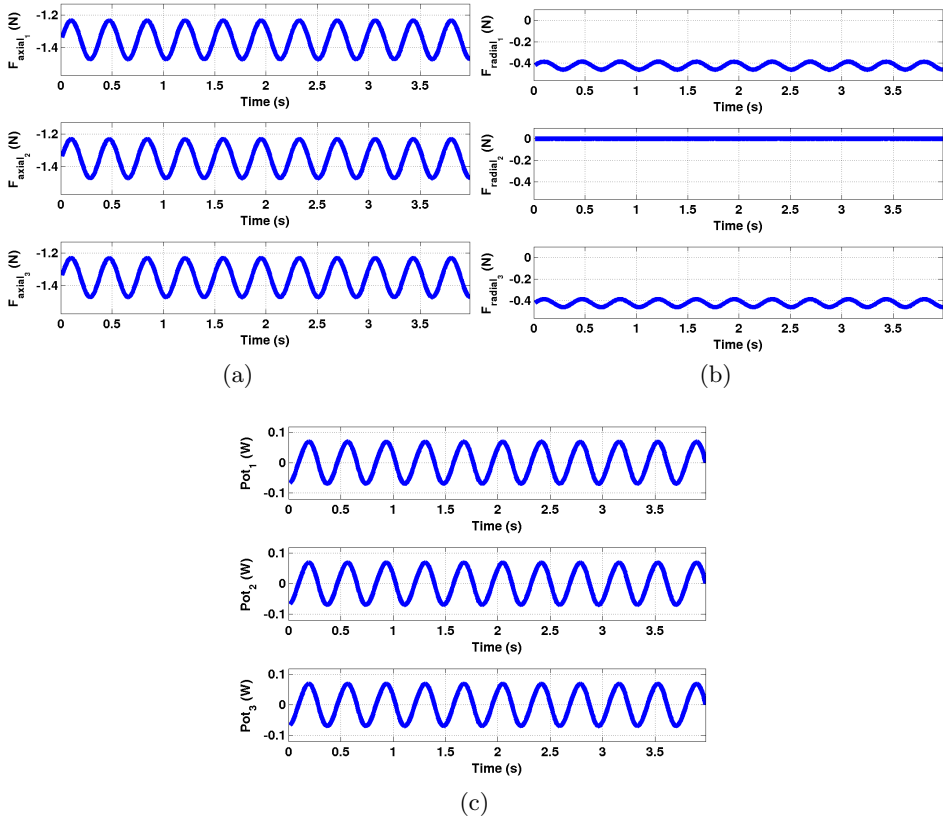


Figure 12.11: Trajectory III: (a) axial force in the linear guides ; (b) radial force in the linear guides

12.3. Interpreting results

We have applied the two optimization methods proposed in Chapter 11 to the 2PRU-1PRS parallel manipulator and we now summarize briefly to aide interpreting the results obtained.

We applied the WS optimization method to 1000 GP combinations and obtained the GP combinations that lead to the biggest sphere in the useful WS. The biggest sphere has a radius of 7 discretization points. There are 15 GP combinations whose useful WS house the biggest sphere. For six of those GP combinations, the biggest sphere can be placed in two positions, while for the other nine, the biggest sphere can be placed in four different positions in the useful WS. Thus, we get 9 best GP combinations.

We define the *StudyVariables* of the power optimization method as the GP combinations that lead to a useful WS containing a sphere at least $0.5 \cdot S_{max}$. In this way, we get 325 *StudyVariables* to analyse in the power optimization method. The best GP combination of this method is the one that leads to the lowest power consumption.

The power consumption depends on the trajectory of the manipulator. We define three different harmonic trajectories to be studied – one rotation about the X-axis, one rotation about the Y-axis and one translation along the Z-axis. We see that for the case of the rotations the best GP combination is $(H, L, R) = (0.35, 0.2, 0.2)$ m. For the translation along the Z-axis we get two best combinations: $(H, L, R) = (0.35, 0.2, 0.2)$ m and $(H, L, R) = (0.3, 0.2, 0.2)$ m. Since $(H, L, R) = (0.35, 0.2, 0.2)$ m is optimal solution for the three trajectories, we define it as the best GP combination according to the power consumption.

Part V

Prototype

13

Solution Chosen

The solution chosen to build the prototype is not an optimal solution, but it is close to them. The aim of building a prototype is basically to have a tool that allows us to validate the theoretical results as we obtain them.

We chose the radius of the fixed and mobile platforms to be 0.4 m and 0.35 m, respectively. The length of the legs is 0.264 m. The thickness of the mobile platform is 0.004 m and the radius of the legs is 0.005 m. Table 13.1 shows these values and Fig. 13.1 shows the CAD model of the prototype. In next Chapter we will present the characteristics of the linear guides, motors and joints.

Table 13.1: Geometry parameters

	Description	Value
H (m)	Fixed platform radius	0.4
L (m)	Limb length	0.264
R (m)	Mobile platform radius	0.35
s (m)	Limbs radius	0.005
e (m)	Mobile platform thickness	0.004

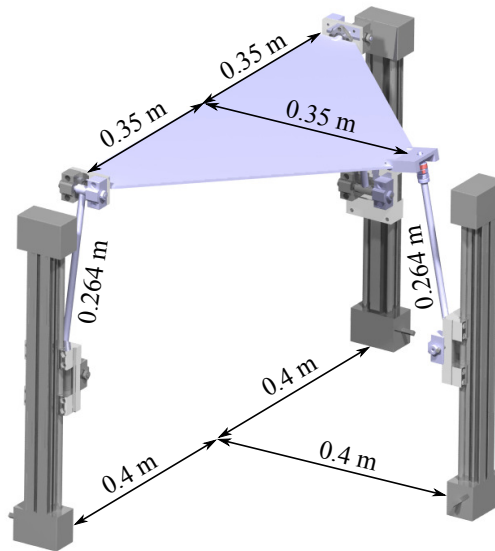


Figure 13.1: Dimensions of the prototype

Design of the Prototype

14.1. Component design

The main idea when designing the prototype is to have a manipulator with the smallest clearances as possible. In order to do it, we try to use commercial products as much as possible.

In this Chapter we describe the chosen components and we validate the solution.

14.1.1. Linear guides, motors and gearheads

Since there is not an unique set of products that fulfil the requirements of power, load capacity and displacement of our manipulator, our first option is to use components that we already know. In previous projects, we have worked with motors and gear heads from Maxon and linear guides from Igus, so we search for a combination suitable for our manipulator.

Figure 14.1 shows the solution chosen. The motor, shown in in Fig. 14.1a, is a Maxon RE Num. 148867. It is a DC motor, with a nominal current of 24 A, a maximum power of 150W and a nominal voltage and torque of 6 A and 0.177 Nm, respectively.

The gear-head is a Maxon Planetary Gearhead GP 42 C Num. 203116, which allows a reduction of 15:1. It is shown in Fig. 14.1b.

We choose the maximum displacement of the liner guides to be 0.3 m, which is enough to run the trajectories we desire. Using linear guides with a larger displacement would lead to a bigger workspace, but also to a lower stiffness. We select the Igus ZLW-1040-02-S-100-L(R)-300 linear guide, seen in Fig. 14.1c. The maximum radial load that it can support is 300 N, while the maximum belt tension is 200 N. Its displacement ratio is 0.07 m per revolution.

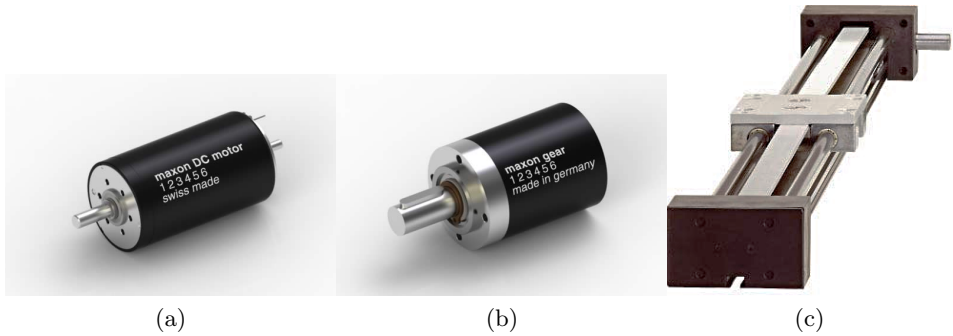


Figure 14.1: Chosen products: (a) DC motor. Courtesy of Maxon; (b) planetary gearhead. Courtesy of Maxon; (c) linear guide. Courtesy of Igus

Table 14.1 presents the data of the three components – the motor, the gearhead and the linear guide – and Fig. 14.2 shows the assembly of the three components.



Figure 14.2: Assembly

Table 14.1: Motor, gearhead and linear guide data

		Value
Motor-Gear	Nominal current	24 A
	Max. power	150 W
	Nominal voltage	6 A
	Nominal torque	0.177 Nm
	Reduction	15:1
LG	Max. displacement	0.3 m
	Radial Load	300 N
	Belt Tension	200 N
	Displacement Ratio	0.07 m/rev

14.1.2. Revolute, universal and spherical joints

The revolute joints connect the actuators with the limbs, allowing a rotational degree of freedom about the Y-axis for the first and third limbs and about the X-axis for the second limb. Figure 14.3 represents the rotations that we should get by using the revolute joints.

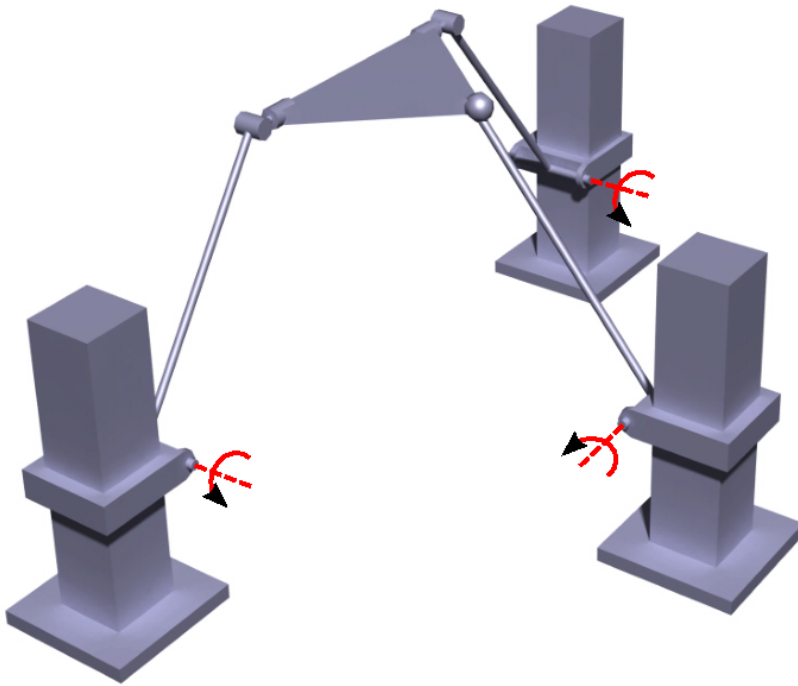


Figure 14.3: Revolute joint axes

In order to get those rotations, we attach each limb to a shaft. We insert the extremes of the shaft into two bearings that are placed in two shaft supports. The shaft supports have to be always collinear along the axis about which the shaft has to rotate. To ensure this, we use an intermediate piece that connects the shaft supports to the linear guide making the shaft support and the rotation axis to be collinear. We can see all the parts of the revolute joint in Fig. 14.5.

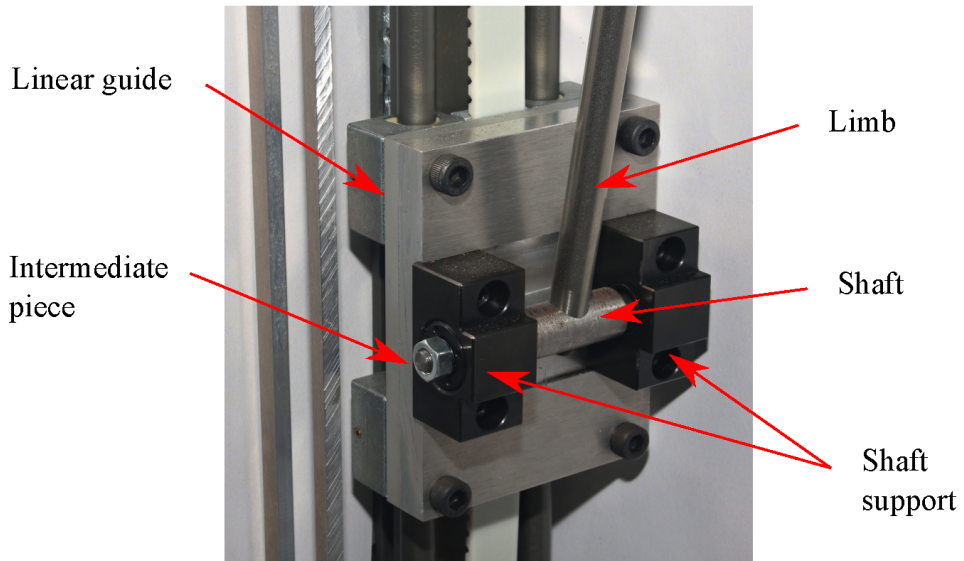


Figure 14.4: Revolute joint parts

Figure 14.5a shows the revolute joint drawn in CATIA, while Fig. 14.5b shows the final solution already built in the prototype.

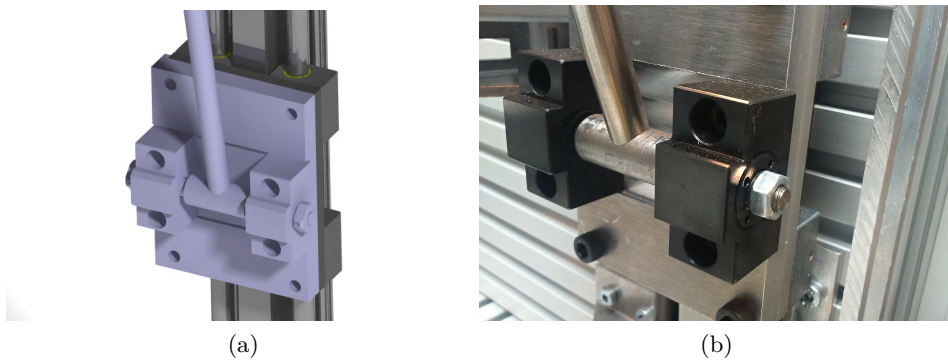


Figure 14.5: Revolute joint: (a) CATIA drawing; (b) final solution

For the universal joint we need to build a union between the platform and the limbs 1 and 3 that allows two DOF of rotation about the X- and Y-axes, as see in Fig. 14.6.

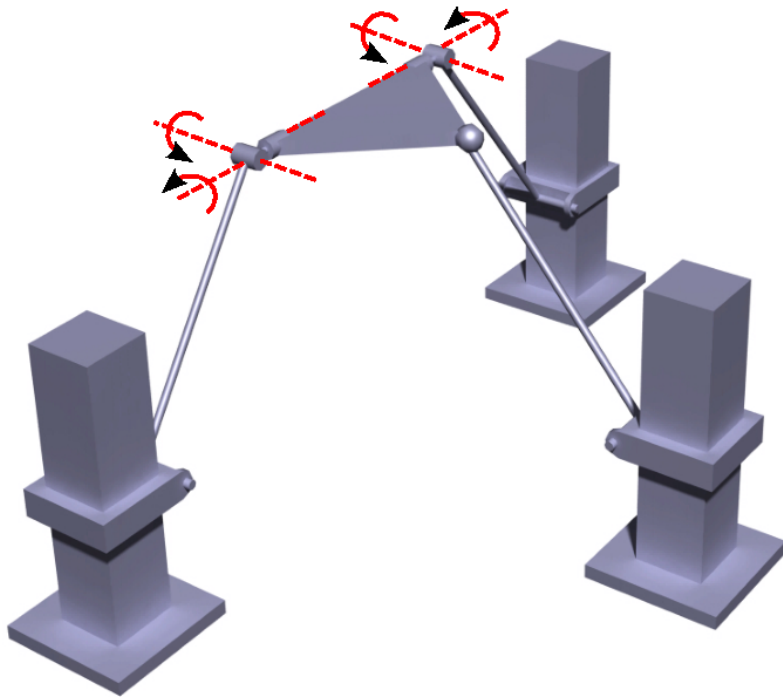


Figure 14.6: Universal joint axes

The typical universal joints that we can find in commercial catalogues allow two rotations about perpendicular axes, but those rotation axes do not coincide with the ones we need – they are about the X- and Z-axes. Figure 14.7a shows in red the axes about which rotation is allowed in common

universal joints, while in Fig. 14.7b we see the axes about which we need our manipulator to be able to rotate represented in blue. As we appreciate, the typical universal joints are not suitable for our manipulator and, thus, we need another solution to build our universal joint.

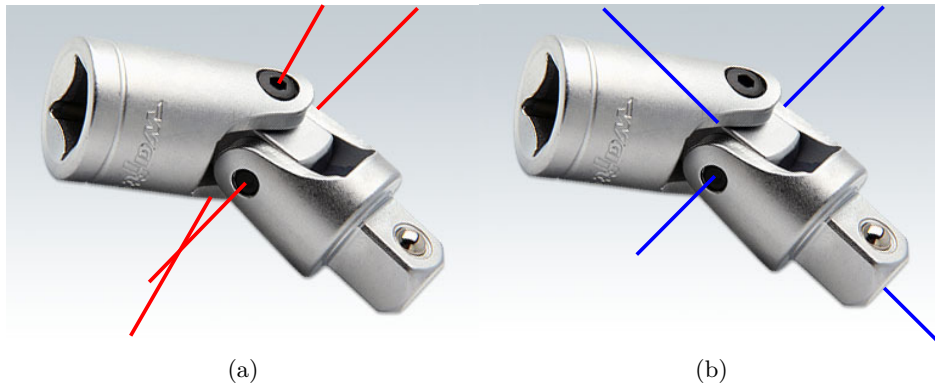


Figure 14.7: Typical universal joint courtesy of Waft: (a) real rotation axes (b) desired rotation axes

In order to create the rotation about the Y-axis, we connect the limb to a shaft whose extremes rotate inside two bearings, placed in two shaft supports, in a similar way as we did for the revolute joints. The bearings have to be collinear along the Y-axis. To ensure this, we attach them to a guidance piece. We see all the parts that allow the revolution about Y-axis in Fig. 14.8.

The spherical joint must allow 3 rotation dof about X-, Y- and Z-axes, as we can see in Fig. 14.10.

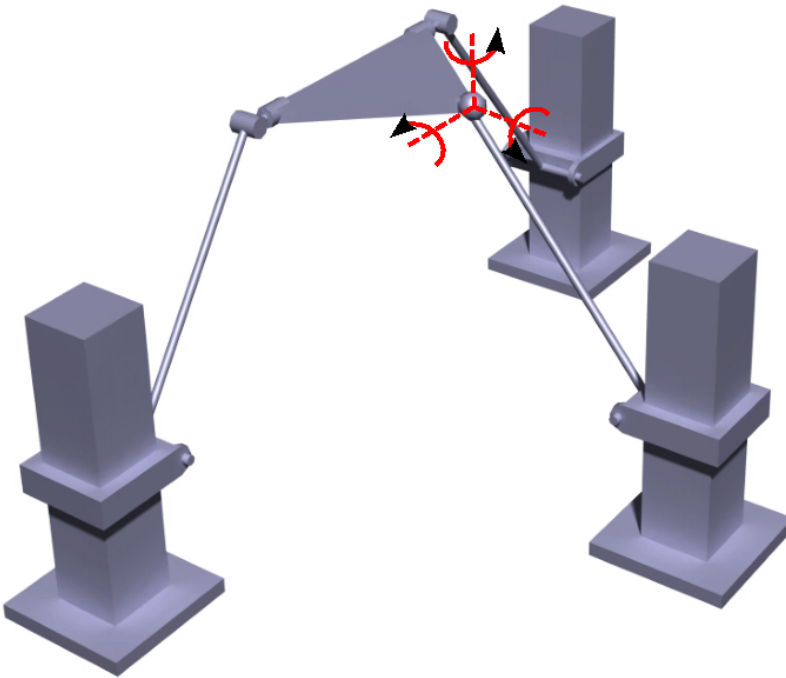


Figure 14.10: Spherical joint axes

An ideal spherical joint has no restriction in its rotations but, in practice, real ones can only rotate between a known range of angles. As we have already seen, that range affects the dimension of the useful WS – for a bigger rotation range, bigger useful WS. The maximum rotation range that we find for spherical joints of these dimensions is $[-25^\circ, 25^\circ]$. In the commercial spherical joints, a ball joint rotates inside a socket, the extremes being male or female, thread or smooth.

Between the ball joint and the socket there is usually a clearance that guarantees the rotation about the three axes, but that would be too big for our application. Thus, we choose a spherical joint with a thread that allows the control of a preload. We choose the Elesa Ganter GN 782-M6-KS-2 spherical joint, with male extremes and metric 6, seen in Fig. 14.11.



Figure 14.11: Spherical joint

To reduce the clearance even more, we place a spring between the spherical joint and the limb. To join the spherical joint to the mobile platform, we design an intermediate piece. The assembly is shown in Fig. 14.12.

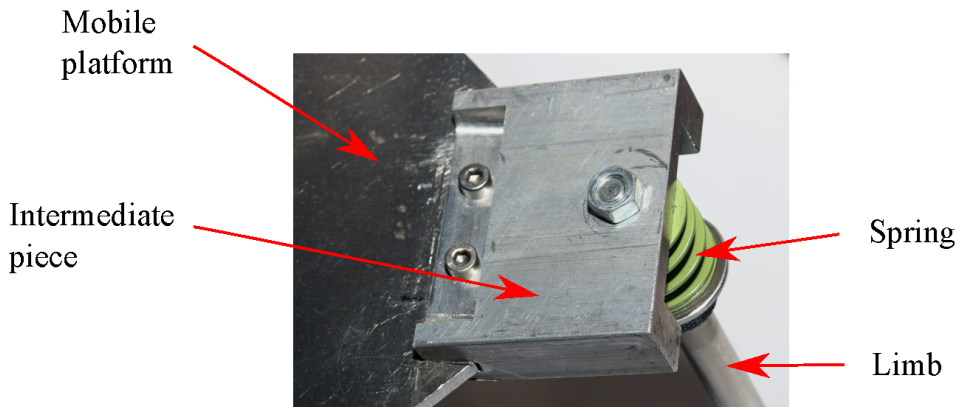


Figure 14.12: Assembly of the spherical joint

One side of that intermediate piece has a shape of fork to hold the mobile platform, while the other side has a flat surface where we thread one extreme of the spherical joint, as we see in Fig. 14.13a. The other extreme of the spherical joint is fixed to the second limb, as Fig. 14.13b shows.

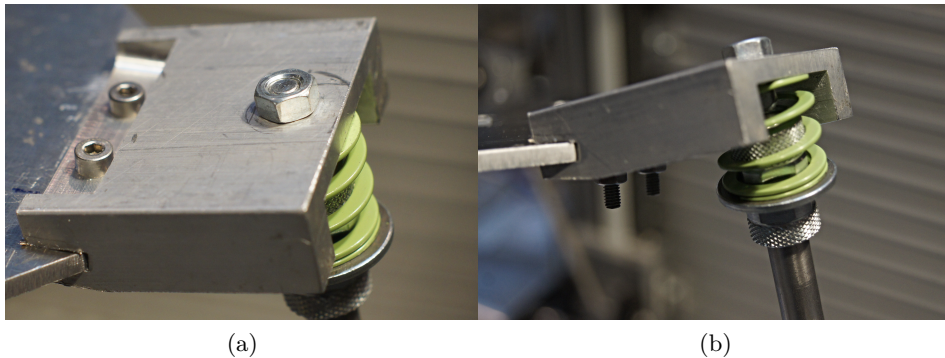


Figure 14.13: Spherical joint: (a) union with the platform; (b) spring

14.1.3. Fixed platform, mobile platform and limbs

The fixed platform is the responsible for supporting the entire manipulator. It has to allow the assembly of the linear guides in vertical position and ensure that the distances between them are correct. It also has to ensure that the linear guides do not change their positions when the manipulator moves. Besides, it can not obstruct the movement of the manipulator. Thus, it has to be as rigid as possible without colliding with the mobile platform or the limbs.

We design the fixed platform as seen in Fig. 14.14, with three metallic surfaces perpendicular to each other, fixed to a horizontal surface, also metallic.

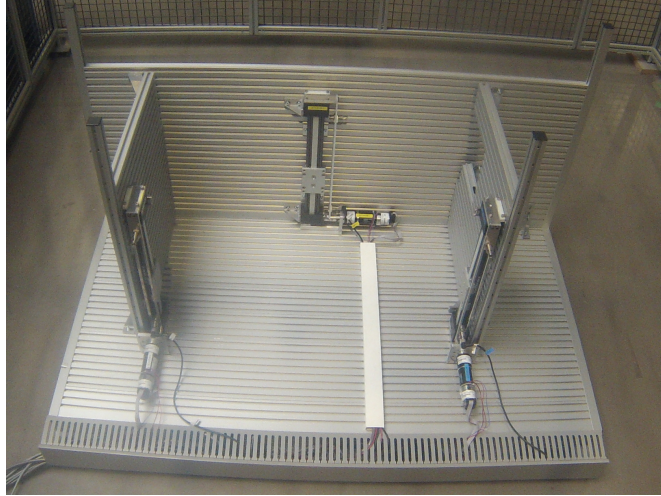


Figure 14.14: Fixed platform

The mobile platform is, ideally, an isosceles triangle. However, to account for the intermediate pieces shown in Fig. 14.12 and Fig. 14.9, the actual shape of the platform is not triangular. The kinematic equivalent of the mobile platform is obtained by joining the centres of the spherical and universal joints and is given by an isosceles triangle. This difference between the kinematic equivalent (i.e ideal shape) and the actual shape of the platform is shown in Fig. 14.15a. The shaded region is the actual shape, while the unshaded portions belong to the additional region accounted for by the kinematic equivalent. We build the mobile platform in aluminium, so it does not add too much weight that could affect the inertia of the manipulator while moving. We make holes all over the surface, as seen in Fig. 14.15b. Those holes have two objectives – the first one is to reduce even more the weight of the platform, and the second one is to allow us to attach different pieces or measurement tools that we may need while working with the manipulator.

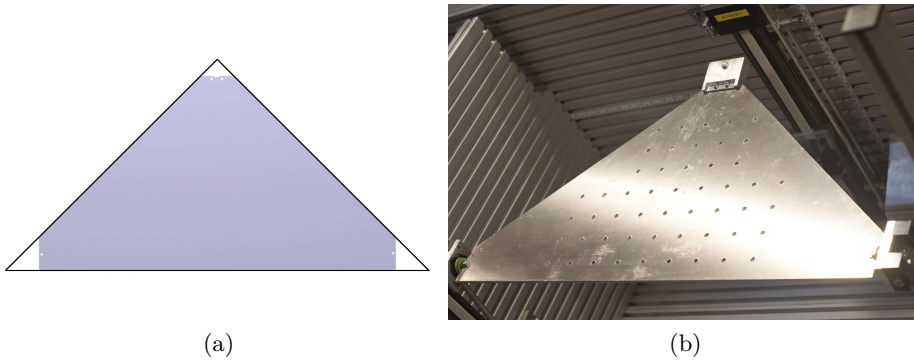


Figure 14.15: Mobile platform: (a) ideal shape; (b) real platform

The limbs are cylindrical bars. We build them in steel, so the stiffness of the whole manipulator increases. In order to be able to join them to the different joints, we machine female threads in the extremes. Figure 14.16 shows the assembly of the whole manipulator.



Figure 14.16: Assembly of the whole manipulator

14.2. Validation of the design

In this Section we validate the prototype by comparing theoretical results with real measurements of the position and parasitic motion value done with the prototype.

First of all, we calculate the theoretical distance that the linear guides have to move in order to reach certain positions of the mobile platform. We remember the expression we use to get those values, given by Eq. (14.1).

$$\begin{aligned}\rho_1 &= z - R \cdot s\theta - \sqrt{L^2 - (R \cdot (c\theta - s\theta \cdot s\psi) - H)^2} \\ \rho_2 &= z + R \cdot c\theta \cdot s\psi - \sqrt{L^2 - (R \cdot c\psi - H)^2} \\ \rho_3 &= z + R \cdot s\theta - \sqrt{L^2 - (-R \cdot (c\theta + s\theta \cdot s\psi) + H)^2}\end{aligned}\quad (14.1)$$

Then, we give those values to the linear guides and measure the real position reached by using two inclinometers in the way shown in Fig. 14.17 – one inclinometer measures the rotation about X-axis and the other one, the rotation about Y-axis.



Figure 14.17: Inclinometers to measure the real position

Table 14.2: Theoretical and real angles for given value of the linear guides

		Act ₁ (m)	Act ₂ (m)	Act ₃ (m)	Real (ψ, θ)
Theoretical (ψ, θ)	(-15°, -15°)	0.2907	0.1051	0.0976	(-14.7°, -15.5°)
	(-5°, -15°)	0.286	0.1612	0.1003	(-4.9°, -14.9°)
	(0°, -15°)	0.284	0.195	0.102	(0.1°, -14.8°)
	(5°, -15°)	0.2823	0.2203	0.1040	(5.1°, -14.8°)
	(15°, -15°)	0.2796	0.2809	0.1088	(15°, 15.1°)
	(-15°, -5°)	0.223	0.1024	0.1587	(-14.8°, -5.3°)
	(-5°, -5°)	0.2219	0.1602	0.1596	(-4.9°, -5.1°)
	(0°, -5°)	0.2214	0.1905	0.1601	(0°, -5°)
	(5°, -5°)	0.2209	0.2213	0.1606	(5.1°, -5°)
	(15°, -5°)	0.22	0.2836	0.1618	(15°, -5.1°)
	(-15°, 0°)	0.1905	0.1020	0.1905	(-14.8°, -0.1°)
	(-5°, 0°)	0.1905	0.1601	0.1905	(-4.9°, 0°)
	(0°, 0°)	0.1905	0.1905	0.1905	(0°, 0°)
	(5°, 0°)	0.1905	0.2214	0.1905	(5.1°, 0°)
	(15°, 0°)	0.1905	0.284	0.1905	(15°, 0°)
	(-15°, 5°)	0.1587	0.1024	0.223	(-14.8°, 5°)
	(-5°, 5°)	0.1596	0.1602	0.2219	(-4.9°, 4.9°)
	(0°, 5°)	0.1601	0.1905	0.2214	(0°, 4.9°)
	(5°, 5°)	0.1606	0.2213	0.2209	(5°, 4.9°)
	(15°, 5°)	0.1618	0.2836	0.22	(14.9°, 5.1°)
	(-15°, 15°)	0.0976	0.1051	0.2907	(-14.8°, 15.3°)
	(-5°, 15°)	0.1003	0.1612	0.286	(-5°, 14.8°)
	(0°, 15°)	0.102	0.1905	0.284	(0°, 14.8°)
	(5°, 15°)	0.1040	0.2203	0.2823	(4.9°, 14.8°)
	(15°, 15°)	0.1088	0.2809	0.2796	(14.7°, 15.1°)

Table 14.2 shows both the theoretical and the real data. In the column titled Theoretical (ψ, θ) we have the theoretical positions we want to reach. The columns titled Act₁ (m), Act₂ (m) and Act₃ (m) give the value of the displacement of the first, second and third actuators, respectively, that we would theoretically need to reach those positions. Finally, the column titled Real (ψ, θ) gives the real position that the manipulator reaches when the actuators take those values.

The parasitic motion, as we have already seen, is observed only in the X-axis and we can calculate its theoretical value by applying Eq. (14.2). We apply this equation to calculate the theoretical value of the parasitic motion that appears when the mobile platform reaches the same previous positions of the workspace, given by Table 14.3.

$$x = R \cdot (s\theta \cdot s\psi) \quad (14.2)$$

Table 14.3: Theoretical value of the parasitic motion (m)

		θ				
		-15°	-5°	0	5°	15°
ψ	-15°	-0.0235	-0.0079	0	0.0079	0.0235
	-5°	-0.0079	-0.0027	0	0.0027	0.0079
	0°	0	0	0	0	0
	5°	0.0079	0.0027	0	-0.0027	-0.0079
	15°	0.0235	0.0079	0	-0.007	-0.0235

We check if those values are the ones that appear also for the real case of the prototype. We move the mobile platform to each of the positions and measure the parasitic motion by using a laser pointer and a ruler placed on the fixed platform, as we see in Fig. 14.18. The values we obtain are given in Table 14.4.



Figure 14.18: Measurement system

Table 14.4: Real value of the parasitic motion (m)

		θ				
		-15°	-5°	0	5°	15°
ψ	-15°	-0.024	-0.008	0	0.009	0.026
	-5°	-0.009	-0.003	0	0.003	0.0098
	0°	0	0	0	0	0.001
	5°	0.0085	0.0025	0	-0.0025	-0.0075
	15°	0.0255	0.0085	0.001	-0.007	-0.0235

We plot both the theoretical and the real values of the parasitic motion in Fig. 14.19. The real value is plotted in red, while the blue one is plotted in blue. As we see from the tables and the plot, the values obtained from applying the theoretical equation are numerically close to the measured values.

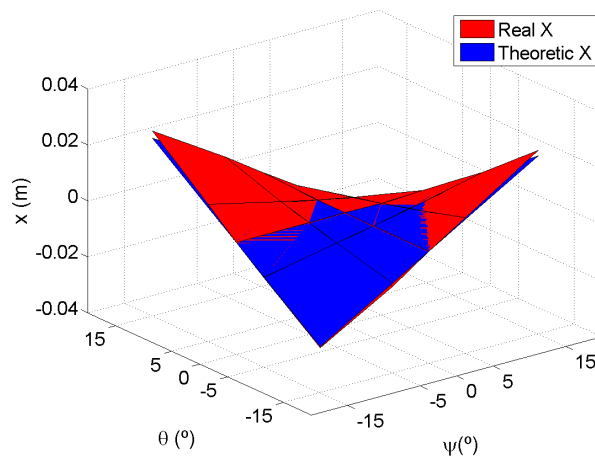


Figure 14.19: Parasitic motion

Analysis

In this Chapter we analyse the behaviour of the prototype described in Chapter 14. First, we solve the inverse kinematic problem for three study trajectories. Then, we analyse the singularities and the useful WS of the manipulator, checking how different parameters affect it. We also calculate the stiffness of the prototype placed in different positions of the useful WS. We do it using an analytical method, finite elements method and an experimental method. We solve the dynamics of the prototype and get the value of the forces in the linear guides and the power consumption in each actuator for the three trajectories analysed. Finally, we study the natural frequencies and modes of the manipulator using both FEM and experimental methods.

15.1. Kinematic Problem

We already know that the outputs of the 2PRU-1PRS parallel manipulator are one translation and two rotations of the mobile platform. We will solve the inverse kinematic problem for the *Study Trajectories* defined in Chapter 12. We reproduce those *Study Trajectories* in Table 15.1. We define the total duration of the movement to be 4 seconds and the initial position to be horizontal with z being 0.5 m.

Table 15.1: Harmonic trajectories definition

	$traject(t) = C + A \cdot \sin(\omega t)$			
	C	A	$f = \omega / (2 \cdot \pi)$	t
X- and Y axes	0	3°	2,7 Hz	4 s
Z-axis	0,5 m	0,003 m	2,7 Hz	4 s

We note again that both the linear guides and the motors have restricted movement. The linear guides have a displacement range of [0, 0.3] m and a maximum velocity allowed of 5 m/s. The maximum speed of the motors is 12000 r.p.m. We calculate the speed of the motors along the trajectories by applying Eq. (15.1). We calculate the mean value and check that it is lower than the maximum speed,

$$Speed_i = \frac{d\rho_i}{R_{gearhead}} \cdot \frac{60}{2\pi} \cdot Reduction \ Ratio \ (r.p.m) \quad (15.1)$$

where *Reduction Ratio* is the reduction ratio of the gear-head and equal to 15 and $R_{gearhead}$ is the radius of the gear-head and is obtained by applying Eq. (15.2). *Displacement Ratio* is the displacement of the linear guide per revolution of the gear-head and is equal to 0.07 m/rev.

$$R_{gearhead} = \frac{Displacement \ Ratio}{2\pi} \ (m) \quad (15.2)$$

According to this, we have to check that all the requirements – the displacement range and velocity limit of the linear guides, and the speed limit of the motors – are fulfilled for the three trajectories.

15.1.1. Trajectory I

The first trajectory is a rotation about X-axis with amplitude of 3° and frequency of 2.7 Hz. Figure 15.1 represents the displacement profiles

as functions of time – rotation about X-axis, (ψ), the rotation about Y-axis (θ) and the translation along Z-axis (z). Since this trajectory is a pure rotation about X-axis, ψ follows the defined trajectory. θ and z are constant and their values are 0 and 0.5 m, respectively. Thus, the parasitic motion – $x = R \cdot (-\sin\psi \cdot \sin\theta)$ – does not appear in this case.

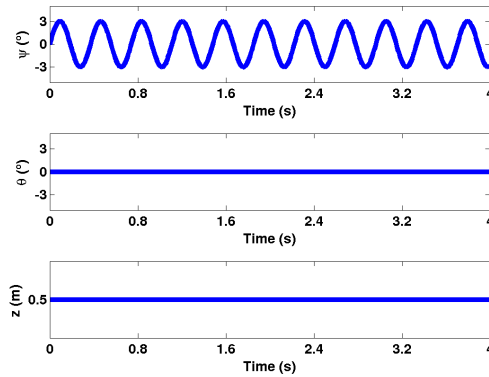


Figure 15.1: Trajectory I

We calculate the displacement of the actuators along the trajectory, as well as calculate their velocity and acceleration. We represent them in Fig. 15.2. Figure 15.2a shows the displacement of the three actuators. As we see, in the initial position the three actuators are placed at the same distance from the XY plane, 0.04 m. The first and third actuators are placed along the X-axis, so when the mobile platform rotates about that axis the only actuator displacing is the second one. The movement range of the second actuator is $[0.226, 0.2592]$ m. Since the displacement range of the linear guides is $[0, 0.3]$ m, the manipulator fulfils the requirement of displacement limits of the linear guides for the first trajectory.

We obtain the velocity of the actuators by differentiating their displacement. The first and third linear guides remain at a constant position,

so their velocity is null. The velocity of the second actuator is harmonic. Figure 15.2b shows these velocities. We see that the maximum value of the velocity of the second actuator is 0.3107 m/s and the minimum, -0.3107 m/s, both lower than the velocity limit of the linear guides.

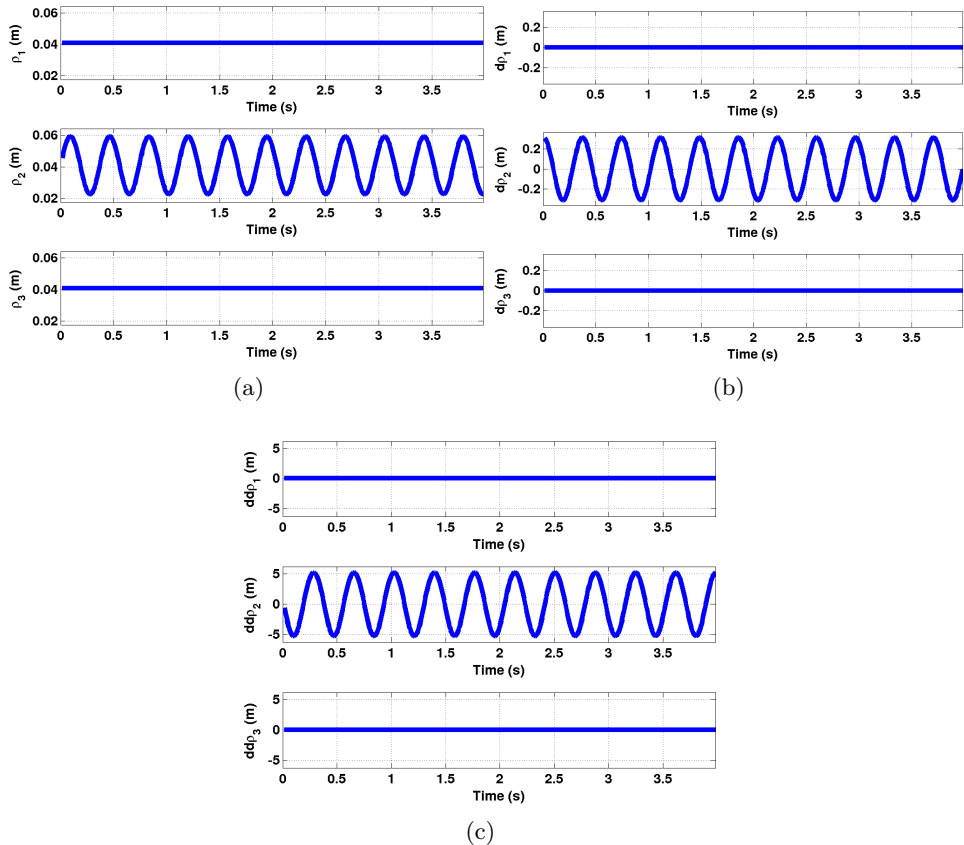


Figure 15.2: Kinematics for trajectory I: (a) actuators' displacement; (b) actuators' velocity; (c) actuators' acceleration

Similarly, we get the acceleration of the actuators by differentiating the

velocity. We see their representations in Fig. 15.2c. The acceleration of the first and third actuators is -0.0535 m/s^2 , constant along all the movement. The acceleration of the second actuator is harmonic with maximum value of 5.2053 m/s^2 and minimum value of -5.3123 m/s^2 . The mean speed of the second motor is 2537.2 r.p.m. , much lower than the maximum speed allowed for the motors.

15.1.2. Trajectory II

The second trajectory corresponds to a rotation with amplitude of 3° and frequency of 2.7 Hz about Y-axis. Thus, the value of ψ and z are constant, unlike the value of θ , which follows the trajectory defined, as seen in Fig. 15.3. Since ψ is null along all the trajectory, the parasitic motion does not appear.

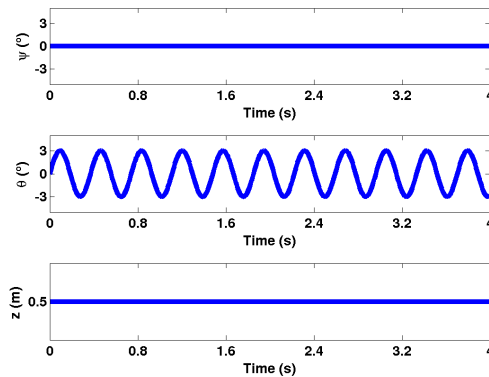


Figure 15.3: Trajectory II

We solve the inverse kinematic problem and get the displacement of the three linear guides. Figure 15.4a shows their values. The second actuator is on the Y-axis, so when the mobile platform rotates about Y-axis – like in this trajectory– the displacement of the second actuator remains constant,

the first and third actuators being the ones moving. They follow harmonic trajectories with the same amplitude and frequency but opposite direction. Their maximum and minimum displacement values are 0.0592 m and 0.0226 m, respectively. Thus, they are in the valid displacement range.

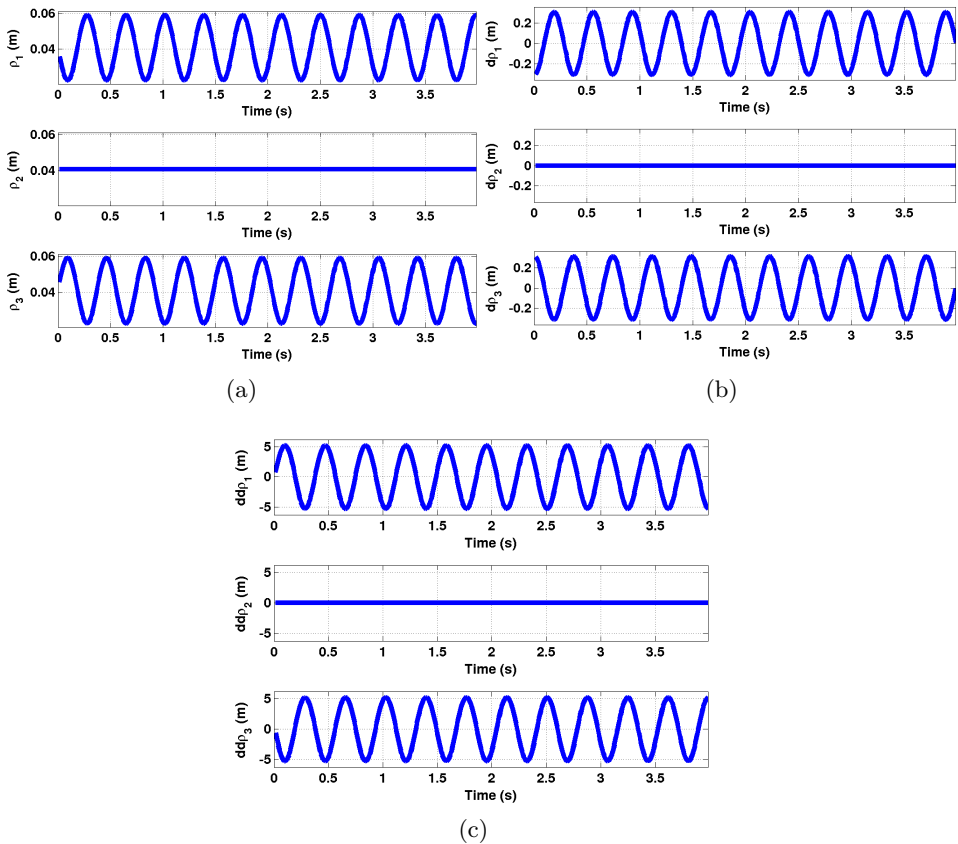


Figure 15.4: Trajectory II kinematics: (a) actuators displacement; (b) actuators velocity; (c) actuators acceleration

We find the derivative of the displacements of the actuators and get their velocities, shown in Fig. 15.4b. The velocity is null for the second actuator and harmonic for the first and third actuators. The maximum and minimum values of the velocity of the first and third actuators are equal to the maximum and minimum values of the velocity of the second actuator in Trajectory I – 0.3107 m/s and -0.3107 m/s, respectively. They fulfil the velocity limit restriction of the linear guides. We get the value of the accelerations of the actuators by differentiating a second time. We see the values in Fig. 15.4c. The acceleration of the second actuator is -0.0534 m/s^2 and constant. The accelerations of the first and third actuators are harmonic with a maximum value of 5.2054 m/s^2 and a minimum value of -5.3123 m/s^2 . The mean value of the speed of the motors is 2536.6 r.p.m., much lower than the maximum speed permitted.

15.1.3. Trajectory III

We define Trajectory III as a harmonic trajectory along the Z-axis, with an amplitude of 0.003 m and a frequency of 2.7 Hz. This trajectory defines the outputs of the manipulator, shown in Fig. 15.5.

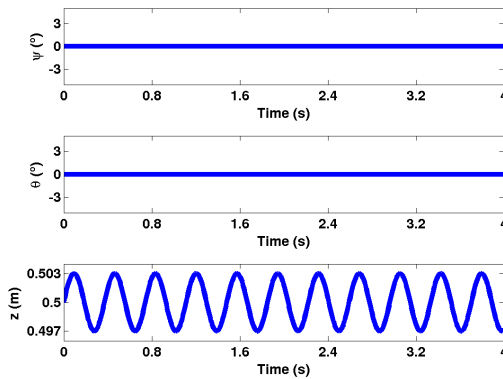


Figure 15.5: Trajectory III

The parasitic motion does not depend on the value of z , so it does not exist for this trajectory either. Since the trajectory is a pure translation along the Z -axis, the value of the displacement of the three linear guides is the same, as we see in Fig. 15.6a.

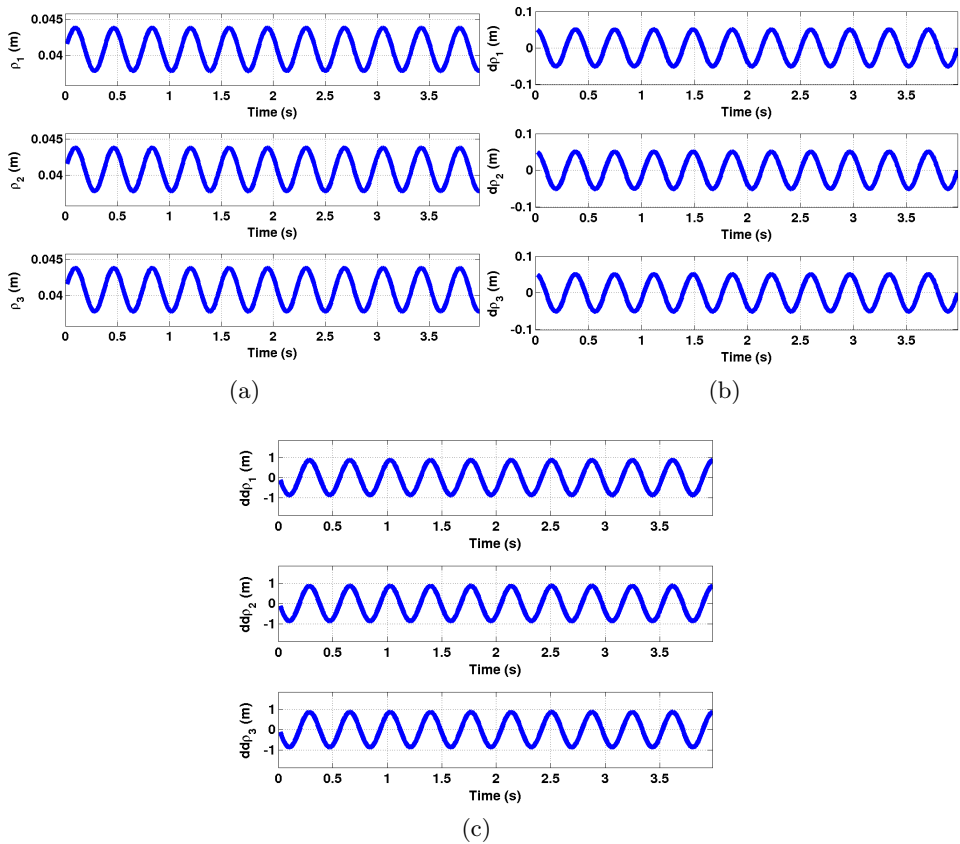


Figure 15.6: Trajectory III kinematics: (a) actuators displacement; (b) actuators velocity; (c) actuators acceleration

The value in the initial position is 0.2408 m starting from the XY plane. The amplitude of their movement is 0.003 m, so the maximum value of the position is 0.2438 m and the minimum, 0.2378 m.

We get the velocity and the acceleration of the actuators by deriving the displacement once and twice, respectively. In Fig. 15.6b we see the values of the velocity obtained, which are in the range of $[-0.0509, 0.0509]$ m/s. Figure 15.6c shows the acceleration. The value of the acceleration of the three linear guides is also the same, the maximum value being 0.862 m/s² and the minimum value being -0.8621 m/s². The mean speed of the motors is 415.48 r.p.m., so it is lower than the maximum speed allowed.

15.1.4. Interpreting results

We have obtained the displacement, the velocity and the acceleration of the linear guides for three different harmonic trajectories – one rotation about X-axis, one rotation about Y-axis and a translation along Z-axis.

We have seen that for the rotation about X-axis the first and third linear guides stay at the same position while the second one describes a harmonic trajectory. However, if the trajectory is about Y-axis, it is the second linear guide that remains at the same position while first and third linear guides describe harmonic trajectories with same amplitude and frequency but opposite direction. For the trajectory along Z-axis the three linear guides describe the same trajectory. In each of the three cases the displacement of the linear guides is in the acceptable range.

We have also calculated the velocities and accelerations of the linear guides. We have seen that the velocity and acceleration for the second actuator during the rotation about X-axis are equal to the velocity and acceleration of the first and third actuators during the rotation about Y-axis. For the translation along Z-axis, though, the velocity and acceleration of the three linear guides have the same value and they are smaller than for any other trajectory.

15.2. Singularities

As seen in Chapter 7, there are two types of singularities that we have to analyse – singularities of the inverse kinematic problem and singularities of the direct kinematic problem.

Equation (15.3) gives the expression of the Jacobian matrix of the direct kinematic problem. The manipulator is in a singular position of the DKP when the determinant of the direct Jacobian matrix, $|\mathbf{J}_x|$, is null.

$$\mathbf{J}_x = \begin{bmatrix} \mathbf{s}_1^T & (\mathbf{PA}_1 \times \mathbf{s}_1)^T \\ \mathbf{s}_2^T & (\mathbf{PA}_2 \times \mathbf{s}_2)^T \\ \mathbf{s}_3^T & (\mathbf{PA}_3 \times \mathbf{s}_3)^T \\ \mathbf{u}_1^T & (\mathbf{PA}_1 \times \mathbf{u}_1)^T \\ \mathbf{u}_2^T & (\mathbf{PA}_2 \times \mathbf{u}_2)^T \\ \mathbf{u}_3^T & (\mathbf{PA}_3 \times \mathbf{u}_3)^T \end{bmatrix} \quad (15.3)$$

We define the *Study Points* by dividing the axes in 60 parts each. The ranges of the axes are given in Table. 15.2.

Table 15.2: Output limits

	Description	Value
ψ ($^\circ$)	Rotation about X-axis	(-90, 90)
θ ($^\circ$)	Rotation about Y-axis	(-90, 90)
z (m)	Translation along Z-axis	(0,3, 0,8)

We calculate the $|\mathbf{J}_x|$ for each *Study Point* and we get the singular positions of the prototype for the direct kinematic problem. These singularities are shown in Fig. 15.7. As we see, they divide the working area in 5 sub-areas.

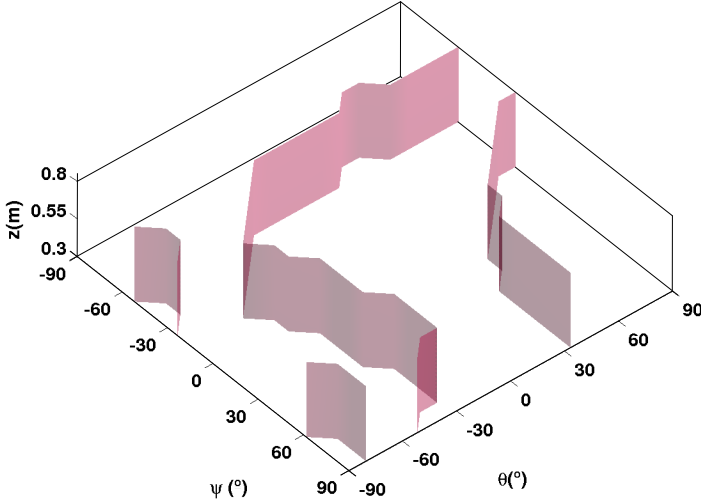


Figure 15.7: DKP singularities

Similarly, the manipulator is in a singular position of the inverse kinematic problem when the determinant of the inverse Jacobian matrix, $|\mathbf{J}_q|$, is null. Equation (15.4) gives the expression of the inverse Jacobian matrix.

$$\mathbf{J}_q = \begin{bmatrix} s_1 \mathbf{k} & 0 & 0 \\ 0 & s_2 \mathbf{k} & 0 \\ 0 & 0 & s_3 \mathbf{k} \\ 0 & 0 & 0 \\ 0 & 0 & 0 \\ 0 & 0 & 0 \end{bmatrix} \quad (15.4)$$

We calculate the value of $|\mathbf{J}_q|$ for the *Study Points* previously defined and get the singular positions of the manipulator for the inverse kinematic problem. Figure 15.8 shows these singularities. In this case, the working area is divided in two sub-areas.

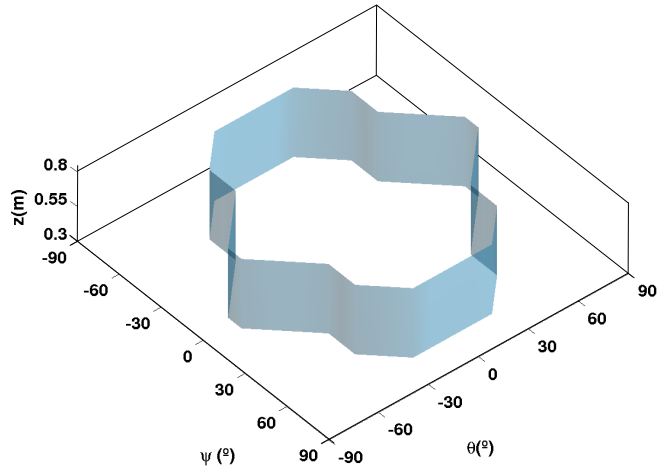


Figure 15.8: IKP singularities

15.2.1. Interpreting results

We have studied the singularities of the prototype for the direct and inverse kinematic problems. In order to do that, we have defined finite *Study Points* for which we have obtained the determinant of the Jacobian matrices.

For the case of the direct kinematic problem, the singularities define five sub-areas in the working area, while for the inverse kinematic problem singularities define only two sub-areas in the working area.

Since singularities mean a loss of control of the manipulator, we have to ensure that the manipulator works inside those limited sub-areas, without crossing any singular position.

15.3. Workspace

The useful workspace denotes the region of the workspace free of singularities of the inverse and direct kinematic problems. Additionally, the physical restrictions of the spherical joint and the linear guides are fulfilled. We get that useful WS and study its regularity by obtaining the biggest sphere in it.

We set the *StudyPoints* by dividing the three axes in 60 parts each, so the number of points we have to check to get the WS is 216000. In this case, *StudyPoints* is the set of points which lie in the 3 dimensional space bounded by the ranges given by Table 15.3.

Table 15.3: Output limits

	Description	Value
ψ ($^\circ$)	Rotation about X-axis	(-90, 90)
θ ($^\circ$)	Rotation about Y-axis	(-90, 90)
z (m)	Translation along Z-axis	(0,3,0,8)

We also define the physical restrictions given by the range of the linear guides and the spherical joint as shown in Table 15.4.

Table 15.4: Physical restrictions

	Description	Value
LG (m)	Linear Guide Ranges	(0, 0,3)
SJ ($^\circ$)	Spherical Joint Range	(-25, 25)

We solve the IKP for all the candidate-poses and get the WS_0 for the prototype, shown in Fig. 15.9. Out of the 216000 *StudyPoints*, only 76320 belong to the WS_0 , so we have reduced the number of point to check by 64.66 %. We have to check now whether the points of the WS_0 fulfil or not the restrictions of the direct kinematic problem, the spherical joint and the linear guides.

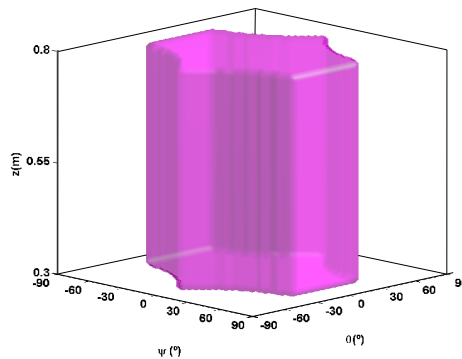


Figure 15.9: WS_0

As seen in Section 15.2, the WS_0 is divided into five sub-areas depending on the sign of the determinant of the Jacobian matrix of the DKP. We define WS_1 to be the area free of singularities where the sign of the determinant of the Jacobian matrix is the same as for the initial position of the manipulator. We define the initial position to be horizontal with $z=0.5$ m. The determinant of the Jacobian matrix for that initial position is given by Eq. (15.5).

$$|\mathbf{J}_x|_0 = -0,0341 \quad (15.5)$$

Accordingly, our WS_1 is defined by the points of the WS_0 whose determinant of the Jacobian matrix is negative and placed in the same sub-area as the initial position. Figure 15.10a shows WS_1 .

The rotation range of the spherical joint is $[-25^\circ, 25^\circ]$. We define the WS_2 to be the set of point sof the WS_0 that fulfil the restriction of the spherical joint. Figure 15.10b shows WS_2 . Out of the 76320 points in WS_0 , 41640 belong to WS_2 .

Similarly, we get WS_3 by applying Eq. (15.6). We see WS_3 in Fig. 15.10c. Out of the 76320 points of the WS_0 , only 5520 belong to WS_3 .

$$0 < \rho_i < 0,3m \quad (15.6)$$

If we apply all the previous conditions at the same time, we get the useful WS, seen in Fig. 15.10d. Out of the 76320 points of the WS_0 , 2059 belong to the useful WS.

The biggest sphere in the useful WS has a radius of 4 discretizations of the workspace and can be placed in 6 different positions in the useful WS. Figure 15.11 shows the useful WS and the biggest sphere placed in the first possible position.

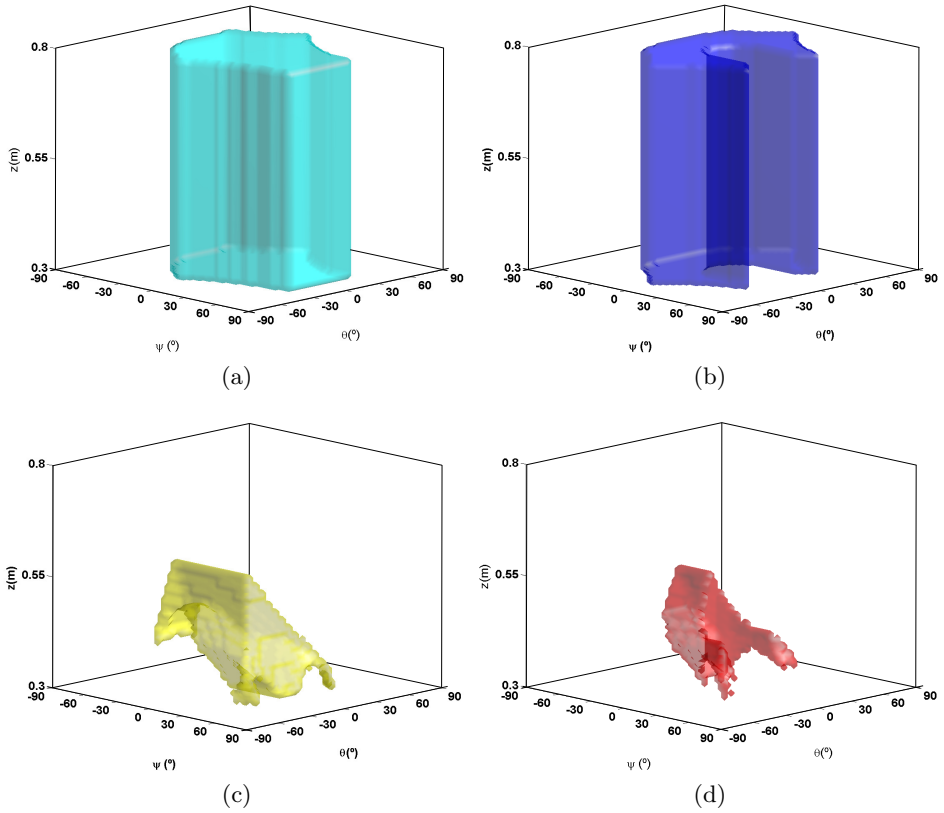


Figure 15.10: Workspaces: (a) WS_1 ; (b) WS_2 ; (c) WS_3 ; (d) WS_{use}

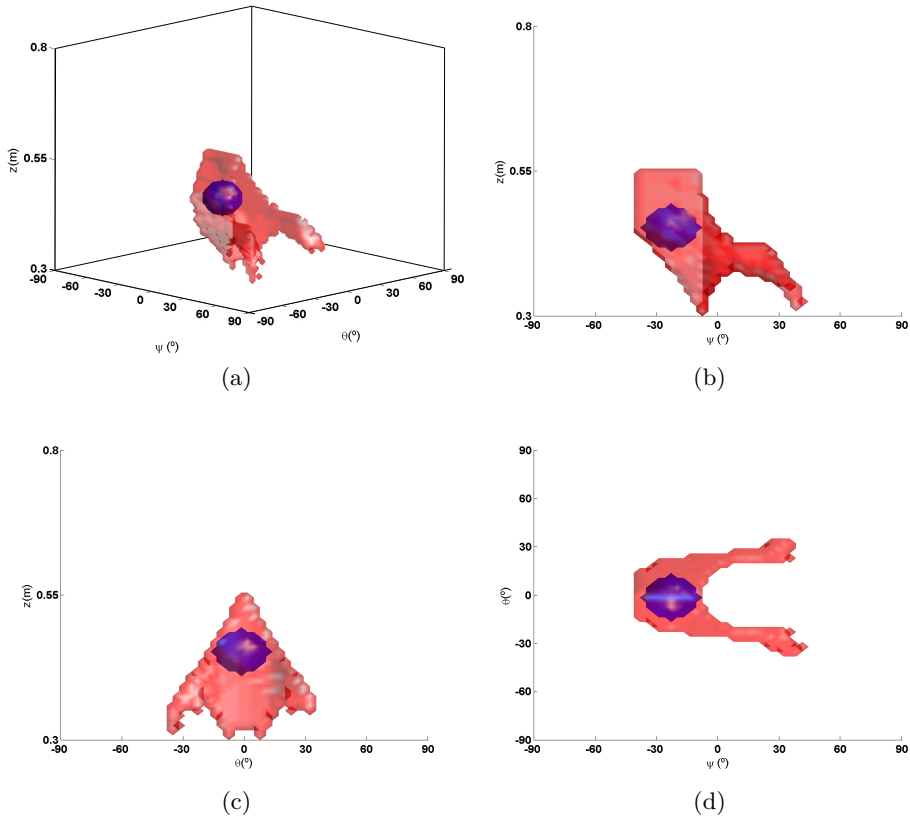


Figure 15.11: Useful WS with the S_{max} placed in the first possible position: (a) general view; (b) plane YZ view; (c) plane XZ view; (d) plane XY view

15.3.1. Interpreting results

We have defined the useful WS of the manipulator as the singularity-free space that the manipulator can reach taking the restrictions of the linear guides and the spherical joint into account. Out of the 216000 initial study points, only 2059 points belong to the useful WS. We have seen that the most restrictive condition is the rotation range of the spherical joint.

We have also studied the regularity of the useful WS by finding the biggest sphere that fits in it and the number of positions where it can be placed. The radius of the biggest sphere in the useful WS of the prototype is 4 discretization of the workspace and we can place it in 6 different positions.

15.4. Stiffness

We get the stiffness of the manipulator by using three different methods. First of all, we calculate the stiffness at different points in the WS by applying the analytical method described in Section 9.2. Then, we get the stiffness for the same positions by applying a finite element method (FEM). Finally, we obtain the stiffness of the prototype experimentally only for the initial position.

Since the manipulator is symmetric with respect to Y-axis, the stiffness should also be symmetric respect to Y-axis. We check that this characteristic is fulfilled by analysing the positions given by the combination of $\psi = [-15^\circ -5^\circ 0^\circ 5^\circ 15^\circ]$ and $\theta = [-15^\circ, -5^\circ, 0^\circ 5^\circ 15^\circ]$. In this way, we have 25 positions of the WS to be analysed. Figure 15.12 shows the prototype in the extreme positions studied.

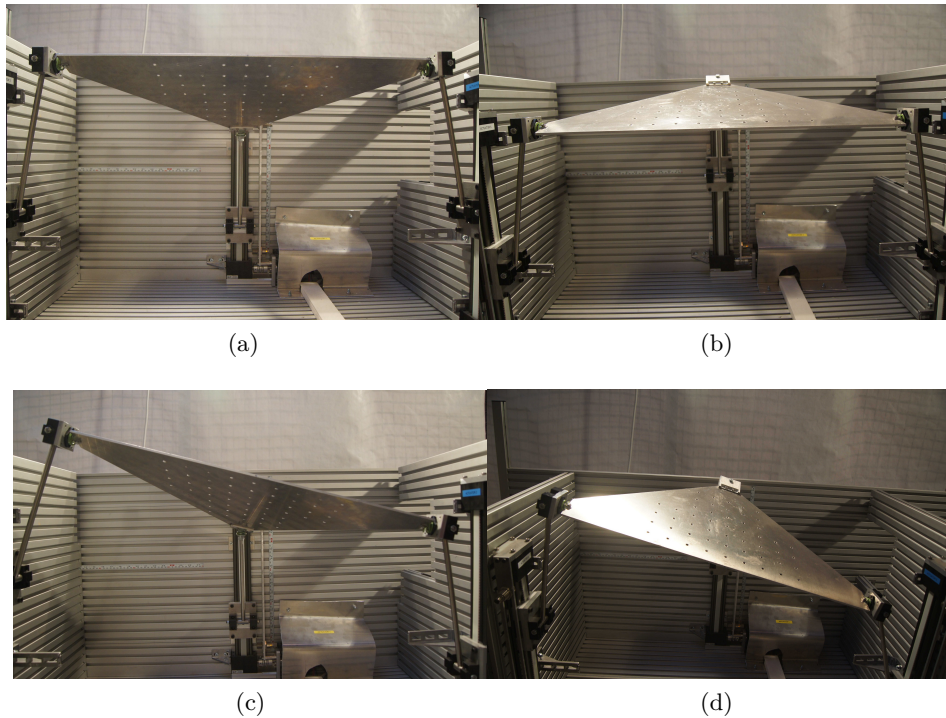


Figure 15.12: Extreme positions analysed: (a) $(\psi, \theta) = (-15^\circ, 0^\circ)$; (b) $(\psi, \theta) = (15^\circ, 0^\circ)$; (c) $(\psi, \theta) = (-15^\circ, 15^\circ)$; (d) $(\psi, \theta) = (15^\circ, 15^\circ)$

15.4.1. Analytical method

We apply the analytical method presented in Section 9.2 to calculate the stiffness of the prototype in the 25 positions of the WS we have chosen. Table 15.5 shows the results we get and Fig. 15.13 shows the same results graphically. The maximum value of the stiffness is $2.9313 \cdot 10^4$ N/m and corresponds to the positions $(\psi, \theta) = (0^\circ, 15^\circ)$ and $(\psi, \theta) = (0^\circ, -15^\circ)$. The minimum value is 2.7275×10^4 N/m and appears when θ is null. For the initial position of the manipulator – horizontal position – the value of the stiffness is $K = 2.7275 \cdot 10^4$ N/m.

Table 15.5: Stiffness obtained analytically ($\times 10^4$ N/m)

		ψ				
		-15°	-5°	0°	5°	15°
θ	-15°	2.9014	2.9207	2.9313	2.9312	2.9200
	-5°	2.7711	2.7760	2.7787	2.7789	2.7766
	0°	2.7275	2.7275	2.7275	2.7275	2.7275
	5°	2.7711	2.7760	2.7787	2.7789	2.7766
	15°	2.9014	2.9207	2.9313	2.9312	2.9200

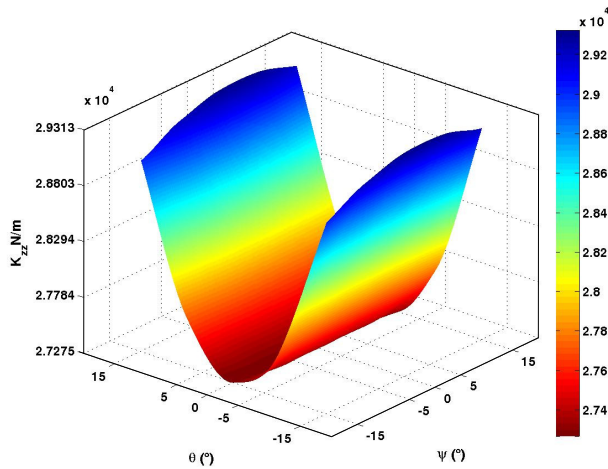


Figure 15.13: Stiffness of the prototype calculate analytically

We see that the stiffness is, indeed, symmetric respect to the Y-axis. Thus, when applying FEM to verify the stiffness, we will do it only for positive values of θ .

15.4.2. Finite element method

We apply the finite element method (FEM) to calculate the stiffness of the prototype by using ANSYS Workbench. We run a Static Structural analysis to get the deformation of the manipulator for a vertical force of 1 N applied on the gravity centre. The stiffness expression is given by Eq. (15.7), K being the stiffness, F being the applied force and δ being the value of the displacement generated by the force F .

$$K = F/\delta \quad (15.7)$$

First of all, we define the geometry of the manipulator. We have two ways to do it – we can generate it in ANSYS Workbench or we can import it directly from a CAD program. In our case, we draw the manipulator in CATIA in such a way that we can change its position by just editing the value of the displacements of the linear guides, as we see in Fig. 15.14.

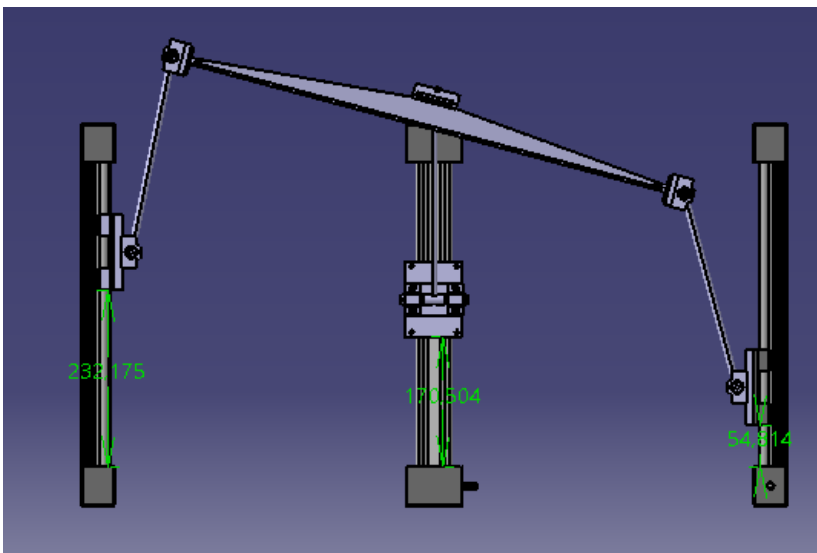


Figure 15.14: Manipulator drawn in CATIA

We export the geometry to ANSYS Workbench for each position we want to analyse. Once we have the geometry ready, we define the constraints between all the components. We analyse the manipulator without the linear guides, so we have to fix the rotational joints to the fixed frame. We free the rotation about X-axis for the second limb and about Y-axis for the first and the third limbs. To do that, we use cylindrical supports applied on the rotational joints, as we see in Fig. 15.15a. For the rest of the joints, we define the contact restrictions between elements. Figure 15.15b shows the example of one rotation in the universal joints.

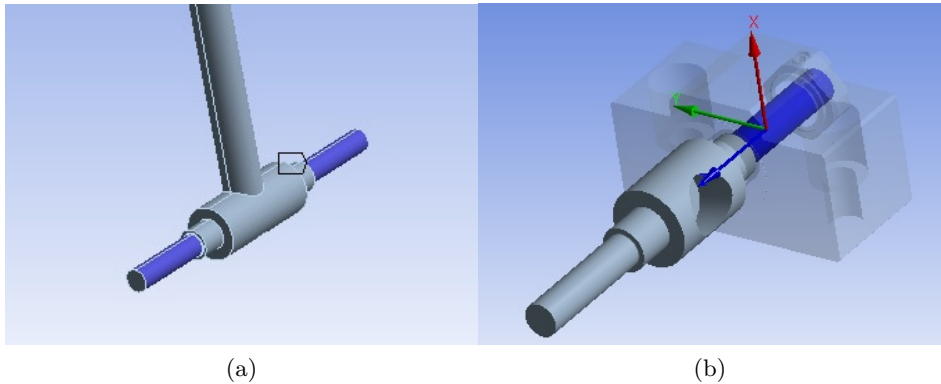


Figure 15.15: Constraints in ANSYS: (a) cylindrical support; (b) revolute condition

Before generating the mesh, we define two different element sizes – one for the joints and the mobile platform and another one for the limbs. The size of the elements for the joints is 0.002 m, while for the mobile platform and the limbs it is 0.004 m. We generate the mesh of the model by using the auto generated mesher. We see the resulting mesh in Fig. 15.16.

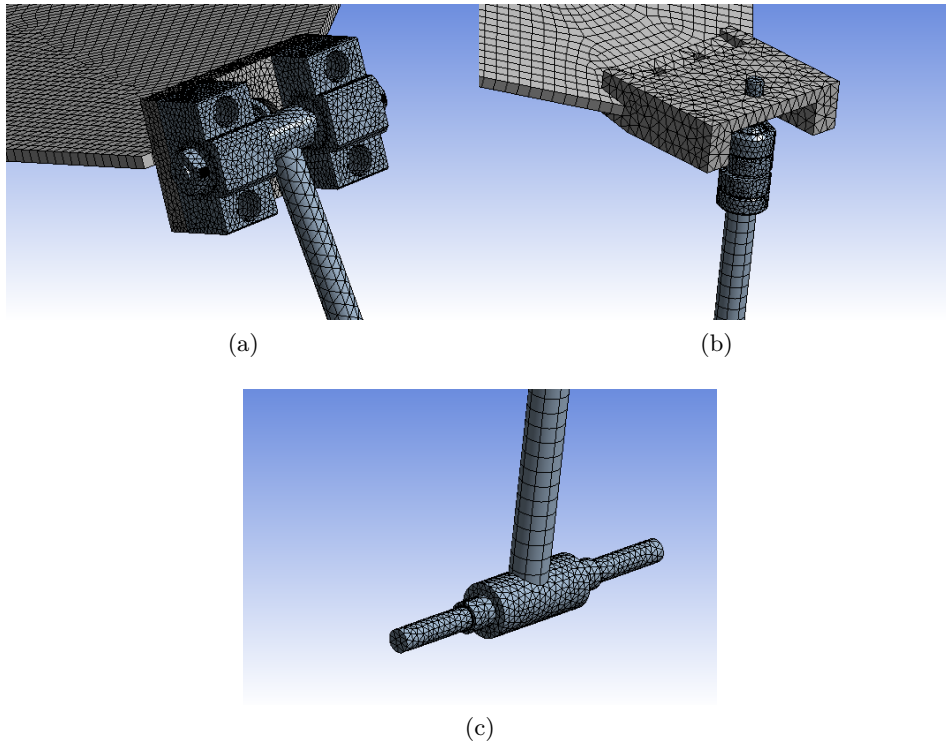
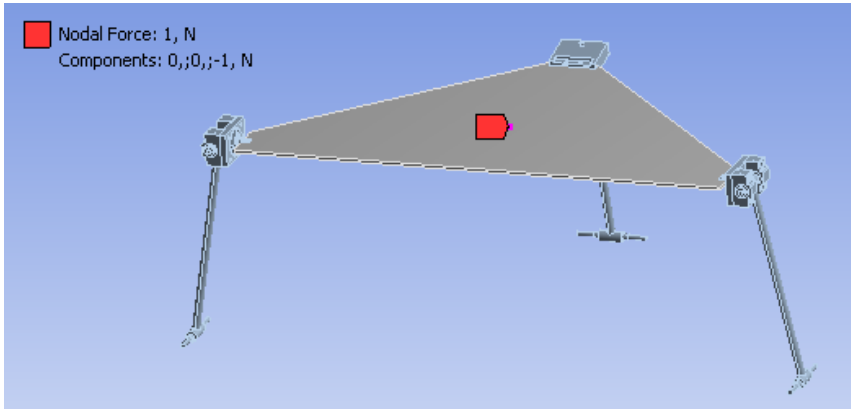
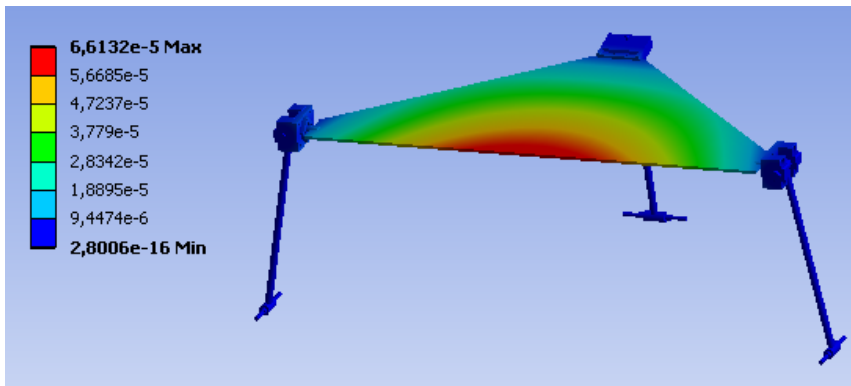


Figure 15.16: Mesh generated on ANSYS for: (a) universal joint; (b) spherical joint; (c) revolute joint

We define a unit vertical force applied on gravity centre of the mobile platform, as shown in Fig. 15.17a. Then we run the Static Structural analysis obtaining the deformation as result. Figure 15.17b shows the deformation of the manipulator obtained for a horizontal position and a unit force applied on the gravity centre. We calculate the stiffness by dividing the unit force by the displacement of the gravity centre. The stiffness of the manipulator under all these conditions is $2.138 \cdot 10^4$ N/m.



(a)



(b)

Figure 15.17: Result for horizontal position: (a) definition of the unit applied force; (b) deformation for that force

We run an analogue analysis for the different positions of the workspace we want to study. Table 15.6 shows the value of the stiffness of the manipulator for those positions and Fig. 15.18 represents them. As we see, a higher rotation of the mobile platform corresponds to a higher value of the stiffness of the manipulator, the maximum value of the stiffness being

$3.4876 \cdot 10^4$ N/m and corresponding to the position $(\psi, \theta) = (-15^\circ, 15^\circ)$.

Table 15.6: Stiffness obtained with ANSYS ($\times 10^4$ N/m)

		ψ				
		-15°	-5°	0°	5°	15°
θ	0°	3.2518	2.27024	2.138	2.2609	3.2117
	5°	3.2778	2.138	2.1544	2.2782	3.2361
	15°	3.4876	2.433	2.4235	2.4235	3.4429

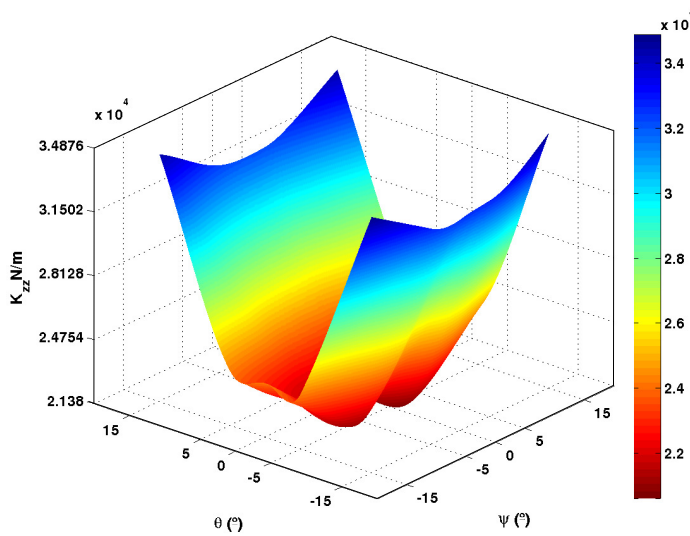


Figure 15.18: Stiffness of the manipulator in the positions analysed

15.4.3. Experimental analysis

In order to get the stiffness of the prototype experimentally, we apply a vertical force on the gravity centre and measure the deformation that it generates in the same point.

We apply the force by placing a mass on the gravity centre and measure the deformation it causes by using a dial gauge. In Fig. 15.19a we see the dial gauge before applying the force and in Fig. 15.19b we see the manipulator with the mass on top and the dial gauge measuring the deformation. We repeat this process three times, with three different forces. Table 15.7 presents the resulting measurements.

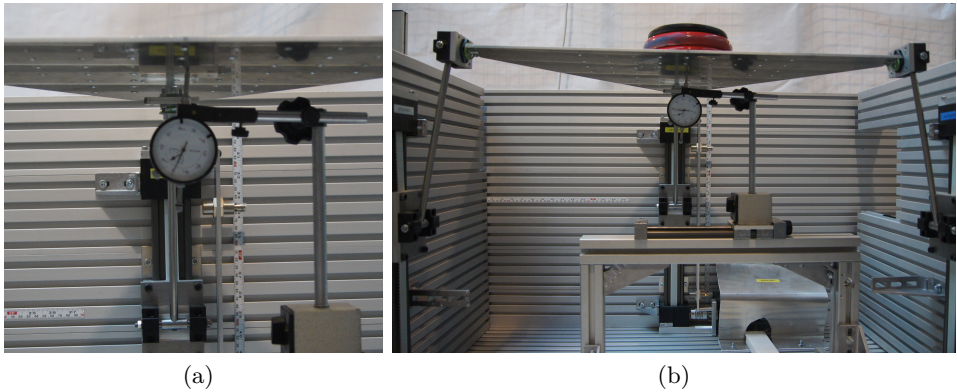


Figure 15.19: Stiffness experimental measurement: (a) dial gauge; (b) force applied on the GC

We define $K_{experimental}$ to be the stiffness of the manipulator measured experimentally. We consider that its value is the mean value of the three measurements. In our case, the value of $K_{experimental}$ is given by Eq. (15.8).

$$K_{experimental} = \frac{(2,07 + 2,06 + 2,0946) \cdot 10^4}{3} = 2,07487 \cdot 10^4 (N/m) \quad (15.8)$$

Table 15.7: Experimental data of the stiffness measurement

mass (kg)	Force, F (N)	Deformation, δ (m)	Stiffness, K (N/m)
5	49.05	0.002366	$2.07 \cdot 10^4$
10	98.1	0.004762	$2.06 \cdot 10^4$
15	147.15	0.007025	$2.0946 \cdot 10^4$

15.4.4. Interpreting results

We have obtained the stiffness of the prototype for different positions in the useful WS by applying, first, an analytical method and, then, FEM. The results obtained in both ways are very similar, even though the stiffness calculated analytically is slightly smaller than the one using FEM.

We have also measured the stiffness experimentally for the prototype in horizontal position. We have applied a force on the gravity centre of the prototype and measured the displacement that the gravity centre suffers. We have repeated this process three times with three different forces. We have defined $K_{experimental}$ to be the mean value of the experimental measurements. For our prototype, $K_{experimental} = 2.07487 \cdot 10^4$ (N/m).

The value of the stiffness obtained experimentally is very similar to the value of the stiffness for the prototype in horizontal position obtained when applying the analytical method and the finite elements method. Thus, we validate the analytical and FEM methods proposed.

15.5. Dynamics

In this Section, we solve the inverse dynamics for the three harmonic trajectories whose kinematic problem we have already analysed and which we list again in Table 15.8.

Table 15.8: Harmonic trajectories definition

	$traject(t) = C + A \cdot \sin(\omega t)$			
	C	A	$f = \omega / (2 \cdot \pi)$	t
X- and Y axes	0	3°	2,7 Hz	4 s
Z-axis	0,5 m	0,003 m	2,7 Hz	4 s

By solving the inverse dynamic problem, we obtain the reaction forces in the linear guides. We know that the maximum radial load that the linear guides can support is 300 N and the maximum belt tension, 200 N. Thus, we have to check that the reaction forces in the linear guides do not exceed those values.

Once we have the reactions in the linear guides we obtain the power required for each position (Pot_i) by applying Eq. (15.9), where F_i is the axial reaction on the linear guides and $d\rho_i$ is the velocity for the corresponding linear guide. The motors can supply a maximum power of 150 W, so we have to make sure that the power that each motor requires is lower than that limit.

$$Pot_i = F_i \cdot d\rho_i \quad (15.9)$$

We also check that the mean value of the torque in the motors does not exceed their torque limit, which is equal to 0.177 N · m. The torque in the

motors is given by Eq. (15.10).

$$T_i = \frac{\text{mean}(F_{axial_i}) \cdot R_{gearhead}}{\text{Reduction Ratio}} \quad (N \cdot m) \quad (15.10)$$

We analyse the reaction forces in the linear guides, as well as the torque and power in the motors for the three harmonic trajectories.

15.5.1. Trajectory I

We solve the inverse dynamic problem for the first trajectory. Figure 15.20a shows the axial forces for the rotation about X-axis. As we see, they exhibit harmonic behaviour. The axial forces for the first and third linear guides are the same, their values being between -2.5404 N and -2.2632 N. For the second linear guide, though, they vary from -3.4278 N to -1.2756 N. In the three cases the axial forces are under the maximum belt tension value.

The radial forces are shown in Fig. 15.20b. They are the same for the first and third linear guides – from -0.2976 N to -0.0164 N – and null for the second linear guide, so they do not exceed the maximum radial load allowed. We also calculate the power required by the motors, shown in Fig. 15.20c. Since the first and third linear guides stay motionless, the corresponding motors do not need power at all. The second motor, however, requires a maximum power of 0.811 W in absolute value. This value is much lower than the maximum power that the motors can provide. Finally, we get the torque in the motors, which is 0.0017 N·m.

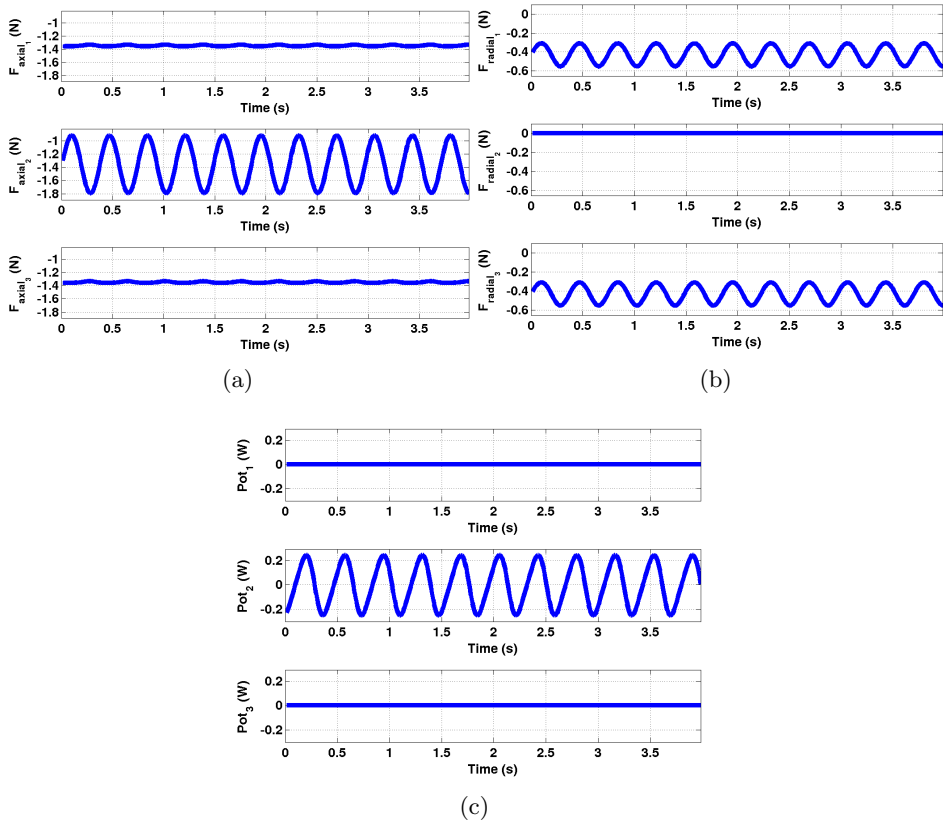


Figure 15.20: Trajectory I: (a) axial force in the linear guides ; (b) radial force in the linear guides; (c) power required by the motors

15.5.2. Trajectory II

For Trajectory II, the axial reaction forces for both the first and third linear guides vary in the range of $(-3.4284, -1.275)$ N. They also have the same frequency but with opposite direction. The axial reaction in the second linear guide, though, has double the frequency and a value varying from

-2.358 N to -2.3481 N. Figure 15.21a shows the axial reaction forces for the three linear guides.

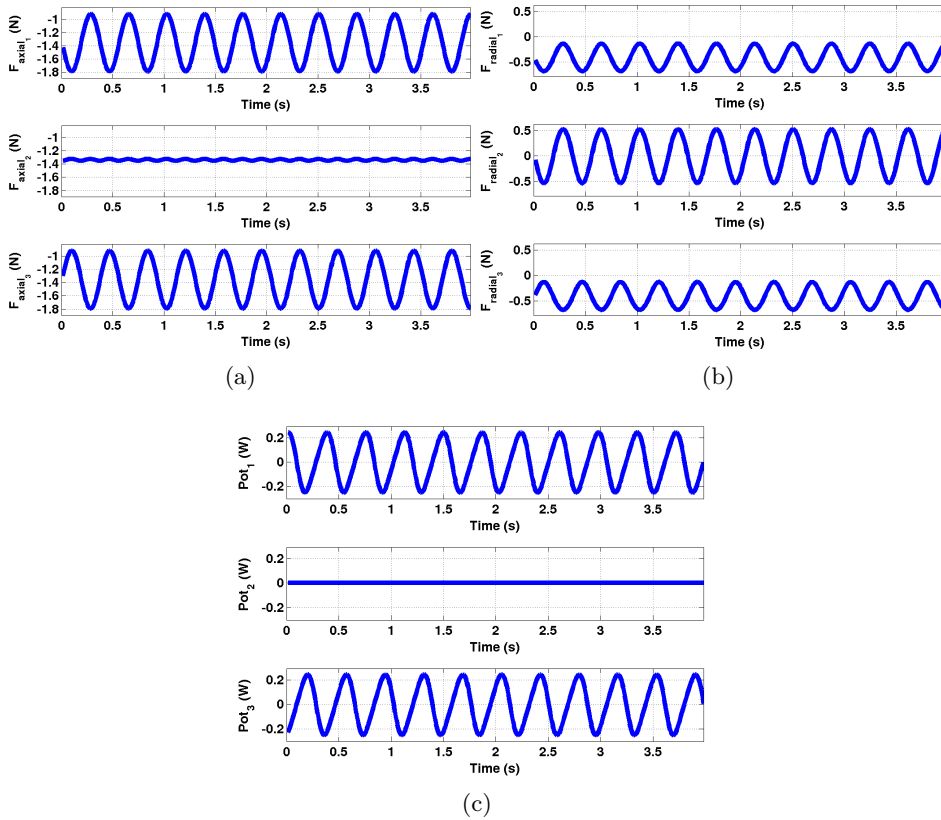


Figure 15.21: Trajectory II: (a) axial force in the linear guides ; (b) radial force in the linear guides; (c) power required by the motors

The radial reaction forces are shown in Fig. 15.21b. They are very similar for the three linear guides – (-0.164, -0.1421) N for the first one, (-0.163, 0.1476) N for the second one and (-0.1576, -0.1369) N for the third one.

They are all lower than limit of the radial load that the linear guides can support.

Since the second linear guide is motionless for this trajectory, only the first and third motors have to supply power, the maximum value being 0.7723 W, as we see in Fig. 15.21c. The torque in the three motors is equal to 0.0017 N·m, lower than the maximum torque that the motors can support.

15.5.3. Trajectory III

The third trajectory is a translation along Z-axis. During this trajectory, the three linear guides support the same axial reaction force. As we see in Fig. 15.22a, they are harmonic functions with a minimum value of -3.8771 N and a maximum value of -2.1495 N.

The radial reaction forces are shown in Fig. 15.22b. They are the same for the first and third linear guides – varying from -0.2472 N to -0.1371 N – while the radial reaction force in the second linear guide is null.

We obtain the power required by the motors and see that it is the same for the three of them, the minimum value being -0.1967 W and the maximum value being 0.1196 W. Besides, the torque supported by the three motors is 0.0017 N·m.

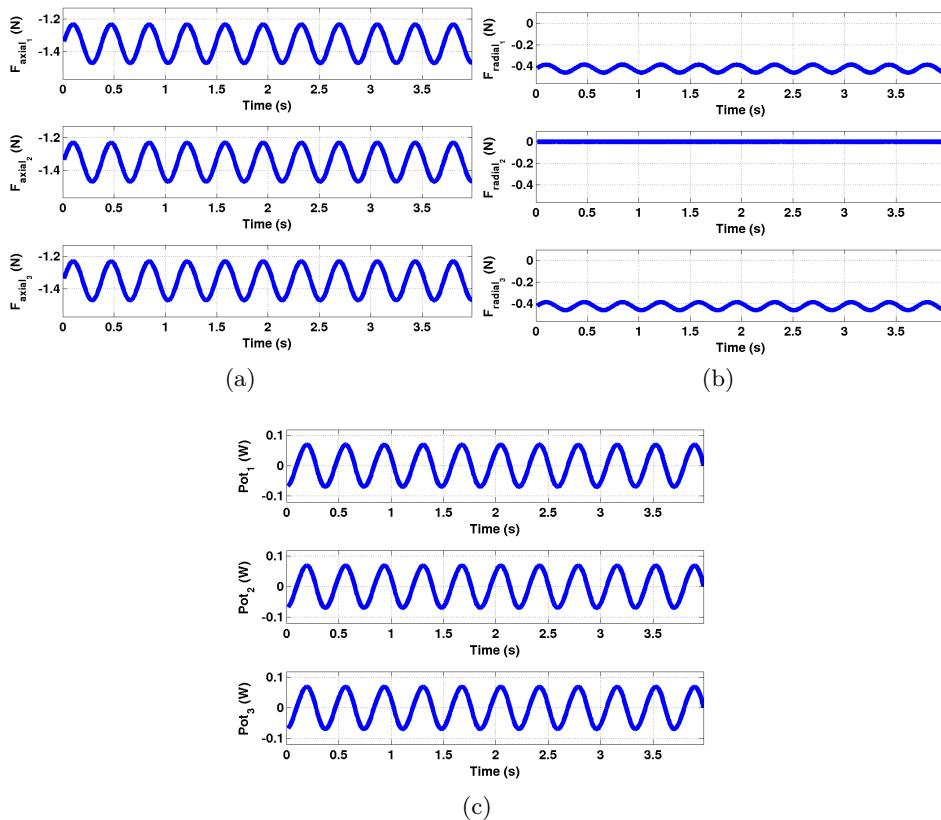


Figure 15.22: Trajectory III: (a) axial force in the linear guides ; (b) radial force in the linear guides; (c) power required by the motors

15.5.4. Interpreting results

We have solved the inverse dynamic problem for the three harmonic trajectories previously presented – a rotation about X-axis, a rotation about Y-axis and a translation along Z-axis. We have obtained the reaction forces in the linear guides and the power required by the motors during the three trajectories.

We have seen that for the rotation about X-axis the amplitude and the maximum value of the reaction force in the first and third linear guides are smaller than for the second one, the frequency of all of them being the same. In this case, the power required by the first and the third motors is null and the power in the second motor, harmonic.

For the rotation about Y-axis, due to the symmetry of the manipulator, the frequency of the reaction force in the second linear guide is twice the frequency of the first and third linear guides. For this trajectory, even if the amplitude of the force in the second linear guide is smaller than the force in the first and third linear guides, its maximum value is again larger. The force in the first and the third linear guides are of the same frequency and amplitude but opposite direction, just as the power needed by the motors. The power required by the second actuator is null for this case.

In all the cases the reaction forces in the linear guides, the power and torque of the motors fulfil the working restrictions of the linear guides and the motors.

15.6. Natural Frequencies

In this Section, we obtain the natural frequencies and modes of the manipulator. We apply two methods – finite element method and experimental method. We analyse the value of the natural frequencies and the shape of the mode for each of them and compare the results obtained with both methods.

15.6.1. Finite element method

We first present the steps to obtain the natural frequencies and modes for the manipulator in horizontal position by applying FEM. We apply it to analyse different positions of the useful WS. As we did in Section 15.4, we work with ANSYS Workbench. We import the geometry drawn in Catia and define the joints and the mesh in the same way we did for the stiffness. We run the analysis and get the first 5 natural frequencies and their corresponding modes.

The first mode appears for a frequency of 22.48 Hz. As we see in Fig. 15.23, it corresponds to the flexion of the mobile platform.

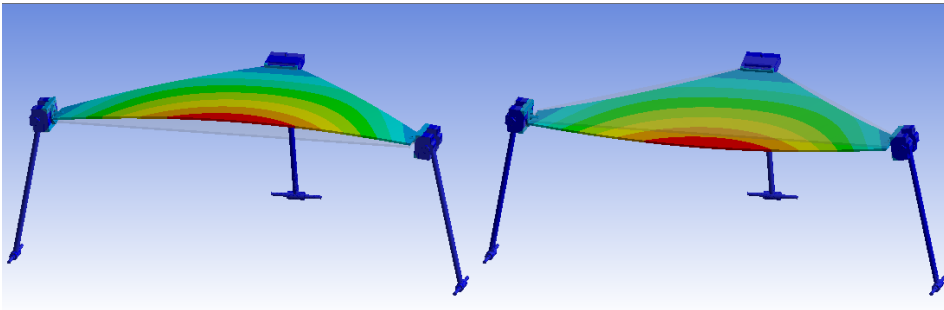


Figure 15.23: First mode obtained with FEM: flexion of the mobile platform at 22.48 Hz

The second mode of the manipulator is also a flexion of the mobile

platform, but in this case there is a node along Y-axis, shown in Fig. 15.24. This mode appears at a frequency of 58.839 Hz.

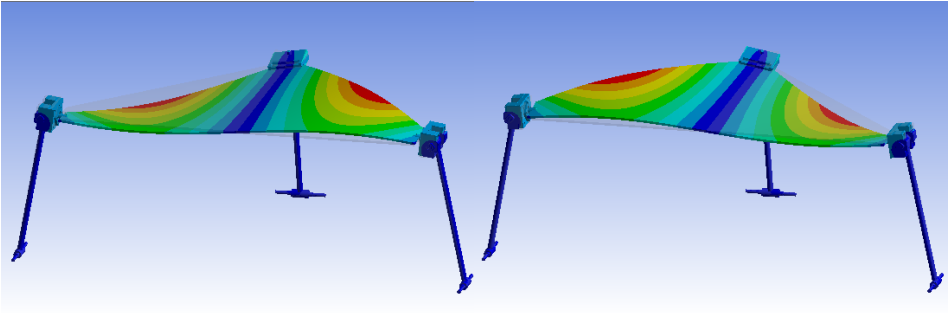


Figure 15.24: Second mode obtained with FEM: flexion of the mobile platform with a node along Y-axis direction at 58.839 Hz

The third mode appears at a frequency of 71.759 Hz. As represented in Fig. 15.25, it corresponds to the flexion of the limbs in the direction of X-axis.

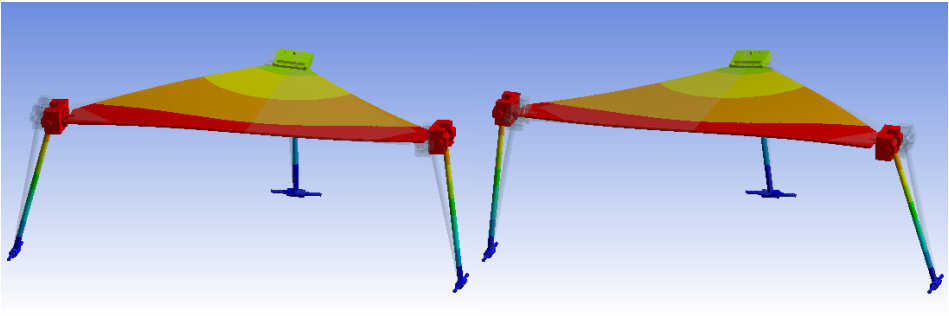


Figure 15.25: Third mode obtained with FEM: flexion of the limbs in X-axis direction at 71.759 Hz

In Fig. 15.26 we see the fourth mode of the manipulator. It is another flexion of the mobile platform, this time with a semi circle shaped node that goes from the first limb to the third. It appears at the frequency of 79.49 Hz.

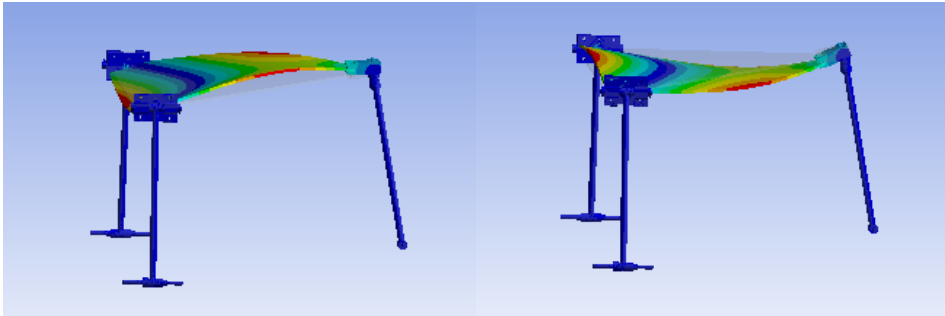


Figure 15.26: Fourth mode obtained with FEM: flexion of the mobile platform with a node from limb 1 to limb 3 at 79,493 Hz

The fifth mode appears at a frequency of 125.72 Hz and it corresponds to the flexion of the limbs in the direction of Y-axis, as we see in Fig. 15.27.

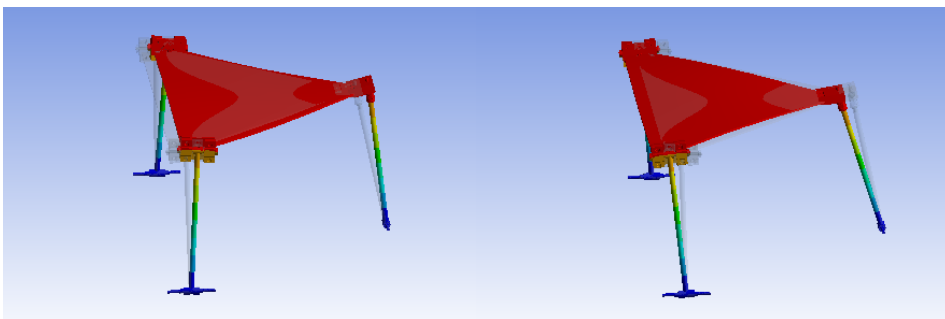


Figure 15.27: Fifth mode obtained with FEM: flexion of the limbs in Y-axis direction at 125.72 Hz

In order to see if the value of the natural frequencies varies in the workspace, we run the modal analysis in ANSYS Workbench for different positions of the workspace. The results are independent of the translation along the Z-axis, so we keep z constant and vary the value of the angles about X- and Y-axes. The manipulator is symmetric respect to Y-axis, so we only check the positive rotation about Y-axis. We create a grid of discrete points of the workspace by dividing X-axis in five points from -15° to 15° and Y-axis in three points from 0° to 15° . We analyse, thus, the natural frequencies of the prototype for 15 positions of the workspace.

Table 15.9 shows the values obtained for the five first natural frequencies for the different points of the useful WS of the manipulator and Fig. 15.28 plots them. As we see, the value of the natural frequencies stay almost constant along the useful WS and the modes do not cross each other.

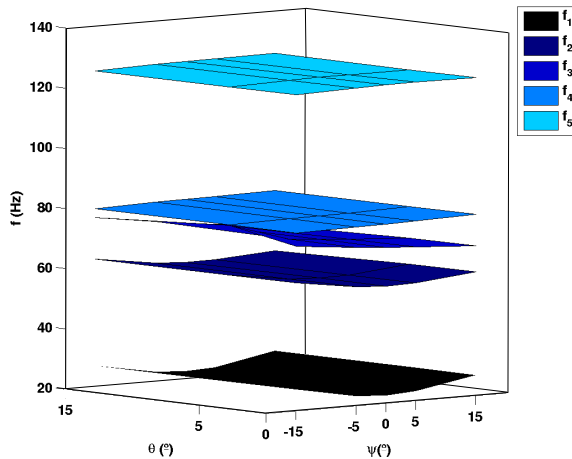


Figure 15.28: Natural frequencies obtained with FEM

Table 15.9: Frequencies obtained with FEM

			θ		
			0°	5°	15°
f_1	ψ	-15°	26.883	26.879	26.822
		-5°	23.09	23.08	23.039
		0°	22.48	22.475	22.432
		5°	23.051	23.045	23.001
		15°	26.746	26.736	26.649
f_2	ψ	-15°	62.418	62.422	62.414
		-5°	59.448	59.441	59.375
		0°	58.839	58.824	58.681
		5°	59.011	58.98	58.709
		15°	61.004	60.92	59.958
f_3	ψ	-15°	74.7	78.87	76.06
		-5°	72.63	72.709	73.175
		0°	71.76	71.76	71.8
		5°	70.981	70.893	70.51
		15°	69.8	69.673	68.552
f_4	ψ	-15°	79.032	79.039	79.144
		-5°	79.346	79.37	79.50
		0°	79.49	79.51	79.64
		5°	79.66	79.67	79.78
		15°	80.14	80.15	80.16
f_5	ψ	-15°	124.93	124.89	124.93
		-5°	125.56	125.45	125.31
		0°	125.72	125.65	125.5
		5°	125.76	125.63	125.48
		15°	125.65	125.59	125.66

15.6.2. Experimental results

We get the natural frequencies experimentally by applying an impulse force on the manipulator prototype in the directions of the natural modes. Thus, we need 3 accelerometers, one harmer and an analyser.

We choose shear accelerometers manufactured by PCB Piezotronics, model 352C33, with a sensitivity of 102.6 mV/g. The harmer is an impulse force harmer also manufactured by PCB Piezotronics, model 086C02, with a sensitivity of 11.49 mV/N. We use a medium hardness point. In order to process all the data, we use a Siemenes LMS TestLab analyser, seen in Fig. 15.29.



Figure 15.29: Siemenes LMS TestLab analyser

We place one of the accelerometers on the intersection of X- and Y-axes, as seen in Fig. 15.30a. This accelerometer allows us to get the natural frequencies that correspond to the flexion of the mobile platform. To do it, we excite that accelerometer by applying an impulse force perpendicular to the mobile platform, as shown in Fig. 15.30b.

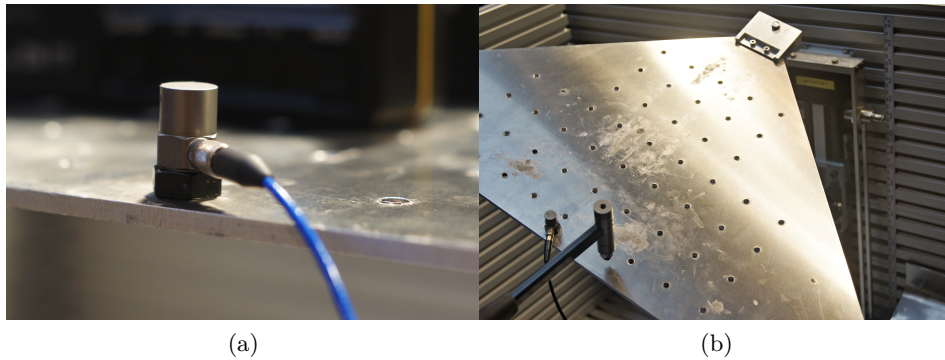


Figure 15.30: Measurement along Z-axis: (a) accelerometer on X-axis; (b) vertical impulse

We place another accelerometer on the universal joint of the first limb in X-axis direction, as we see in Fig. 15.31a. We excite it by applying an impulse force in the same direction on the universal joint of the third limb, as shown in Fig. 15.31b.

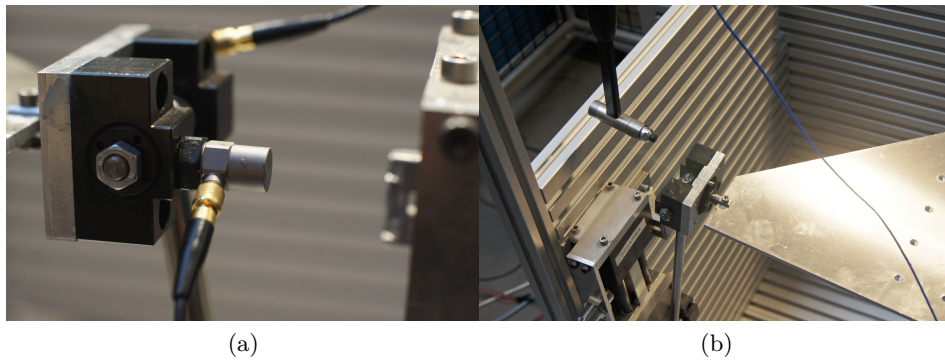


Figure 15.31: Measurement along X-axis: (a) accelerometer on joint U in X-axis direction; (b) impulse in X-axis direction

We place the last accelerometer also on the universal joint of the first limb, but in Y-axis direction, as seen in Fig. 15.32a. We excite the accelerometer by applying the impulse force in the Y-axis direction, as Fig. 15.32b shows.

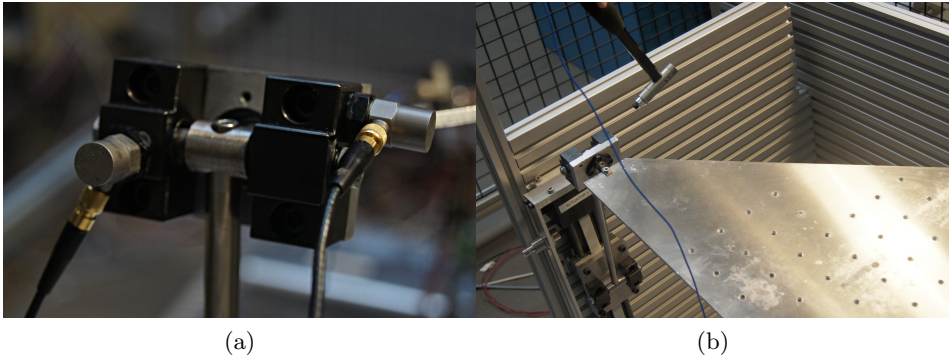


Figure 15.32: Measurement along Y-axis: (a) accelerometer on joint U in X- and Y-axis direction; (b) impulse in Y-axis direction

We apply the described impulses in X-, Y- and Z-axis direction for different points of the workspace. As we did for the analysis with FEM, we fix a value of z and we modify the angles ψ and θ . We discretize the plane for the range of $[-15^\circ, 15^\circ]$ with a step of 5° for the rotation about X-axis and the range of $[-20^\circ, 20^\circ]$ for the rotation about Y-axis.

According to the results obtained with FEM, the first natural frequency should correspond to the first flexion of the mobile platform. However, when we apply the impulse force in X-axis direction, we see that the flexion mode of the limbs in X-axis direction is the first natural mode of the prototype. Figure 15.33 shows the response we get in the accelerometer in X-axis direction for the horizontal position of the manipulator and for the position ($\psi = -15^\circ, \theta = 5^\circ$). As we see, the first natural frequency appears now at

9.38 Hz. This value does not vary for the different positions of the manipulator.

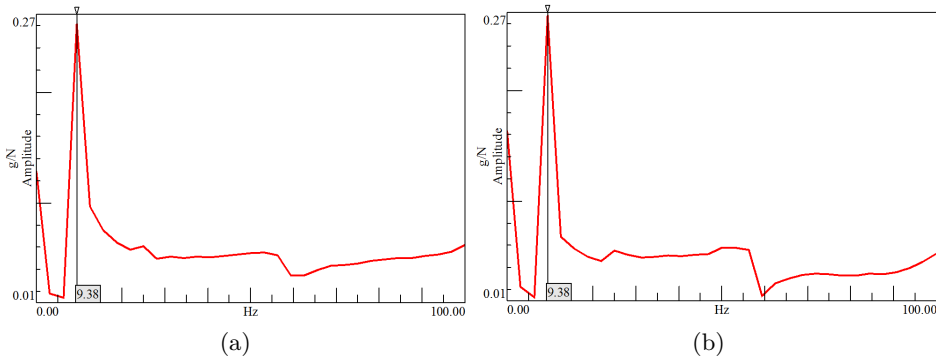


Figure 15.33: Response obtained in the accelerometer in X-axis direction for the positions: (a) $\psi = 0^\circ, \theta = 0^\circ$; (b) $\psi = -15^\circ, \theta = 5^\circ$

The second natural mode of the manipulator that appears is the flexion of the limbs in the Y-axis direction. It occurs at a frequency of 15.63 Hz, as we see in Fig. 15.34. Finally, we get the natural frequency that corresponds to the natural mode of the first flexion of the mobile platform. It appears at a frequency of 21.88 Hz, 24.93 Hz or 25 Hz, depending on the position of the manipulator. This value is lower than the one we got using FEM, but very similar. In Fig. 15.35 we see the response obtained by the accelerometer in Z-axis direction for the horizontal position as well as for the position where $\psi = -15^\circ, \theta = 5^\circ$.

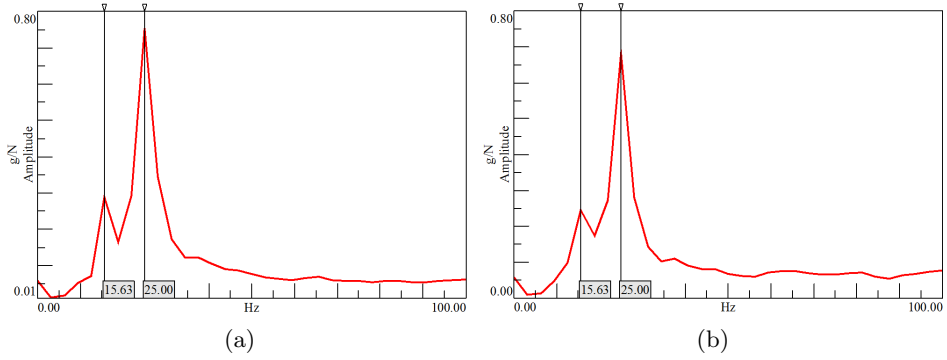


Figure 15.34: Response obtained in the accelerometer in Y-axis direction for the positions: (a) $\psi = 0^\circ, \theta = 0^\circ$; (b) $\psi = -15^\circ, \theta = 5^\circ$

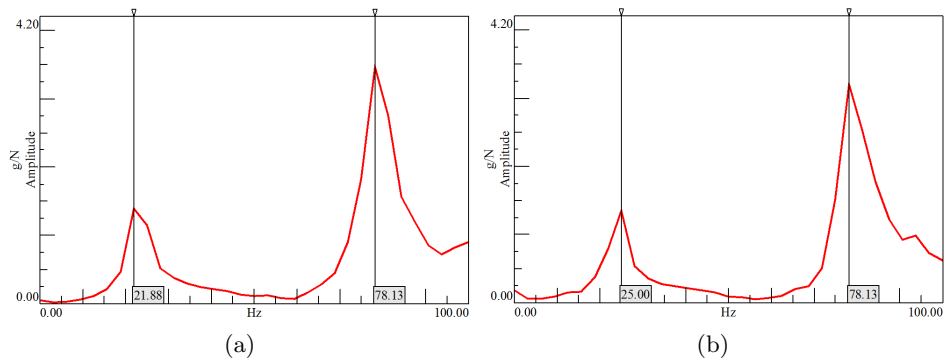


Figure 15.35: Response obtained in the accelerometer in Z-axis direction for the positions: (a) $\psi = 0^\circ, \theta = 0^\circ$; (b) $\psi = -15^\circ, \theta = 5^\circ$

Table 15.10 presents the value of the natural frequencies along the useful WS and Fig. 15.36 plots them.

Table 15.10: Frequencies obtained experimentally

			θ		
			0°	5°	15°
f_1	ψ	-15°	9.38	9.38	9.38
		-5°	9.38	9.38	9.38
		0°	9.38	9.38	9.38
		5°	9.38	9.38	9.38
		15°	9.38	9.38	9.38
f_2	ψ	-15°	15.63	15.63	15.63
		-5°	15.63	15.63	15.63
		0°	15.63	15.63	15.63
		5°	15.63	15.63	15.63
		15°	15.63	15.63	15.63
f_3	ψ	-15°	25	25	24.93
		-5°	21.88	21.88	24.93
		0°	21.88	21.88	24.93
		5°	21.88	21.88	24.93
		15°	25	25	24.93
f_4	ψ	-15°	78.13	78.13	78.08
		-5°	78.13	78.08	78.08
		0°	78.13	78.13	78.08
		5°	78.13	78.13	78.08
		15°	78.13	78.13	78.08

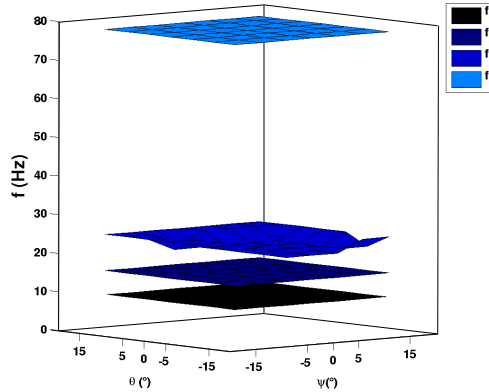


Figure 15.36: Experimental natural frequencies

15.6.3. Interpreting results

We have analysed the natural frequencies and vibration modes of the prototype placed in different positions of the useful WS. We have first applied FEM and then an experimental method.

When applying FEM, we have obtained the five first vibration modes. The first and second modes are flexions of the mobile platform that correspond to natural frequencies at 22.48 Hz and 58.839 Hz. The third mode is the flexion of the limbs along X-axis and appears at 71.759 Hz. The fourth mode occurs at a frequency of 79.493 Hz and is another flexion of the mobile platform. Finally, the fifth mode appears at 125.72 Hz, being the flexion of the limbs along the Y-axis.

However, we have seen that in the real model the order of the natural frequencies changes. For the experimental measurements done on the prototype, the first natural frequency appears at 9.38 Hz and corresponds to the flexion of the limbs in X-axis. The second frequency corresponds to the flexion of the limbs along Y-axis for a frequency of 15.63 Hz. The flexion of

the mobile platform appears now at a frequency of 21.88 Hz, 24.93 Hz or 25 Hz, depending on the position of the manipulator.

This difference in the results is most likely due to the small clearances between the joints that appear in the prototype.

Part VI

Conclusions and Future Work

Conclusions

This Ph.D. thesis is about effecting gains in performance in parallel manipulators, with a special focus on Multi Axial Shaking Tables (MAST). Bibliographies have either high kinematic capacities – having too complex position, velocity and acceleration problems – or good structural performance – requiring machines with big dimensions and, thus, they have seen limited development. As a result, in this Ph.D. thesis we have developed two methodologies based on kinematic, resistance and power consumption criteria, along with a simple design, but with high movement capacity. The two methodologies are valid for any kind of MAST parallel manipulator, but we have validated them for a parallel manipulator for testing automobile pieces.

We need three degrees of freedom for this application – two rotations and one translation. The lower-mobility parallel manipulator family with those degrees of freedom is the 1T2R. The most well known parallel manipulator of that family is the 3PRS, but it has two main drawbacks – a low orientation capability and parasitic motions in the three degrees of freedom where there was supposed to be no motion. In order to overcome those problems, we have proposed to use instead the 2PRU-1PRS parallel manipulator. It has the same degrees of freedom as the 3PRS parallel ma-

nipulator but it has higher orientation capability and its parasitic motion is only along one axis.

In the analysis methodology, we have analysed the manipulator for its kinematics, dynamics, stiffness, singularities and workspace. We have first developed the equations of the kinematic problem by using the loop equation of the limbs. We have obtained the position, velocity and acceleration of every element of the manipulator along a given trajectory. From the velocity problem we have obtained the Jacobian matrices, which we have used to define the condition when there are singularities in the manipulator.

Then, we have proposed a stiffness analysis based on the matrix structural method. This analysis allows us to get the stiffness of the manipulator at any position. Due to the importance of high stiffness in parallel manipulators, this is a remarkable step in the analysis.

We have also presented a method to get the useful workspace of the manipulator. The useful workspace is the singularity-free space that the end-effector can reach taking into account the limits of the joints and actuators, as well as possible collisions between the limbs. In order to get an idea not only about the size of the useful workspace but also about its regularity, we define the biggest geometry object in it.

In the optimization methodology we have taken into account two performances – the size and regularity of the useful workspace, and the power consumption along a defined trajectory. Thus, we have obtained two best geometric parameters combinations, one for each objective function. We have obtained the useful workspace and the biggest sphere in it for a finite set of geometric parameters combinations. We have labelled the best geometry parameters combination for the workspace objective function to be the one that leads to the biggest sphere contained in the useful workspace. The best solution for the power objective function is the one that leads to the lowest power consumption along a given trajectory. We have used analytical tools to analyse the kinematic and dynamic problems. They allow us to solve the

problem in an iterative way with a reduced computational cost. We have obtained all the possible solutions and get the optimum or optimum ones.

In order to apply both methodologies easily, we have developed a program in MATLAB with several easy-to-use graphical user interfaces. By using this program, the user can choose the problem to analyse and the range of the variables. The results of the analyses are then presented graphically. Figure 16.1 shows the interface that we have developed for the optimization of the parameters when the power consumption is to be taken into account

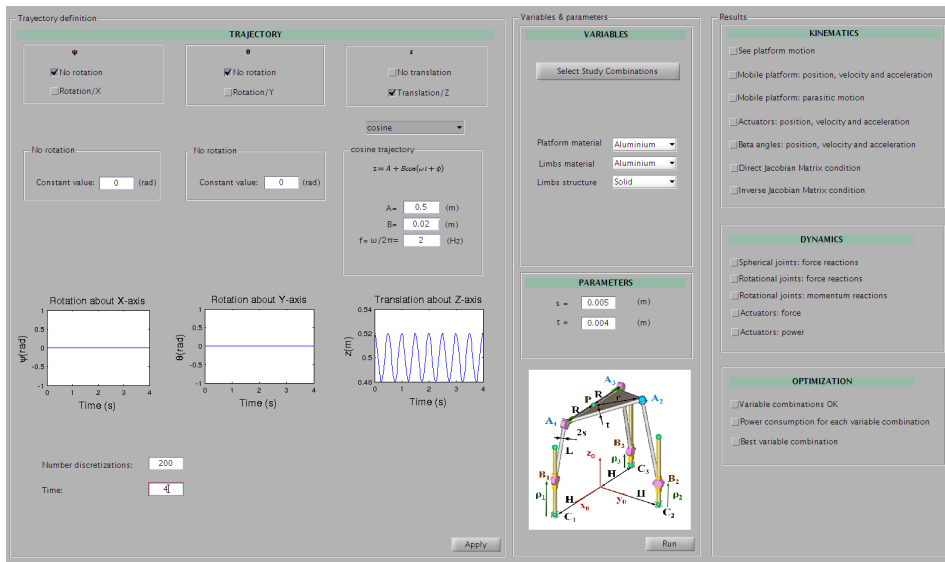


Figure 16.1: Interface for power optimization

Besides, we have designed and built a prototype in the laboratory of COMPMECH research group to validate the previous theoretical developments and detect possible errors that the models do not take into account.

We have designed specific kinematic joints with the aim of increasing the rotation range of the universal joints. In this way, the manipulator can achieve rotations from -15° to 15° without interferences between the elements of the manipulator. We have also designed the actuators with the same objective. We have developed the control system by avoiding a closed-CNC-type system. Thanks to this, we have achieved high dynamic performances, with a frequency of 15 Hz with the only weight of the system.

We have designed and built the whole prototype, including the actuation system. This fact has allowed us to reach extreme movement performances, that we have also simulated on the virtual model. We have checked the accuracy in the movement and measured the parasitic motions, seeing that the errors in position are really small and that the parasitic motions are the ones expected. We have also obtained the stiffness for different positions of the workspace by using a finite element experimental methods. We have seen that the values obtained correspond to the ones obtained by using the matrix structural method. We have checked that there are no collisions or singularities in the real useful workspace and that that real useful workspace has the size as the one obtained theoretically. Finally, we have obtained the natural frequencies and vibration modes by using a finite element method and from experiments. We have seen that in the real model some vibration modes appear at lower frequencies than in the finite elements analysis. This may be due to clearances or inexactitudes in the building process. In this way, we have increased the limits of the prototype with the only limitations being the ones given by the design itself.

Future Work

There are some related research topics that we have not included in this work which offer an interesting avenue for future work. We describe them below:

- The models developed in this work can be improved by taking the experimental results into account. We have seen that some vibration modes appear at a lower frequency in the real model than in the theoretical results. This is due to the clearances in the joints of the prototype. We can try to reduce them while building the prototype, but it is not possible to make them completely disappear. If we accept that there will always be some clearances, what we can do is to include them in the theoretical model. Besides, in the theoretical model, we could also consider the torque applied in the joints when building the prototype. A model that considers the clearances and the torque in the joints would be more complicated but also more accurate.
- We have optimized the geometric parameters by taking into account the size and regularity of the workspace and the power consumption along a given trajectory. These two parameters are very important in parallel manipulators, but the stiffness is another very decisive

parameter that we have to consider when designing a new parallel manipulator. Thus, we can also optimize the geometric parameters so the stiffness is the highest possible.

- We have based this work on the ideal behaviour of the system, but in real models phenomena such as friction and big deformations can occur. The friction in ideal joints is null, but in real models there is always friction – even if it is small – between the different parts of the manipulator. Thus, if we want to get an even more precise model, we can introduce the friction as a force in the dynamic equations. Similarly, depending on the behaviour of the material, we cannot work under the hypothesis of small deformations and have to consider possible big deformations of the elements of the system.
- Finally, we could improve our models by including the characteristics of actuators and transmission type, that would affect the model in different ways depending on if they are hydraulic, gear-based or belt-based ones, for example.

References

- [1] Robotic Industries Association (RIA). Web site: www.robotics.org/.
- [2] British Automation and Robot Association (BARA). Web site: www.bara.org.uk.
- [3] ABB Group. Web site: www.abb.com.
- [4] iRobot Corporation. Web site: www.irobot.com.
- [5] Intuitive Surgical Company. Web site: www.intuitivesurgical.com/.
- [6] NASA. Web site: <http://www.nasa.gov/>.
- [7] RTS Lab. Web site: www.rtsideas.com.
- [8] Korean Institute of Ocean Science and Technology (KIOST). Web site: eng.kiost.ac.
- [9] Boston Dynamics. Web Site: <http://www.bostondynamics.com/>.
- [10] Sony Aibo. Web site: www.sony-aibo.com/.
- [11] J. Engelberger. *Robotics in Practice*. KOGAN PAE in association with Avebury Publishing Company, 1980.
- [12] Inc. Web site: www.adept.com Adept Technology.

-
- [13] KUKA Robot Group. Web site: www.kuka-robotics.com.
 - [14] J.-P. Merlet. *Parallel Robots*. Kluwer academic publishers, 2000.
 - [15] U. Uchiyama, K. Iimura, F. Pierrot, P. Dauchez, K. Unno, and O. Toyama. A new design of a very fast 6-dof parallel robot. In *International Symposium Industrial Robots*, pages 771–776, 1992.
 - [16] Bonev. The true origins of parallel robots. Web site: www.parallelic.org/reviews/review007p.html.
 - [17] J.E. Gwinnett. Amusement device, US Patent No. 1,789,680, 1931.
 - [18] Pollard W. Jr. Spray Painting Machine. US Patent No. 2,213,108, 1940.
 - [19] V.E. Gough and S.G. Whitehall. Universal tyre test machine. In *Proceedings of the FISITA Ninth International Technical Congress*, pages 117–137, 1962.
 - [20] D. Stewart. A platform with six degrees of freedom. In *Proceedings of the IMechE*, volume 180, pages 371–385, 1965.
 - [21] K.L. Cappel. Motion simulator. US Patent No. 3,295,244, 1967.
 - [22] R. Clavel. Delta, a fast robot with parallel geometry. *Proceedings of the 18th International Symposium on Industrial Robots (ISIR)*, pages 91–100, 1988.
 - [23] R. Clavel. Device for displacing and positioning an element in space, WO 87/03528, 1985.
 - [24] R. Clavel. Device for the movement and positioning of an element in space. US Patent No. 4,976,582, 1990.
 - [25] R. Clavel. Device for displacing and positioning an element in space. EP 0 250 470, 1991.

-
- [26] Bosch Packaging Technology. Web site: www.boschpackaging.com/en/pa/homepage/homepage.html.
- [27] FANUC Company. Web site: www.fanuc.co.jp/en/product/robot/genkotu.html.
- [28] J. Hoekstra. Grace researchflight simulator. Technical report, National Aerospace Laboratory (NLR), 2005.
- [29] J.C.M Carvalho and M. Ceccarelli. Seismic motion simulation based on cassino parallel manipulator. *Journal of the Brazilian Society of Mechanical Sciences*, 24(3):213–219, 2002.
- [30] M. Shoham, M. Burman, E. Zehavi, L. Joskowicz, E. Batkilin, and Y. Kunicher. Bone-mounted miniature robot for surgical procedures: Concept and clinical applications. *IEEE Transaction on Robotics and Automations*, 19(5):893–900, 2003.
- [31] Mazor Robotics. Web site: www.mazorrobotics.com.
- [32] W. Sukovich, S. Brink-Danan, and M. Hardenbrook. Miniature robotic guidance for pedicle screw placement in posterior spinal fusion: Early clinical experience with the Spine Assist. *International Journal of Medical Robotics and Computer Assisted Surgery*, 2(2):114–122, 2006.
- [33] C. Plaskos, P. Cinquin, S. Lavallée, and A.J. Hodgson. Praxiteles: a miniature bone-mounted robot for minimal acces total knee arthroplasty. *The International Journal of Medical Robotics and Computer Assisted Surgery*, 1(4):67–79, 2005.
- [34] S. Song, A. Mor, and B. Jaramaz. HyBAR: hybrid bone-attached robot for joint arthroplasty. *The International Journal of Medical Robotics and Computer Assisted Surgery*, 5(2):223–231, 2009.
- [35] A. Wolf, B. Jaramaz, B. Lisien, and A.M. DiGioia. MBARS: Mini bone-attached robotic system for joint arthroplasty. *The International Journal of Medical Robotics and Computer Assisted Surgery*, 1(2):101–121, 2005.

- [36] Y. Li and Q. Xu. Design and development of a medical parallel robot for cardiopulmonary resuscitation. *IEEE/ASME Transactions on Mechatronics*, 12(3):265–273, 2007.
- [37] H. Takanobu, T. Mamyma, A. Takanishi, K. Ohtsuki, and M. Ohnishi. Mouth opening and closing training with 6-dof parallel robot. In *In Proceedings of the 2000 IEEE International Conferenc on Robotics and Automation*, 2000.
- [38] J-P. Merlet. Marionet, a family of modular wire-driven parallel robots. In J. Lenarčič and Stanišić, editors, *Advances in Robot Kinematics: Motion in Man and Machine*, pages 53–61. Springer, 2010.
- [39] INRIA Sophia Antipolis. Web site: www.inria.fr/en/centre/sophia.
- [40] M. Harshe. *A multi-sensor, cable-driven parallel manipulator based lower limb rehabilitation device : design and analysis*. PhD thesis, Ecole Nationale Supérieure des Mines de Paris, 2012.
- [41] K. Ibrahim, A. Ramadan, M. Fanni, Y. Kobayashi, A. Abo-Ismael, and M.G. Fujie. Development of a new 4-dof endoscopic parallel manipulator based on screw theory for laparoscopic surgery. *Mechatronics*, 28:4–17, 2015.
- [42] I. Fassi and G.J. Wiens. Multiaxis machining: Pkms and traditional machining centers. *Journal of Manufacturing Processes*, 2(1):1–14, 2000.
- [43] D. Zhang. *Parallel Robotic Machine Tools*. Springer, 2010.
- [44] Z. Pandilov and V. Dukovski. Parallel kinematics machine tool: overview - from history to future. *Annals of Faculty Engineering Hunedoara - International Journal of Engineering*, X(2):111–124, 2012.
- [45] Fives Giddings & Lewis. Web site: www.fivesgroup.com.

-
- [46] M. Geldart, P. Webb, H. Larsson, M. Backstrom, N. Gindy, and K. Rask. A direct comparison of the machining performance of a vari-ax 5 axis parallel kinetic machining centre with conventional 3 and 5 axis machine tools. *International Journal of Machine Tools & Manufacture*, 43:1107–1116, 2003.
- [47] J. Wahl. Articulated tool head. WIPO Patent, No. WO/20 00/25976, 2000.
- [48] J. Carretero, R. Podhorodeski, M. Nahon, and C. Gosselin. Kinematic analysis and optimization of a new three degree-of-freedom spatial parallel manipulator. *Journal of Mechanical Design*, 122:17–24, 2000.
- [49] G. Pond and J.A. Carretero. Architecture optimization of three 3prs variants for parallel kinematic machining. *Robotics and Computer-Integrated Manufacturing*, 25:64–72, 2009.
- [50] T. Huang and H.T. Liu. A parallel device having double rotation freedom and one translation freedom. PCT Patent No. WO2007/124637, 2007.
- [51] X. Chen, X-J. Liu, F. Xie, and T. Sun. A comparison study on motion/force transmissibility of two typical 3-dof parallel manipulators: The sprint z3 and a3 tool heads. *International Journal of Advanced Robotic Systems*, 11(5), 2014.
- [52] Index Traub. Web site: www.index-traub.com/en/.
- [53] R. Boudreau and C.M. Gosselin. The synthesis of planar parallel manipulators with a generic algorithm. *ASME Journal of Mechanical Design*, 121(4):533–537, 1999.
- [54] J. Duffy. *Statics and kinematics with applications to robotics*. Cambridge University Press, 1996.

- [55] F. Pierrot, P. Dauchez, and A. Fournier. Hexa: a fast six-dof fully-parallel robot. In *Fifth International Conference on Advanced Robotics, 1991. 'Robots in Unstructured Environments', 91 ICAR.*, volume 2, pages 1158 – 1163, 1991.
- [56] L.-W. Tsai, G.C. Walsh, and R.E. Stamper. Kinematics of a novel three dof translational platform. *IEEE International Conference on Robotics and Automation, Proceedings*, 4:3446–3451, 1996.
- [57] R. Di Gregorio and V. Parenti-Castelli. *Advances in Robot Kinematics: Analysis and Control*, chapter A Translational 3-DOF Parallel Manipulator, pages 49–58. Kluwer Academic Publishers, 1998.
- [58] M. Carriato and V. Parenti-Castelli. A family of 3-dof translational parallel manipulators. *Journal of Mechanical Design*, 2003.
- [59] Fatronik Tecnia. Web site: www.tecnalia.com/en/.
- [60] C.M. Gosselin and J-F. Hamel. The agile eye: a high-performance three-degree-of-freedom camera-orienting device. In *Proceeding of the IEEE International Conference on Robotics and Automation*, volume 1, pages 781–786. IEEE, 1994.
- [61] C.M. Gosselin, E. St-Pierre, and M. Gagné. On the development of the agile eye. *IEEE Robotics & Automation Magazine*, 3(4):29–37, 1996.
- [62] R. Di Gregorio. Kinematics of a new spherical parallel manipulator with three equal legs: The 3-urc wrist. *Journal of Robotic Systems*, 18(5):213–219, 2001.
- [63] J. Enferadi and A. Shahi. On the position analysis of a new spherical parallel robot with orientation applications. *Robotics and Computer-Integrated Manufacturing*, 37:151–161, 2016.
- [64] K. H. Hunt. Structural kinematics of in-parallel-actuated robot-arms. *Journal of Mechanisms, Transmissions, and Automation in Design*, 105:705–712, 1983.

-
- [65] J.A. Carretero, M. Nahon, C.M. Gosselin, and B. Buckham. Kinematic analysis of a three-dof parallel mechanism for telescope applications. In *In: Proceedings of the ASME design automation conference*, 1997.
- [66] A. Hernández, O. Altuzarra, Ch. Pinto, and E. Amezua. Transitions in the velocity pattern of lower mobility parallel manipulators. *Mechanism and Machine Theory*, 43(6):738–753, 2008.
- [67] T. Itul and D. Pisla. Three degrees of freedom parallel structure used for the tv satellite dish orientation. In IEEE, editor, *Proceedings of the International Conference of Intelligent Engineerig Systems*, pages 261–266, 2004.
- [68] T.J. Teo, G. Yang, I.M. Chen, and W. Lin. A 3-dof spatial motion flexure-based parallel manipulator with large workspace and high payload for uv nanoimprint lithography application. In *EUSPEN*, volume 1, pages 360–363, 2010.
- [69] Q. Hao, L. Wang, L. Guan, and X-J Liu. Dynamic analysis of a novel 3-pp 3-dof parallel manipulator. In J.S. Dai, M. Zappi, and X. Kong, editors, *ASME/IFTOMM International Conference on Reconfigurable Mechanisms and Robots*, pages 309–314, 2009.
- [70] M.A. Hosseini and P. Ebrahimi. Kinematic analysis of a novel complex dof parallel manipulator. In *World Academy of Science, Engineering and Technology*, volume 67, pages 413–417, 2012.
- [71] M.A. Hosseini. Kinematic synthesis of a novel rapid spherical crs/ps parallel manipulator. *Mechanism and Machine Theory*, 93:26–38, 2015.
- [72] D. Zlatanov and C.M. Gosselin. A family of new parallel architecture with four degrees of freedom. *Electronic Journal of Computational Kinematics*, 1(1), 2002.

- [73] Z. Huang and Q.C. Li. General methodology for type synthesis of symmetrical lower-mobility parallel manipulators and several novel manipulators. *The International Journal of Robotics Research*, 21(2):131–145, 2002.
- [74] S-J. Zhu and Z. Huang. Emanipulators symmetrical 5-dof 3r2t parallel manipulators with better actuating modes. *International Journal in Advanced Manufacturing Technology*, 34:406–412, 2007.
- [75] Moog. Web site: <http://www.moog.com/>.
- [76] U. Füllekrug. Utilization of multi-axial shaking tables for the modal identification of structures. *Philosophical transactions of the Royal Society - Mathematical, phical and engineering sciences*, 359:1753–1770, 2001.
- [77] A.C. Ruge. The determination of earthquake stresses in elastic structures by means of mmodel. *Bulletin of the Seismological Society of America.*, 24(3):169–230, 1934.
- [78] A.C. Ruge. A machine for reproducing earthquake motion direct from a shadowgraph of the earthquake. *Bulletin of the Seismological Society of America.*, 26(3):201–205, 1936.
- [79] R.T. Severn. The development of shaking tables - a historical note. *Earthquake engineering and structural dynamics.*, 40:195–213, 2011.
- [80] R. Muir-Wood. Robert mallet and john milne,Äearthquakes incorporated in victorian britain. *Earthquake Engineering & Structural Dynamics*, 17(1):107–142, 1988.
- [81] F.J. Rogers. Experiments with a shaking machine. the californian earthquake of april 1906. *Report of the State Investigation Commission.*, 1(2):326–335, 1906.
- [82] S.L. Jacobsen. Experimental study of the dynamic behaviour of mmodel of timber walls. *Bulletin of the Seismological Society of America.*, 20:115–146, 1930.

-
- [83] S.L. Jacobsen. Motion of soil subjected to a simple harmonic ground vibration. *Bulletin of the Seismological Society of America.*, 20:160–195, 1930.
- [84] L.M. Hoskins and S.L. Jacobsen. Water pressure in a tank caused by a simulated earthquake. *Bulletin of the Seismological Society of America.*, 24(1):1–22, 1934.
- [85] S.L. Jacobsen, S. Lydik, and S.A. Roberts. Hydrodynamic experiments with rigid cylindrical tank subjected to transient motions. *Bulletin of the Seismological Society of America.*, 41:313–345, 1951.
- [86] N. Monobe, A. Takata, and H. Matumura. Seismic stability of earth dams. In *Second World Congress on Large Dams.*, 1936.
- [87] G. Oberti. Development of aseismic design and construction in Italy by means of research on large model test. In *Proceedings of First World Conference on Earthquake Engineering.*, 1936.
- [88] R.W. Clough and D. Pirtz. Earthquake resistance of rockfill dams. *Transactions of the American Society of Civil Engineers.*, 123:792–816, 1958.
- [89] A. Sesan, G. D'Albon, I. Congrati, and L. Strat. A new shaking table used to test structure at seismic actions. *Buletunal Institutulu Politehnic Din Iasi.*, 15, 1969.
- [90] M.A. Sozen, S. Otani, P. Gulkan, and N.N. Nielsen. The university of Illinois earthquake simulator. In *Proceedings of Fourth WCEE*, volume 111, pages 140–149, 1969.
- [91] M.A. Sozen and S. Otani. Performance of the university of Illinois earthquake simulator for reproducing scaled earthquake motion. In *Proceedings of U.S.-Japan Seminar in Earthquake Engineering.*, 1970.
- [92] J. Penzien, J.G. Bouwkamp, R.W. Clough, and D. Rea. Feasibility study large earthquake simulator. Technical Report Report no. EERC-67-1, University of California, Berkeley., 1967.

- [93] D. Rea and J. Penzien. Dynamic response of a 20x20ft shaking table. In *Proceedings of Fifth WCEE.*, volume 2, pages 1447–1456, 1973.
- [94] K. Sawada. Strength and vibration characteristics of large type shaking table. Technical Report Technical Review No. 3, Mitsubishi Heavy Industries Ltd., 1970.
- [95] French Alternative Energies and Atomic Energy Commission. Web site: http://www.cea.fr/english_portal/cea/identity.
- [96] K.H. Hunt. *Kinematic Geometry of Mechanisms*. Oxford University Press, 1978.
- [97] M-S. Tsai, T-N Shiau, Tsai Y-J., and T-H. Chang. Direct kinematic analysis of a 3-prs parallel manipulator. *Mechanism and Machine Theory.*, 38(1):71–83, 2002.
- [98] J-P. Merlet. Micro parallel robot mips for medical applications. In *Proceedings of the eighth international conference on emerging technologies and factory automation (ETFA2001)*, 2001.
- [99] Q. Li, Z. Chen, Q. Chen, C. Wu, and X. Hu. Parasitic motion comparison of 3-prs parallel mechanism with different limb arrangements. *Robotics and Computer-Integrated Manufacturing*, 27:389–396, 2011.
- [100] F. Xie, X.-J. Liu, and T. Li. A comparison study on the orientation capability and parasitic motions of two novel articulated tool heads with parallel kinematics. *Advances in Mechanical Engineering*, 2013:ID 249103, 11 pages, 2013.
- [101] C.M Gosselin and J. Angeles. The optimum kinematic design of a spherical 3-dof parallel manipulator. *ASME Journal of Mechanisms, Transmissions and Automation in Design*, 111(2):202–207, 1989.
- [102] A. Rezaei, A. Akbarzadeh, P.M. Nia, and Akbarzadeh-T. Position, jacobian and workspace analysis of a 3-psp spatial parallel manipulators. *Robotics and Computer-Integrated Manufacturing.*, 29:158–173, 2013.

-
- [103] Y. Zhao, K. Qiu, S. Wang, and Z. Zhang. Inverse kinematics and rigid-body dynamics for a three rotation degrees of freedom parallel manipulator. *Robotics and Computer-Integrated Manufacturing.*, 31:40–50, 2015.
- [104] O. Altuzarra, O. Salgado, A. Hernández, and Ch. Pinto. Analytical determination of the instantaneous motion capabilities of robotic manipulators. In F. Viadero and M. Ceccarelli, editors, *New Trends in Mechanism and Machine Theory - Theory and Applications in Engineering.*, pages 95–103. Springer, 2013.
- [105] Y. Li and Q. Xu. Kinematic analysis of a 3-prs parallel manipulator. *Robotics and Computer-Integrated Manufacturing.*, 23:395–408, 2007.
- [106] G. Cheng, S-T. Wang, D-H. Yang, and J-H. Yang. Finite element method for kinematic analysis of parallel hip joint manipulator. *Journal of Mechanisms and Robotics.*, 7(4), 2015.
- [107] J-P. Merlet. Direct kinematics of parallel manipulators. *IEEE Transaction on Robotics and Automation*, 9(6):842–846, 1993.
- [108] L. Tancredi, M. Teillaud, and O. Devillars. Symbolic elimination for parallel manipulators. Technical Report 2809, INRIA, France, 1996.
- [109] A. Sommese, J. Verschelde, and C.W. Wampler. Advances in polynomial continuation for solving problems in kinematics. In *Proceedings of DETC' 02. ASME Design Engineering Technical Conferences.*, 2002.
- [110] A.K. Dhingra, A. Almadi, and D. Kohli. A gröbner-sylvester hybrid method for closed-form displacement analysis of mechanisms. *ASME Journal of Mechanical Design*, 122(4):431–438, 2000.
- [111] L. Jaulin, M. Kiefer, O. Didrit, and E. Walter. *Applied Interval Analysis*. Springer, London, 2001.

-
- [112] O. Didrit, M. Petitot, and E. Walter. Guaranteed solution of direct kinematic problems for general configurations of parallel manipulators. *IEEE Transaction on Robotics and Automation*, 14(2):259–266, 1998.
- [113] J-P. Merlet. Solving the forward kinematics of a gough-type parallel manipulator with interval analysis. *International Journal of Robotics Research.*, 23(3):221–235, 2004.
- [114] V. Petuya, Ch. Pinto, A. Alonso, O. Altuzarra, and A. Hernández. A general method based on geometrical constraints to solve the forward position problem in mechanisms. In T. Huang, editor, *Proceedings of the 11th World Congress in Mechanism and Machine Science.*, pages 110–114, 2003.
- [115] V. Petuya, A. Alonso, O. Altuzarra, and A. Hernández. Resolution of the direct position problem of parallel kinematic platforms using the geometrical-iterative method. In *Proceedings of the IEEE International Conference on robotics and Automation.*, pages 3255–3260, 2005.
- [116] L. Baron and J. Angeles. The decoupling of the direct kinematics of parallel manipulators using redundant sensors. In *IEEE International Conference on Robotics and Automation.*, volume 2, pages 974–979, 1994.
- [117] L. Baron and J. Angeles. The isotropic decoupling of the direct kinematics of parallel manipulators under sensor redundancy. In *IEEE International Conference on Robotics and Automation.*, volume 2, pages 1541–1546, 1995.
- [118] L. Baron and J. Angeles. A linear algebraic solution of the direct kinematics of parallel manipulators using a vision camera. In *Proceedings of the Ninth World Congress on the Theory of Machines and Mechanisms.*, volume 3, pages 1925–1929, 1995.

-
- [119] L. Baron and J. Angeles. The direct kinematics of parallel manipulators under joint-sensor redundancy. *IEEE Transaction on Robotics and Automation.*, 16(1):1–8, 2000.
- [120] L. Baron and J. Angeles. The kinematic decoupling of parallel manipulators using joint-sensor data. *IEE Transactions on Robotics and Automation.*, 16(6):644–651, 2000.
- [121] I. Bonev, J. Ryu, S.G. Kim, and S.K. Lee. A closed-form solutsol to the direct kinematics of nearly general parallel manipulators with ooptimal located three linear extra sensors. *IEEE Transaction on Robotics and Automation.*, 17(2):148–156, 2001.
- [122] Y. Chiu and M.H. Perng. Forward kinematics of a general fully parallel manipulator with auxiliary sensors. *International Journal of Robotics Research.*, 20(5):401–414, 2001.
- [123] S. Venanzi and V. Parenti-Castelli. A new technique for clearance influence analysis in spatial motions. *ASME Journal of Mechanical Design.*, 127(3):446–455, 2005.
- [124] Y. Zhang, H. Liu, and X. Wu. Kinematics analysis of a novel parallel manipulators. *Mechanism and Machine Theory.*, 44:1648–1657, 2009.
- [125] J. García de Jalón, M.A. Serna, and R. Avilés. Computer method for kinematic analysis of lower-pair mechanisms - i velocities and accelerations. *Mechanism and Machine Theory.*, 16(5):543556, 1981.
- [126] J.W. Eischen, H.K. Sun, and M.E. Marler. Multi-rigid-body kinematic analysis with elastic finite eelement. In *Proceedings of the 1990 ASME International Computers in Engineerings Conference.*, 1990.
- [127] A. Hernández, O. Altuzarra, R. Avilés, and V. Petuya. Kinematic analysis of mechanims via a velocity equation based in a geometric matrix. *Mechanism and Machine Theory.*, 38(12):1413–1429, 2003.

-
- [128] O. Altuzarra, O. Salgado, V. Petuya, and A. Hernández. Point-based jacobian formulation for computational kinematics of manipulators. *Mechanism and Machine Theory.*, 41(12):1407–1423, 2006.
- [129] O. Salgado. *Síntesis, Análisis y Diseño de Manipuladores Paralelos de Baja Movilidad*. PhD thesis, University of the Basque Country., 2008.
- [130] C. Gosselin and J. Angeles. Singularity analysis of closed-loop kinematic chains. *IEEE Transaction on Robotics and Automations*, 6:281–290, 1990.
- [131] D. Chablat and P. Wenger. Working modes and aspects in fully parallel manipulators. In *Proceeding IEEE International Conference Robotics and Automation.*, pages 1964–1969, 1998.
- [132] D. Zlatanov, R. G. Fenton, and B. Benhabib. Identification and classification of the singular configurations of mechanisms. *Mechanism and Machine Theory.*, 33(6):743–760, 1998.
- [133] L. Notash. Uncertainty configurations of parallel manipulators. *Mechanism and Machine Theory.*, 33(1):123–138, 1998.
- [134] M. López, E. Castillo, G. García, and A. Bashir. Delta robot: inverse, direct and intermediate jacobian. *Journal of Mechanical Engineering Science.*, 220:103–109, 2006.
- [135] O. Altuzarra, Ch. Pinto, R. Aviles, and A Hernandez. A practical procedure to analyze singular configurations in closed kinematic chains. *IEEE Transactions on Robotics*, 20:929–940, 2004.
- [136] V. Kumar. Characterization of workspaces of parallel manipulators. *Transactions of ASME Journal of Mechanical Design.*, 114:368–375, 1992.
- [137] F.C. Park and J.W. Kim. Singularity analysis of closed kinematic chains. *ASME Journal of Mechanical Design.*, 121:32–38, 1999.

-
- [138] H. Nigatu, A.P. Singh, and P. Prabhu. Jacobian analysis of limited dof parallel manipulator using wrench and reciprocal screw principle. *International Journal of Engineering Research & Technology.*, 3(4):354–357, 2014.
- [139] T. Yoshikawa. Manipulability of robotic mechanisms. *International Journal of Robotics Research.*, 1(1), 1982.
- [140] J. Corral, Ch. Pinto, F-J. Campa, and O Altuzarra. Performance index of an industrial parallel robot. In *Proceedings of ISR 2012*, 2012.
- [141] O. Altuzarra, S. Bogdan, C. Pinto, and V. Petuya. A symmetric parallel schoenflies-motion manipulator for pick-and-place operations. *Robotica* 29, 6:853–862, 2011.
- [142] S.K. Agrawal. Workspace boundaries of in-parallel manipulator systems. In *in ICAR*, pages 1147–1152, 1991.
- [143] R. Di Gregorio and R. Zanforlin. Workspace analytic determination of two similar translational parallel manipulators. *Robotica.*, 2003.
- [144] I.A. Bonev and C-M. Gosselin. Analytical determination of the workspace of symmetrical spherical parallel mechanisms. *IEEE Transaction on Robotics.*, 22(5):1011–1017, 2006.
- [145] J-P. Merlet. Geometrical determination of the workspace of a constrained parallel manipulator. In *in ARK*, pages 326–329, 1992.
- [146] J-P. Merlet. Determination of the orientation workspace of parallel manipulators. *Journal of Intelligent and Robotic Systems.*, 13:143–160, 1995.
- [147] X-J. Liu, J. Wang, and H. Zheng. Workspace atlases for the computer aided design of the delta robot. *Journal of Mechanical Engineering Science*, 217:861–869, 2003.

- [148] X-J Liu, J. Wang, K-K. Oh, and J. Kim. A new approach to the design of a delta robot with a desired workspace. *Journal of Intelligent and Robotic Systems.*, 39:209–225, 2004.
- [149] J-P. Merlet. Determination of 6d workspaces of gough-type parallel manipulator and comparison between different geometries. *The International Journal of Robotics Research*, 18:902–916, 1999.
- [150] D. Andrioaia, M. Pascu, L. Mihaila, and C. Obrea. Determining the workspace in case of the robots with parallel structure delta 3dof. In B. Katalinic, editor, *Annals of DAAAM for 2012 & Proceedings of the 23rd International DAAAM Symposium.*, volume 23, pages 1123–1126. DAAAM International, 2012.
- [151] S Herrero, T. Mannheim, I. Prause, Ch. Pinto, B Corves, and O. Altuzarra. Enhancing the useful workspace of a reconfigurable parallel manipulator by grasp point optimization. *Robotics and Computer-Integrated Manufacturing*, 31:51–60, February 2015.
- [152] E Macho, O Altuzarra, E Amezua, and A Hernandez. Obtaining configuration space and singularity maps for parallel manipulators. *Mechanism and Machine Theory*, 44:2110–2125, 2009.
- [153] L. Haidong, C-M. Gosselin, and M-J. Richard. Determination of the maximal singularity-free zones in the six-dimensional workspace of the general gough-stewart platform. *Mechanism and Machine Theory*, 42:497–511, 2007.
- [154] R. Avilés. *Métodos de análisis para diseño mecánico. Vol II: elementos finitos en estática.* Escuela de Ingeniería de Bilbao, 2002.
- [155] B. Bouzgarrou, J. Fauroux, G. Gogu, and Y. Heerah. Rigiditstiffness of t3r1 parallel robot with uncoupled kinematics. In *Proceedings of the 35th International Symposium on Robotics (ISR)*, Paris, France, 2004.

-
- [156] A. Kozyrev and Glazunov V. *Finite Element Modeling and Analysis of an Isoglide-Type Parallel Manipulator to Determine Its Rigidity/Stiffness. New Trends in Mechanism and Machine Science.* Number 24 in 2211-0984. Springer International Publishing, 2015.
- [157] H.C. Martin. *Matrix structural analysis.* 1966.
- [158] C. M. Clinton, G. Zhang, and A.J. Wavering. Stiffness modeling of a stewart-platform-based miling machine. *Transactions of the North America Manufacturing Research Institution of SME*, XXV:335–340, 1997.
- [159] D. Deblaise, X. Hernot, and P. Maurine. A systematic analytical method for pkm stiffness matrix calculation. In *Conference on Robotics and Automation, 2006. ICRA 2006. Proceedings IEEE International*, pages 4213 – 4219, 2006.
- [160] R. Sales Goncalves and J.C. Mendes Carvalho. Stiffness analysis of parallel manipulator using matrix structural analysis. In Ceccarelli, editor, *Proceedings of EUCOMES08.* Springer, 2008.
- [161] J. Corral. *Caracterizacion del comportamiento estructural de manipuladores de cinemática paralela.* PhD thesis, University of the Basque Country, Spain, 2011.
- [162] K. Salisbury. Active stiffness control of a manipulator in cartesian coordinates. In *19th IEEE Conference on Decision and Control including the Symposium on Adaptative Processes*, pages 95–100, 1980.
- [163] C. Gosselin. Siffness mapping for parallel manipulators. *IEEE Transaction on Robotics and Automations*, 6:377–382, 1990.
- [164] D. Zhang. *Kinetostatic analysis and optimization of parallel and hybrid aarchitecture for machine toolds.* PhD thesis, Laval University, Quebec, Canada, 2000.

-
- [165] S-F. Chen and I. Kao. Conservative congruence transformation for joint and cartesian stiffness matrices of robotic hands and fingers. *The International Journal of Robotics Research*, 19(9):835–847, September 2000.
- [166] S-F. Chen and I. Kao. Geometrical approach to the conservative congruence transformation (cct) for robotic stiffness control. In *Proceedings of the 2002 IEEE International Conference on Robotics & Automation*, 2002.
- [167] G. Alici and B. Shirinzadeh. Enhanced stiffness modeling, identification and characterization for robot manipulators. *IEEE Transaction on Robotics*, 21(4):554–564, 2005.
- [168] C. Gosselin and D. Zhang. Stiffness analysis of a parallel mechanism using a lumped model. *International Journal of Robotics and Automation*, 17:17–27, 2002.
- [169] T. Pigoski, M. Griffis, and J. Duffy. Stiffness mapping employing different frames of reference. *Mechanism and Machine Theory*, 33:825–838, 1998.
- [170] F. Majou, C. Gosselin, P. Wenger, and D. Chablat. Parametric stiffness analysis of the orthoglide. *Mechanism and Machine Theory*, 42:296–311, 2007.
- [171] A. Pashkevich, D. Chablat, and P. Wenger. Stiffness analysis of over-constrained parallel manipulators. *Mechanism and Machine Theory*, 44:966–982, 2009.
- [172] A. Klimchik, A. Pashkevich, and D. Chablat. Cad-based approach for identification of elasto-static parameters of robotic manipulators. *Finite Elements in Analysis and Design*, 75:19–30, 2013.
- [173] A. Rezaei, A. Akbarzadeh, and M. Akbarzadeh-T. An investigation on stiffness of a 3-psp spatial parallel mechanism with flexible mo-

- ving platform using invariant form. *Mechanism and Machine Theory*, 51:195–216, 2012.
- [174] A. Klimchik, D. Chablat, and A. Pashkevich. Stiffness model for perfect and non-perfect parallel manipulators under internal and external loadings. *Mechanism and Machine Theory*, 79:1–28, 2014.
- [175] ANSI/ASME. *B5.54-1992 Methods for Performance Evaluation of Computer Controlled Machining Centers*. ASME, 1993.
- [176] J. Aginaga, I. Zabala, O. Altuzarra, and Jasiel Nájera. Improving static stiffness of the 6Rus parallel manipulator using inverse singularities. *Robotics and Computer-Integrated Manufacturing*, 28:458–471, 2012.
- [177] O. Company, F. Pierrot, and J. Faroux. A method for modeling analytical stiffness of a lower mobility parallel manipulator. In *Proceedings of the 2005 IEEE international conference on robotics and automation*, pages 3232–3237, 2005.
- [178] M. Ceccarelli and G. Carbone. Numerical and experimental analysis of the stiffness performance of parallel manipulators. In *Second international colloquium . Collaborative Research Centre 562.*, 2005.
- [179] Ch. Pinto, J. Corral, O. Altuzarra, and A. Hernández. A methodology for static stiffness mapping in lower mobility parallel manipulators with decoupled motions. *Robotice*, 28(5):719–735, 2010.
- [180] B. Dasgupta and T.S. Mruthyunjaya. Closed-form dynamic equation of the stewart platform through the newton-euler approach. *Mechanism and Machine Theory.*, 33(7):993–1012, 1998.
- [181] B. Dasgupta and T. Mruthyunjaya. A newton-euler formulation for the inverse dynamics of the stewart platform manipulator. *Mechanism and Machine Theory.*, 33(8):1135–1152, 1998.

- [182] P. Gugliemetti and R. Longchamp. A closed form inverse dynamic model of the delta parallel robot. In *In 4th Symposium on Robot Control.*, pages 51–56, 1994.
- [183] W. Khalil and S. Guegan. Inverse and direct dynamic modeling of gough-stewart robots. *IEEE Transaction on Robotics and Automation.*, 20(4):754–762, 2004.
- [184] J.C.M Carvalho and M. Ceccarelli. A closed-form formulation for the inverse dynamics of a cassino parallel manipulator. *Multibody System Dynamics*, 5(2):185–210, 2001.
- [185] J.S. Wang, J. Wu, L.P. Wang, and T.M. Li. Simplified strategy of the dynamic model of a 6-ups parallel kinematic machine for real-time control. *Mechanism and Machine Theory.*, 42(9):1119–1140, 2007.
- [186] W. Khalil and O. Ibrahim. General solution for the dynamic modeling of parallel robots. *Journal of Intelligent and Robotic Systems: Theory and Applications.*, 49(1):19–37, 2007.
- [187] J.D. Lee and Z. Geng. A dynamic model of a flexible stewart platform. *Computers & Structures.*, 48(3):367–374, 1993.
- [188] H. Abdellatif and B. Heimann. Computational efficient inverse dynamics of 6-dof fully parallel manipulators by using lagrangian forforma. *Mechanism and Machine Theory.*, 44:192–207, 2009.
- [189] X. Liu, Q. Wang, A. Malikov, and H. Wang. The design and dynamic analysis of a novel 6-dof parallel mechanism. *International Journal of Machine Learning and Cybernetics.*, 3:27–37, 2012.
- [190] T. R. Kane. *Dynamics: Theory and Applications*. McGraw-Hill Book Company, 1985.
- [191] T. R. Kane and D.A. Levinson. The use of kane’s dydynamic equation in robotics. *International Journal of Robotics Research.*, 2(3), 1983.

- [192] Y. Wang, S. Zheng, J. Jin, H. Xu, and J. Han. Dynamic modeling of spatial 6-dof parallel manipulator using kane method. In IEEE 978-1-4244-7159-1, editor, *International Conference on E-Product E-Service and E-Entertainment (ICEEE)*, pages 1–5, 2010.
- [193] M-J. Liu, C-X. Li, and C-N. Li. Dynamics analysis of the gough-stewart platform manipulator. *IEEE Transaction on Robotics and Automation.*, 16(1):94–98, 2000.
- [194] P. Wu, H. X, and J. K. Dynamic analysis of 6-sps parallel mechanism. *International Journal of Mechanics and Materials in Design*, 8:121–128, 2012.
- [195] T. Geike and J. McPhee. Inverse dynamic analysis of parallel manipulators with 3 or 6 degrees of freedom. In G. Bianchi, J-C. Guinot, and C. Rzymkowski, editors, *Romansy 14 - Theory and practice of robots and manipulators. Proceeding of the 14th CISM-IFTOMM Symposium.*, pages 49–58, 2002.
- [196] Y. Zhao and F. Gao. Inverse dynamics of the 6-dof out-parallel manipulator by means of the principle of virtual work. *Robotica.*, 27:259–268, 2008.
- [197] Y. Zhao. Dynamic performance evaluation of a three translational degrees of freedom parallel robot. *International Journal of Robotics and Automation.*, 27(1):31–40, 2012.
- [198] M. García-Murillo, E. Castillo-Castaneda, and J. Gallardo-Alvarado. Dynamics of a 2(3-rrps) parallel manipulators. In *Proceedings of the 9th International Workshop on Robot Motion and Control.*, pages 270–275, 2013.
- [199] G. Piras, W. Cleghorn, and J. Mills. Dynamic finite-element analysis of a planar high-speed, high-precision parallel manipulator with flexible links. *Mechanism and Machine Theory.*, 40(7):849–862, 2005.

- [200] Z. Du, Y. Yu, and J. Yang. Analysis of the dynamic stress of planar flexible-links parallel robots. *Frontiers of Mechanical Engineering.*, 2(2):152–158, 2007.
- [201] A. Müller and P. Maiber. A lie-group formulation of kinematics and dynamics of constrained mbs and its application to analytical mechanics. *Multibody System Dynamics.*, 9(4):311–352, 2003.
- [202] T. Geike and J. McPhee. Inverse dynamic analysis of parallel manipulators with full mobility. *Mechanism and Machine Theory.*, 38(6):549–562, 2003.
- [203] J. McPhee, P. Shi, and J.C. Piedboeuf. Dynamics of multibody systems using virtual work and symbolic programming. *Mathematical and Computer Modelling of Dynamical Systems.*, 8(3):137–155, 2002.
- [204] M. Hüsing, M. Riedel, B. Corves, and M. Nefzi. Development of tailor-made robots - from concept to realization for small and medium-sized enterprises. In *13th World Congress in Mechanism and Machine Science*, 2011.
- [205] D. Modungwa, N.S. Tlale, and B. Twala. Ttechnique applied in design optimization of parallel manipulators. In *4th Robotics and Mechatronics Conference of South Africa (ROBMECH)*, 2011.
- [206] J-P. Merlet. desdesign a parallel manipulator for a specific workspace. *The International Journal of Robotics Research.*, 16:545–556, 1997.
- [207] M.A. Laribi, L. Romdhane, and S. Zeghloul. Analysis and dimensional synthesis of the delta robot for a prescribed workspace. *Mechanism and Machine Theory.*, 42:859–870, 2007.
- [208] A. Kosinska, M. Galicki, and K. Kedzior. Desdesign and optimization of parameters of delta-4 parallel manipulator for a given workspace. *Journal of Robotic Systems.*, 20:539–548, 2003.

-
- [209] T. Huang, B. Jiang, and D.J. Whitehouse. Determination of the carriage stroke of 6-pss parallel manipulators having the specific orientation capability in a prescribed workspace. In *in Proceedings 2000 ICRA. Millennium Conference. IEEE International Conference on Robotics and Automation.*, pages 2382–2385, 2000.
- [210] S. Zhao, J. Zhang, J. Dong, Z. Feng, and K. Zhou. Optimizing the kinematic chains for a spatial parallel manipulator via searching the desired dexterous workspace. *Robotics and Computer-Integrated Manufacturing.*, 23:38–46, 2007.
- [211] L.W. Tsai and S. Joshi. Kinematics and optimization of a spatial 3-UPU parallel manipulator. *Journal of Mechanical Design*, 122:439–446, 2000.
- [212] X. Zhang and H. Fang. Optimization of a 3-prs parallel manipulator based on interval analysis. In *Proceedings of the 10th World Congress on Intelligent Control and Automation.*, pages 2452–2456, 2012.
- [213] Y. Hou and Y. Zhao. Workspace analysis and optimization of 3-puu parallel mechanism in medicine base on genetic algorithm. *The open Biomedical Engineering Journal.*, 9:214–218, 2015.
- [214] K.H. Pittens and R.P. Podhorodeski. A family of stewart platforms with optimal dexterity. *Journal of Robotic Systems.*, 10(4):463–479, 1993.
- [215] C-M. Gosselin and J. Angeles. A global performance index for the kinematic optimization of robotic manipulators. *Journal of Mechanical Design.*, 113:220–226, 1991.
- [216] M.R. Barbosa, E.J. Solteiro Pires, and A.M. Lopes. Design optimization of a parallel manipulator based on evolutionary algorithms. In *International Symposium on Computation Intelligence for Engineering.*, 2009.

- [217] A.M. Lopes, E.J. Solteiro Pires, and M.R. Barbosa. Design of a parallel robotic manipulator using evolutionary computing. *International Journal of Advanced Robotic Systems.*, 9(26), 2012.
- [218] Marwène Nefzi, Clément Gosselin, Martin Riedel, Mathias Hüsing, and Burkhard Corves. *Intelligent Robotics and Applications: 4th International Conference, ICIRA 2011, Aachen, Germany, December 6-8, 2011, Proceedings, Part I*, chapter Dimensional Synthesis of Parallel Manipulators Based on Direction-Dependent Jacobian Indices, pages 152–161. Springer Berlin Heidelberg, Berlin, Heidelberg, 2011.
- [219] D. Chakarov. Optimization synthesis of parallel manipulators with desired stiffness. 1998.
- [220] S.R. Babu, V.R. Raju, and K. Ramji. Design for optimal performance of 3-rps parallel manipulator using evolutionary algorithms. *Transactions of the Canadian Society for Mechanical Engineering.*, 37(2):135–155, 2013.
- [221] G. Wu, S. Caro, S. Bai, and J. Kepler. Dynamic modeling and design optimization of a 3-dof spherical parallel manipulator. *Robotics and Autonomous Systems.*, 62:1377–1386, 2014.
- [222] X-J. Liu and J. Wang. A new methodology for optimal kinematic design of parallel manipulators. *Mechanism and Machine Theory.*, 42:1210–1224, 2007.

Figure Index

1.1.	Types of robots by applications	7
1.2.	Unimate robot. Courtesy of Unimation	8
1.3.	PUMA robot. Courtesy of Unimation	9
1.4.	SCARA robot. Courtesy of Adept	10
1.5.	6-axis serial robot. Courtesy of KUKA Robotics	11
1.6.	Possibly the first spatial parallel mechanism, by Gwinnett	15
1.7.	Spray painting machine patented by Pollard Jr.	16
1.8.	Gough's platform at Dunlop factory: (a) in 1950; (b) in 2000	17
1.9.	Flight simulator proposed by Stewart	18
1.10.	Platform proposed by Cappel: (a) patent; (b) flight simulator	19
1.11.	Schematic representation of the Delta robot	20
1.12.	Felxpicker model IRB 360-6. Courtesy of ABB	21
1.13.	Packaging system Paloma. Courtesy of Bosch	22
1.14.	M-2 <i>i</i> A robot in: (a) food application; (b) packaging application	22
1.15.	GRACE flight simulator. Courtesy of NLR	23
1.16.	Medical PM for resuscitation: (a) force to be done; (b) CAD	25
1.17.	MARIONET: (a) REHAB CAD; (b) REHAB prototype; (c) CRANE taking a victim; (D) CRANE freeing a victim. Courtesy of INRIA	26
1.18.	Typical tool heads: (a) the Sprint Z3; (b) A3 tool head	28
1.19.	Two PKMs: (a) Cosmo Center. Courtesy of Okuma; (b) V100. Courtesy of Index	29
1.20.	Hexa 6-DOF parallel manipulator	30

1.21.	Two machine centres with PKMs: (a) Cosmo Center PM-600. Courtesy of Okuma; (b) Vertical Turning Machine V100. Courtesy of Index	31
1.22.	Spherical manipulators: (a) Agile Eye; (b) 3(RSS)-S PM	32
1.23.	1T2R PMs: (a) 3-PRS PM; (b) 3-CRS/PS PM	33
1.24.	Novel lower mobility PMs: (a) 5-(RRR)(RR) proposed by Zhu PM; (b) endoscopic PM proposed by Ibrahim	34
2.1.	Multi-axis machines: (a) multi-axis shaking table. Courtesy of Moog; (b) multi-axis simulation table. Courtesy of Lufthansa; (c) multi-axis positioning system	38
2.2.	The Milne-Omori railway truck shaking table	41
2.3.	Shaking table proposed by Rogers	42
2.4.	Shaking table designed by Jacobsen	43
2.5.	Sketch of Ruge's shaking table	44
2.6.	6-DOF SAMSON shaking table	47
3.1.	3PRS PM proposed by Carretero	52
3.2.	3PRS PM proposed by Tsai: (a) CAD; (b) geometry sketch	53
3.3.	3PRS PM proposed by Merlet: (a) sketch; (b) prototype	54
3.4.	Different 3PRS PMs compared: (a) Carretero et al.; (b) Tsai et al.; (c) Merlet	54
3.5.	Categories of the 3PRS PM: (a) category 1; (b) subcategory 2.1; (c) subcategory 2.2; (d) subcategory 3.1; (e) subcategory 3.2; (f) subcategory 4.1; (g) subcategory 4.2	56
3.6.	Novel architectures compared by Xie et al.: (a) 2PRU-1PRS PM; (b) 2PRU-1PUR	57
3.7.	Manipulator analysed in this work	58
4.1.	Analysis methodology	61
4.2.	Optimization methodology	63
5.1.	Sketch of the manipulator	68
6.1.	Sketch of the manipulator	74

8.1.	Flowchart for obtaining the useful WS	101
8.2.	Division of the WS based on polarity of $ J_x $	102
8.3.	Sphere Joint	103
9.1.	Equivalent stiffness for: (a) two serial chains; (b) two parallel chains	106
9.2.	Basic steps of the stiffness matrix method	114
9.3.	Elements and nodes numeration	115
9.4.	Beams axes	116
9.5.	Degrees of freedom allowed in: (a) revolution joint; (b) universal joint; (c) spherical joint	119
9.6.	Degrees of freedom numeration	119
10.1.	Reaction forces, moments and weights in the manipulator . . .	127
10.2.	Parameters of the dynamic problem	128
11.1.	Optimization of GP to maximise the GO in the WS	159
11.2.	Optimization of GP to maximise the GO in the WS	161
12.1.	Possible configurations (a) $H > R$; (b) $H < R$	165
12.2.	Two optimal GP: (a) sketch of $(H, L, R) = (0.35, 0.25, 0.2)$ m; (b) WS_{use} & S_{max} for $(H, L, R) = (0.35, 0.25, 0.2)$ m; (c) sketch of $(H, L, R) = (0.6, 0.6, 0.2)$ m; (d) useful WS & S_{max} for $(H, L, R) = (0.6, 0.6, 0.2)$ m	169
12.3.	Power consumption for all the suitable GP for trajectory I . .	174
12.4.	Trajectory I: (a) displacement of the linear guides ; (b) velocity of the linear guides	175
12.5.	Trajectory I: (a) axial force in the linear guides ; (b) radial force in the linear guides; (c) power required by the motors	176
12.6.	Power consumption for all the suitable GP for trajectory II . .	177
12.7.	Trajectory II: (a) displacement of the linear guides ; (b) velocity of the linear guides	178
12.8.	Trajectory II: (a) axial force in the linear guides ; (b) radial force in the linear guides	179

12.9. Power in the actuators for all the suitable the best GP for translation about Z-axis	180
12.10. Trajectory III: (a) displacement of the linear guides ; (b) velocity of the linear guides	181
12.11. Trajectory III: (a) axial force in the linear guides ; (b) radial force in the linear guides	182
13.1. Dimensions of the prototype	188
14.1. Chosen products: (a) DC motor. Courtesy of Maxon; (b) planetary gearhead. Courtesy of Maxon; (c) linear guide. Courtesy of Igus	190
14.2. Assembly	191
14.3. Revolute joint axes	192
14.4. Revolute joint parts	193
14.5. Revolute joint: (a) CATIA drawing; (b) final solution	193
14.6. Universal joint axes	194
14.7. Typical universal joint courtesy of Waft: (a) real rotation axes (b) desired rotation axes	195
14.8. Universal joint parts for the rotation about Y-axis	196
14.9. Universal joint seen from different views	196
14.10. Spherical joint axes	197
14.11. Spherical joint	198
14.12. Assembly of the spherical joint	198
14.13. Spherical joint: (a) union with the platform; (b) spring	199
14.14. Fixed platform	200
14.15. Mobile platform: (a) ideal shape; (b) real platform	201
14.16. Assembly of the whole manipulator	201
14.17. Inclinometers to measure the real position	202
14.18. Measurement system	205
14.19. Parasitic motion	206
15.1. Trajectory I	209

15.2. Kinematics for trajectory I: (a) actuators' displacement; (b) actuators' velocity; (c) actuators' acceleration	210
15.3. Trajectory II	211
15.4. Trajectory II kinematics: (a) actuators displacement; (b) actuators velocity; (c) actuators acceleration	212
15.5. Trajectory III	213
15.6. Trajectory III kinematics: (a) actuators displacement; (b) actuators velocity; (c) actuators acceleration	214
15.7. DKP singularities	217
15.8. IKP singularities	218
15.9. WS_0	220
15.10. Workspaces: (a) WS_1 ; (b) WS_2 ; (c) WS_3 ; (d) WS_{use}	222
15.11. Useful WS with the S_{max} placed in the first possible position: (a) general view; (b) plane YZ view; (c) plane XZ view; (d) plane XY view	223
15.12. Extreme positions analysed: (a) $(\psi, \theta) = (-15^\circ, 0^\circ)$; (b) $(\psi, \theta) = (15^\circ, 0^\circ)$; (c) $(\psi, \theta) = (-15^\circ, 15^\circ)$; (d) $(\psi, \theta) = (15^\circ, 15^\circ)$	225
15.13. Stiffness of the prototype calculate analytically	226
15.14. Manipulator drawn in CATIA	227
15.15. Constraints in ANSYS: (a) cylindrical support; (b) revolute condition	228
15.16. Mesh generated on ANSYS for: (a) universal joint; (b) spherical joint; (c) revolute joint	229
15.17. Result for horizontal position: (a) definition of the unit applied force; (b) deformation for that force	230
15.18. Stiffness of the manipulator in the positions analysed	231
15.19. Stiffness experimental measurement: (a) dial gauge; (b) force applied on the GC	232
15.20. Trajectory I: (a) axial force in the linear guides ; (b) radial force in the linear guides; (c) power required by the motors	236
15.21. Trajectory II: (a) axial force in the linear guides ; (b) radial force in the linear guides; (c) power required by the motors	237
15.22. Trajectory III: (a) axial force in the linear guides ; (b) radial force in the linear guides; (c) power required by the motors	239

15.23. First mode obtained with FEM: flexion of the mobile platform at 22.48 Hz	241
15.24. Second mode obtained with FEM: flexion of the mobile platform with a node along Y-axis direction at 58.839 Hz	242
15.25. Third mode obtained with FEM: flexion of the limbs in X-axis direction at 71.759 Hz	242
15.26. Fourth mode obtained with FEM: flexion of the mobile platform with a node from limb 1 to limb 3 at 79,493 Hz	243
15.27. Fifth mode obtained with FEM: flexion of the limbs in Y-axis direction at 125.72 Hz	243
15.28. Natural frequencies obtained with FEM	244
15.29. Siemens LMS TestLab analyser	246
15.30. Measurement along Z-axis: (a) accelerometer on X-axis; (b) vertical impulse	247
15.31. Measurement along X-axis: (a) accelerometer on joint U in X-axis direction; (b) impulse in X-axis direction	247
15.32. Measurement along Y-axis: (a) accelerometer on joint U in X- and Y-axes direction; (b) impulse in Y-axis direction	248
15.33. Response obtained in the accelerometer in X-axis direction for the positions: (a) $\psi = 0^\circ, \theta = 0^\circ$; (b) $\psi = -15^\circ, \theta = 5^\circ$	249
15.34. Response obtained in the accelerometer in Y-axis direction for the positions: (a) $\psi = 0^\circ, \theta = 0^\circ$; (b) $\psi = -15^\circ, \theta = 5^\circ$	250
15.35. Response obtained in the accelerometer in Z-axis direction for the positions: (a) $\psi = 0^\circ, \theta = 0^\circ$; (b) $\psi = -15^\circ, \theta = 5^\circ$	250
15.36. Experimental natural frequencies	252
16.1. Interface for power optimization	259

Table Index

1.1. Parallel manipulators vs serial manipulators	14
3.1. Categories of the 3PRS PM	55
7.1. Singularity classes presented by Zlatanov et al.	90
12.1. GP ranges for the optimization process	164
12.2. Output limits	166
12.3. Physical restrictions	166
12.4. GP combinations for biggest sphere in WS	167
12.5. Best GP combinations for biggest sphere in maximum number of positions in WS	168
12.6. Parameters	170
12.7. Motor, gearhead and linear guide data	171
12.8. Harmonic trajectories definition	173
13.1. Geometry parameters	188
14.1. Motor, gearhead and linear guide data	191
14.2. Theoretical and real angles for given value of the linear guides	203
14.3. Theoretical value of the parasitic motion (m)	204
14.4. Real value of the parasitic motion (m)	205
15.1. Harmonic trajectories definition	208
15.2. Output limits	216

15.3. Output limits	219
15.4. Physical restrictions	219
15.5. Stiffness obtained analytically ($\times 10^4$ N/m)	226
15.6. Stiffness obtained with ANSYS ($\times 10^4$ N/m)	231
15.7. Experimental data of the stiffness measurement	233
15.8. Harmonic trajectories definition	234
15.9. Frequencies obtained with FEM	245
15.10. Frequencies obtained experimentally	251